Acoustical Physics, Vol. 49, No. 2, 2003, pp. 119–124. Translated from Akusticheskiĭ Zhurnal, Vol. 49, No. 2, 2003, pp. 149–155.

Active Minimization of Acoustic Potential Energy in a Two-Dimensional Multimode Waveguide

G. V. Alekseev and T. S. Komashinskaya

Institute of Applied Mathematics, Far East Division, Russian Academy of Sciences, ul. Radio 7, Vladivostok, 690041 Russia

e-mail: alekseev@iam.dvo.ru

Received August 22, 2001

Abstract—The nonlinear inverse problem of active sound control in a two-dimensional waveguide is addressed. To solve the problem, a numerical algorithm based on an exhaustive search for coordinates of the desired sources over a curvilinear mesh and on the regularized quadratic algorithm for minimization with respect to their intensities is proposed. Numerical results for circular and elliptical antenna arrays are discussed. *© 2003 MAIK "Nauka/Interperiodica".*

Linear and nonlinear problems of active sound control in both space and waveguides have been much investigated in the last ten years. The development of efficient numerical algorithms for solving these problems has been the objective of a number of works. Among these, we should mention [1–19], in which efficient numerical algorithms of active sound control are elaborated for free-space and layered-waveguide problems and the results of numerical experiments are discussed.

In the framework of the theory developed in the aforementioned works, linear and nonlinear sound control problems are solved in terms of the minimization of certain goal functions, which depend on a number of controlled parameters. If the sound is controlled with the help of a secondary antenna array, the controlled parameters may include complex amplitudes of the point sources, as well as their coordinates. A series of works [16–19] is devoted to solving the general nonlinear sound control problems in two-dimensional and three-dimensional waveguides through the optimal choice of coordinates and intensities of the point monopoles. The goal function is defined in these works as the total power of the primary and secondary acoustic fields carried to the far zone of the waveguide.

An alternative approach defines the goal function to be minimized in terms of the potential energy of the acoustic field created by the primary source and by the secondary compensating antenna. This approach is used in [6, 7], where the intensities of several vibrating pistons located on the walls of a three-dimensional waveguide were chosen as the controls.

Note that the numerical experiments on active sound control that are described, for example, in [16–19] cover only shallow waveguides in which no more than several tens of normal modes can propagate. However, in practice, one also has to deal with deep-water waveguides with several hundred to several thousand modes propagating in them.

The purpose of this paper is to consider the general nonlinear problem of the active minimization of the potential energy of acoustic field in a two-dimensional waveguide. This problem consists in finding the coordinates, the complex intensities, and the number of the compensating antenna elements from the condition of minimal potential energy of the total acoustic field within a certain region of the waveguide. To solve this problem, we adapt the numerical algorithm developed in [16–19] to the active sound control problem. Unlike [16–19], we consider a multimode waveguide where hundreds of modes can propagate and use curvilinear (circular or elliptic) arrays as the compensating antennas.

Let a primary source operating at the frequency ω be placed into a planar regular waveguide $D = D_H = \{\mathbf{x} = (x, z) : 0 < z < H, -\infty < x < \infty\}$ of depth H with density $\rho(z)$ and velocity of sound $c(z)$. The acoustic field emitted by the source can be written as

$$p_b(x, z) = -\frac{i}{2}\sum_{n=1}^{\infty} \xi_n^{-1/2} b_n \varphi_n(z) \exp(i\xi_n x). \qquad (1)$$

Here, b_n are the given values characterizing the primary source and ξ_n^2 and φ_n are the eigenvalues and eigenfunctions of the spectral problem

$$\rho(z)\frac{d}{dz}\left[\frac{1}{\rho(z)}\frac{d\varphi}{dz}\right] + [k^2(z) - \xi^2]\varphi = 0, \quad z \in (0, H),$$
$$\varphi(0) = 0, \quad \sin\beta\varphi(H) + \cos\beta\varphi'(H) = 0, \qquad (2)$$
$$\beta \in [0, \pi/2],$$

where the parameter β determines the acoustic properties of the lower boundary. We consider this waveguide

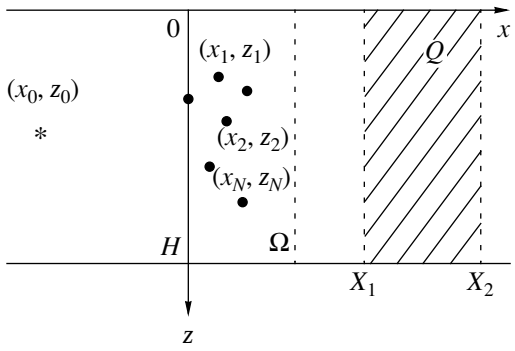

Fig. 1. Geometry of a two-dimensional waveguide.

as shallow if $M \approx 10$, of medium depth if $M \approx 100$, and a deep-water waveguide if $M \approx 1000$.

It is well known that problem (2) has a countable set of eigenvalues and that the following conditions are satisfied beginning with a certain $M \geq 1$:

$$\xi_1^2 > \xi_2^2 > \ldots > \xi_M^2 \geq 0 > \xi_{M+1}^2 > \ldots \longrightarrow -\infty. \quad (3)$$

We also assume that $\xi_M^2 > 0$, which means that the waveguide D is a nonresonance one. Consider the $(2 \times N)$ matrix (array) $\mathbf{Z}$ and the vector $\mathbf{q} \in \mathbb{C}^N$ of intensities of the secondary sources:

$$\mathbf{Z} = \begin{pmatrix} x_1 & x_2 & \ldots & x_N \\ z_1 & z_2 & \ldots & z_N \end{pmatrix}, \quad \mathbf{q} = (q_1, q_2, \ldots, q_N). \quad (4)$$

The pair $(\mathbf{Z}, \mathbf{q})$ describes an antenna array of N elements located at the coordinates (x_j, z_j) and excited with intensities q_j, $j = 1, 2, \ldots, N$. Let us call this antenna the secondary or compensating antenna. The field emitted by the antenna $(\mathbf{Z}, \mathbf{q})$ has the form [16]

$$p(x, z) = \frac{i}{2}\sum_{n=1}^{\infty}\sum_{j=1}^{N}\xi_n^{-1} q_j \varphi_n(z_j)\varphi_n(z)\exp(i\xi_n(x - x_j)). \quad (5)$$

Let us derive a formula to describe the potential energy of the acoustic field. For the sake of simplicity, assume that the acoustic velocity is constant, $c = \text{const}$. In this case, the potential energy W of the acoustic field in the region Q (the suppression region) is calculated as

$$W = \frac{1}{2c^2}\int_Q \frac{|p|^2}{\rho(z)}\mathrm{d}x\mathrm{d}z. \quad (6)$$

Let the suppression region Q be the rectangle $Q = \{\mathbf{x} = (x, z) : X_1 < x < X_2, 0 < z < H\}$ located on the right of the array $\mathbf{Z}$ (see Fig. 1). Consider the infinite rectangular $(\infty \times N)$ matrix $A = A(\mathbf{Z})$ with the components a_{nj}, where

$$a_{nj} = (X_2 - X_1)^{1/2}\frac{\varphi_n(z_j)}{\xi_n}\exp(-i\xi_n x_j), \quad j = 1, 2, \ldots, N, \quad n \leq M, \quad (7)$$

$$a_{nj} = \left[\frac{\exp(-2|\xi_n|X_1) - \exp(-2|\xi_n|X_2)}{2|\xi_n|}\right]^{1/2}\frac{\varphi_n(z_j)}{|\xi_n|} \times \exp(-i|\xi_n|x_j), \quad n > N. \quad (8)$$

By substituting Eq. (5) into Eq. (6), with allowance for Eqs. (7) and (8), we arrive at the following formula for the potential energy W of the acoustic field created by the pair $(\mathbf{Z}, \mathbf{q})$ in the region Q:

$$W = W(\mathbf{Z}, \mathbf{q}) = \frac{1}{8c^2}|[A\mathbf{q}]|_\infty^2 \equiv \frac{1}{8c^2}\sum_{n=1}^{\infty}\left|\sum_{j=1}^{N} a_{nj}q_j\right|^2. \quad (9)$$

Consider an infinite-dimensional vector $\mathbf{b} \in \mathbb{C}^\infty$ with the components b_n, where

$$b_n = \frac{b_n}{\sqrt{\xi_n}}(X_2 - X_1)^{1/2}, \quad n \leq M, \quad (10)$$

$$b_n = \frac{b_n}{\sqrt{|\xi_n|}}\left[\frac{\exp(-2|\xi_n|X_1) - \exp(-2|\xi_n|X_2)}{2|\xi_n|}\right]^{1/2}, \quad n > M. \quad (11)$$

As above, it can easily be shown that the potential energy W_b of the field p_b and the potential energy $W(\mathbf{Z}, \mathbf{q}, \mathbf{b})$ of the total field $p + p_b$ in the region Q can be written as

$$W_b = \frac{1}{8c^2}|[\mathbf{b}]|_\infty^2 \equiv \frac{1}{8c^2}\sum_{n=1}^{\infty}|b_n|^2, \quad W(\mathbf{Z}, \mathbf{q}, \mathbf{b}) = \frac{1}{8c^2}|[A\mathbf{q} - \mathbf{b}]|_\infty^2. \quad (12)$$

Formula (12) for the potential energy of the acoustic field $p + p_b$ in the region Q has the form of an infinite series. However, since, according to Eqs. (8) and (11), its terms corresponding to $n > M$ decay exponentially with $n \longrightarrow \infty$, series (12) can be approximated by a finite sum to a sufficiently high accuracy. To this end, let M_ε $(\varepsilon \geq 0)$ be the number of the eigenvalues that satisfy the condition $\xi_n^2 > -\varepsilon^2$, $n = 1, 2, \ldots, M_\varepsilon$, instead of conditions (3). With only these modes taken into

account in Eq. (12), we obtain the following approximate formula:

$$W(\mathbf{Z}, \mathbf{q}, \mathbf{b}) \approx W_\varepsilon(\mathbf{Z}, \mathbf{q}, \mathbf{b}_\varepsilon)$$
$$= \frac{1}{8c^2}\sum_{n=1}^{M_\varepsilon}\left|(A\mathbf{q})_n - b_n\right|^2 \equiv \frac{1}{8c^2}\sum_{n=1}^{M_\varepsilon}\left|\sum_{j=1}^{N} a_{nj}q_j - b_n\right|^2. \quad (13)$$

The greater ε is, the higher the accuracy of this formula and the greater the number M_ε (see the analysis of numerical results below). The structure of formula (13) is close to that of the formula for the acoustic field power emitted to the far zone of the waveguide (see [16]). This will be the key factor in the numerical analysis of the extremal problems of active sound control.

Consider the region Ω, in which the array elements can be located, and the set $B = \{\mathbf{q} = (q_1, q_2, \ldots, q_N) : \sum_{j=1}^{N}|q_j|^2 \le Q_0^2\}$ in the space $\mathbb{C}^N$. Introduce the notation $J(\mathbf{Z}, \mathbf{q}; \mathbf{N}) = \sum_{n=1}^{M_\varepsilon}\left|(A\mathbf{q})_n - b_n\right|^2$. Let us formulate the following two problems.

Problem 1. (Nonlinear problem.) Given the number $N_0 \in \mathbb{N}$ and the vector $\mathbf{b}_\varepsilon \in \mathbb{C}^{M_\varepsilon}$, find the number of elements $N \le N_0$, the array $\mathbf{Z} \in \Omega$, and the vector $\mathbf{q} \in B$ that minimize the functional $J(\mathbf{Z}, \mathbf{q}; N)$.

Problem 2. (Linear problem.) Given the number $N_0 \in \mathbb{N}$, the vector $\mathbf{b}_\varepsilon \in \mathbb{C}^{M_\varepsilon}$, and the array $\mathbf{Z}_0 \in \Omega$, find the vector $\mathbf{q} \in B$ that minimizes the functional $J(\mathbf{Z}_0, \mathbf{q}; N_0)$.

For the case when J is the power emitted to the far zone, linear problem 2 was solved in [3, 4] using the regularized constrained quadratic optimization technique. Based on this technique and on a modified exhaustive search for coordinates of the point sources over a rectangular mesh, an efficient numerical algorithm for solving nonlinear problem 1 was developed in [16–19]. It has been shown that the power emitted by the primary source can be considerably decreased when the number of sources is close to the number of propagating modes.

Below, to improve this algorithm, we superimpose a mesh $\omega_L = \{(x_j, z_j), j = 1, 2, \ldots, L\}$ of L nodes, which is in general curvilinear, on the region Ω. As in [16], we assume that the desired monopoles can reside only at the nodes (x_j, z_j) of the mesh ω_L. In this case, the algorithm for solving nonlinear problem 1 consists in sequentially solving problem 2, first, for one source, looking through the mesh ω_L in search for the first optimal source; then, for two sources, assuming that coordinates (x_1^*, z_1^*) of the first optimal source are already found, while the second optimal source is sought over the mesh $\omega_{L-1} = \omega_L \backslash \{(x_1^*, z_1^*)\}$; and so on. The process terminates when, at a certain number N of the sources, the residual potential energy takes such a value $W_{\text{res}}^{(N)}$ that $W_{\text{res}}^{(N)}/W_b \le \varepsilon$, where ε is a small number. Our calculations assumed that $\varepsilon = 10^{-5}$, which corresponds to a 50-dB suppression of the acoustic energy. We usually took N to be no greater than the number M of the propagating modes.

We should emphasize that this method is rather simple and is easy to code, but its computational cost increases with N, because, when passing from an n-element antenna to an $(n + 1)$-element antenna, one has to solve problem 2 with an $M_\varepsilon \times N$ matrix $L - N$ times, which takes considerable computer time and memory. Therefore, while a single-processor computer can solve linear problem 2 in an admissible time even for a deep-water waveguide where thousands of modes can propagate [20, 21], the corresponding nonlinear problem can be solved in an admissible time (without using parallel algorithms) only for medium-depth waveguides, which allow the propagation of one to two hundred modes. Therefore, our numerical experiments will refer to a planar regular waveguide D of a medium depth with the parameters

$$H = 1000 \text{ m}, \ \rho = 1 \text{ g/cm}^3, \quad c = 1450 \text{ m/s},$$
$$\omega = 200\pi, \quad M = 138, \text{ and } \lambda = 14.5 \text{ m}.$$

Here, $\lambda = 2\pi c/\omega$ is the wavelength and $M = 138$ is the number of propagating modes. For this waveguide, the eigenfunctions and eigenvalues of the problem are determined by the explicit formulas $\xi_n^2 = k^2 - \mu_n^2$, $\mu_n = (n - 1/2)\pi/H$, and $\varphi_n(z) = \sqrt{2/H}\sin(\mu_n z)$, where $n = 1, 2, \ldots$. As the primary acoustic field p_b, we use the field

$$p_b(x, z) = -\frac{i}{2}\sum_{n=1}^{\infty}\xi_n^{-1}\varphi_n(z_0)\varphi_n(z)\exp(i\xi_n|x - x_0|) \quad (14)$$

created by a unit point source located at the point $(x_0, z_0) \in D$. All our calculations are performed on a computer with one AMD Athlon (950 MHz) processor and 128-Mbytes of RAM. The calculation time for one test was 30 to 80 min.

Active sound control problems usually employ antenna arrays of one of two types: linear (vertical, horizontal, or inclined) or curvilinear. A comparative analysis of solutions to active sound control problems with antennas of various configurations can be found in [20]. In particular, it was shown there that, if the primary source and the secondary antenna are sufficiently far apart, a strong acoustic field suppression can be achieved with antennas of two types: vertical linear arrays that cover the full depth of the waveguide or arrays of circular or elliptic shape. Below, we focus on arrays of the second type, which have the form of a circle, an ellipse, or a part of these forms. The respective

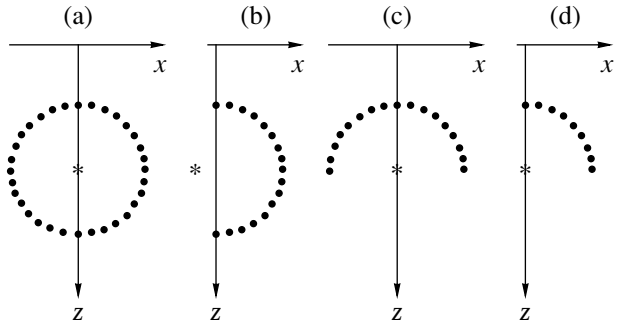

Fig. 2. Schematic diagrams of the antenna arrays in the waveguide.

mesh whose nodes can be used as locations of the secondary array elements is defined as

$$x_j = r_x \cos\left(\alpha - \frac{k\pi}{L} j\right),$$
$$z_j = z_0 - r_z \sin\left(\alpha - \frac{k\pi}{L} j\right), \quad j = 1, 2, \ldots, L. \tag{15}$$

Here, L is the number of the mesh nodes; r_x and r_z are the ellipse semiaxes along the x and z axes, respectively; (x_0, z_0) are the coordinates of the primary source; and α and k are the variable parameters, which define the shape of the mesh. Several meshes used in our numerical experiments are illustrated in Fig. 2.

As we noted above, in the calculations, the exact formula for the energy W in the form of series (12) was replaced with approximate finite sum (13), where M_ε is a certain number. It seems that the simplest way is to choose M_ε equal to the number M of the propagating modes. In this case, the structure of formula (13) is close to that of the formula for the power emitted to the far zone [16]. However, calculations [20] show that the error that results from such a choice of M_ε may be too large, especially when the secondary antenna is close to the region Q. This means that the solution (the secondary antenna) obtained in such a manner is actually a pseudosolution, because it does not noticeably suppress the true potential energy of the primary field. To avoid this error, we assume that the distance between the secondary antenna and the region Q is no smaller than two wavelengths and choose $M_\varepsilon = M + 10$ in accordance with the results presented in [20].

We divide all our numerical experiments into two groups. The first group consists of the sound control experiments with secondary antenna arrays in the form of a circle ($r_x = r_z$) or a circular arc. The second group comprises the arrays in the form of an ellipse with $r_x > r_z$ or in the form of an elliptic arc. Figures 3 and 4 illustrate the numerical experiments of the first group. Curves *1–6* in Fig. 3 show the suppressed potential energy ΔW in decibels versus the number N of the elements of the circular secondary array (see Fig. 2a) at $r = 10\lambda$, 15λ, 20λ, 22λ, 33λ, and 34λ, respectively. The primary source is located at the point $(0, H/2)$. The mesh is given by formula (15) at $r_x = r_z = r$, $L = 138$, $\alpha = \pi/2$, and $k = 2$. The parameter Q_0^2 is equal to 10.

As can be seen from Fig. 3, when the radius r of the circle is less than 20λ (in this case, the distance d between the mesh nodes is less than the wavelength λ),

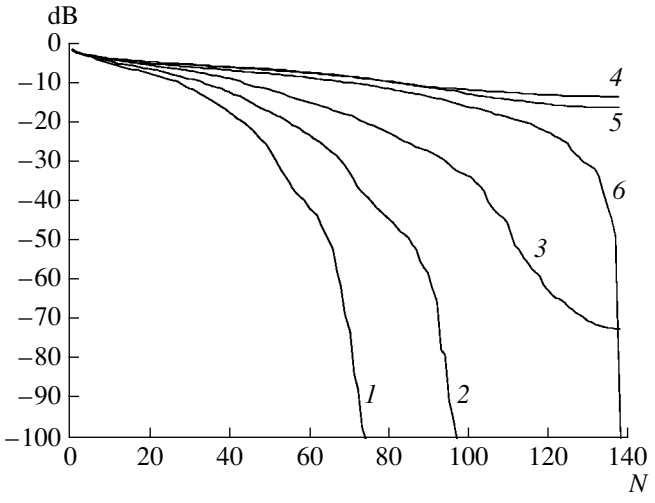

Fig. 3. Suppressed potential energy ΔW versus the number N of elements of the circular secondary antenna: results of solving problem 1 for $x_1 = 36\lambda$, $x_2 = 37\lambda$, $Q_0^2 = 10$, and $r =$ (*1*) 10λ, (*2*) 15λ, (*3*) 20λ, (*4*) 22λ, (*5*) 33λ, and (*6*) 34λ.

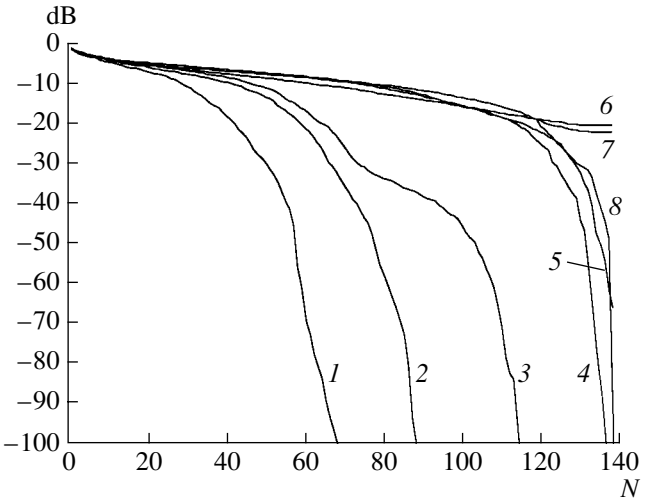

Fig. 4. Suppressed potential energy ΔW versus the number N of elements of the semicircular secondary antenna: results of solving problem 1 for $x_1 = 36\lambda$ and $x_2 = 37\lambda$ with the parameters $Q_0^2 = 10$, and $r =$ (*1*) 10λ, (*2*) 15λ, (*3*) 20λ, and (*4*) 34λ; $r = 34\lambda$, $Q_0^2 = 10$, and $x_0 =$ (*5*) -10λ and (*6*) -100λ; and $x_0 = -100\lambda$ and $Q_0^2 =$ (*7*) 10^3 and (*8*) 10^7.

complete suppression of the potential energy occurs when $N \le M$. For $20\lambda \le r \le 21\lambda$, when $d \approx \lambda$, the suppression is satisfactory. For $r > 21\lambda$, the quantity $|\Delta W|$ is less than 40 dB and decreases with increasing r. However, at $r = 34\lambda$, when the antenna occupies the full depth of the waveguide, the potential energy is suppressed completely.

Figure 4 illustrates the solutions to problem 1 for the mesh in the form of a semicircle (see Fig. 2b). The mesh is given by formula (15) at $L = 138$, $r_x = r_z = r$, $\alpha = \pi/2$, and $k = 1$. The primary source is located at the point $(0, H/2)$. Curves *1–4* in Fig. 4 show ΔW versus the number N of the secondary antenna elements at $Q_0^2 = 10$ and $r = 10\lambda$, 15λ, 20λ, and 34λ, respectively. At $r = 34\lambda$, the antenna actually occupies the full depth H of the waveguide. As can be seen, in all cases, complete suppression occurs when the number N of the array elements is less than the number M of the propagating modes: $N = 68$, 88, 114, and 136, respectively.

Curves *5* and *6* in Fig. 4 refer to the situation when $r = 34\lambda$ and the primary source is at a distance of 10λ and 100λ from the z axis at the points $(-10\lambda, H/2)$ and $(-100\lambda, H/2)$, respectively. At $Q_0^2 = 10$, the maximal possible suppression of the potential energy achieved at $N = M \equiv 138$ is 60 dB in the first case and 20 dB in the second case. Theoretically, the energy suppression $|\Delta W|$ can be increased by increasing Q_0^2, which can easily be seen from curves *7* and *8* calculated at $x_0 = -100\lambda$ and $Q_0^2 = 10^3$ and 10^7, respectively. It can be seen that, in the latter case, the complete suppression of the potential energy occurs at $N = M$.

Figure 5 presents ΔW versus the number N of the elements in the elliptic secondary antenna at $r_z = 34\lambda$. Curves *1–3* refer to $r_x = 100\lambda$, 340λ, and 500λ, respectively. The number L of the mesh elements is increased from 138 to 200. As can be seen from Fig. 5, these three curves differ only slightly and the complete suppression of the potential energy is observed in all cases at $N = M$. Moreover, if the positions of the secondary antenna elements are chosen on the semiellipse located to the right of the primary source (see Fig. 2b) at a distance of several hundred or even thousand wavelengths, the corresponding curves representing ΔW versus N have similar shapes. However, if the mesh has the form of an upper semiellipse, as in Fig. 2c, or a quarter of the ellipse, as in Fig. 2d, the suppression abruptly degrades and becomes 60 and 16 dB, respectively, at $N = M$ (see curves *5* and *4* in Fig. 5). This is further evidence for the importance of the optimal choice of the secondary antenna geometry with respect to the primary source and to the waveguide.

Thus, considerable suppression of the potential energy of the primary source in a multimode waveguide was achieved in the above tests when the number N of elements in an optimally chosen antenna approached or

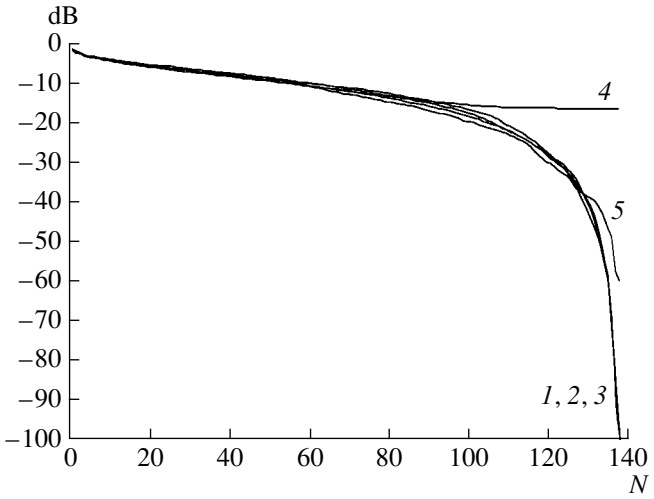

Fig. 5. Suppressed potential energy ΔW versus the number N of elements of the elliptic secondary antenna: results of solving problem 1 for $x_1 = r_x + 2\lambda$, $x_2 = r_x + 3\lambda$, $Q_0^2 = 10$, $r_z = 34\lambda$, and r_2 = (*1*) 100λ, (*2*) 340λ, and (*3*) 500λ; (*4*) array in the form of a quarter of the ellipse; and (*5*) array in the form of a semiellipse.

became equal to the number M of modes propagating in the waveguide. This fact testifies to the high efficiency of the algorithm proposed in this paper for solving nonlinear problem 1.

It should be noted that the use of this algorithm for a deep-water waveguide that allows the propagation of several hundreds to several thousands of normal modes requires a great deal of computations and is practically impossible with a single-processor computer. From this viewpoint, it seems reasonable to use multiprocessor computers or clusters containing up to several hundred processors. The use of multiprocessor computers is possible, because our algorithms can be deparallelized. The application of parallel algorithms and multiprocessor computers for solving the problems of active sound control in two-dimensional and three-dimensional deep-water waveguides will be discussed in a separate paper.

ACKNOWLEDGMENTS

This work was supported by the Russian Foundation for Basic Research, project no. 99-01-00214.

REFERENCES

1. A. A. Mazannikov, V. V. Tyutekin, and M. V. Fedoryuk, Akust. Zh. **26**, 759 (1980) [Sov. Phys. Acoust. **26**, 428 (1980)].
2. P. A. Nelson, A. R. D. Curtis, S. J. Elliot, and A. J. Bullmore, J. Sound Vibr. **117** (1), 1 (1987).
3. G. V. Alekseev and E. G. Komarov, Mat. Model. **3** (12), 52 (1991).

4. G. V. Alekseev and E. G. Komarov, Akust. Zh. **39**, 5 (1993) [Acoust. Phys. **39**, 1 (1993)].
5. G. V. Alekseev and E. G. Komarov, J. Inv. Ill-Posed Probl. **2** (2), 85 (1994).
6. J. D. Stell and R. J. Bernhard, J. Sound Vibr. **173** (2), 179 (1994).
7. J. D. Stell and R. J. Bernhard, J. Sound Vibr. **173** (2), 197 (1994).
8. V. P. Ivanov, Akust. Zh. **33**, 658 (1987) [Sov. Phys. Acoust. **33**, 383 (1987)].
9. B. Nayroles, G. Touzot, and P. Villon, J. Sound Vibr. **171** (1), 1 (1994).
10. E. Benzaria and V. Martin, J. Sound Vibr. **173** (1), 137 (1994).
11. G. V. Alekseev and E. N. Martynenko, Akust. Zh. **41**, 381 (1995) [Acoust. Phys. **41**, 331 (1995)].
12. M. E. Johnson and S. J. Elliott, J. Acoust. Soc. Am. **98**, 2174 (1995).
13. C. R. Fuller, S. J. Elliott, and P. A. Nelson, *Active Control of Vibration* (Academic, London, 1996).
14. G. V. Alekseev and E. G. Komarov, J. Inv. Ill-Posed Probl. **4** (1), 1 (1996).
15. V. V. Tyutekin, Akust. Zh. **43**, 238 (1997) [Acoust. Phys. **43**, 202 (1997)].
16. G. V. Alekseev, Akust. Zh. **43**, 737 (1997) [Acoust. Phys. **43**, 639 (1997)].
17. G. V. Alekseev and E. G. Komarov, **358** (1), 27 (1998).
18. G. V. Alekseev and A. S. Panasyuk, Akust. Zh. **45**, 723 (1999) [Acoust. Phys. **45**, 649 (1999)].
19. G. V. Alekseev, A. S. Panasyuk, and V. G. Sin'ko, *Numerical Analysis of Nonlinear Problems of Active Sound Field Control in Three-Dimensional Regular Waveguides* (Dal'nauka, Vladivostok, 1998).
20. G. V. Alekseev and T. S. Komashinskaya, *Numerical Analysis of Inverse Extremal Problems of Sound Radiation in Two-Dimensional Deep-Water Waveguides* (Dal'nauka, Vladivostok, 2000).
21. G. V. Alekseev and T. S. Komashinskaya, in *Acoustics of Inhomogeneous Media* (Inst. Gidrodin. Sib. Otd. Ross. Akad. Nauk, Novosibirsk, 2001), No. 117, pp. 3–10.

Translated by A. Khzmalyan

Acoustical Physics, Vol. 49, No. 2, 2003, pp. 125–128. Translated from Akusticheskiĭ Zhurnal, Vol. 49, No. 2, 2003, pp. 156–160.

Scattering of Acoustic Waves by Small Crustaceans

I. B. Andreeva† and L. L. Tarasov

Andreev Acoustics Institute, Russian Academy of Sciences, ul. Shvernika 4, Moscow, 177036 Russia

e-mail: tarasov@akin.ru

Received March 18, 2002

Abstract—Features of underwater sound scattering by small crustaceans are considered. The scattering data are obtained with the use of unique instrumentation that allows one to measure quantitative scattering characteristics (backscattering cross sections and angular scattering patterns) for crustaceans of different sizes, at different frequencies (20–200 kHz) and different insonification aspects. A computational model of crustaceans is considered with allowance for both the soft tissues of the main massive part of the animal's body and the stiff armour. The model proves to be advantageous for explaining some scattering features observed in the experiments. The scattering cross sections of crustaceans measured by other researchers are presented in a unified form appropriate for comparison. Based on such a quantitative comparison, relatively simple approximate empirical formulas are proposed for estimating the backscattering cross sections of small (within several centimeters) marine crustaceans in a broad frequency range. © *2003 MAIK "Nauka/Interperiodica".*

Among the groups of marine animals inhabiting the deep scattering layers (DSL) of the ocean, crustaceans (primarily, such as euphausiids, sergestides, and copepodes) play an important part. In addition to the deep scattering layers, some euphausiids (antarctic krill) can form extended and much denser accumulations of commercial value. A distinctive feature of all crustaceans is the simple structure of the main massive part of their body: it consists of muscular tissues embedded in a thin, but much stiffer, chitin armour. The shape of this part of the body resembles a slightly bent cylinder or an elongated ellipsoid. We will use the length of this part of the body l as the characteristic size of the animal.

The basic characteristic of sound scattering by a discrete underwater obstacle is the scattering cross section as a function of frequency, insonification aspect, and scattering direction. In practice, especially in problems of applied hydroacoustics, the most widely used characteristic is the backscattering cross section per unit solid angle σ, or the total target strength $TS = 10\log\sigma$ normalized by a chosen unit area. To make quantitative comparisons of the scattering features of similar animals with different sizes more convenient, we introduce the normalized backscattering cross section $\sigma^* = \sigma/l^2$ and the normalized animal size (or insonification frequency) $l^* = l/\lambda$, where λ is the acoustic wavelength.

A unique measuring apparatus for studying the sound scattering by small water animals was built at the Andreev Acoustics Institute in the 1980s. This apparatus allowed one to follow closely the mutual orientation of objects under investigation (in particular, small-size zooplankton), the source and receiver positions, and the insonification and scattering directions. Using this instrument in the synchronous recording mode, we were able to measure the absolute values of the scattering cross sections and their angular characteristics (backscattering patterns and scattering patterns) for frequencies that smoothly and continuously vary from 20 to 200 kHz and for insonification and scattering directions varying within a solid angle of 4π [1].

A series of laboratory measurements was carried out with *Palaemonidae* freshwater shrimps, because they resemble small marine crustaceans in both size (several centimeters) and body structure. Marine crustaceans could hardly be delivered alive to the measuring apparatus located in Moscow and, being preserved, they drastically changed their scattering properties. We experimentally studied the sound scattering by living shrimps for l^* varying from 0.5 to 15. These experiments revealed some scattering features that escaped other researchers who had no such instrumentation.

In parallel with the experiments, we considered some problems of theoretical modeling. As a basic model for calculating the backscattering cross section σ_{max} of a crustacean insonified perpendicularly to the axis of the main massive part of its body, we considered a stiff elastic shell in the form of a finite-length cylinder (armour) filled with an elastic liquid (muscular tissues). First, we calculated the backscattering cross section of an infinitely long cylindrical body of the same structure (σ^{∞}_{max}) and, then, passed to a body of a finite length l using the formula [2]

$$\sigma_{max} = \sigma^{\infty}_{max}(l/r_F)^2, \quad (1)$$

where r_F is the radius of the central Fresnel zone, which always exceeds the crustacean size in actual measurements. Formula (1) was multiply tested in experiments

† Deceased.

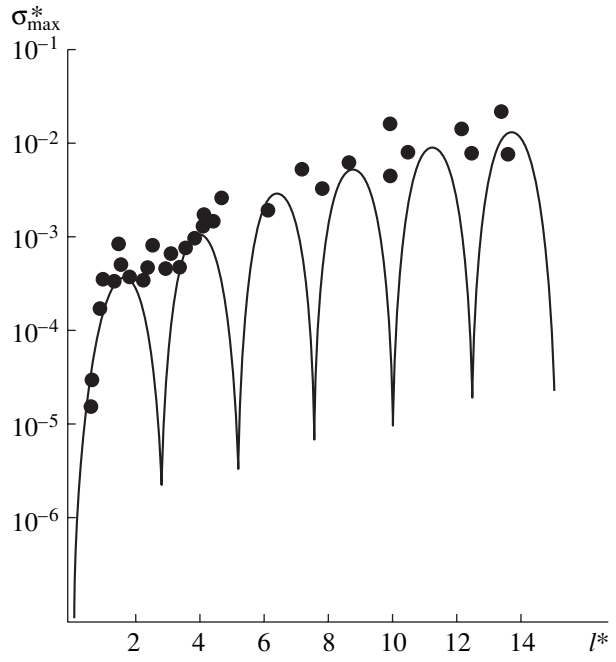

Fig. 1. Normalized frequency dependences of the backscattering cross sections of living shrimps and their cylindrical model given by Eq. (1). The dots correspond to the experiment and the solid line corresponds to the model calculation.

with different types of cylindrical bodies [1]. The behavior of the quantity σ_{max} as a function of size l and insonification frequency f makes it possible to consider the normalized function $\sigma^*_{max}(l^*)$. For higher frequencies ($l^* > 1$), this function oscillates, and for lower frequencies, it decays proportionally to $(l^*)^4$ (see Fig. 1). Experimentally, the oscillations were never observed for actual animals. Their presence in the calculated curve may result from the imperfection of the model, which does not take into account the small structural features of crustaceans and the sound absorption in their tissues. The experimental points obtained from the measurements with living animals concentrate along the line connecting the peaks of the oscillating portion of the calculated curve $\sigma^*_{max}(l^*)$. For lower frequencies when $l^* \ll 1$, experimental data are much more scarce; however, they cannot contradict the laws of low-frequency scattering: the backscattered intensity is independent of the insonification aspect and decreases proportionally to the fourth power of frequency.

The best agreement between the peaks of the calculated curve and the experimental points occurs (see Fig. 1) for the model with the parameters corresponding to the body structure of the shrimps studied in the experiment: the ratio of the length l to the diameter $2a$ is equal to five, and the shell thickness measures about 3% of the diameter. The tissue parameters used in the calculations agree with the basic characteristics of living tissues: for the shell, we used the bulk modulus $K_1 = 4.3 \times 10^{10}$ N/m^2, a Poisson ratio equal to 0.32, and a density equal to 1.06×10^3 kg/m^3; for soft tissues, we used a sound velocity of 1530 m/s and a density of 1.05×10^3 kg/m^3.

Within the bounds of the model, for small normalized sizes $l^* \cong 1$–3, the main contribution to scattering is formed by the animal's soft tissues, and for large sizes $l^* \cong 10$–20, by the armor. This fact results in a general increase in the scattering cross section with increasing l^* [3]. At low frequencies, the cross section value is mainly governed by the volume and material characteristics of the soft tissues, and at higher frequencies, by the thickness and the material characteristics of the shell. For this reason, models neglecting the shell are not quite adequate for $l^* \gg 1$.

Careful experiments showed that, for $l^* > 1$, both scattering and backscattering patterns of crustaceans, just like similar characteristics of fish, have maxima corresponding to the insonification directions from the back, pleon, and side and minima corresponding to the head and tail aspects (Fig. 2). However, as distinct from fish, in the angular characteristics of shrimps, maxima appear in the form of groups of narrow peaks, and the number and height of these peaks in a maximum increase as the frequency (parameter l^* in Fig. 2) increases. The second distinctive feature of the angular characteristics of shrimps in comparison with fish consists in the less pronounced dependence of the total angular width of a maximum on the insonification frequency. One can easily observe these features in Fig. 2, which shows the backscattering patterns $\sigma(\alpha)$ for shrimps and fish.

In full-scale measurements in the ocean, the tilt of floating crustaceans with respect to the horizon exhibits a natural scatter, which automatically smoothes out the oscillations in the backscattering pattern obtained with the use of the vertical acoustical sensing of crustacean accumulations. Hence, for estimating the contribution of every crayfish to the total field, it is more appropriate to use the cross section averaged over some angular sector about the aspect of the animal's back, σ_{av}, rather than the maximal cross section σ_{max}. For the sector, we used the angular width of ±25°. The corresponding averaging was performed with the use of the experimental records of $\sigma(\alpha)$ obtained for different values of the normalized size l^*.

Among the papers that present data on the angular characteristics of acoustic wave scattering by small crustaceans, we single out [4], which gives the backscattering cross sections of euphausiids for different insonification aspects. Unfortunately, these aspects correspond to only a few discrete angles and do not reflect the lobe structure of the angular characteristics, which makes them inappropriate for estimating the average cross section σ_{av}.

With the use of the above-mentioned measuring apparatus, we obtained a relatively large body of backscattering patterns measured for different insonification

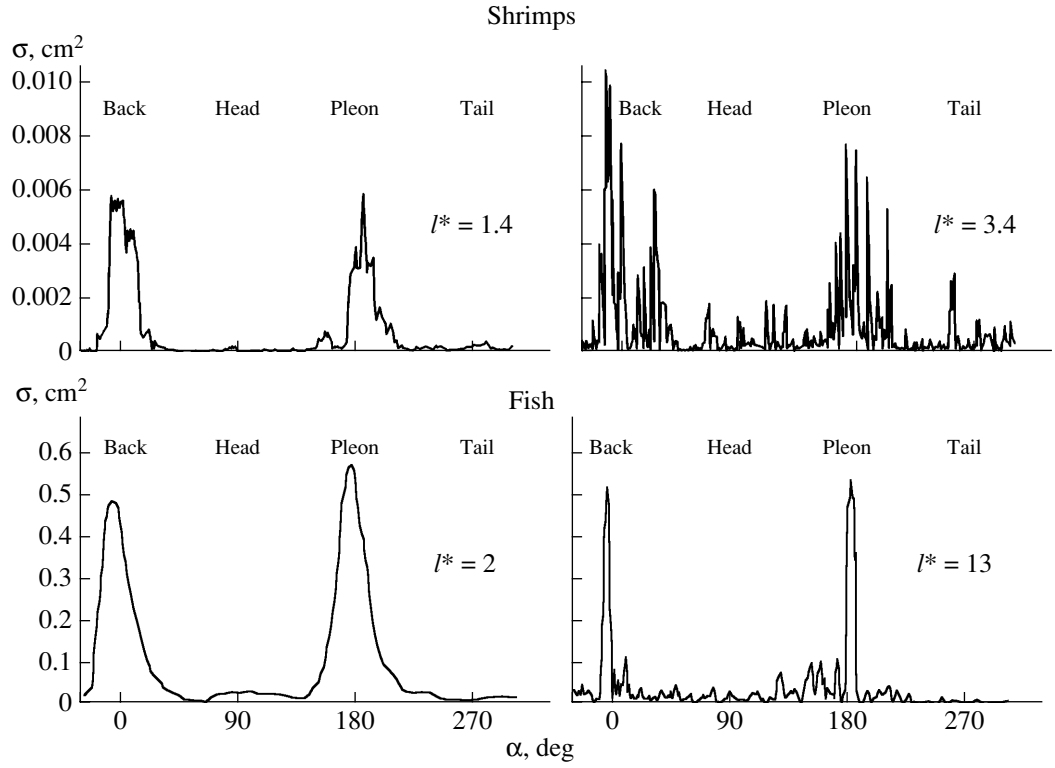

Fig. 2. Angular backscattering patterns of shrimps and fish as functions of the insonification aspect. The insonification aspects $\alpha = 0°$, 90°, 180°, and 270° correspond to the animal's back, head, pleon, and tail, respectively.

frequencies and different sizes of shrimps. These data were recalculated into the functions $\sigma_{av}(f)$ for every shrimp used in the experiments. The corresponding normalization provided a set of comparable frequency characteristics $\sigma^*_{av}(l^*)$. These quantities may be two or three times smaller than the cross section σ^* determined in the experiment as the maximal cross section measured within the specified sector.

Other researchers also constructed acoustic models for calculating the sound scattering by crustaceans. Generally, they refined the models by taking closer approximations to the actual shape of the animals' bodies. A representative of this approach is Stanton. He calculated the scattering from several model bodies of complex shapes, including a cylinder with a bent axis [5, 6]. Macaulay developed this approach further in his generalizing paper [7], where he took into account the fact that the optimal shape of the model depends on the ratio of the animal's size to the sound wavelength. To calculate the scattering cross sections, he suggested a spherical model for lower frequencies, a bent cylinder model for medium frequencies, and a bent ellipsoid model for higher frequencies. In the calculations, he assumed that the model body is made of a homogeneous liquid material whose characteristics are independent of frequency. He neglected the animal's stiff armour in all his models. His final formulas always included several parameters, whose values were chosen from the standpoint of the best agreement with the experimental data published in [4].

All the above models, including our models, use very cumbersome formulas for calculating the backscattering cross sections of zooplankton. In our opinion, the use of such formulas is unnecessary because of the inaccuracies in the initial data, such as the neglect of many structural features of the animal's body and the lack of data on both the sound scattering by living animals and the acoustic and mechanical characteristics of the animal's body tissues. Relatively simple empirical formulas derived from the ample experimental data obtained by many researchers are apparently more appropriate for application purposes.

Figure 3 shows the empirical function $\sigma^*_{av}(l^*)$, which was obtained from the experimental points of Fig. 1 using the averaging procedure described earlier, and its confidence intervals (curves *1*, *2*, and *3*, respectively). For lower frequencies, the proposed empirical formula has the form

$$\sigma^*_{av} \cong \sigma^*_{\max} \cong 10^{-4}(l^*)^4 \quad \text{for} \quad l^* < 1.1. \tag{2}$$

For higher frequencies, the formula becomes more complicated:

$$\sigma^*_{av} \cong 7 \times 10^{-5} \times 10^{0.13l^*} \quad \text{for} \quad l^* \cong 1.1\text{–}15. \tag{3}$$

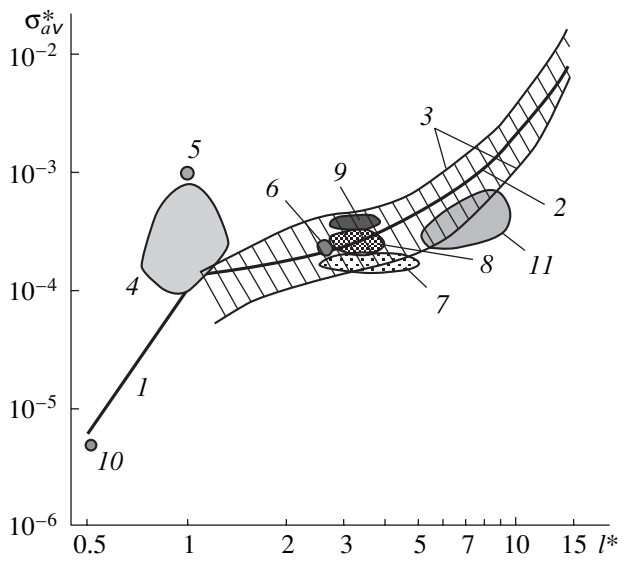

Fig. 3. Experimental data obtained by different researchers and the approximating curves. Curve *1* is the approximating curve according to Eq. (2), curve *2* is the approximating curve according to Eq. (3), and curves *3* show the boundaries of the 90% confidence interval. Regions *4–11* correspond to the following data: (*4*) [8], (*5*, *6*) [9], (*7*) [10], (*8*) [11], (*9*) [12], (*10*) [13], and (*11*) [14].

Figure 3 additionally shows the scattering cross sections measured for zooplankton by some other researchers who worked with euphausiids and other types of zooplankton with similar body structure and size. For comparison purposes, we recalculated the experimental data into the normalized backscattering cross sections and normalized sizes. The experimental data of each researcher are shown in Fig. 3 as regions 4–11, so that every region approximately corresponds to the position of their experimental data on (σ^*, l^*) plane. As follows from Fig. 3, relatively simple formulas proposed by us provide a fair agreement with the majority of experimental data despite the difference in the measurement procedures and insonification frequencies.

The angular characteristics of acoustic scattering by small-size zooplankton are similar to the corresponding characteristics of fish with swim bladders. However, they differ in that they have highly oscillating pattern of maxima, which essentially impedes the quantitative estimation of the scattering cross sections of such zooplankton from the available theoretical (even fairly complicated) models. Based on an analysis of the vast experimental material obtained by different researchers in different experimental conditions, we were able to propose relatively simple empirical formulas for estimating the backscattering cross sections in a wide frequency range.

ACKNOWLEDGMENTS

This work was supported by the Russian Foundation for Basic Research, project no. 01-05-64735.

REFERENCES

1. I. B. Andreeva and V. G. Samovol'kin, *Scattering of Acoustic Waves by Marine Animals* (Agropromizdat, Moscow, 1986).
2. L. M. Lyamshev, Dokl. Akad. Nauk SSSR **115**, 271 (1957) [Sov. Phys. Dokl. **2**, 332 (1957)].
3. I. B. Andreeva and D. P. Lysak, Oceanology **25** (3), 425 (1985).
4. A. Kristansen and J. Dalen, J. Acoust. Soc. Am. **80**, 601 (1986).
5. T. K. Stanton, J. Acoust. Soc. Am. **86**, 691 (1989).
6. T. K. Stanton, J. Acoust. Soc. Am. **86**, 1499 (1989).
7. M. C. Macaulay, J. Acoust. Soc. Am. **95**, 2452 (1994).
8. R. E. Pieper, Deep-Sea Res. **26**, 687 (1979).
9. *Report on Post-FIBEX Acoustic Workshop, Frankfurt, 1984*; *BIOMASS R.S.* (1986), Vol. 40.
10. O. Guzman *et al.*, in *Proceedings of Symposium on Fishery Acoustics* (Bergen, 1982), No. 12, p. 111.
11. V. A. Protashchuk and T. A. Lukashova, in *Problems of Industrial Hydroacoustics* (VNIRO, Moscow, 1983), pp. 21–25.
12. J. Kalinowski, Prace MIR **19**, 111 (1984).
13. P. C. Beamish, Deep-Sea Res. **18** (8), 811 (1971).
14. K. J. Benoit-Bird and W. W. L. Au, J. Acoust. Soc. Am. **110**, 812 (2001).

Translated by A. Vinogradov

Acoustical Physics, Vol. 49, No. 2, 2003, pp. 129–133. Translated from Akusticheskiĭ Zhurnal, Vol. 49, No. 2, 2003, pp. 161–166.

Correlation of Signals of Thermal Acoustic Radiation

A. A. Anosov[1, 2] and V. I. Passechnik[1†]

[1] *ÉLDIS Research Center, Institute of Radio Engineering and Electronics, Russian Academy of Sciences, Starosadskiĭ per. 8, Moscow, 101000 Russia*

e-mail: anosov@hotmail.ru

[2] *Sechenov Medical Academy, Moscow, Russia*

Received October 23, 2001

Abstract—The spatial correlation function is measured for the pressure of thermal acoustic radiation from a source (a narrow plasticine plate) whose temperature is made both higher and lower than the temperature of the receiver. The spatial correlation function of the pressure of thermal acoustic radiation is found to be oscillatory in character. The oscillation amplitude is determined not by the absolute temperature of the source but by the temperature difference between the source and the receiver. The correlation function changes its sign when a source heated with respect to the receiver is replaced by a cooled one. © *2003 MAIK "Nauka/Interperiodica".*

In recent years, various versions of passive acoustic thermotomography proposed for biomedical applications have been studied both theoretically [1–6] and experimentally [7–11]. The correlation reception of thermal acoustic radiation is believed to be one of the most promising methods of measuring the in-depth temperature [1, 3, 12] and, probably, the absorption coefficient as well [4]. However, theoretical and experimental studies of the correlation properties of thermal acoustic radiation are currently at the initial stage of their development. The simplest schemes of correlation reception were considered theoretically [13], and the first experiments on measuring the correlation function of the thermal acoustic radiation produced by a small object heated with respect to the surrounding medium were carried out [14]. In these experiments, the temperature of the receiver coincided with the temperature of the surrounding medium. The received signal was found to be proportional not to the absolute temperature of the object under study but to the temperature difference between the receiver and the source. This result was somewhat unexpected: it suggests that the correlation function should change sign when the source temperature becomes lower than the receiver temperature.

The purpose of this study is to measure the correlation function of thermal acoustic radiation from a source whose temperature can be made not only higher but also lower than the receiver temperature.

The experimental setup was analogous to the one shown in [14]. The measurements were conducted in (*1*) an aquarium (Fig. 1) with dimensions $40 \times 28 \times 30$ cm^3 filled with an immersion liquid (water). The source of thermal acoustic radiation was (*2*) a long narrow plate made of plasticine with a width of $\Delta = 3$ mm, a length of about 100 mm, and a thickness of 5 mm. The energy absorption coefficient of plasticine, $\gamma_P = 5$ cm^{-1}, far exceeds that of water, $\gamma_W = 2 \times 10^{-3}$ cm^{-1} (at $f = 2$ MHz). The plate was placed in (*3*) a cell with acoustically transparent windows, which was filled with water of temperature T. The water in the cell was heated by $\Delta T = 23$ K and cooled by $\Delta T = -14$ K with respect to the

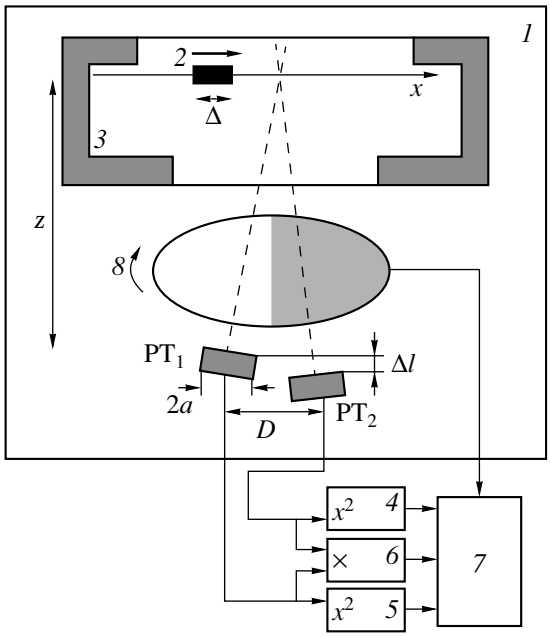

Fig. 1. Experimental setup: (*1*) an aquarium, (*2*) a plasticine plate of width Δ that was moved along the x axis, (*3*) a cell, (*4–6*) three inputs of a multiplier, (*7*) a personal computer, and (*8*) a chopper; PT_1 and PT_2 are the radiation receivers (piezoelectric transducers with the radius a); D is the distance between their centers; z is the distance from the x axis to the piezoelectric transducers; and Δl is the shift of piezoelectric transducers with respect to each other.

† Deceased.

aquarium temperature T_0 ($\Delta T = T - T_0$). The plate temperature coincided with the cell temperature.

The receivers were two circular flat piezoelectric transducers (PT_1 and PT_2) of radius $a = 5$ mm placed in the cell. The distance between their centers was $D = 18$ mm. The receiver temperature coincided with the aquarium temperature T_0. The acoustic axes of the piezoelectric transducers lay in the horizontal xz plane and intersected on the x axis at the distance $z = 200$ mm from the middle of the interval connecting the centers of the two piezoelectric transducers (Fig. 1).

The plate was positioned vertically and moved along the x axis with a step of about 2 mm (thus, the distance from the plane, where the plate was moved, to the piezoelectric transducers was ~200 mm). The origin of coordinates was at the intersection point of the axes of the piezoelectric transducers and the x axis. The transducer PT_1 was shifted to the distance Δl with respect to the transducer PT_2, as is shown in Fig. 1. This shift was caused by the inaccuracy in the transducer positioning, and its value Δl was small compared to the distance z from the piezoelectric transducers to the origin of coordinates: $\Delta l < 1$ mm $\ll z = 200$ mm.

The piezoelectric transducers were equipped with one quarter-wave layer, loaded on matching transformers, and tuned to the frequency $f_0 = 2.2$ MHz (the transmission band of the amplifiers was 200 kHz). The piezoelectric transducers had approximately equal sensitivities. The sound pressures at PT_1 and PT_2, p_1 and p_2, were transformed into the electric signals u_1 and u_2, which were amplified and fed to the three inputs *4*, *5*, and *6* of the multiplier (MLT04 Analog Devices). The mean squares of the voltages obtained at each piezoelectric transducer, $\overline{u_1^2}$ and $\overline{u_2^2}$ (the line above means time averaging), and the mean value of the product of the voltages obtained at different piezoelectric transducers, i.e., the correlated signal $\overline{u_1 u_2}$, were determined. The signals were recorded through amplifiers with the transmission band 1–15 Hz during 50 s using an L-154 interface card (L-card SoftWare Lab Limited, Russia) to (*7*) a personal computer. A modulation reception was used to exclude the signal drift, i.e., the radiation from the plate was periodically interrupted with a frequency of ~4 Hz by (*8*) a chopper. Thus, thermal acoustic signals from the plate and from the aquarium were detected (for example, $\overline{u_{1\mathrm{pl}}^2}$ and $\overline{u_{1\mathrm{aq}}^2}$ for PT_1), while the temperatures of these objects were different. The reference signal (a square waveform) determining the chopper position was also recorded to the computer, where a synchronous detection procedure was performed. The differences (increments) of the average values of the signals $\Delta\overline{u_1^2}$ and $\Delta\overline{u_2^2}$ received by the piezoelectric transducers from the plate and the aquarium were measured ($\Delta\overline{u_1^2} = \overline{u_{1\mathrm{pl}}^2} - \overline{u_{1\mathrm{aq}}^2}$ for PT_1 and $\Delta\overline{u_2^2} = \overline{u_{2\mathrm{pl}}^2} - \overline{u_{2\mathrm{aq}}^2}$ for PT_2). It should be noted that, for a correlated signal in the case of a closed chopper, i.e., in the case of radiation detection from the aquarium, the average value of the product of the voltages obtained at different piezoelectric transducers is equal to zero, $\overline{u_1 u_{2\mathrm{aq}}} = 0$. Thus, for a correlated signal, we have $\Delta\overline{u_1 u_2} = \overline{u_1 u_{2\mathrm{pl}}}$. Further, we denote the correlated signal from the plate as $\overline{u_1 u_2}$ for simplicity.

It is convenient to express the measured signals in degrees Kelvin and thus obtain the increments of the acoustic brightness temperatures ΔT_A (for example, in the case of PT_1, the signal $\Delta\overline{u_1^2}$ expressed in degrees determines the increment of the acoustic brightness temperature ΔT_{A1}). An acoustic blackbody heated with respect to the aquarium to ΔT_{BB} was placed into the cell for calibration. The transverse dimension of the blackbody exceeded the apertures of both piezoelectric transducers. In this case, the measured increment of acoustic brightness temperature ΔT_{ABB} of the blackbody is equal to the increment of its thermodynamic temperature $\Delta T_{ABB} = \Delta T_{BB}$. Using this relation, it is possible to calibrate the measured signals in degrees Kelvin. It is necessary to note that, in the case of a narrow plate heated to the same temperature as the acoustic blackbody, the measured signals are smaller and determined by the plate width Δ [14]. The measured correlated signal $\overline{u_1 u_2}$ was also expressed in degrees (i.e., the so-called correlated acoustic brightness temperature T_{AC} was obtained).

In the case of a wide plate with a transverse dimension exceeding the size of the piezoelectric transducer aperture, the correlated signal was equal to zero in all cases, i.e., when the plate temperature coincided with the aquarium (receiver) temperature $\Delta T = 0$ and when the plate temperature differed (was higher or lower) from the aquarium (receiver) temperature $\Delta T \neq 0$. For a narrow plate, the correlated single was equal to zero only at $\Delta T = 0$.

Figure 2 presents the experimental dependences of the received signals on the x coordinate in the case of the movement of the narrow plate. The increments of acoustic brightness temperature ΔT_{A1}, ΔT_{A2} and the correlated acoustic brightness temperature T_{AC} were measured at each position of the plate (at a fixed x). At first, the measurements were conducted with a heated plate. The dependences $\Delta T_{A1}(x)$ (curve *1*), $\Delta T_{A2}(x)$ (curve *2*), and $T_{AC}(x)$ (curve *3*) were obtained in the course of the plate movement along the x axis. After that, the same measurements were conducted with a cooled plate (curves *4–6*, respectively). Thus, curves *1* and *4* (*2* and *5*) show the dependences of the increments of acoustic brightness temperatures $\Delta T_{A1}(\Delta T_{A2})$ measured by PT_1 (PT_2) for the heated and cooled plates, respectively. Curves *3* and *6* show the dependences of the correlated

acoustic brightness temperature T_{AC} for the heated and cooled plates, respectively. For illustration we performed the interpolation of the experimental points of the correlated acoustic brightness temperature T_{AC} by cubic splines and the interpolation of the experimental points of the increments of acoustic brightness temperature ΔT_{A1} and ΔT_{A2}, by intervals.

One can see from Fig. 2 that the increments of acoustic brightness temperature, $\Delta T_{A1}(x)$ and $\Delta T_{A2}(x)$, and, therefore, the difference signals $\Delta\overline{u_1^2}(x)$ and $\Delta\overline{u_2^2}(x)$ received by PT_1 and PT_2 are positive at all values of x when the plate is heated (see curves *1* and *2*) and negative (see curves *4* and *5*) when the plate is cooled. This corresponds to the direction of the energy flux from the plate to the piezoelectric transducer in the case of the heated plate and in the opposite direction in the case of the cooled plate. As x varies, the correlated signals $\overline{u_1u_2}(x)$ change their sign in both cases of the heated (curve *3*) and cooled (curve *6*) plate. However, these curves oscillate in antiphase. It is necessary to note that the oscillating dependence $T_{AC}(x)$ for a heated plate was already obtained in our previous study [14]: if the propagation difference of acoustic waves from a plate to piezoelectric transducers is equal to an integer number of wavelengths λ_0 ($\lambda_0 = 0.68$ mm at the average reception frequency $f_0 = 2.2$ MHz), the correlation signal is positive, and if the propagation difference is equal to an uneven number of half-wavelengths, the correlation signal is negative.

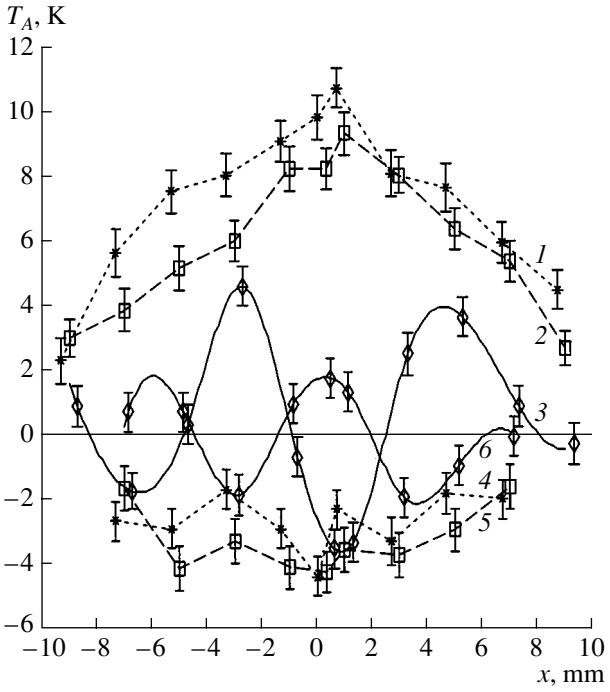

Fig. 2. Experimental dependences of the acoustic brightness temperatures T_A on the x coordinate with a moving narrow plate: the dependences of the increments of acoustic brightness temperature ΔT_{A1} and ΔT_{A2} measured by PT_1 and PT_2 for (*1*, *2*) a heated and (*4*, *5*) a cooled plate, respectively; the dependence of the correlated acoustic brightness temperature T_{AC} for (*3*) a heated and (*6*) a cooled plate.

The correlated signals $\overline{u_1u_2}(x)$ in both cases of the heated (curve *3*) and cooled (curve *6*) plate periodically vary with the same spatial period about $\Lambda = 8$ mm. The shape of the signal envelopes on the whole repeats the shape of the spread function of the receivers. In both cases of heating and cooling, the magnitude of the signal $|\overline{u_1u_2}(x)|$ at any x is smaller than the values of $\Delta\overline{u_1^2}(x)$ and $\Delta\overline{u_2^2}(x)$. These data confirm the results of [14], where the calculation of the theoretical dependence $\overline{u_1u_2}(x)$ for a narrow heated plate was performed.

Note that the correlated signal is determined not by the absolute temperature of the plate but by the temperature difference between the aquarium and the heated plate ΔT. First, as one can see from Fig. 2 (curves *3* and *6*), in the case of a fixed plate position, the correlated signal changes its sign depending on the sign of ΔT. For example, at $x = 0$, for a heated plate (curve *3*), the correlated signal is negative (the acoustic propagation difference Δl is approximately equal to $\lambda_0/2$: $\Delta l = 0.35$ mm), and in the case of a cooled plate (curve *6*), it is positive. Second, the amplitude of the correlated signal is proportional not to the plate temperature T but to the magnitude of the temperature difference between the aquarium and the heated plate $|\Delta T|$. Indeed, the temperature difference differs in its magnitude by approximately a factor of 2, and the signal amplitudes *3* and *6* differ to the same extent.

Let us formulate two basic results to be discussed.

(i) If the source of an acoustic thermal signal is a wide plate with a size exceeding that of the piezoelectric transducer aperture, the measured correlated signal is equal to zero independently of the plate temperature.

(ii) In the case of a narrow plate, the maximal value of the measured correlated signal is determined by the difference ΔT between the temperatures of the source of radiation T and the receiver T_0, $\Delta T = T - T_0$. In particular, if the receivers and the source have equal temperatures, the correlated signal is equal to zero, and if the sign of the temperature difference ΔT changes to the opposite, the sign of the correlated signal changes also while the plate position remains constant.

The zero correlated signal for a wide plate is evident for the case of equal source and receiver temperatures, $T = T_0$. In this case, the receiver of thermal radiation cannot acquire information from the surrounding medium. The case when the receiver and source temperatures are different, $T \neq T_0$, the source size exceeds the receiver aperture, and the receivers are separated was treated theoretically for the Fraunhofer zone [15], and it was demonstrated that the total correlated signal should be equal to zero. The same result was obtained

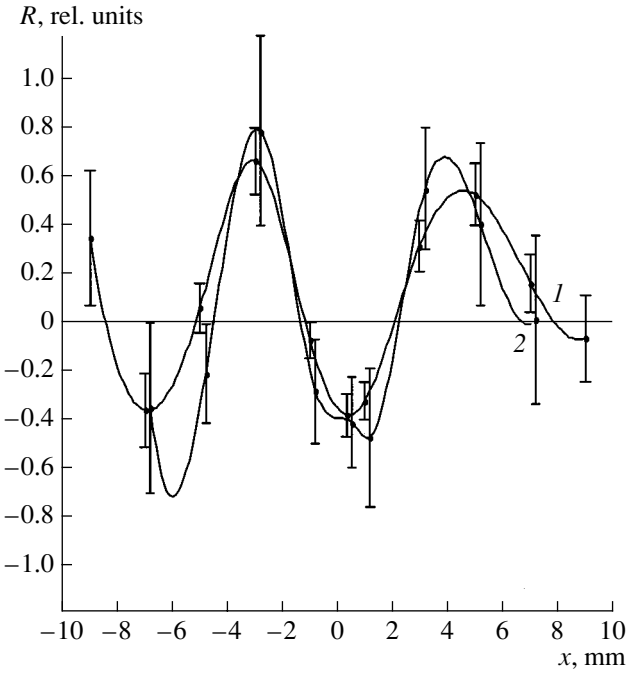

Fig. 3. Correlation functions $R(x)$ of thermal acoustic radiation that are calculated from the experimental data given in Fig. 2 for (*1*) a heated and (*2*) a cooled plate. The sign of curve *2* is changed for the sake of illustration.

theoretically for a space that is homogeneous in absorption with a small absorption coefficient. Thus, in our experiment, we had conditions in which the source size was greater than the transverse dimension of spatial coherence [16]. In this case, the measured correlated signal should be equal to zero, which was confirmed experimentally.

The second result obtained is a consequence of the first one. In the experiment, the source of the total correlated signal was a complex source: a heated (or cooled) narrow plate with the temperature T and also the whole surrounding medium with the temperature T_0. Thus, in the case of a heated plate, a nonzero correlated signal was produced only by the effective source with the size of the narrow plate with the temperature ΔT, and the total correlated signal from the whole space with the temperature T_0 was equal to zero. It is clear that, in this case, the correlated signal was determined by the quantity ΔT.

The analysis of the results for a narrow plate cooled with respect to the receiver is more complicated. We only note that, when the propagation difference of signals from the plate to the receiver is equal to zero (at $x \approx -3$ mm, see Fig. 2), the correlated signal must be close to the value of the signal measured by a single receiver with allowance for natural corrections for the width of the spread function and the signal nonmonochromaticity, which reduce this value. In other words, it must have the same sign; i.e., it must be negative. The detailed microscopic physical mechanism of obtaining a negative correlated signal needs a special investigation.

In conclusion, we consider the correlation functions measured by the modulation reception and the correlation functions that can be obtained by a nonmodulation reception of thermal acoustic radiation. As we have mentioned before, the value of the correlated signal $\overline{u_1 u_2}$ does not depend on the reception technique and is determined by the temperature difference ΔT between the plate and the aquarium. The signals obtained at the outputs of the piezoelectric transducers in the case of the modulation reception have the increments of the average values $\Delta\overline{u_1^2}$ and $\Delta\overline{u_2^2}$. These quantities are proportional to the temperature difference ΔT between the plate and the receivers [18]. According to the experimental data given in Fig. 2, it is possible to calculate the correlation function $R(x)$ for thermal acoustic radiation by the formula

$$R(x) = \overline{u_1 u_2}(x)/\sqrt{\Delta\overline{u_1^2}(x)\Delta\overline{u_2^2}(x)}. \qquad (1)$$

The resulting data approximated by cubic splines are presented in Fig. 3. Curve *1* was obtained from the experimental data for a heated plate, and curve *2*, from the data for a cooled plate, the sign of curve *2* being changed for better comparison with curve *1*. Greater errors of indirect measurements of $R(x)$ for a cooled plate are connected with the considerably smaller values of the signals $\Delta\overline{u_1^2}(x)$ and $\Delta\overline{u_2^2}$ for a cooled plate, as compared to those for a heated one (approximately two times smaller, as one can see from Fig. 2). The coincidence of the functions presented within the error can be seen in Fig. 3. It follows from the results presented that the correlation function calculated by Eq. (1) is determined only by the correlation properties of thermal acoustic radiation and does not depend on the temperature of the medium under investigation. As one can see, the maximal value of the correlation coefficient that was obtained experimentally reaches 0.6–0.8. Similar values were obtained earlier for a heated plate [14].

If nonmodulation reception is used, the average values of the signals received by piezoelectric transducers from the plate, $\overline{u_{1\text{pl}}^2} = \overline{u_1^2}$ and $\overline{u_{2\text{pl}}^2} = \overline{u_2^2}$, are measured. These values are determined by both the plate temperature T and the temperature of the piezoelectric transducer T_{TR}, although the informative part of the signal from the medium under study, i.e., the informative part of the voltage measured at the piezoelectric transducer, is determined by the difference between the temperatures of the medium and the piezoelectric transducer, $T - T_{TR}$ [17]. Note that, if we take into account the total voltage at the output of a nonmodulation acoustic thermometer (i.e., if we take into account, for example, the constant component of the signal, which is determined by the receiver noise), the formula for the correlation

function $R_\Sigma(x)$ in the case of the nonmodulation reception takes the form

$$R_\Sigma(x) = \overline{u_1 u_2}(x)/\sqrt{\overline{u_1^2}\,\overline{u_2^2}}. \quad (2)$$

As one can see from the comparison of Eqs. (1) and (2), the correlation function R_Σ is much smaller in its absolute value than the correlation function R, namely, smaller by a factor of $\Delta T/T + T_{TR}$.

The choice of the formula for calculating the correlation function is determined by the experimental setup. The function R calculated by Eq. (1) expresses the correlation properties of thermal acoustic radiation, does not depend on the temperature of the medium, and does not take into account the noise of the receiving equipment. The function R_Σ calculated by Eq. (2) also includes the receiver noise characteristics, which are not connected with the thermal acoustic radiation of the medium, and depends on temperature.

Thus, the measured correlated signal of thermal acoustic radiation is determined not by the absolute temperature of the source (a narrow plate) but by the difference in temperature between the source and the receiver; the signal changes its sign when the source heated with respect to the receiver is replaced by a cooled one.

ACKNOWLEDGMENTS

This work was supported by the Russian Foundation for Basic Research, project no. 00-02-16370.

REFERENCES

1. A. I. Chmill, V. V. Gerasimov, Yu. V. Guluaev, *et al.*, in *Acoustical Imaging*, Ed. by S. Lees (Plenum, New York, 1997), Vol. 23, pp. 77–86.
2. S. Yu. Ksenofontov, A. D. Mansfel'd, and A. M. Reiman, Izv. Vyssh. Uchebn. Zaved. Radiofiz. **40** (6), 752 (1997).
3. V. A. Burov and E. E. Kasatkina, Akust. Zh. **43**, 162 (1997) [Acoust. Phys. **43**, 135 (1997)].
4. V. I. Pasechnik, Akust. Zh. **43**, 563 (1997) [Acoust. Phys. **43**, 485 (1997)].
5. V. I. Passechnik, A. A. Anosov, and M. G. Isrefilov, Int. J. Hyperthermia **15** (2), 123 (1999).
6. K. M. Bograchev and V. I. Pasechnik, Akust. Zh. **45**, 742 (1999) [Acoust. Phys. **45**, 667 (1999)].
7. A. A. Anosov, V. I. Pasechnik, and K. M. Bograchev, Akust. Zh. **44**, 725 (1998) [Acoust. Phys. **44**, 629 (1998)].
8. E. V. Krotov, S. Yu. Ksenofontov, A. D. Mansfel'd, *et al.*, Izv. Vyssh. Uchebn. Zaved. Radiofiz. **42** (5), 479 (1999).
9. R. A. Kruger, D. R. Reinecke, and G. A. Kruger, Med. Phys. **26**, 1832 (1999).
10. V. I. Pasechnik, A. A. Anosov, and K. M. Bograchev, Biomed. Radioélektron., No. 2, 3 (1999).
11. V. I. Passechnik, A. A. Anosov, M. G. Isrefilov, and A. V. Erofeev, Ultrasonics **37**, 63 (1999).
12. R. Hessemer, T. Perper, and T. Bowen, U.S. Patent No. 4,416,552 (22 November 1983).
13. Yu. N. Barabanenkov and V. I. Pasechnik, Akust. Zh. **41**, 563 (1995) [Acoust. Phys. **41**, 494 (1995)].
14. A. A. Anosov, M. A. Antonov, and V. I. Pasechnik, Akust. Zh. **46**, 28 (2000) [Acoust. Phys. **46**, 21 (2000)].
15. V. I. Passechnik, Akust. Zh. **48** (5), 666 (2002) [Acoust. Phys. **48**, 589 (2002)].
16. N. A. Esepkina, D. V. Korol'kov, and Yu. N. Pariĭskiĭ, *Radio Telescopes and Radiometers* (Nauka, Moscow, 1973), pp. 261–268.
17. A. A. Anosov and V. I. Pasechnik, Akust. Zh. **48**, 16 (2002) [Acoust. Phys. **48**, 12 (2002)].

Translated by M. Lyamshev

Acoustical Physics, Vol. 49, No. 2, 2003, pp. 134–142. Translated from Akusticheskiĭ Zhurnal, Vol. 49, No. 2, 2003, pp. 167–177.

Simulation of the Tomographic Reconstruction of Thermoacoustic Sources: Iteration-Correlation Methods

V. A. Burov, E. E. Kasatkina, O. D. Rumyantseva, and S. A. Filimonov

Physical Faculty, Moscow State University, Vorob'evy gory, Moscow, 119992 Russia

e-mail: burov@phys.msu.su

Received February 22, 2002

Abstract—Schemes for improving the resolution of thermal tomographs using multielement receiving arrays are considered. Algorithms for processing the space-time correlation information are developed on the basis of the generalization of the high-resolution spectral analysis techniques in application to the problems of medical acoustic thermotomography in narrow-band and wide-band modes of operation. Special attention is given to Capon-type algorithms, which allow an increase in the spatial resolution of the fine structure of the power density distribution of thermoacoustic radiation sources. © *2003 MAIK "Nauka/Interperiodica".*

The solution of important problems of medical diagnostics calls for the development of new methods of noninvasive imaging that are safer and less expensive than those in current use. The techniques based on the detection of the intrinsic radiation of a heated object (a biological tissue) are of special interest in this connection. The development of devices for measuring the distribution of the in-depth temperature of an object by its thermal acoustic radiation was much discussed in the literature [1–12]. The correlation approaches provide an opportunity to realize the potentialities originating from the wave nature of the field and obtain a rather high spatial resolution [2, 3, 6–12]. However, only the use of multielement arrays containing hundreds of receiving elements in combination with high-resolution computational algorithms makes it possible to reach a sensitivity sufficient for the determination of a temperature contrast of 1 K against the background of an average temperature of about 300 K, with a resolution of several millimeters, which correspond to the requirements of early medical diagnostics. Still, even in this case, it is difficult to solve the problem of acoustic thermotomography in its standard formulation (the search for somewhat more heated, i.e., more noisy, areas against a hot noisy background) [2].

This paper proposes a somewhat different approach to the formulation of the acoustic thermotomography problem itself and to its utilization in medical applications. In particular, the possibility of analyzing the state of the system of blood supply on the basis of a noninvasive investigation by acoustic thermotomography is considered. The results of solving the noncoherent inverse problem considered by us are such important diagnostic factors as the map of blood vessels and the degree of blood saturation of tissues. The proposed technique is based on the utilization of the effect of a considerable decrease (in comparison with the surrounding tissues) in the spatial power density of thermal sources (thermoacoustic brightness) related to the blood vessels. The point is that the coefficient of sound absorption in blood is 6–8 times smaller than that in the surrounding biological tissues, and, hence, blood vessels are 6–8 times "darker" objects (in the sense of the power density distribution of thermal sources). Therefore, in the case of such a nonstandard approach, the contrast between the biological tissue and the vessels is much higher than in the case of the standard formulation of the problem of acoustic thermotomography. The increased contrast provides an opportunity to obtain the high resolution desired. Naturally, only large enough vessels can be distinguished. Capillaries with a thickness of fractions of a millimeter cannot be resolved, but their clusters can possibly be detected by the acoustic thermotomography technique. The scattering in blood at an operational frequency of ~1 MHz, which is common with medical diagnostics, is small, and we can ignore its contribution to attenuation [13]. For example, the scattering cross section of a single erythrocyte is two orders of magnitude smaller than the absorption cross section. The scattering in blood is essential starting from approximately 5 MHz, and it decreases rapidly with decreasing frequency because of Rayleigh-type scattering in the frequency range under consideration.

Apart from the direct investigation of the state of blood vessels, the technique proposed here can be useful as a source of additional information for the diagnostics of certain diseases. For example, the growth of a malignant tumor and cirrhosis changes of tissues are accompanied by an impairment of the regularity of the blood system, its anomalous development, and a change in blood circulation ("tumor angiogenesis")

1063-7710/03/4902-0134$24.00 © 2003 MAIK "Nauka/Interperiodica"

[14, 15]. It is also found that a significant correlation between the density of microscopic vessels and the development of metastases in the case of the carcinoma of a mammary gland takes place. This is the reason why the use of passive acoustic thermotomography for the investigation of the state of the blood-supply system seems to be a quite interesting and promising field in the development of new methods of noninvasive diagnostics.

In this connection, we consider here some possible variants of the space–time processing of a sample coherence matrix [16], which allow a reconstruction of the spatial distributions of certain characteristics of a biological medium. Thermoacoustic sources are random in their nature, and the fields emitted by them are described to a high precision by a normal multidimensional distribution law. Therefore, the reconstruction of the desired parameters by using one of the optimal or quasi-optimal methods is based in fact on the verification of one or another hypothesis concerning the measured thermoacoustic fields and is reduced to operations over the space–time coherence matrix. Quantitative methods with high resolution from the point of view of both unbiased estimates and high spatial resolution are needed. Then it will be possible not only to evaluate the spatial power density of thermoacoustic sources but also to reconstruct separately the absorption coefficient, the local ultrasonic velocity, and the local temperature of the medium (when a high accuracy of evaluation is achieved) [17].

Below, we present the results of solving the model problems of acoustic thermotomography, which demonstrate the possibility of evaluation with a high spatial resolution for "dark" sources against a "bright" noise background by using the modified Capon method. The method is one of a number of nontraditional methods of spatial and time-spectral evaluation that provide a better resolution than the Rayleigh limit and are intended for both spectral analysis and for processing signals obtained from an array of high spatial resolution. As in the standard algorithms of spectral evaluation, in the Capon algorithm, the sample matrix of coherence is phased to obtain the evaluation of the power density distribution of sources (in directions, frequencies, etc.), but, initially, the matrix is inverted and the result of phasing is inverted again to obtain the final evaluation of the local power of sources. With the growth of the signal-to-noise ratio, such a logic leads to an excess of resolution over the Rayleigh limit.

However, the Capon algorithm in its classical form, like standard algorithms, loses efficiency in the case of solving the problem of detecting weaker thermoacoustic sources (blood vessels) against a background of stronger ones (surrounding tissues) and the evaluation of the power density distribution $I(\mathbf{r})$ of both types of sources. From the point of view of the values of $I(\mathbf{r})$, weak and strong sources are "dark" and "bright," respectively, since, as was already mentioned, in the case of equal temperature, the absorption in blood is almost one order of magnitude smaller than in tissue. Thus, unlike the situation that is standard for the detection theory ("bright" sources against a "dark" noisy background), the problem statement under consideration ("dark" sources against a "bright" background) requires a different way of seeking the optimal solution in comparison with the common case. As a problem of statistical verification of hypotheses, it can be formulated as follows: the hypothesis "there are no dark, i.e., less noisy, local regions against a more or less uniformly noisy bright background" and the alternative "there are such regions in a given direction (space region)." A modified method (described briefly in [18]) that allows one to realize the potential resolution with the help of the Capon algorithm was proposed to bring it closer to the resolution of such high-resolution methods as the method of maximal entropy and various generalizations of the Pisarenko's method of harmonic expansion.

The solution implies the construction of a sample coherence matrix W with the elements $W_{ik} = \overline{V_i V_k^*}$ ($i, k = 1, \ldots, K$). Here, V_i is the noise signal arriving from the studied region, i and k are the indices of a fixed pair of receivers, and the asterisk means complex conjugation. The estimate $\hat{I}(\mathbf{r})$ of the quantity $I(\mathbf{r})$ at each fixed point $\mathbf{r}$ can be obtained using the classical methods of spectral evaluation by Bartlett or Capon, which assume phasing of the matrices W or W^{-1}, respectively [19]:

$$\hat{I}_{\mathrm{Bar}}(\mathbf{r}) = \frac{\langle \phi(\mathbf{r})|W|\phi(\mathbf{r})\rangle}{(\langle \phi(\mathbf{r})|\phi(\mathbf{r})\rangle)^2};$$
$$\hat{I}_{\mathrm{Cap}}(\mathbf{r}) = \frac{1}{\langle \phi(\mathbf{r})|W^{-1}|\phi(\mathbf{r})\rangle}. \quad (1)$$

Here, $|\phi(\mathbf{r})\rangle$ and $\langle\phi(\mathbf{r})| \equiv |\phi(\mathbf{r})\rangle^+$ are the column and row of the phasing factors in Dirac's notations and the symbol "+" means Hermitian conjugation. Each element $\phi_k(\mathbf{r})$ in its physical meaning is a signal arriving at the receiver k from a probe point (δ-like) source of unit power, which is placed conditionally at the point $\mathbf{r}$. Since the dark sources against a bright background are to be separated in the problem considered, the modification of the Capon method by the compensation of the background is proposed:

$$I(\mathbf{r}) = aI_{\mathrm{comp}}(\mathbf{r}) - I'(\mathbf{r}),$$
$$\text{where} \quad I'(\mathbf{r}) = \frac{1}{\langle \phi(\mathbf{r})|(aW_{\mathrm{comp}} - W)^{-1}|\phi(\mathbf{r})\rangle}. \quad (2)$$

Equations (2) assume that the difference $I'(\mathbf{r}) = aI_{\mathrm{comp}}(\mathbf{r}) - I(\mathbf{r})$ is evaluated by the classical Capon method. Here, $I_{\mathrm{comp}}(\mathbf{r})$ is the power density of the sources considered as the compensating background distribution (I_{comp} is evaluated in a way that will be explained later) and W_{comp} is the coherence matrix corresponding to these background sources. The coeffi-

cient a must provide the stability of the evaluation of $I'(\mathbf{r})$ on account of the sign definiteness of the matrix $(aW_{comp} - W)$. In the problem under study, $a > 0$ and the positive definiteness of this matrix means that $I'(\mathbf{r}) > 0\ \forall\mathbf{r}$. The matrices W in Eqs. (1) and $(aW_{comp} - W)$ in Eqs. (2) are additionally regularized before their inversion by adding μE to them, where E is the unit matrix and μ is the regularization coefficient, which makes 10^{-5}–10^{-2} of the maximal absolute value of the corresponding matrix or, more correctly, of the average value of its diagonal elements.

In the physical sense, subtracting the initial desired power density $I(\mathbf{r})$ from the power density of the bright background plays a double role. First, after the compensation, the difference distribution $I'(\mathbf{r})$ has [as distinct from $I(\mathbf{r})$] a common form of bright sources against a dark background, and, therefore, it can be evaluated more effectively using the classical Capon method. Second, the relative contrast of dark and bright sources increases due to the subtraction. The more precisely the relative contrast is determined and, therefore, the more precisely the background power density is compensated in the function $I'(\mathbf{r})$, the higher the relative contrast of dark and bright sources in the difference distribution and the higher the resolution of the evaluation $I'(\mathbf{r})$. According to Eq. (2), the compensated background $aI_{comp}(\mathbf{r})$ is returned into the final pattern $I(\mathbf{r})$. Thus, the background compensation leads to a more distinct reconstruction of those local changes of the power density of sources, which are informative from the point of view of diagnostic problems.

The utilization of the procedure of background compensation is a well known tool for enhancing the resolution of the Capon method in standard problems of detection and power evaluation of bright sources against a noise background [20]. In this case, the noise component is subtracted from the sample coherence matrix (the resolution of Capon-type algorithms is closely related to the value of the signal-to-noise ratio, and, therefore, the noise compensation leads to an essential enhancement of resolution). The noise component is either measured in the absence of the desired signals, or, if such measurement seems impossible, one can use a model matrix of noise coherence the formation of which is based on both *a priori* data on the noise and on experimental data. For example, in the case of uncorrelated noise, a matrix in the form $\varepsilon_0\Lambda_{min}E$, where Λ_{min} is the smallest eigenvalue of the sample matrix of coherence and ε_0 is the coefficient taking on values close to 1, can be used as the model matrix of noise coherence.

Various adaptive techniques can be proposed for evaluating the background component in the considered problem of detecting and evaluating the power density of weak (dark) sources against a background of stronger ones. The development of these methods is an interesting task and constitutes the subject of a separate study. For example, the model matrix of background coherence W_{comp} can be set in the form of a unit matrix multiplied by a certain coefficient (the maximal diagonal element of the sample matrix of coherence W can serve as this coefficient). However, such an approximation based on the dominance of the diagonal elements of the true matrix W_{comp} over nondiagonal ones is rough. A more exact technique is the evaluation of W_{comp} obtained by averaging the matrix W by smoothing out the influence of weak sources. The point is that the presence of dark regions violates the Toeplitz and cyclic character of the matrix of coherence of a uniform radiation background. Therefore, it is possible, for example, to form W_{comp} by the corresponding averaging of the elements of the matrix W on the main and secondary diagonals, which restores the Toeplitz and cyclic character of the matrix. Finally, the most efficient way of evaluating W_{comp} (which is described later in detail) is the iteration technique based on the gradual refinement of the reconstructed pattern of source distribution.

The matrix W_{comp} obtained in one way or another is multiplied by the coefficient $a > 1$. The coefficient value is determined by the accumulation parameters and is selected to be such that a definite sign of the matrix is guaranteed $(aW_{comp} - W)$. In the opposite case, the absence of a definite sign of the difference matrix leads to its singularity and the solution fails. The origin of such an instability may be the fluctuations of the evaluation of the signal power because of noise, oscillations of sensitivity of receivers or distortions of their directivity patterns, as well as the finiteness of the time of signal averaging. Thus, as one could expect, the price for the "super-resolution" obtained in the modified Capon algorithm is increased sensitivity to noise and uncertainty in the characteristics of the receiving system. However, the selection of an excessive coefficient a provides sufficient stability of the solution. The coefficient a can be estimated, for example, as the ratio of the sums of the main diagonals of the matrices W and W_{comp} multiplied by the coefficient $a_0 > 1$. The value of a_0 is selected so as to provide definiteness of the matrix sign $(aW_{comp} - W)$ on the one hand and maximal sharpness of the reconstructed image on the other (if the coefficient is too small, the solution fails, and if it is too large, the image loses its resolution).

The power density estimate obtained from Eqs. (1) and (2) is the result of the convolution of the spread function of this method with the true power density of thermoacoustic sources; i.e., it represents the average power of the true pattern that corresponds to the resolution spot of the spread function. The value of the average power is influenced also by the fact that thermoacoustic sources in a real tissue are spatially distributed. Eventually, the estimate turns out to be shifted. Therefore, a multistep procedure is proposed to obtain the estimates close to the true values. First, the estimate $\hat{I}_{Bar}(\mathbf{r})$ is constructed on the basis of W using one of the classical techniques (for example, the Bartlett method). Simultaneously, a homogeneous distribution with the

unit power density $I(\mathbf{r}) \equiv I^{\text{compl}} \equiv 1$ is considered for a preset size and shape of the studied region $\Re$. A direct problem on the formation of the model coherence matrix W_{compl} is solved for I^{compl}. Then, the corresponding calibration estimate of the form of Eq. (1) is constructed on the basis of this matrix: $\hat{I}_{\text{Bar}}^{\text{comp1}}(\mathbf{r})$. This estimate is not only shifted but also inhomogeneous within the region $\Re$: in the model considered, at the region boundaries, its values are smaller than at the center, since there are no thermoacoustic sources outside $\Re$. In this case, it is possible to adopt the corrected values $I_{\text{comp}}^{(0)}(\mathbf{r}) = \hat{I}_{\text{Bar}}(\mathbf{r})/\hat{I}_{\text{Bar}}^{\text{comp1}}(\mathbf{r})$ as the initial background distribution. The model coherence matrix $W_{\text{comp}} = W_{\text{comp}}^{(0)}$ is constructed according to these values. Since the classical methods of the type of Eq. (1) do not have a very high resolution, the estimate $I_{\text{comp}}^{(0)}(\mathbf{r})$ adequately reproduces the background structure and smoothes out the fine structural details.

The estimate $\hat{I}'(\mathbf{r})$ of the quantity $I'(\mathbf{r})$ that is obtained further from Eq. (2) has an essentially smoothed (i.e., averaged and shifted) character, and, therefore, the difference $aI_{\text{comp}}^{(0)}(\mathbf{r}) - \hat{I}'(\mathbf{r})$ cannot serve directly as the desired estimate $\hat{I}(\mathbf{r})$. In this connection, it is expedient to use an iteration cycle ($n \geq 1$ is the number of the iteration step):

$$\begin{gathered}\hat{I}'^{(n)}(\mathbf{r}) = \frac{1}{\langle \phi(\mathbf{r}) | (aW_{\text{comp}}^{(n-1)} - W)^{-1} | \phi(\mathbf{r}) \rangle}, \\ \hat{I}^{(n)}(\mathbf{r}) = aI_{\text{comp}}^{(n-1)}(\mathbf{r}) - \kappa^{(n)}\hat{I}'^{(n)}(\mathbf{r}), \\ I_{\text{comp}}^{(n)}(\mathbf{r}) = \hat{I}^{(n-1)} + \theta[\hat{I}^{(n)} - \hat{I}^{(n-1)}] \quad (0 < \theta \leq 1),\end{gathered} \tag{3}$$

where $\hat{I}^{(0)} = I_{\text{comp}}^{(0)}(\mathbf{r})$. Namely, the values of $I_{\text{comp}}^{(n-1)}(\mathbf{r})$ are considered as the power density of the background that is refined in the process of iterations. The model coherence matrix $W_{\text{comp}}^{(n-1)}$ constructed on the basis of $I_{\text{comp}}^{(n-1)}(\mathbf{r})$ is involved in Eq. (2) as the background matrix W_{comp} in the process of evaluating $\hat{I}'^{(n)}(\mathbf{r})$ by the modified Capon method. Finally, according to Eq. (3), the estimate of the desired distribution $\hat{I}^{(n)}(\mathbf{r})$ at the current iteration and a new estimate for the background distribution $I_{\text{comp}}^{(n)}(\mathbf{r})$ are formed. Since $I_{\text{comp}}^{(n)}(\mathbf{r})$ and $\hat{I}^{(n)}(\mathbf{r})$ must converge as the result of iterations to the estimate $\hat{I}(\mathbf{r})$ close to the true distribution $I(\mathbf{r})$, the coefficient $\kappa^{(n)}$ in Eq. (3) is evaluated by the method of least squares from the expressions

$$\hat{I}'^{(n)}(\mathbf{r})\kappa^{(n)} = (a-1)I_{\text{comp}}^{(n-1)}(\mathbf{r}), \quad \forall \mathbf{r} \in \Re.$$

To reduce the influence of the edge effects, the peripheral sources are given the values of power density close to the background values of the true distribution. Moreover, in the process of iterations, the parameter a can be selected to have different values to improve the convergence. The convergence of iterations was controlled by calculating the rms discrepancy with respect to the coherence matrix: $\chi_W^{(n)} \equiv \sqrt{\sum_{i,k=1}^{K} |W_{ik} - W_{ik}^{(n)}|^2}$, where $W_{ik}^{(n)}$ is the coherence matrix corresponding to the current estimate $\hat{I}^{(n)}(\mathbf{r})$. The final estimate corresponded to the minimal $\chi_W^{(n)}$.

The methods given by Eqs. (1)–(3) can be used in both narrow-band and wide-band modes of reception and processing of thermoacoustic signals. In the case of the narrow-band mode ($\Delta f \ll f_0$, where f_0 is the central frequency corresponding to the wavelength λ_0 in the operation frequency band with the width Δf), the spatial coherence matrices and phasing factors in Eqs. (1)–(3) are constructed as quasi-monochromatic. For example, in the case of a two-dimensional problem considered in the process of numerical simulation, it is assumed that

$$\begin{gathered}\phi_k(\mathbf{r}) = \exp(i2\pi f_0 \tau_k)/\sqrt{r_k} \\ \text{(the time dependence } \sim \exp(-i\omega t);\ r_k > 3\lambda_0),\end{gathered} \tag{4}$$

where τ_k is the propagation time of a signal through the distance r_k from the reconstruction point $\mathbf{r}$ to the receiver k. In the general case, in practical problems, when calculating τ_k, it is necessary to take into account the refraction inhomogeneities in the object's region under study. In the opposite case, the resolution of the estimate $\hat{I}(\mathbf{r})$ is reduced. It is necessary to note that the form of the phasing factors of Eqs. (4) is given for the case when the coherence matrices correspond to signals with the removed carrier frequency f_0. Then, the elements of these matrices in the quasi-monochromatic case depend only on the indices of receivers and are equal for all points $\mathbf{r}$, which saves the computation resources in determining the estimate $\hat{I}(\mathbf{r})$.

The numerical simulation was used to reconstruct the distribution of the power density of thermoacoustic sources in the two-dimensional region $\Re$ with the size $(32\lambda_0/3) \times (32\lambda_0/3)$. The object under study was surrounded by a circular antenna array. The signals from the array receivers were processed by a multichannel correlation system (see Fig. 1). Bright and dark sources with the power densities taken to be $I_{\text{bright}} = 3$ and $I_{\text{dark}} = 1$, respectively, were positioned in such a way that the structure formed by the dark sources against a light background simulated blood vessels against the background of surrounding tissues (Fig. 2a). The ratio $I_{\text{bright}}/I_{\text{dark}}$ corresponds to the real ratio of absorption in tissues and blood. The array receivers, whose total

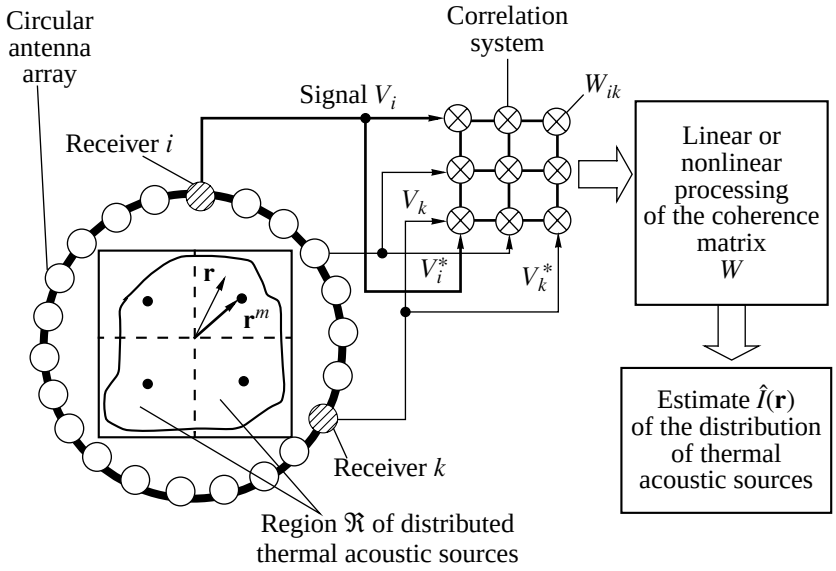

Fig. 1. Schematic diagram of an acoustic thermotomograph.

number was $K = 128$, were positioned uniformly in a circle with the radius $R = 10\lambda_0$. In the regularization, it was assumed that $\mu = 10^{-5}$.

The corrected estimate $I^{(0)}_{\text{comp}}(\mathbf{r})$ and the final iteration estimate $\hat{I}(\mathbf{r})$ obtained by the modified Capon method (3) (the result of 12 iterations performed with the parameters $a = 1.15$ and $\theta = 1/8$ for $n = 1$–10 and $a = 1.12$ and $\theta = 0.1$ for $n = 11$–12) are given in Fig. 2b and 2c, respectively. For comparison, all three figures (Figs. 2a–2c) are given on a single scale of brightness determined by the range of the estimate $\hat{I}(\mathbf{r})$. One can see that, in the estimate $I^{(0)}_{\text{comp}}(\mathbf{r})$, the values of the power density of bright background sources are close to the true values, but the contrast between bright and dark sources is strongly biased downwards. However, the reproduced contrast in the estimate $\hat{I}(\mathbf{r})$ after 10–12 iterations is close to the true contrast. The final estimate weakly depends on the initial step. For example, if the initial background is set to be homogeneous with the power density $I^{(0)}_{\text{comp}}(\mathbf{r}) \equiv 3$, the quality of the final estimate $\hat{I}(\mathbf{r})$ changes insignificantly.

It is necessary to note that the step of spatial scanning $\lambda_0/3$ for $\hat{I}(\mathbf{r})$ in Fig. 2c coincides with the discretization step, which determines the approximation of the initial structure in the numerical simulation (Fig. 2a). In the case of a smaller scanning step $\lambda_0/24$ (Fig. 2d, the result of ten iterations, $a = 1.15$, and $\theta = 0.1$), the width of thin lines corresponds to the resolution of the modified Capon method in the narrow-band mode of operation, since the initial structure is simulated in the form of chains of point noise sources. This width is close to the value $\cong(\lambda_0/4$–$\lambda_0/3)$. In the case of a simpler structure, the resolution of the modified method is considerably higher, which is illustrated below by the example of the wide-band case.

The wide-band mode ($\Delta f \cong f_0$) is more adequate to thermal tomographic systems, where it is desirable to use as large a value of the accumulation parameter $\cong 2\Delta f T_{\text{samp}}$ (T_{samp} is the sampling length) as possible. However, this mode needs tremendous computer power in the case of a standard approach. This is connected with the large dimension of the complete space–time matrix of coherence $W(\tau)$ with the elements $W_{ik}(\tau) = \overline{V_i(t)V_k^*(t+\tau)}$, where τ is the delay time. For example, when the linear dimension of the object is $L \cong$ (0.15–0.2) m, the propagation velocity of sound is $c \cong$ 1500 m/s, and the frequency bandwidth is $\Delta f \cong 1$ MHz, it is necessary to take into account about 600 discrete readouts for the time delays (with allowance for the delay signs) of the received signals, because the number of discrete time readouts of the same sign is $\cong 2\Delta f(L/c) \cong 200$–300. Then, in the case of 256 receivers, the matrix $W(\tau)$ has a dimension of about $256 \times 256 \times 600$, and the calculation of W^{-1} is barely possible. A two-stage technique of scanning was proposed and used to overcome such computation difficulties arising in the standard approach to the solution. The technique allows one to reduce the amount of simultaneously processed experimental information and utilize efficient processing methods while remaining within the limits of the technical capabilities of the computational systems.

At the first stage, the total region under study is divided into the subregions $\Re^m$ with the centers $\mathbf{r}^m$ (Fig. 1), $m = 1, \ldots, M$. The linear dimension l of each

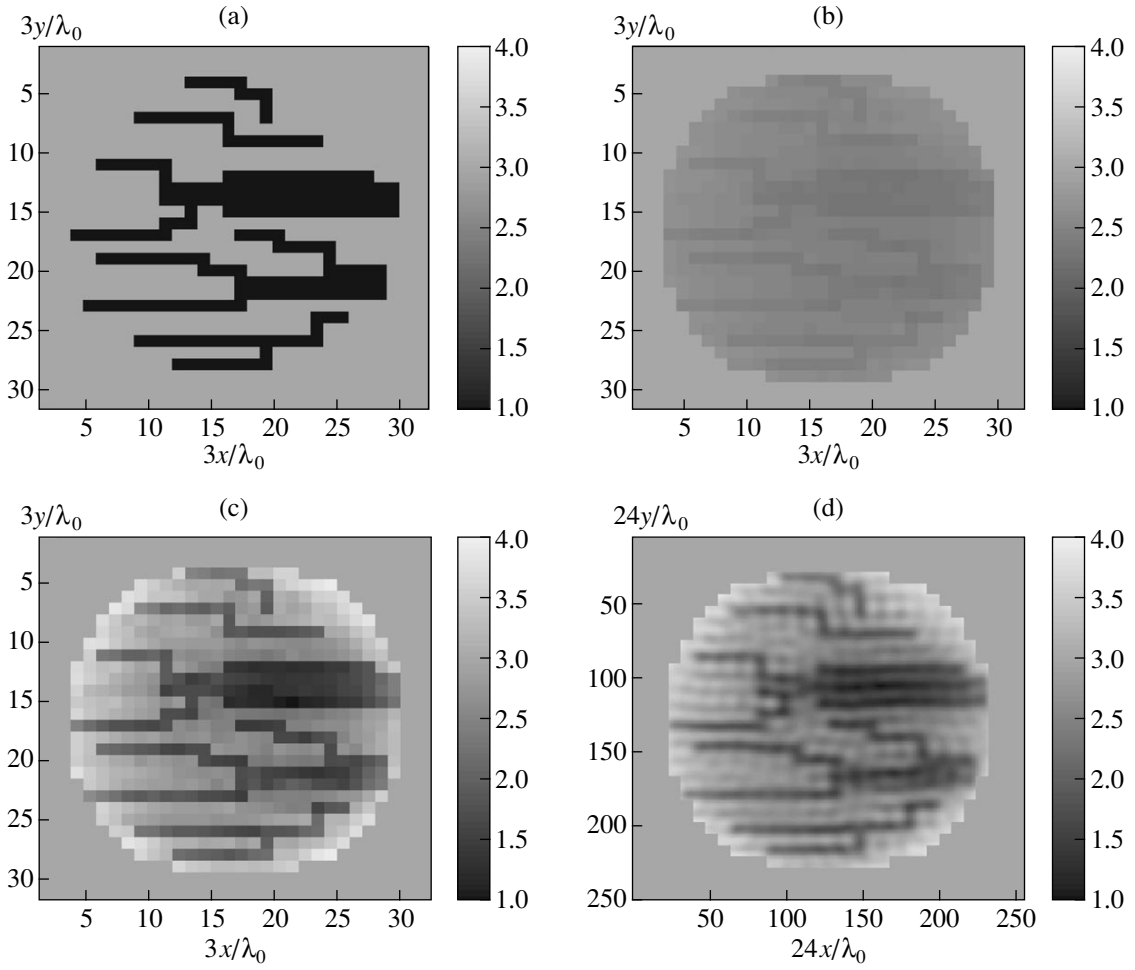

Fig. 2. Case of narrow-band signals. The distribution of the power density of the sources of thermal acoustic field. (a) The model of the initial structure; (b) the estimate by the Bartlett method; and (c, d) the final iteration estimates by the modified Capon method with the scanning step equal to (c) $\lambda_0/3$ and (d) $\lambda_0/24$ (the background for the first iteration is the estimate by the Bartlett method).

subregion is selected proceeding from the following requirement. The decorrelation of thermoacoustic radiation signals, which is connected with their wide-band spectrum, must be inessential at the distance between the center $\mathbf{r}^m$ of a given subregion $\Re^m$ and the boundary points $\mathbf{r} \in \Re^m$ of this subregion; i.e., the additional phase shift must not exceed fractions of π:

$$\frac{l}{2}\frac{\Delta\omega}{c} \le \frac{\pi}{4}, \quad \text{i.e.,} \quad l \le \frac{c}{4\Delta f}. \tag{5}$$

Then, the submatrices $W^m = \{W_{ik}(\tau_{ik}^m)\}$ are separated from the complete space–time matrix of coherence $W(\tau)$. Each of the submatrices is characterized by the delay time τ_{ik}^m. This time is determined by the relative positions of the center $\mathbf{r}^m$ of a given subregion $\Re^m$ and a pair of receivers (i, k): $\tau_{ik}^m = \tau_k^m - \tau_i^m$, where τ_k^m and τ_i^m are the propagation times from the point $\mathbf{r}^m$ to the receivers k and i. The background submatrices W_{comp}^m for the complete background matrix $W_{\text{comp}}(\tau)$ are constructed in an analogous way.

At the second stage, the phase spatial scanning within the subregions $\Re^m$ is performed. In this case, the matrices W and W_{comp} in Eqs. (1)–(3) are replaced by W^m and W_{comp}^m; i.e., they are assumed to be independent of the points $\mathbf{r} \in \Re^m$ due to the satisfied condition (5), as in the narrow-band case. The phasing factors are also set as quasi-monochromatic by virtue of the quasi-narrow-band character of the problem in each subregion.

In the numerical simulation, the full two-dimensional region $\Re$ with the dimension $2\lambda_0 \times 2\lambda_0$ was divided into $M = 4$ square subregions with the side length λ_0. In this case, $K = 16$, $R = 8\lambda_0$, and $\mu = 10^{-2}$. The selected frequency band $\Delta f = f_0/4$ satisfies requirement (5), since $l \cong \lambda_0$. In the initial structure (Fig. 3a), the power density of bright and dark sources is still $I_{\text{bright}} = 3$ and $I_{\text{dark}} = 1$. The signal emitted by each elementary segment of the structure was simulated in time

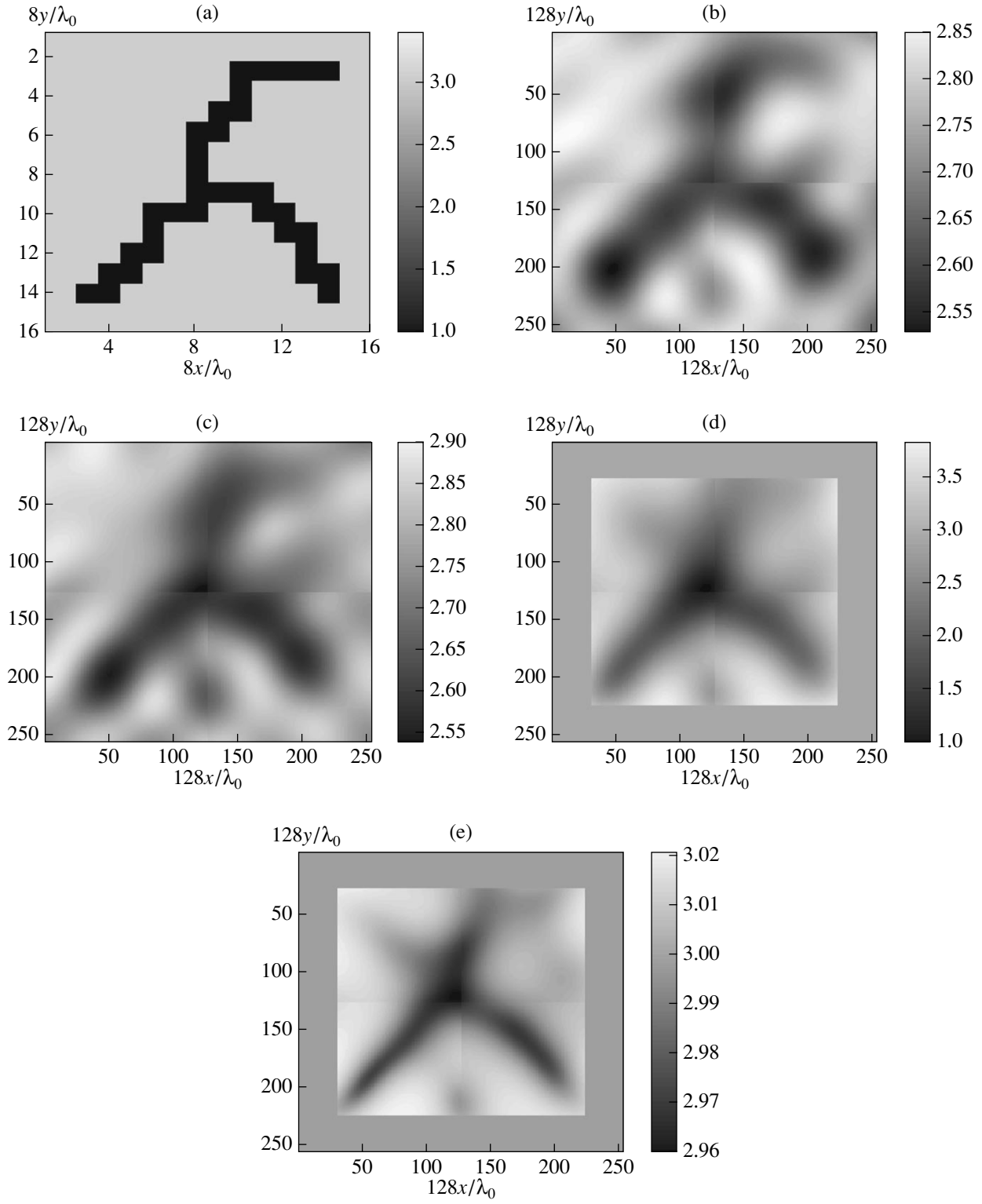

Fig. 3. Case of wide-band signals. The distribution of the power density of the sources of thermal acoustic field. (a) A model of the initial structure; the estimates by the (b) Bartlett and (c) Capon methods represented on a transformed scale; (d) the final iteration estimate by the modified Capon method with the scanning step $\lambda_0/128$ (the background for the first iteration is the estimate by the Bartlett method); and (e) the estimate obtained at the first iteration by the modified Capon method with the scanning step $\lambda_0/128$ (the background is homogeneous).

as a random quantity with a normal distribution, a zero average, and a variance equal to the local value of power density at a given segment. The complex values of the signal are assumed to be independent at a time step of discretization no smaller than $1/\Delta f$. The estimates $I^{(0)}_{\text{comp}}(\mathbf{r})$ by the classical Bartlett and Capon methods that are given in Figs. 3b and 3c on a stretched scale increasing the image contrast [scale range from $\min_{\mathbf{r}} I^{(0)}_{\text{comp}}(\mathbf{r})$ to $\max_{\mathbf{r}} I^{(0)}_{\text{comp}}(\mathbf{r})$] distinctly reproduce the structure of the dark sources (with the resolutions $\cong\lambda_0/4$ and $\cong\lambda_0/6$ for the Bartlett and Capon methods, respectively). This fact confirms the possibility of dividing $\Re$ into subregions with a subsequent scanning of subregions by a single phase adjustment. The form of the same estimates $I^{(0)}_{\text{comp}}(\mathbf{r})$ on the brightness scale, the same as the scale of the initial structure (Fig. 3a), and the iteration estimate $\hat{I}(\mathbf{r})$ (Fig. 3d) is similar to Fig. 2b. The contrast of the final iteration estimate $\hat{I}(\mathbf{r})$ by the modified Capon method (the result of eight iterations, $a = 1.15$ and $\theta = 0.1$) fits the truth much better than the contrast in $I^{(0)}_{\text{comp}}(\mathbf{r})$, but the bias is still noticeable. The resolution obtained in this example is $\cong\lambda_0/6$. Such a resolution is not the highest accessible for the modified Capon method in the case of simple structures (the structure considered in Fig. 3a belongs to them). One can see this from the example of the estimate $\hat{I}^{n=1}(\mathbf{r})$ that is obtained at the first iteration step on the assumption of a homogeneous background with the power density $I^{(0)}_{\text{comp}}(\mathbf{r}) = 3$ ($a = 1.01$) and is given in Fig. 3e on a stretched scale: the resolution reaches $\cong\lambda_0/12$.

Thus the modified Capon method in the absence of noise provides a high spatial resolution of images (no worse than $\cong\lambda_0/6$) in the problems of the type under consideration. The resolution becomes worse in the presence of additive noise. The nonlinear character of processing in the Capon-type algorithms leads to the deterioration of the sharpness of the response to a local source with an increase in the noise level. It is important in this case that the estimate stability persists. In the examples considered, a noticeable decrease in the resolution occurs when the noise-to-signal ratio in the sample matrix of coherence is $\cong$(1–2)%. However, a sufficiently accurate selection of the coefficient of background compensation a is required. This coefficient depends on the noise level and must provide definiteness of the sign of the noisy difference matrix of coherence on the one hand and a high resolution on the other. At the same time, *a priori* knowledge of the additive noise level provides an opportunity to subtract the noise coherence function from the sample coherence function and thereby compensate (if this is possible) the effect of noise and increase the resolution.

The finiteness of the time of averaging causes additional fluctuations of the coherence matrix that have a nonadditive character. However, errors of this type do not cause any noticeable deterioration of the resolution of correlation methods, and their main consequence are the errors in the evaluated values of power density. For example, the introduction of fluctuations with a level of 10^{-3} about the matrix element with the maximal absolute value into the sample matrix of coherence (that corresponds to matrix fluctuations in the case of the accumulation coefficient ~10^6) does not lead to any noticeable deterioration of the reconstructed pattern.

For the practical applications of the method under consideration, it is convenient to use its special feature that allows one to obtain images independently at different spatial points **r** (the locality of the method). The main shortcoming of this method is the bias of the estimates because of the spatially distributed character of thermoacoustic sources and the relatively small contrast of power density of bright and dark sources. Even multiple iterations cannot provide (within the framework of the selected method) the final image accuracy needed for further separation of the contributions from the inhomogeneities of the absorption coefficient, the temperature, and the velocity component [17]. Therefore, it is expedient to use the Capon method to obtain a general image structure. Knowledge of it provides an opportunity to reveal the pathologically significant individual regions. If the aforementioned separation of contributions is further needed, it is necessary to use one of the methods that provide an unbiased estimate for the selected regions. The price for the absence of bias is the nonlocality of such methods with respect to **r**. For example, when using the maximum-likelihood method [2, 3, 18, 21], the result of the numerical reconstruction in the absence of interference coincides precisely with the initial structure in Fig. 2a.[1]

Various schemes of practical realization of thermal acoustic tomography were considered in [2]. In connection with the high computational complexity of the correlation method (in its full realization) in wide-band systems with a large number of receiving elements, the possibility of simplifying the design and reducing the amount of calculation was examined. In tomographic schemes, this is attained by the use of transducers with large receiving surfaces or receivers combined into subarrays, which can be phased according to the required law with the help of a computer code. Figure 4 presents an example of a tomographic system where signals from the receivers of a circular array are combined in such a way that two plane receiving apertures are synthesized. The angle of relative inclination of the apertures and their angular positions on the circle can change. This is represented schematically in Fig. 4 by the dashed lines and an arrow denoting the rotation of

[1] We plan to publish a separate paper on the application of the maximum-likelihood method to problems of the type under consideration.

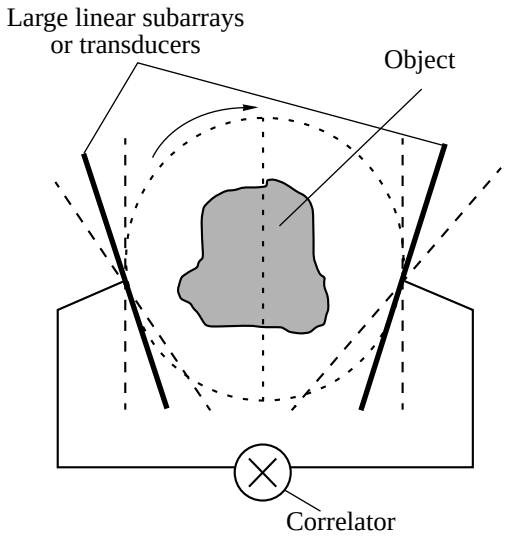

Fig. 4. Schematic diagram of the realization of an acoustic thermotomograph with plane receiving elements.

the synthesized apertures. Using preliminary additive processing, it is possible to reduce the amount of experimental information processed with the help of the correlation technique by restricting it to the data from a small number of synthesized apertures. However, simplification in such a scheme is obtained by reducing the temperature sensitivity or resolution or by increasing the time of information accumulation. Additional degrees of freedom, which are obtained by extending the frequency spectrum of the received thermoacoustic radiation and (or) by changing the angle between the subarrays, are used in the spatial scanning. Different schemes of data acquisition and different processing algorithms for tomographic information can be considered, depending on the problem to be solved. Further advances in thermotomographic designs and the development of methods of optimal evaluation in problems of acoustic thermotomography allow us to hope that passive thermoacoustic introscopy can be a valuable diagnostic tool in medicine and in nondestructive testing.

ACKNOWLEDGMENTS

This work is dedicated to the memory of L.M. Lyamshev, whose many works were concerned with correlation methods and thermoacoustic phenomena [22].

The work was supported by the Russian Foundation for Basic Research (project nos. 01-02-16282 and 00-15-96530 “Scientific Schools”).

REFERENCES

1. V. V. Gerasimov, V. I. Mirgorodskiĭ, S. V. Peshin, *et al.*, Akust. Zh. **41**, 651 (1995) [Acoust. Phys. **41**, 574 (1995)].
2. V. A. Burov and E. E. Kasatkina, Akust. Zh. **43**, 162 (1997) [Acoust. Phys. **43**, 135 (1997)].
3. V. A. Burov and E. E. Kasatkina, Acoust. Imaging **23**, 309 (1997).
4. A. A. Anosov, K. M. Bograchev, and V. I. Pasechnik, Akust. Zh. **44**, 725 (1998) [Acoust. Phys. **44**, 629 (1998)].
5. E. V. Krotov, S. Yu. Ksenofontov, A. D. Mansfel’d, *et al.*, Izv. Vyssh. Uchebn. Zaved., Radiofiz. **42** (5), 479 (1999).
6. R. A. Hessemer, Jr., T. Perper, and T. Bowen, U.S. Patent No. 4,416,552 (22 November 1983).
7. V. I. Pasechnik and Yu. N. Barabanenkov, Akust. Zh. **41**, 563 (1995) [Acoust. Phys. **41**, 494 (1995)].
8. V. I. Mirgorodskiĭ, V. V. Gerasimov, and S. V. Peshin, Zh. Tekh. Fiz. **66**, 196 (1996) [Tech. Phys. **41**, 514 (1996)].
9. A. I. Chmill, V. V. Gerasimov, Yu. V. Guluaev, *et al.*, Acoust. Imaging **23**, 607 (1997).
10. V. I. Passechnik, A. A. Anosov, M. G. Isrefilov, and A. V. Erofeev, Ultrasonics **37**, 63 (1999).
11. V. V. Gerasimov, Yu. V. Gulyaev, A. V. Mirgorodskiĭ, *et al.*, Akust. Zh. **45**, 487 (1999) [Acoust. Phys. **45**, 433 (1999)].
12. A. A. Anosov, M. A. Antonov, and V. I. Pasechnik, Akust. Zh. **46**, 28 (2000) [Acoust. Phys. **46**, 21 (2000)].
13. A. Ishimaru, *Wave Propagation and Scattering in Random Media* (Academic, New York, 1978; Mir, Moscow, 1981), Vols. 1, 2.
14. J. Folkman, J. Natl. Cancer Inst. **82**, 4 (1990).
15. S. B. Fox, K. C. Gatter, and A. L. Harris, J. Pathol. **179**, 232 (1996).
16. M. Born and E. Wolf, *Principles of Optics*, 4th ed. (Pergamon, Oxford, 1969; Nauka, Moscow, 1973).
17. V. A. Burov, P. I. Darialashvili, and O. D. Rumyantseva, Akust. Zh. **48**, 474 (2002) [Acoust. Phys. **48**, 412 (2002)].
18. V. A. Burov, E. E. Kasatkina, O. D. Rumyantseva, and S. A. Filimonov, Acoust. Imaging **26**, 265 (2002).
19. S. L. Marple, Jr., *Digital Spectral Analysis with Applications* (Prentice Hall, Englewood Cliffs, NJ, 1987; Mir, Moscow, 1990).
20. D. H. Jonson and S. R. DeGraaf, IEEE Trans. Acoust., Speech, Signal Process. **30**, 638 (1982).
21. V. A. Burov and O. V. Dmitriev, Radiotekh. Élektron. (Moscow), No. 6, 1276 (1973).
22. L.M. Lyamshev and M.L. Lyamshev, Akust. Zh. **43**, 821 (1997) [Acoust. Phys. **43**, 716 (1997)].

Translated by M. Lyamshev

Acoustical Physics, Vol. 49, No. 2, 2003, pp. 143–147. Translated from Akusticheskiĭ Zhurnal, Vol. 49, No. 2, 2003, pp. 178–182.

Determination of the Target Strength of a Scatterer with the Use of Surface Reverberation

V. A. Zverev and P. I. Korotin

Institute of Applied Physics, Russian Academy of Sciences, ul. Ul'yanova 46, Nizhni Novgorod, 603600 Russia

e-mail: zverev@hydro.appl.sci-nnov.ru

Received February 22, 2002

Abstract—Results of measuring the target strength of a scatterer by using the data on the sound propagation and surface reverberation in the basin are presented. The proposed technique implies the use of a receiving antenna array with a narrow directivity pattern and a bistatic scheme of location. © *2003 MAIK "Nauka/Interperiodica".*

A number of publications [1–3] concerned with studying surface reverberation consider the latter as an interfering noise in underwater echolocation. In our study, we use the properties of surface reverberation to experimentally determine the decay law of the sound field level produced by a point source as a function of distance.

For the bistatic location scheme depicted in Fig. 1, the following equation of active location [4] is valid:

$$\mathrm{TL} = \mathrm{RL} + \mathrm{PL}_{1,3} + \mathrm{PL}_{2,3} - \mathrm{TS}. \qquad (1)$$

Here, TL is the transmitted sound level reduced to a 1-m distance from the source and expressed in decibels relative to the unit pressure; RL is the level of the received signal scattered by the body, which is also expressed in decibels relative to the same unit pressure; and PL is the propagation loss caused by the divergence of the wave front and sound absorption in the medium (this value is expressed in decibels relative to the initial level). The subscripts "1, 3" and "2, 3" indicate the paths from the source (1) to the scatterer (3) and from the scatterer (3) to the receiver (2), respectively. The initial level is specified as the pressure in the spherical wave at a 1-m distance from the center of the sphere. The last term TS is the target strength of the scatterer, which is also expressed in decibels: TS is equal to zero when the scattered signal is equal to the incident one at a 1-m distance from the scatterer's center. If the incident and scattered sound fields become equal at a distance R from the scatterer's center, we have $\mathrm{TS} = 20\log(R)$. So defined target strength proves to be reduced to that of a sphere of radius R on the assumption that the spherical law of field decay is valid within this radius.

According to Eq. (1), it is insufficient to receive and measure the RL signal scattered by the object for determining the value of TS from the location experiment. In addition, one should measure TL and know PL. Among these parameters, the value of PL is most difficult to measure, because, in acoustics, it may depend on the distance in a complicated manner, this being especially true for shallow-water basins [4].

The objective of our paper is to show that, with certain positions of the omnidirectional sound source, beamed receiving array, and location object, one can use pulsed signals to simultaneously measure all terms of Eq. (1) and thereby obtain the estimate of TS. The main idea consists in extracting and making use of the surface reverberation signal. The latter serves to calibrate the path for simultaneously measuring the values of PL and RL. To avoid the need to measure TL, we use a bistatic scheme of location.

The experimental layout is illustrated in Fig. 1. The experiment was carried out at the Gorki reservoir. The water depth was about 7–8 m at the experimental site. The duration of the transmitted pulse was 2 ms, the carrier frequency was 2 kHz, and the repetition rate was 200 ms. For the signal reception, a 6-m-long horizontal antenna array consisting of 32 individual hydrophones

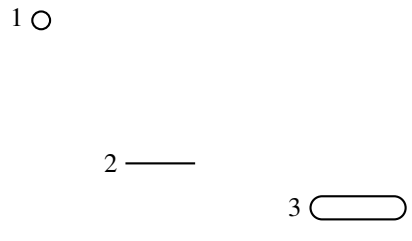

Fig. 1. Experimental layout (from above): (1) the omnidirectional sound source, (2) the phased horizontal antenna array, and (3) the object of location.

1063-7710/03/4902-0143$24.00

was used. From each hydrophone of the array, the signals were recorded in a broad frequency band. Hence, we could phase the array to separate a certain reception direction. The object of location was a hollow cylindrical tube with a ballast, 8 m in length and 0.6 m in diameter. The tube was towed by a rowing boat at a depth of 3 m with a constant speed of about 0.5 m/s in different directions and at different distances from the sound source and the receiving array. The same technique was used in the experiment reported in [5].

For the experimental layout shown in Fig. 1, Eq. (1) can be supplemented with an equation that describes the signal transmitted by the source (1) upon its reception by the array (2):

$$\mathrm{TL} = \mathrm{RL}_{\mathrm{rec}} + \mathrm{PL}_{1,2}. \tag{2}$$

Here, $\mathrm{RL}_{\mathrm{rec}}$ is the signal directly received by the array (the direct field) and $\mathrm{PL}_{1,2}$ is the propagation loss characterizing the signal propagation from the source to the receiving array.

By subtracting Eq. (2) from Eq. (1), we obtain

$$\mathrm{RL}_{\mathrm{rec}} = \mathrm{RL} + \{\mathrm{PL}_{1,3} - \mathrm{PL}_{1,2}\} + \mathrm{PL}_{2,3} - \mathrm{TS}. \tag{3}$$

To use Eq. (3) for estimating the value of TS, one should know how the propagation losses on the paths between the points shown in Fig. 1 depend on the distance.

We assume that the medium is homogeneous and that the propagation losses depend on nothing but the distance between the points. For the distances (less than 100 m) and frequencies (2 kHz) used in the experiment, the sound absorption in water can be neglected. We also assume that the surface waves do not change their statistical characteristics within the distances at hand.

Theoretically, the problem consists in choosing the transition distance between the two laws of the amplitude decay. At short distances from the source, the spherical law is valid. Starting from a certain transition distance, this law transforms into the cylindrical law. It is possible to distinguish between the two laws and determine the transition distance by observing the decay of surface reverberation.

However, with all the aforementioned assumptions, it is difficult to determine PL from the reverberation decay for the omnidirectional reception and a bistatic location scheme. This difficulty is caused by the fact that the reverberation signals depend not only on the distance from the receiver and the surface state but also on the distance from the source. They also exhibit a complicated angular dependence [2, 3] in a bistatic location. The locus of the points from which the signal simultaneously arrives at the omnidirectional receiver has a cumbersome shape, so that one cannot unambiguously determine the contribution of PL to the received reverberation signal. To overcome this difficulty, we used a beamed receiving array.

In addition to the decay law of PL, the reverberation decay is influenced by a number of other factors. As the distance from the array increases, the intensity of the surface insonification decreases, but the area from which the reverberation arrives at the receiver increases linearly with distance. If one places the source at the bearing angle close to zero and receives the reverberation from the same angle (i.e., from a direction that is perpendicular to the array) but with delays greater than the source-to-receiver propagation time, the reception from a single reverberating surface segment can be achieved. With the use of Eq. (3) (see also Section 8.5 in [4]), we obtain

$$\begin{aligned}\mathrm{RL}_{\mathrm{rec}} &= \mathrm{SL}_s + \{\mathrm{PL}_{1,3} - \mathrm{PL}_{1,2}\} \\ &+ \mathrm{PL}_{2,3} - S_s - 10\log(ct_{\mathrm{pulse}}/2) - 10\log(\Phi R).\end{aligned} \tag{4}$$

Here, SL_s is the level of surface reverberation; S_s is the scattering strength of a unit surface area, this scattering strength being assumed to be constant; c is the sound speed; t_{pulse} is the pulse duration; the product of $(ct_{\mathrm{pulse}})/2$ and ΦR determines the area of the scattering surface; and Φ is the known function that characterizes the combined directivity of the source and the receiving array. The subscript "3" denotes the point of the surface at a variable distance R from the receiver along the reception bearing. The direction of reception is chosen so that the maximum of the receiver directivity coincides with the line connecting the receiver and the source, but this direction is opposite with respect to the source. Hence, there is no need to allow for the dependence of S_s on the horizontal angle. At the same time, with the chosen scheme of measurements, the following condition is approximately valid: $\mathrm{PL}_{1,3} - \mathrm{PL}_{1,2} \sim \mathrm{PL}_{2,3}$.

In measuring the range dependence of PL, the signal was processed as follows. First, the signal of surface reverberation was singled out. The bottom reverberation should be eliminated, because the bottom roughness can be arbitrarily distributed in space. The volume reverberation also does not satisfy Eq. (4). To eliminate the bottom and volume reverberations, we used the interperiod subtraction (as in [5]). In all pulsed transmissions involved in the signal processing, the signals are combined in magnitude.

After measuring $\mathrm{RL}_{\mathrm{rec}}$ and SL_s, $\mathrm{PL}(R)$ is determined from Eq. (4). The resulting dependence $\mathrm{PL}(R)$ can be used directly in Eq. (3) or can serve to match a theoretical estimate of the reverberation decay, e.g., a spherical $(1/R)$ or cylindrical one (the spherical law before the transition distance and $1/\sqrt{R}$ after it).

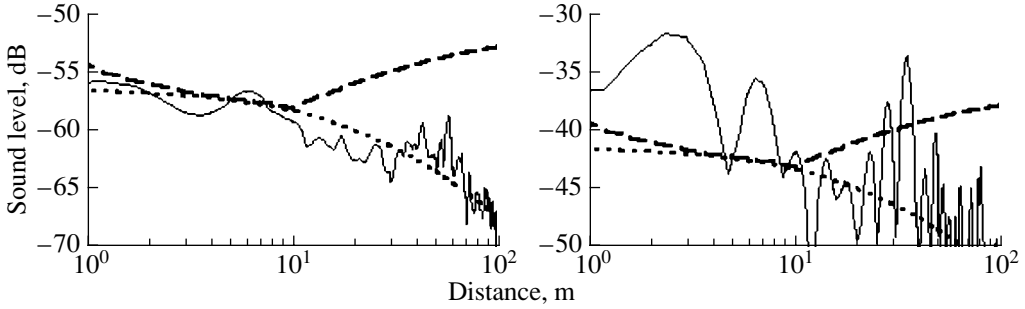

Fig. 2. Experimental range dependence of reverberation (the solid curve) with interperiod subtraction (the left) and without it (the right). The levels are indicated with respect to the direct signal. The spherical (dotted curve) and cylindrical (dashed curve) decay laws are shown for a transition distance of 10 m.

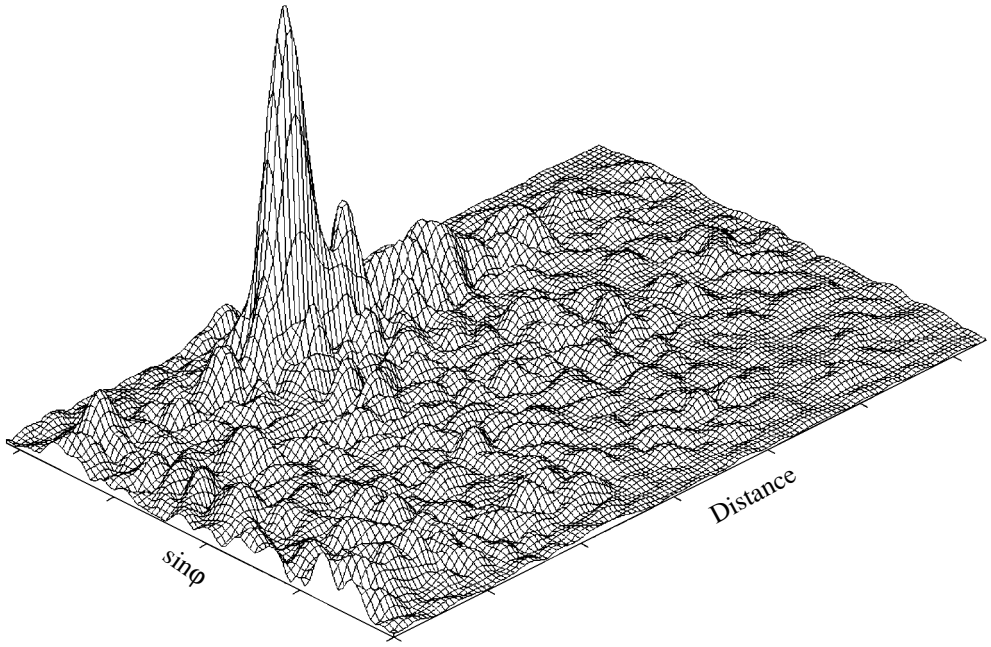

Fig. 3. Detection of the signal scattered by the object for a single observation instant. The signal processing is performed for 24 transmissions. The signal is represented in the range–bearing (sine of the angle) coordinates. The Doppler shift of the signal is 0.68 Hz. The distance (from the receiving array) varies from 6 to 75 m. The sine of the angle varies from +1 to –1. At a bearing close to 80°, the position of the signal maximum corresponds to a distance of 32 m.

In Fig. 2, the calculations are compared with the experimental data. The dashed and dotted curves show the theoretical range dependences of the reverberation level, which are found with the aforementioned technique from Eq. (4). On the left, the reverberation decay obtained by the interperiod subtraction is presented. This decay characterizes the behavior of surface reverberation. On the right, for the sake of comparison, the total reverberation signal is plotted (without interperiod subtraction). The spherical law of the level decay with S_s equal to –58 dB adequately describes the observed range dependence of surface reverberation. The total reverberation level (on the right) is higher by 15 dB.

The resulting relation between the theoretical and experimental reverberation decays is steadily observed for all measurements carried out within one day and does not depend on the motion of the located object. The wind speed and direction did not change during the measurements. Hence, we can conclude that, in our experiment, the decay of sound level is close to the spherical law. Most probably, such a behavior is a consequence of the fact that, for acoustic waves of frequency 2 kHz used in our measurements, the bottom is an absorptive medium rather than a reflective one.

The distance to the scatterer, which appears in PL, was determined from the propagation time for the

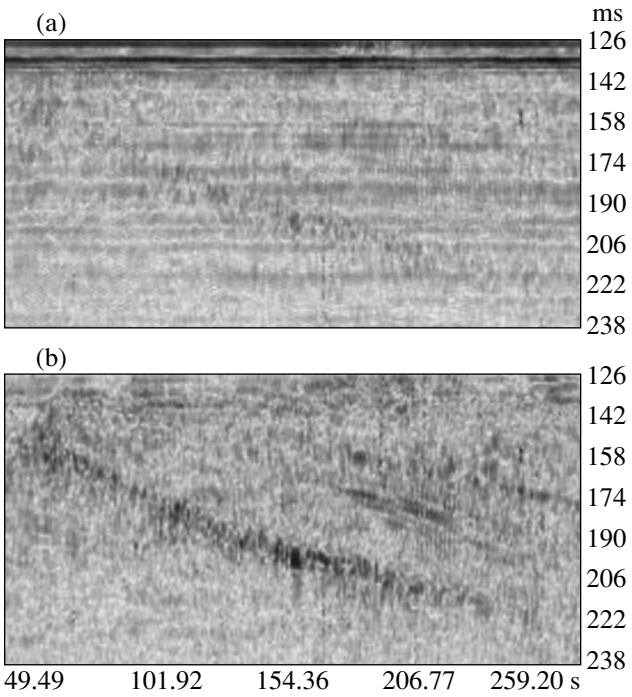

Fig. 4. Signal amplitude at the array output for a single bearing (–50°) as a function of time (number of transmission). The vertical axis represents the delay time for the transmission, starting from the instant of signal arrival at the array (126 ms) to 240 ms. The horizontal axis represents the time (in seconds), starting from the beginning of the tack. (a) The upper plot is obtained without additional processing, and (b) the lower plot, with filtering out the low frequencies from the signals of equal delays (horizontal secant lines in Fig. 4a).

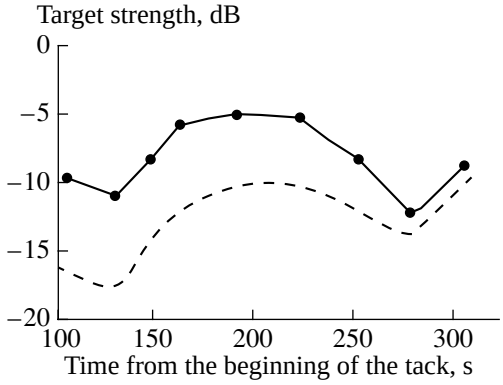

Fig. 5. Target strength as a function of time (the horizontal coordinate of Fig. 4): the spherical (the solid curve) and cylindrical (the dashed curve) laws of the sound level decay for a transition distance of 10 m.

pulses extracted from the reverberation background by filtering. Figure 3 shows an example of detecting a signal that was scattered by the object moving along the path. The echo-signal was detected with the use of the processing procedure including the following stages: phasing of the array (spatial filtering); coherent cumulation for 5 s, i.e., 24 pulsed transmissions (time filtering); and interperiod subtraction (time selection).

Figure 4 shows a set of scattered signals detected within a fraction of a single tack produced by the scatter in its motion. In Fig. 4a, the amplitude of the reflected signal is shown by shading in the range–time (pulse number) plane for a single array bearing (about –50°) with a signal bandwidth of 1 kHz. The horizontal axis represents the time (1024 pulses, which corresponds to about 200 s), and the vertical axis represents the delay time (with 0.8-ms increments) of the pulse arrival, starting from the instant of the signal reception by the array to a range of about 150 m. Each vertical secant line is formed by the echo of a single transmission. At the top of Fig. 4a, two dark parallel strips correspond to the direct signal and the bottom reverberation. The gray horizontal strips at high delays correspond to the echoes of stationary reflectors. Figure 4b shows the same signal after the processing. In the signals of equal range (corresponding to horizontal secant lines in Fig. 4a), low frequencies are filtered out to eliminate the contribution of stationary scatterers, this technique being an improved version of the interperiod subtraction. In Fig. 4b, the desired signal, i.e., the trajectory of the object motion, is clearly pronounced against the background of surface reverberation. The direct signal, the bottom reverberation, and the signals of other stationary scatterers (horizontal lines in Fig. 4a) are absent in Fig. 4b.

The changes in the brightness of the object's echoes, which are clearly visible in Fig. 4b, correspond to the changes in both TS and PL in the process of the object's motion. The values of TS measured according to Eq. (3) for the trajectory along which the object moves (see Fig. 4b) are represented in Fig. 5. To show the limits of the TS variation depending on the model of PL, the curve corresponding to the cylindrical law of level decay is given in the same plot.

Figure 6 shows the calculated values of the cylinder target strength as a function of the insonification angle for the monostatic location scheme; these data are obtained from the formulas given in [4]. It is difficult to directly compare the data shown in Figs. 5 and 6, because the signal levels are different and also because the aforementioned formulas [4] use the condition that the cylinder radius is much greater than the wavelength, and this condition was not met in the experiment. However, one can see that the calculated and measured values of the target strength are close to each other in order of magnitude.

The value of the target strength for surface reverberation S_s, which was experimentally measured by us, is interesting in itself. This value allows one to estimate the lower threshold of the target strength of the located object that can be detected against the background of

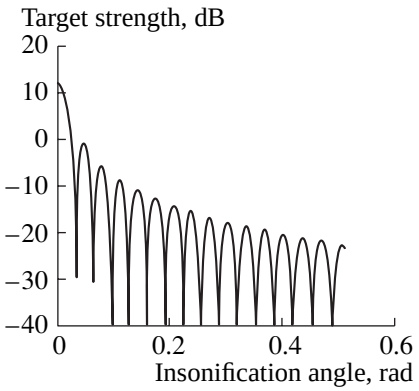

Fig. 6. Calculated target strength of the cylinder versus the insonification angle (from [4]).

the reverberation noise. In our experiment, the value of the object's target strength was below the threshold for location aspects that are close to those of the object's ends. For such aspects, the object could not be detected against the reverberation background.

ACKNOWLEDGMENTS

We are grateful to B.M. Salin, A.L. Matveev, and A.G. Luchinin for useful discussions. This work was supported by the Russian Foundation for Basic Research (project nos. 00-15-96741, 02-02-17056, and 01-02-17380) and by the CRDF (project no. RPO-1346).

REFERENCES

1. Yu. M. Sukharevskiĭ, Dokl. Akad. Nauk SSSR **55** (9), 825 (1947).
2. Y. Y. Dorfman and I. Dyer, J. Acoust. Soc. Am. **106**, 1755 (1999).
3. A. V. Belousov, E. A. Kopyl, and Yu. P. Lysanov, Akust. Zh. **35**, 223 (1989) [Sov. Phys. Acoust. **35**, 134 (1989)].
4. R. Urick, *Principles of Underwater Sound* (McGraw-Hill, New York, 1975; Sudostroenie, Leningrad, 1978).
5. V. A. Zverev and P. I. Korotin, Akust. Zh. **49** (1), 71 (2003) [Acoust. Phys. **49**, 62 (2003)].

Translated by E. Kopyl

Acoustical Physics, Vol. 49, No. 2, 2003, pp. 148–157. Translated from Akusticheskiĭ Zhurnal, Vol. 49, No. 2, 2003, pp. 183–193.

Acoustic Images of Objects Moving under an Inhomogeneous Layer

N. V. Zuikova, T. V. Kondrat'eva, and V. D. Svet

Andreev Acoustics Institute, Russian Academy of Sciences, ul. Shvernika 4, Moscow, 117036 Russia

e-mail: vsvet@akin.ru

Received August 22, 2001

Abstract—The possibilities and limitations of the methods of obtaining acoustic images of objects moving under an inhomogeneous scattering layer are considered. It is shown that the previously proposed algorithms of signal processing that select a random phase modulation from the received field make it possible to reconstruct the images of extended objects observed through an inhomogeneous medium in the presence of strong stationary reflectors. The proposed methods are compared with the Zverev's method of an inverse aperture synthesis in a dark field. *© 2003 MAIK "Nauka/Interperiodica".*

In audiovision a situation when an inhomogeneous scattering layer occurs between an object of interest and the plane of observation is quite common. Depending on the type of the layer, the acoustic image may be slightly distorted or completely deformed. For instance, if such a layer is a diffusion screen, at certain wavelengths it is impossible to obtain the image even of a point object. For objects located in inhomogeneous layered media, the images exhibit a strong ambiguity: they multiply and overlap, which makes it impossible to achieve the required quality.

The classical theory of signal detection is based on the possibility of selecting the coherent and the most stable part of the signal from the received field, this part retaining its shape and phase relations in the process of propagation. All other components are considered as interference. In a homogeneous medium, these components are usually represented by the additive independent noise of other sources or the instrumentation noise. In inhomogeneous media with scattering, other types of additional interference caused by the initial signal are observed. Part of these waves scattered by inhomogeneities give rise to random amplitude–phase modulation forming a multiplicative interference in the received signal. It is this type of interference, stationary or nonstationary, that causes unpredictable deformations of the signal wave front that are impossible to reduce by a simple increase in the signal intensity.

In the simplest signal processing algorithms, the presence of inhomogeneities or scattering is usually ignored, and the processing is carried out by treating the medium as an analog of a free space. The elimination of the interfering effect of phase fluctuations is achieved in this case by afterdetection processing: usually, by averaging, incoherent summation of separate maxima, selection of the threshold and the frequency band, and so on.

More complex algorithms of spatial processing developed in recent decades allow one to take into account the structure and parameters of a multipath channel. If we can compute or measure the transfer function of the medium accurate to phase relations, it is possible to design an optimal filter that can, for example, "compress" a multipath signal. Such processing in statistical acoustics is called channel-matched processing, although its physical foundations were laid long before with the appearance of holography and methods of wave conjugation in linear and nonlinear media. Thus, channel-matched processing suggests that, at least during the interval of the signal observation, the channel characteristics are exactly known and remain constant.

For inhomogeneous media with a random scattering, especially when the scattering is nonstationary in time, matched signal processing is useless, because it is not possible to either calculate or measure the transfer characteristics of the medium. For instance, for the case of a phase screen, it is impossible to construct an image of a point source by the classical method. Instead of an image of one point, the observer will see a set of randomly positioned images of points. Besides, although for various frequencies and distances the multipath propagation and scattering occur in inhomogeneous media in various proportions, in most practical situations one cannot take them into account exactly.

Does this mean that, in the conditions of an unknown inhomogeneous channel, it is impossible to obtain the information of interest about a sound source, for instance, to measure its current coordinates, its velocity, or to reconstruct its image or detect and evaluate the inhomogeneities of the channel? In the framework of the classical methods of signal processing based on the selection of the coherent component of the

1063-7710/03/4902-0148$24.00

received field, no appropriate solutions has been found to this problem in the general case. However, as will be shown below, a significant volume of information on both the inhomogeneous channel and the sound source can be obtained by processing and analyzing only the random multiplicative component of the received field, i.e., the component that is considered in the detection theory as the most serious interference.

One of these methods was proposed and developed by V.A. Zverev *et al*. [1–7] and was called the inverse aperture synthesis in a dark field. From the point of view of the classical detection theory, which is based on the selection of the coherent and stable part of the signal, in the dark field method, the situation is reversed, since the interference is the strong coherent component and the desired information is carried by the signal from a weak inhomogeneity. The dark field method is based on nonlinear operations performed with the received signals, and the image reconstruction is carried out by using the information that is extracted from the phase difference of multiplicative scattered components of the field.

Another approach was developed in our previous papers [8–12]. Being close to the dark field method in its main ideas, this approach is based on the concepts of the double-exposure phase holography and speckle interferometry. In previous papers [8, 9], it was shown that, on the basis of speckle interferometry, it is possible to reconstruct the coordinates (trajectory) of a moving point source of sound in the case of its observation through a strongly scattering or multilayer inhomogeneous medium without matched signal processing. However, it was found that, with only one point of observation, it is possible to reconstruct only relative coordinates of the source, although with the accuracy determined by the angular resolution of the antenna. In article [12], this approach was extended to the solution of the problem of visualization of an inhomogeneous liquid flow observed through an inhomogeneous layer (the visualization of a blood flow through the thick bones of a skull in transcranial ultrasonic diagnostics).

It should be emphasized that, in both approaches, the presence of phase fluctuations in the received signals is crucial. In addition, it is assumed that, in the received field, two spatial structures are always present: a stable coherent component, which can be of high intensity, and a weak scattered component fluctuating in time. Examples of such practical situations may be a sound source moving in a multipath oceanic medium with a signal that is received by a stationary horizontal antenna extended enough to resolve individual normal waves [10], or, vice versa, a stationary sound source and a moving long horizontal antenna that does not retain its linearity and randomly changes its form with time [7]; a sound source moving in a solid layered medium [11]; a moving flow of weak scatterers of ultrasound (for example, signals scattered by a blood flow against a background of strong signals reflected from the vessel walls [12]); and so on. In all these examples, the received field is characterized by phase fluctuations.

In the present paper, we analyze some features of the previously proposed method of reconstructing the image of a point source through an inhomogeneous layer [12], and, in particular, we consider in more detail the following model. Consider a linear multielement antenna extended along the x axis, an inhomogeneous layer located at some distance from it, and an object of our interest. This object creates a reflected field that has two components: coherent and incoherent, the latter being produced, for example, by moving scatterers. An example of such an object may be a blood vessel: the vessel walls produce a coherent reflected signal, and the moving erythrocytes produce an incoherent signal [12]. Below, we will refer to the reflected coherent signals as the background, its level being usually higher than the levels of the incoherent scattered signals.

Let the inhomogeneous layer and the object be irradiated by a field of a pulsed tone signal of frequency f. For simplicity, we assume that the duration of the pulsed signal and the distance from the inhomogeneous layer to the object are such that the signal reflected from the inhomogeneous layer can be ignored and the signal reflected from the object arrives at the receiver after the termination of the pulse. We will also consider the mode of combined reception and radiation.

Let us record the instantaneous distribution of the phase of the received signal along the antenna $\Phi_1(x)$ at the moment t_1 and store it. After some interval at $t_2 = t_1 + \tau$, we make another similar measurement to obtain $\Phi_2(x)$. The interval τ is chosen so that, in the second measurement, the signal phases at the receivers are changed; i.e., $\Phi_2(x)$ is a different distribution. Actually, the interval τ is a correlation interval of a random scattering process. One of the examples of its estimation for a specific model of scattering is given in [12]. Next, we form a new function

$$\Delta\Phi(x) = \Phi_2(x) - \Phi_1(x) \tag{1}$$

and reverse the wave front by function (1).

Depending on the distance from the antenna to the object, the wave front reversal can be performed on the basis of the Fourier–Fresnel transformation or by using the exact expression

$$I(\xi) = \left| \int_0^D \{\Phi_1(x) - \Phi_2(x)\} \exp(ikR)\, dx \right|^2, \tag{2}$$

where $k = 2\pi/\lambda$ and the distance R to every element is calculated as

$$R = \sqrt{R_0^2 + (\xi - x)^2}.$$

Since $I(\xi)$ is a random quantity, the final reconstructed image is obtained by averaging over many results of measuring $I(\xi)$, i.e.,

$$\tilde{I}(\xi) = \sum_{l=1}^{L} I_l(\xi). \tag{3}$$

It is easy to show that the wave front reversal by function (1) generally eliminates all multiplicative distortions introduced by the layer [8, 9]. However, does this operation allow one to reconstruct the image of a dynamic object and to measure its absolute coordinates? What is the quality of the reconstructed image? These are the questions that we will try to answer.

Algorithms (1)–(3) were investigated by computer modeling. The field at the antenna was calculated by the formula

$$P(x) = \sum_{m=0}^{M} A_m(\xi_m)\exp[i\varphi_m(\xi_m)] \times \exp[-ik\sqrt{R_0^2 + (\xi_m - x)^2}], \tag{4}$$

where the sign of the second exponential function is taken opposite to the sign of the exponential function in Eq. (2), A_m is the amplitude of the signal reflected from the mth element of resolution of the object, and φ_m is the signal phase acquired at the reflection from the mth element. The amplitude coefficient $1/R$ of $\exp(-ikR)$ is omitted. The averaging over L images given by Eq. (2) is performed by operation (3) for $2L$ realizations of the random quantities $[A_m(\xi_m), \varphi_m(\xi_m)]$. In the following quantitative estimates and in comparing the energy levels of signals, the amplitude coefficients $A_m(\xi_m)$ are equalized for all elements of the object $m = 1, \ldots, M$. Only the phases $\varphi_m(\xi_m)$ are random. Usually, the phase of the field $P(x)$ at the antenna [Eq. (4)] is found from the relation

$$\Phi(x) = \arctan[\operatorname{Im} P(x)/\operatorname{Re} P(x)]. \tag{5}$$

In this expression, the function $\arctan z$ is determined in the $[-\pi/2, \pi/2]$ half-plane for the values of the argument $z \in [-\infty, \infty]$. To obtain complete information and to construct an undeformed image, the function $\Phi(x)$ is calculated according to the following rules:

$$\left.\begin{aligned}
&\text{if} \quad \operatorname{Re} P(x) > 0,\\
&\text{then} \quad \Phi(x) = \arctan[\operatorname{Im} P(x)/\operatorname{Re} P(x)];\\
&\text{if} \quad \operatorname{Re} P(x) = 0,\\
&\quad \begin{cases}
\operatorname{Im} P(x) < 0, \quad \text{then} \quad \Phi(x) = -\pi,\\
\operatorname{Im} P(x) > 0, \quad \text{then} \quad \Phi(x) = \pi,\\
\operatorname{Im} P(x) = 0, \quad \text{then} \quad \Phi(x) = 0;
\end{cases}\\
&\text{if} \quad \operatorname{Re} P(x) < 0 \text{ and}\\
&\quad \begin{cases}
\text{if} \quad \operatorname{Im} P(x) > 0,\\
\text{then} \quad \Phi(x) = \arctan[\operatorname{Im} P(x)/\operatorname{Re} P(x)] + \pi,\\
\text{if} \quad \operatorname{Im} P(x) = 0, \quad \text{then} \quad \Phi(x) = 0,\\
\text{if} \quad \operatorname{Im} P(x) < 0,\\
\text{then} \quad \Phi(x) = \arctan[\operatorname{Im} P(x)/\operatorname{Re} P(x)] - \pi.
\end{cases}
\end{aligned}\right\} \tag{6}$$

Thus, $\Phi(x)$ is calculated over the whole unit circle within $(-\pi, \pi)$ on an interval equal to 2π with a mean value of zero. Setting the mean value $\Phi(x) = 0$ is important for numerical modeling, as well as for experiment to avoid the accumulation of the steady component in the image, because phase information (4) in Eqs. (2) and (3) acts as amplitude information. Hence, for $\operatorname{Re} P(x) < 0$ and $\operatorname{Im} P(x) = 0$, we determine $\Phi(x) = 0$ as the mean between π and $-\pi$. Operation (6) is ambiguous, accurate to the number of complete periods of 2π.

Operation (6) is nonlinear, but only because of the nonlinearity of (6) do we have a chance to observe the object in the image plane where it is really located. The information about the object's coordinates is retained due to the boundedness of the function $\Phi(x)$ within the limits $(-\pi, \pi)$.

We illustrate this with the example of the reconstruction of a point source by using a linear antenna with N receivers spaced at $\Delta x = \lambda/2$. Figure 1a shows the phase function $\Phi(x)$ calculated by formulas (6) for $N = 128$ with a point source spaced from the antenna at a distance equal to the antenna length $R_0 = D$ and slightly displaced relative to the antenna center. The form of this function represents the structure known in holography as a phase-only synthetic hologram and in acoustics as a "zone lens." The source image obtained by the wave front reversal of this function is almost ideal. The initial phase of the source is arbitrary. At the next moment, when the phase of the radiator changed from φ_1 to φ_2, the distribution shown in Fig. 1a retains its form but shifts by some number of readings proportional to $(\varphi_1 - \varphi_2)$, because the function $\Phi(x)$ is limited by $(-\pi, \pi)$ and the passage over these boundaries occurs elsewhere. The difference $[\Phi_1(x) - \Phi_2(x)]$ has the form of a meander (Fig. 1b) retaining the information about the form of the functions $\Phi_1(x)$ and $\Phi_2(x)$. Since the wave front reversal is performed by a linear opera-

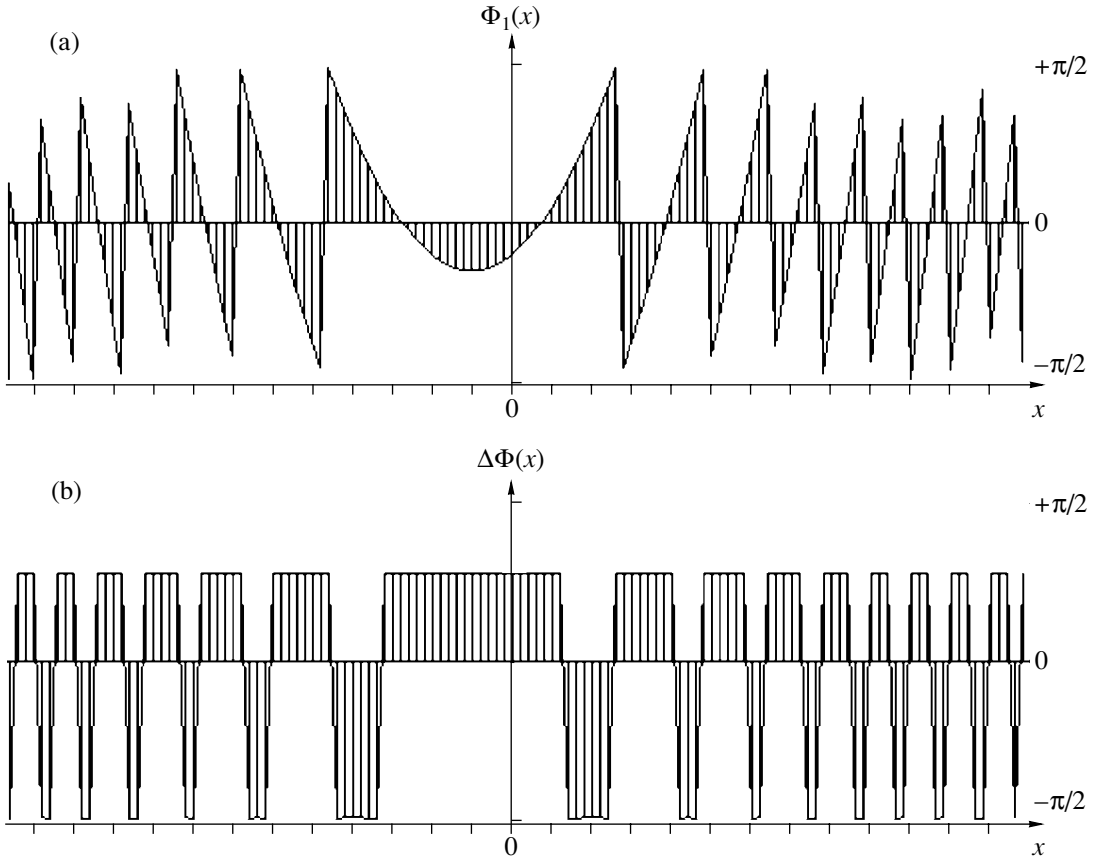

Fig. 1. Phase distribution of the field of a point source at the antenna: (a) one measurement $\Phi_1(x)$ and (b) the difference between two measurements $[\Phi_1(x) - \Phi_2(x)]$.

tor, the resulting image (2) is one image minus another and it retains only part of the image that has changed. Energetically the source image can be compared with the images obtained by using a Fresnel zone plate. If the calculation of the phase were performed not by operation (6), which limits the functions $\Phi(x)$, the difference $[\Phi_1(x) - \Phi_2(x)] = \text{const} = \varphi_1 - \varphi_2$ under the wave front reversal by Eq. (2) would not allow one to obtain the image of a point source in the near field and retain the information about its coordinates. At best, for the source located in the far field of the antenna, we could obtain a point source image that is always located at the center of the field of view, as a Fourier transform of a constant. Binary functions have wide spectra, and in order to narrow these spectra, in paper [6], where a similar problem of determining a phase function of complex functions was considered, special calculations were performed so that the phase function would not have sharp drops and would be defined in much wider limits. But in connection with our problem, it is these drops that create new possibilities. If the object is in the far field of the antenna, in the image plane we observe the spectra of the phase functions $\Phi(x)$. An infinite spectrum of binary functions forms additional diffraction orders in which the same object image is constructed. To avoid overlapping these images, the object should be irradiated by an inclined beam, or the phase function should be multiplied by a harmonic function $\sin\alpha x$ or $\cos\alpha x$ of specially selected frequency α. Figures 2a and 2b display the distributions $\Phi_1(x)$ and $\Delta\Phi(x) = \Phi_1(x) - \Phi_2(x)$, respectively, in the presence of a layer of scatterers lying between the antenna and the source and randomly distorting the phase of the received field $P(x) = A(x)\exp[\Phi(x) + \psi(x)]$, where $\psi(x)$ is a random function changing in the limits $[-\pi, \pi]$. The distribution $\Delta\Phi$ for one source in the presence of an inhomogeneous layer (Fig. 2b) also has the form of a meander that retains the information about the form of the function $\Delta\Phi(x)$, as well as of the function $\psi(x)$. In this case, the phase information is carried by the positions of the passages of the function through the limiting points $(-\pi, \pi)$. The layer is subtracted at the segments $\Delta\Phi(x) = \text{const}$, but the information about the layer is partially retained in the form of the additional passages of the function through the limits. Therefore, as a result of the accumulation, the image of the layer, i.e., the background (additive noise) of the image, is averaged and then the image of the object begins to form. With every new set of φ_{11} and φ_{21}, the functions $[\Phi(x) + \psi(x)]$ reach the limits $(-\pi, \pi)$ at new points, and

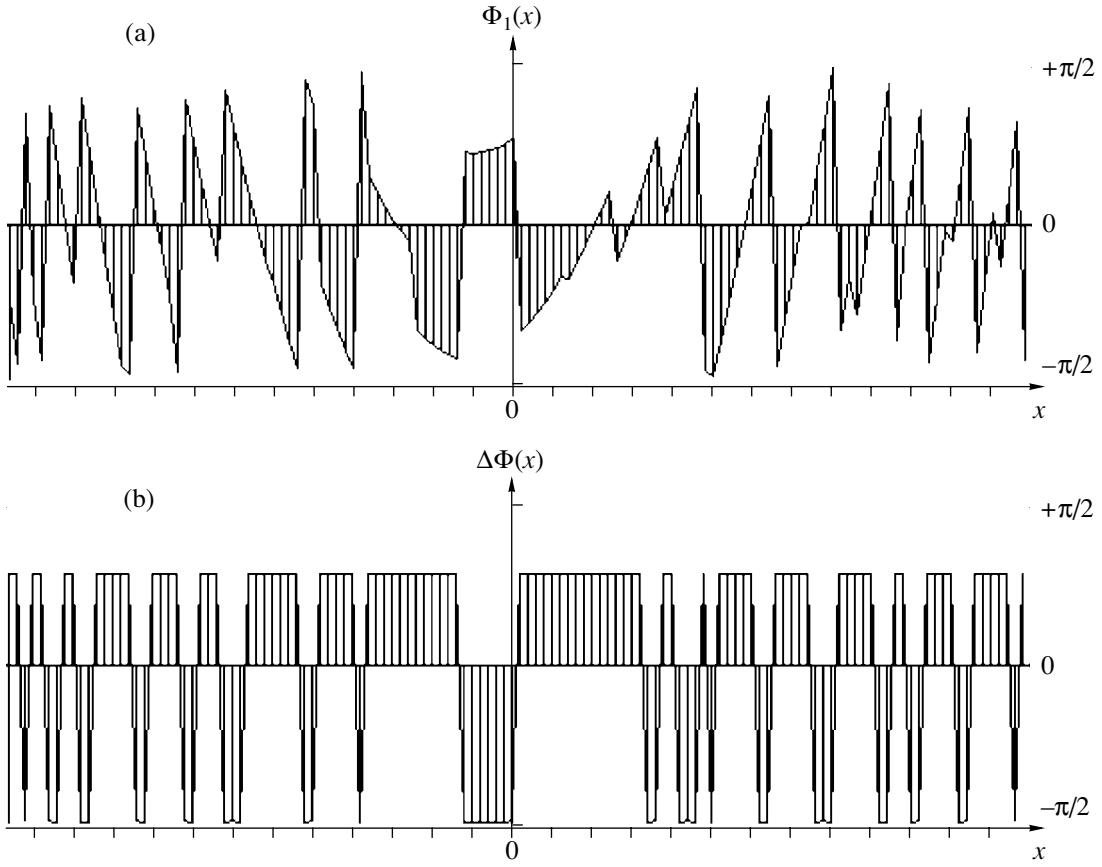

Fig. 2. Phase distribution of the field of a point source at the antenna in the presence of an inhomogeneous layer between the antenna and the source: (a) one measurement $\Phi_1(x)$ and (b) the difference between two measurements $\Delta\Phi(x)$.

at each iteration, the information about different parts of the layer is revealed. The cost of retaining the information about the source coordinates is the incomplete subtraction of the multiplicative interference. Modeling the layer within $\psi(x) \in [-\pi, \pi]$ physically corresponds to the situation when inhomogeneities are represented by inclusions, the sound velocity in which deviates from the mean value to greater or smaller values. The image is reconstructed in a homogeneous space filled with a medium in which the sound velocity is equal to the mean value corresponding to $\psi(x) = 0$. The algorithm of the reconstruction works well when the statistical characteristics of the layer are close to white noise. In its turn, the size of the object, its form, and its position in space determine the spatial frequencies of the function $\Phi(x)$. When the spectrum of the function $\psi(x)$ and the informationally significant part of the spectrum of the function $\Phi(x)$ do not overlap, the reconstruction of the object image proves to be possible, which agrees with the conclusions of [5]. In addition to constant multiplicative interference, the algorithm also subtracts from the image a relatively constant background whose level considerably exceeds the signal of our interest, or, more precisely, reduces its level making it lower than the level of the object image.

Now, we consider the procedure of reconstructing the image of an extended object through an inhomogeneous layer. As an extended object, we chose the letter *F*. Figure 3 shows the results of the reconstruction of its image. The field of view is represented by 16×16 elements of resolution, and the object occupies only 8 elements of resolution. An antenna of size D contains 128×128 receivers with a discretization interval of $\lambda/2$. The object is at a distance $R = 128 \times \lambda/2 = D$ from the antenna. Figure 3.1 shows the arrangement of sound sources in the object plane. Figure 3.1a displays the object and its spatial position in the absence of the background. In this case, a coherent signal reflected from some structures and creating a scattered field that is constant in time may be considered as the background. Figure 3.1b demonstrates the object surrounded by a relatively constant background (a dark rectangle), the level of reflection from which is higher than the level of reflection from the object. Figure 3.2 shows the images of the object obtained by modeling in the absence of the background and the inhomogeneous layer. Let us consider in more detail the result of one iteration shown in Fig. 3.2a. Since this is the result of subtraction of two images, we see only the changes in the images obtained in the first and second measure-

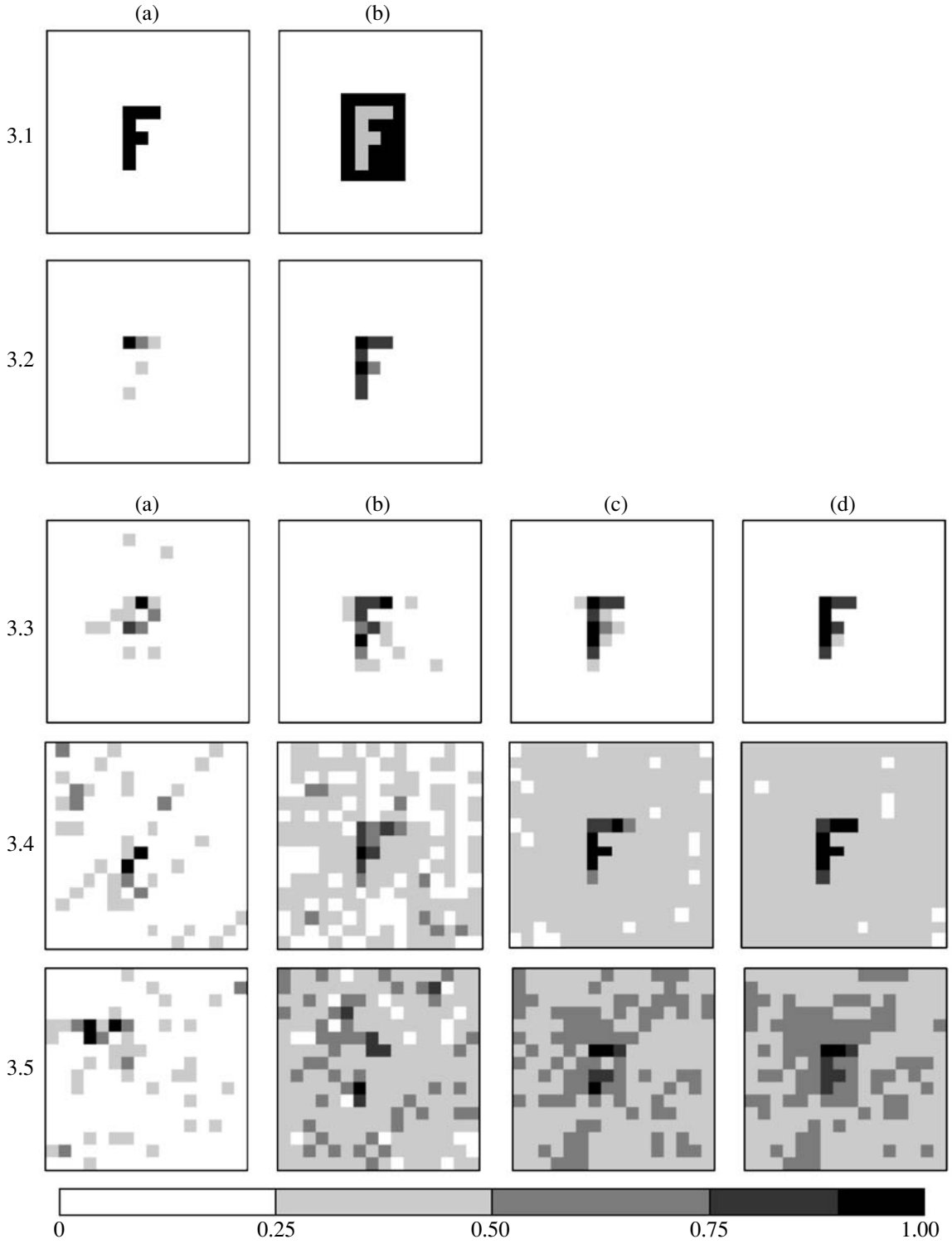

Fig. 3. Images of a dynamic object. (3.1a) View of the object and (3.1b) view of the object and a relatively constant background; (3.2) images of the object in the absence of the background and the inhomogeneous layer: (3.2a) one iteration and (3.2b) averaging over 10 iterations; (3.3) the layer is absent, the amplitude level of the background is ten times higher than the level of the object; (3.4) the layer is absent, the amplitude level of the background is 33 times higher than the level of the object; (3.5) the level of the background is equal to the level of the object, an inhomogeneous layer is added. In plots 3.3–3.5: (a) one iteration and (b, c, and d) averaging over 10, 50, and 100 iterations, respectively.

ments. In the absence of the background and the inhomogeneous layer, all points of the reconstructed image lie inside the region occupied by the object (as could be expected), their amplitudes are random, and the information about these amplitude fluctuations is in the phase distributions $\Phi_{1,2}(x, y)$. In order to obtain a smoother image, further averaging of these images is needed (Fig. 3.2b). Note that, in the image, false maxima are lacking, i.e., points whose position does not coincide with the region occupied by the object. The absence of false maxima demonstrates the efficiency of the idea of reconstructing the image by the phase function $\Delta\Phi(x, y)$, which after all the transformations turns into the amplitude information, this process being essentially nonlinear. Figure 3.2b shows the result of reconstructing the same image averaged over ten iterations.

Figure 3.3 displays the object images in the absence of the inhomogeneous layer but in the presence of a background with an amplitude ten times as large as the amplitude of signals reflected from the object. Figure 3.3a shows the result of one iteration, Fig. 3.3b shows the averaging over 10 iterations, and Figs. 3.3c and 3.3d present the averaging over 50 and 100 iterations, respectively. Figure 3.4 displays similar images of the object without the inhomogeneous layer but in the presence of a background with an amplitude exceeding the amplitudes of signals scattered by the object by a factor of 33. Figure 3.4a is the result of one iteration, while Figs. 3.4b, 3.4c, and 3.4d are the results of averaging over 10, 50, and 100 iterations, respectively.

Finally, Fig. 3.5 demonstrates the object images in the presence of the inhomogeneous layer and the background. The amplitudes of background signals were taken to be equal to the amplitudes of signals reflected from the elements of the object. The phases of the background signals were assumed to be constant within one iteration, and the inhomogeneous layer was modeled by adding the function $\Psi(x, y) \in [-0.9\pi, 0.9\pi]$ to the signal phase, this function randomly changing its parameters at intervals $[\Delta x, \Delta y] = [\lambda, \lambda]$ or at every two antenna receivers. Figure 3.5a shows the image obtained by one iteration, while Figs. 3.5b, 3.5c, and 3.5d show the results of averaging over 10, 50, and 100 iterations.

It is seen that, on averaging, the level of the background surrounding the object increases, and in the image it manifests itself in the form of a steady component of the same level over the whole field of view, which makes it possible to further filter it out. When the inhomogeneous layer is included in the model, a spottiness appears all over the image, but the brightness level of the elements of the object image exceeds these irregularities.

The illumination of the object by a narrow beam of size $\Delta x, \Delta y = 3$–4 elements of resolution was also modeled. The irradiation by a wide beam, when the whole object is illuminated, is inferior in potentialities to scanning over several elements of resolution. Passing through the inhomogeneous layer, an insonifying beam may be distorted or displaced by several elements of resolution, but as a result of scanning, the whole object should be irradiated $2L$ times.

The algorithm retaining the information about the location of every radiator should provide an undeformed image of the object accurate to an element of resolution even in the cases when the exact coordinates of the scanning beam are unknown. Formally, it would be possible to form a cross-correlation function $P_1(x) \times P_2^*(x)$ and find the difference

$$\begin{aligned} \Delta\Phi &= \Phi_1(x) - \Phi_2(x) \\ &= \arctan\{\mathrm{Im}[P_1(x) \times P_2^*(x)]/\mathrm{Re}[P_1(x) \times P_2^*]\}. \end{aligned} \tag{7}$$

However, difference (7) does not give complete information about the phases $\Phi_1(x)$ and $\Phi_2(x)$, because

$$\left.\begin{aligned} &\mathrm{Im}[P_1(x) \times P_2^*(x)] \\ &= \mathrm{Im}\,P_1(x) \times \mathrm{Re}\,P_2(x) - \mathrm{Im}\,P_2(x) \times \mathrm{Re}\,P_1(x), \\ &\mathrm{Re}[P_1(x) \times P_2^*(x)] \\ &= \mathrm{Re}\,P_1(x) \times \mathrm{Re}\,P_2(x) + \mathrm{Im}\,P_2(x) \times \mathrm{Im}\,P_1(x). \end{aligned}\right\} \tag{8}$$

Formulas (8) contain pairwise products $\mathrm{Im}\,P_1(x)$, $\mathrm{Re}\,P_1(x)$ and $\mathrm{Im}\,P_2(x)$, $\mathrm{Re}\,P_2(x)$ in various combinations. The signs of the products are the same for two combinations of cofactors. The square phase shifts that are common for both distributions $\Phi_1(x)$ and $\Phi_2(x)$ and carry the information about the distance from the receivers to the object are subtracted. Therefore, the image can be constructed only in the far field. For instance, for an object of rectangular shape, the reconstructed image will have the form of a triangle. So it is hardly possible to decode an object of more complex shape, since half of the phase information is lost. Consequently, the reconstruction of the image of an object of complex shape by the difference phase function of cross-correlation is practically impossible. In [14], for example, the cross-correlation functions are used for constructing the image of a point object, while for constructing the image of an extended object, scanning is carried out and rather complex procedures of correction are used, which are not required by the method under consideration (at least theoretically).

Note that the suggested algorithm differs from the algorithm given in [4] in that it involves the subtraction of one phase distribution from another, while in the dark field method, the phases at adjacent receivers are subtracted. Furthermore, we do not retain the information about the ratio of the amplitudes of two successive distributions of the field at the antenna, since it is insignificant for the reconstruction of the image of an extended dynamic object. However, although the aforementioned distinctions are determined by the different problems to be solved and, correspondingly, by differ-

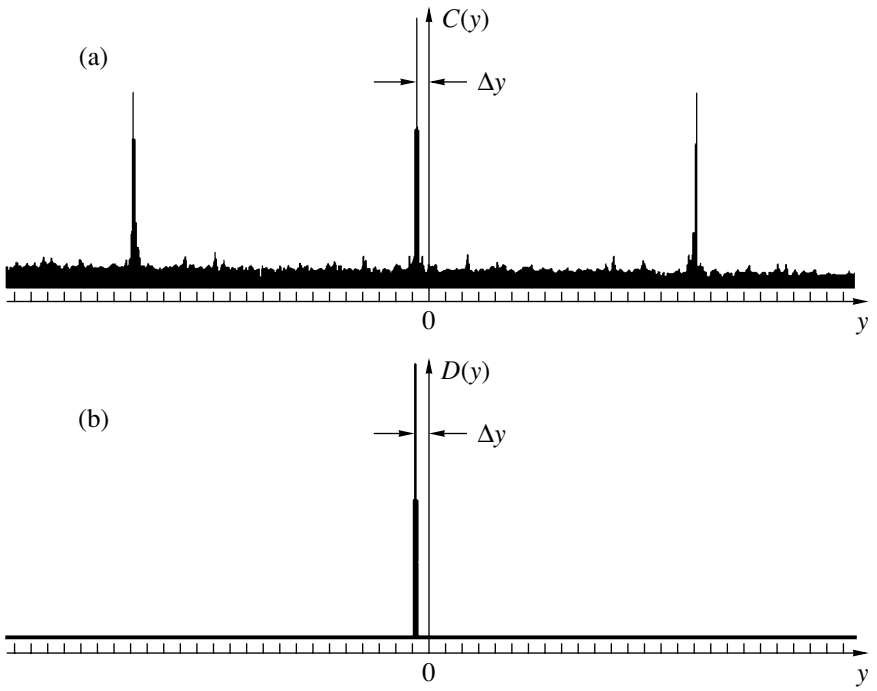

Fig. 4. The correlation and division functions of two energy spectra of a quasiperiodic random function; the spectra are shifted relative to one another by the distance Δy: (a) the correlation function $C(y)$ and (b) the division function $D(y)$.

ent ways of using the algorithms, the estimates of their energy efficiency from the point of view of suppressing the coherent background (signals that are strongly reflected but stable in time) are comparable, because both algorithms are based on the nonlinear operation of calculating the phase difference.

In one of our previous papers we offered a similar algorithm for calculating the shift between two functions called "division" after the division of spectra, which also depends on the way of calculating the phase function [8]. A correlation function is known to be ambiguous in the case of a comparison of quasiperiodic functions. Figure 4a shows a correlation function of two energy spectra of a random function $\psi(x)$, every third value of which is set equal to zero, and the spectra are shifted relative to each other [8]. Figure 4b illustrates the "division" function of the same spectra. The division algorithm transforms the shift to the phase slope by the Fourier transform

$$\begin{aligned} F_\eta[I_1(\xi)] &= \Lambda_1(\eta), \\ F_\eta[I_2(\xi)] &= \Lambda_2(\xi), \end{aligned} \tag{9}$$

where $I_1(\xi)$ and $I_2(\xi)$ are the compared spectra. Then, the phase functions of expressions (9), $\Phi_1[\Lambda_1(\eta)]$ and $\Phi_2[\Lambda_2(\eta)]$, are found by using formulas (6), and the function

$$B(\eta) = \exp\{\Phi_1[\Lambda_1(\eta)] - \Phi_2[\Lambda_2(\eta)]\} \tag{10}$$

is formed. The amplitude information is omitted. The inverse Fourier transform of the function $B(\eta)$ is performed:

$$D(y) = F_\eta^{-1}[B(\eta)].$$

The function $D(y)$ has a single narrow peak for any type of identical compared functions, if the phase functions are calculated by formulas (6). Examples of the form of $D(y)$, when $I_1(\xi)$ and $I_2(\xi)$ slightly differ from each other, are given in [7–9]. Figure 5 shows the functions $D(y)$ and $C(y)$, where the latter is the autocorrelation function of a rectangular pulse. In Fig. 5a, the pulses are not shifted; in Fig. 5b, the second pulse is shifted relative to the first one by the distance Δ; in Fig. 5c, the second pulse is shifted by the distance Δ and the function $D(y)$ is calculated by formula (5). The correlation function is calculated by the same scheme as the function $D(y)$, but instead of operation (10) the operation $\Lambda_1(\eta) \times \Lambda_2^*(\eta)$ is used. Due to Eq. (8), the function $\Lambda_1(\eta) \times \Lambda_2^*(\eta)$ does not retain the signs of imaginary and real parts of its components. Operation (10) performed with the use of formulas (6) makes it possible to preserve complete phase information about both the functions compared. In addition, the function $D(y)$ does not depend on the amplitudes of these functions and, hence, determines the shift accurate to the unit of discretization of the functions. The function $D(y)$ may be useful in problems of pattern recognition, in calculating the time delays at receivers, and everywhere where correla-

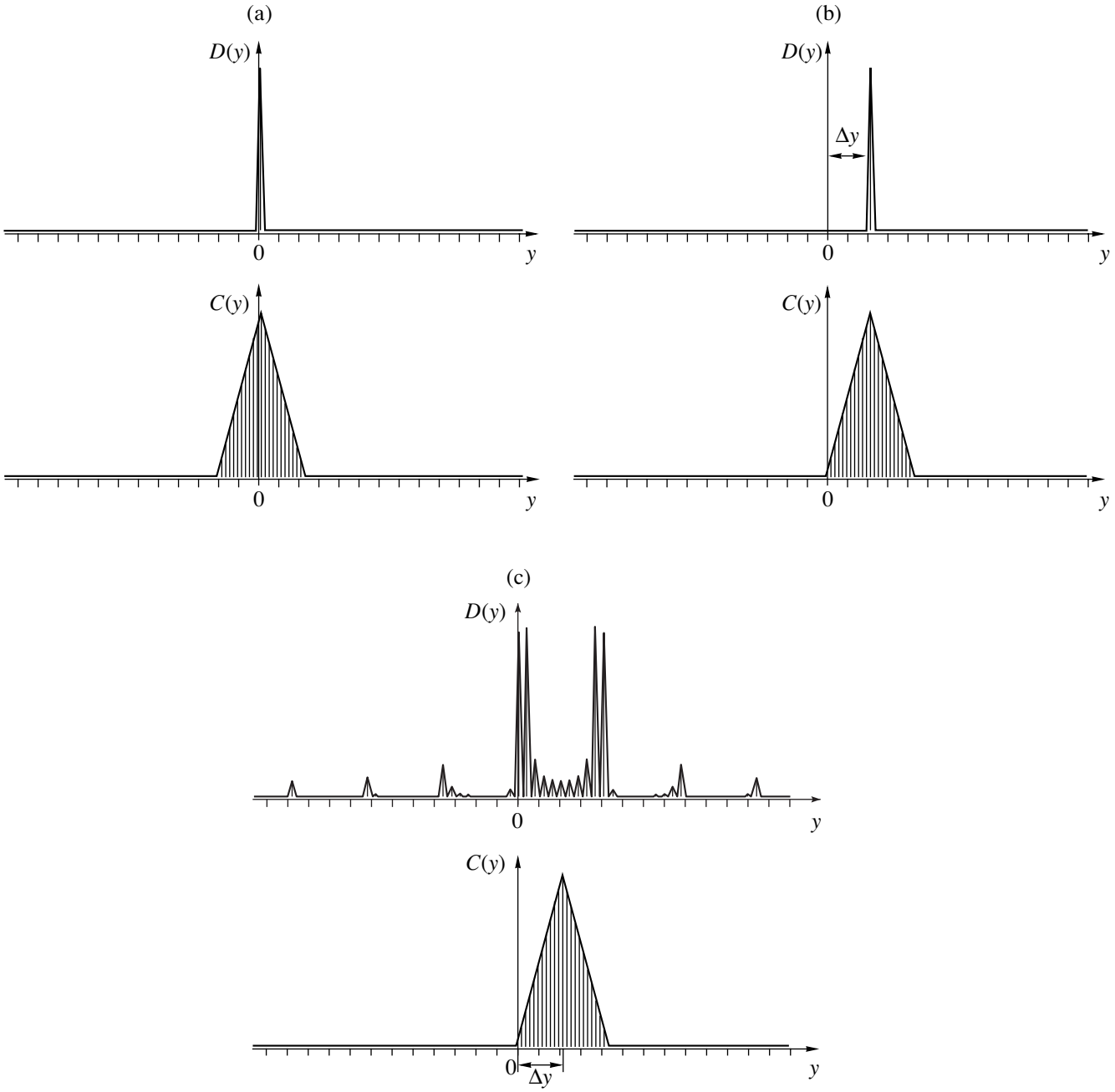

Fig. 5. The autocorrelation function $C(y)$ of a rectangular pulse and the division function $D(y)$ of the same pulse: (a) the pulses are not shifted, (b) the second pulse is shifted by the distance Δ, and (c) the second pulse is shifted by the distance Δ; the function $D(y)$ is calculated by formula (5) without extension to the region $[-\pi, \pi]$.

tion analysis is applied. The only correction in determining the phase by formulas (6) will be the phase value at the points where $\mathrm{Re}P(x) < 0$ and $\mathrm{Im}P(x) = 0$; there, $\Phi(x) = \pi$ (or $-\pi$; it is the same point on the unit circle). In the division algorithm, the operation $\exp\Delta\Phi$ is performed, hence, for the values $\mathrm{Re}P(x) < 0$ and $\mathrm{Im}P(x) = 0$, the phase should be defined so that $\cos\Phi(x) = -1$. In the above formulas (6) at the same point, the phase is taken as equal to zero, so that the mean value of the phase between π and $(-\pi)$ is equal to zero, because, for expression (2) where the phase plays the role of amplitude, this characteristic is important. In [5], a similar operation of division of spectra is proposed for idealizing the response of a system and for constructing images with all the aforementioned differences in the algorithms.

In conclusion we note that, as was rightly stated in [5], the application of methods of the dark field type in acoustics in many respects is based on the analogs of them that were successfully used in optics years ago. In

this connection, in our opinion, the field of application of the difference phase methods in ocean acoustics and in other fields where acoustic waves are used may be very wide. The proposed method of constructing the images of dynamic objects is suitable for solving a vast variety of problems of ocean acoustics and seismology, e.g., for constructing the trajectory of a noise source moving in an inhomogeneous multipath medium while retaining the information about its absolute coordinates [6, 9, 10], for detecting weak inhomogeneities, for the visualization of flows of inhomogeneous liquids and currents, and so on.

For a very wide field of practical problems, the influence of purely additive noise is not as strong, and the main limitation is the phase fluctuations of signals due to scattering. Further study and development of the difference methods apparently will make it possible to take an alternative view of the problems of designing genuinely high-aperture focusing antennas operating in inhomogeneous media, because it proves to be possible to partially lift the stringent requirements on the wave size of the antenna. Traditionally, it is assumed that, in an inhomogeneous oceanic medium, the maximal length of the antenna is limited by a small interval of the spatial correlation of the signal. Other possibilities may be proved by the results of Zverev's paper [7] on the formation of the directivity of an antenna with a geometry changing in time and by the results of our paper [8], where a great number of the spatial correlation intervals of the received field fit within the length of the antenna. In both cases, the reconstruction of the angular position of a point source is carried out with the hardware resolution of the antenna, i.e., according to its wave size.

ACKNOWLEDGMENTS

We are grateful to Prof. V.A. Zverev for fruitful discussions and helpful remarks.

REFERENCES

1. V. A. Zverev, *Radiooptics* (Sovetskoe Radio, Moscow, 1975), p. 170.
2. V. A. Zverev, Akust. Zh. **40**, 401 (1994) [Acoust. Phys. **40**, 360 (1994)].
3. V. A. Zverev, A. L. Matveev, M. M. Slavinskiĭ, and A. A. Stromkov, Akust. Zh. **43**, 501 (1997) [Acoust. Phys. **43**, 429 (1997)].
4. V. A. Zverev, P. I. Korotin, A. L. Matveev, *et al.*, Akust. Zh. **46**, 650 (2000) [Acoust. Phys. **46**, 569 (2000)].
5. V. A. Zverev, Izv. Vyssh. Uchebn. Zaved. Radiofiz. **43** (5), 406 (2000).
6. V. A. Zverev and A. A. Pavlenko, Izv. Vyssh. Uchebn. Zaved. Radiofiz. **43** (7), 652 (2000).
7. V. A. Zverev and A. A. Pavlenko, Akust. Zh. **47**, 352 (2001) [Acoust. Phys. **47**, 297 (2001)].
8. N. V. Zuĭkova, T. V. Kondrat'eva, and V. D. Svet, Akust. Zh. **42**, 225 (1996) [Acoust. Phys. **42**, 196 (1996)].
9. N. V. Zuĭkova, T. V. Kondrat'eva, and V. D. Svet, Akust. Zh. **43**, 187 (1997) [Acoust. Phys. **43**, 157 (1997)].
10. N. V. Zuĭkova, T. V. Kondrat'eva, and V. D. Svet, Akust. Zh. **44**, 220 (1998) [Acoust. Phys. **44**, 180 (1998)].
11. N. V. Zuĭkova, T. V. Kondrat'eva, and V. D. Svet, Akust. Zh. **44**, 779 (1998) [Acoust. Phys. **44**, 678 (1998)].
12. N. V. Zuĭkova, T. V. Kondrat'eva, and V. D. Svet, Akust. Zh. **47**, 664 (2001) [Acoust. Phys. **47**, 578 (2001)].
13. *B-Flow. New Way of Visualizing Blood Flow. Ultrasound Technology*, Preprint of GE Ultrasound Europe (1999), p. 14.
14. W. Walker and G. Trahey, J. Acoust. Soc. Am. **101**, 1847 (1997).

Translated by A. Svechnikov

Acoustical Physics, Vol. 49, No. 2, 2003, pp. 158–162. Translated from Akusticheskiĭ Zhurnal, Vol. 49, No. 2, 2003, pp. 194–198.

Theoretical Simulation of a Rotary Motor Driven by Surface Acoustic Waves[1]

L.-P. Cheng, G.-M. Zhang, S.-Y. Zhang, Z.-N. Zhang, and X.-J. Shui

Laboratory of Modern Acoustics and Institute of Acoustics, Nanjing University, Nanjing, 210093 China

e-mail: paslabn@nju.edu.cn

Received January 24, 2002

Abstract—A simulation model for theoretically studying the operation behavior of a rotary motor driven by surface acoustic waves (SAWs) is proposed. According to the model, some simulation results are obtained as follows: (1) as the rotor is excited by the SAWs, the motor experiences two phases, i.e., the acceleration phase and the steady phase; (2) the normal vibration amplitude *A* of SAWs has a very weak effect on the acceleration in the first phase but an enhancing effect on the steady velocity of the rotary motor; (3) as the number of the contact points between the rotor and the stator increases, the motor rotates more steadily; (4) as the rotor radius becomes smaller, both the acceleration and the steady angular velocity become greater. These features are in agreement with the experimental results. *© 2003 MAIK "Nauka/Interperiodica".*

INTRODUCTION

Ultrasonic motors have advantages over conventional electromagnetic ones owing to their excellent characteristics, such as large torque, easy controllability, quiet operation, and nonelectromagnetic induction, so they are expected to serve as advanced actuators that make sliders or rotors move. A microactuator is the key device for microsystems to perform physical functions [1]. To miniaturize ultrasonic motors, the transducers in the stator should be small, and the frequency should be high. For this purpose, the surface acoustic wave (SAW) motor is a good candidate. Moreover, since the SAW motion is attenuated in the thickness direction, the bottom of the substrate, which does not vibrate, can be fixed. In 1994, Kurosawa *et al.* [2] verified the possibility of an ultrasonic linear motor driven by SAWs (Rayleigh waves) at 10 MHz. At high frequency, the vibration amplitude is very small, the influence of adsorption contaminants or air may become significant, and, therefore, a high contact pressure is required for the friction drive. To obtain sufficient contact pressure, Kurosawa *et al.* [3] introduced small steel balls as slider elements. Later, they investigated elastic contact conditions to optimize the friction drive of the SAW motor [4] and proposed a simulation model to explain their experimental results as well [5]. Based on these works, a novel rotary motor driven by 9.85 MHz surface acoustic waves and some experimental results were presented in [6]. The purpose of the present paper is to develop a theoretical model for simulating the motion of the SAW rotary motor. The parameter dependence of the motion is investigated, and the simulations and numerical results are compared with experimental ones.

CONFIGURATION OF THE PROTOTYPE MOTOR

A schematic diagram of the SAW motor is shown in Fig. 1. A 127.8 *y*-rotated *x*-propagating $LiNbO_3$ substrate with 3827 mm^3 is used to propagate the Rayleigh waves. On the surface of the substrate, two pairs of interdigital transducers (IDTs) operating at 9.85 MHz are arranged in a parallel propagation direction to perform as a stator. A specially designed rotor composed of a disk with small balls uniformly distributed in a circle is put on the substrate, as illustrated in Fig. 2. The circular rotor is made of a 0.7-mm thick PMM disk with a diameter of 25 mm, which has 12 holes distributed in a circle with a diameter of 20 mm. Then, some steel balls (with a diameter of 1.5 mm) are put in these holes, and every ball makes a good contact with the stator. In addition, three little steel balls (with a diameter of 0.7 mm) are glued to the bottom and closed to the axis of the rotor as contact points with the $LiNbO_3$ substrate. Additionally, in order to set the rotor, a steel axle is fixed at the center of the stator surface. When the driving voltage is input to two IDTs (IDT1 and IDT3), two Rayleigh wave beams are generated and propagate in

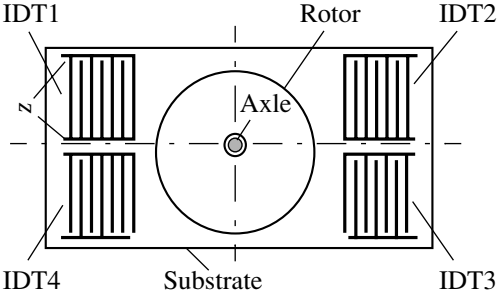

Fig. 1. Schematic diagram of the proposed motor.

[1] This paper was submitted by the authors in English.

parallel and opposite directions with each other on the substrate. Thus, a pair of frictional forces in opposite directions forms a moment to drive the rotor. The rotational direction of the motor can be inverted by driving the other two IDTs (IDT2 and IDT4).

SIMULATION MODEL

Morita *et al.* [5] proposed a simulation model for SAW linear motors, which can successfully explain their experiments. Here, we extend this model to our SAW rotary motor. The coordinates are defined so that the x axis is directed to the right, the y axis is perpendicular to the substrate, and θ is the angular displacement of the rotor. In the experiment, the propagation of the upper SAW beam is along the x direction, while that of the lower beam is opposite to the x direction. Besides, $2n$ ($n = 1, 2, 3, 4, 5, 6$) balls are uniformly distributed in a circle with a radius of 10 mm. For simplicity, only the two-ball model is given in Fig. 3 to proceed with the theoretical analysis. Due to the symmetry, two balls, such as ball (1) and its axial symmetric counterpart, have a similar behavior. Therefore, the whole system can be characterized by the evolution of the angular and the normal displacements of an individual ball.

Since the particle motion of an SAW is elliptical, the normal deformation of the substrate (stator) surface caused by a traveling SAW wave is expressed as

$$y = A\sin(\omega t - kx_{\text{ball}}), \tag{1}$$

where y is the normal displacement of a particle in the stator where the ball contacts; A, ω, and k are the amplitude, angular frequency, and wave number of the SAW, respectively; and x_{ball} is the position of the steel ball. The tangential displacement x is in a retrograde direction, i.e.,

$$x = -\alpha A\cos(\omega t - kx_{\text{ball}}), \tag{2}$$

where $\alpha = 0.7$ is the ratio of the tangential amplitude to the normal amplitude [5]. From Fig. 3, we can get

$$x_{\text{ball}} = x_0 + R(1 + \cos\theta), \tag{3}$$

where x_0 is the minimal distance from the emitting IDT to the rotor and R is the radius of the circle in which the small balls are uniformly distributed. As discussed by Morita *et al.* [5], there are two situations for the ball motion: one is a contact situation and the other is in levitation, as shown in Fig. 4. To judge whether the ball is in contact or levitation, the quantity $d = y_{\text{ball}} - y$ is introduced, where y_{ball} is the normal position of the ball. If $d \le 0$, the ball contacts the stator, and $d > 0$ means that the ball is in levitation. The ball motion equations for these two cases are different. When the ball levitates, namely $y < y_{\text{ball}}$, the motion equations are as follows:

$$m\frac{d^2y_{\text{ball}}}{dt^2} = -mg, \tag{4a}$$

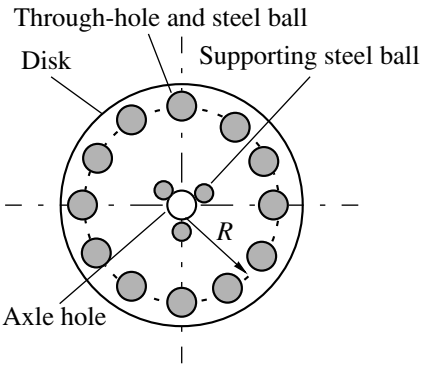

Fig. 2. Bottom view of the rotor of the proposed motor.

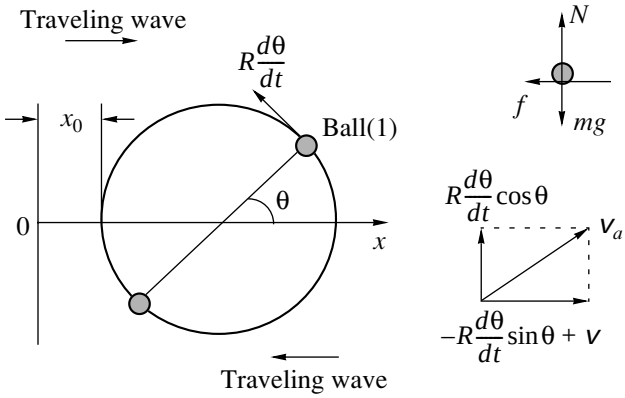

Fig. 3. Movement sketch for the two-ball model.

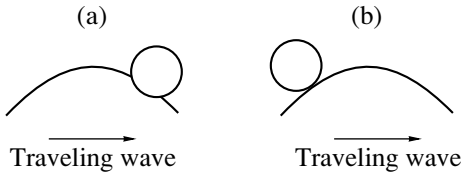

Fig. 4. Two situations with the (a) contact and (b) levitation for the ball motion.

$$I\frac{d^2\theta}{dt^2} = 0, \tag{4b}$$

where m is the mass of the steel ball, g is the acceleration of gravity, and I is the rotary inertia of the rotor to the axle. When the ball contacts the stator, the rotor obtains a frictional force in the opposite direction of the relative velocity v_a between the ball and the local supporting point of the stator. Two components of the frictional force, f_x and f_z, are proportional to the two respective components of the relative velocity, which are shown in Fig. 3. The moment of the frictional force provides a rotational acceleration for the rotor, and, there-

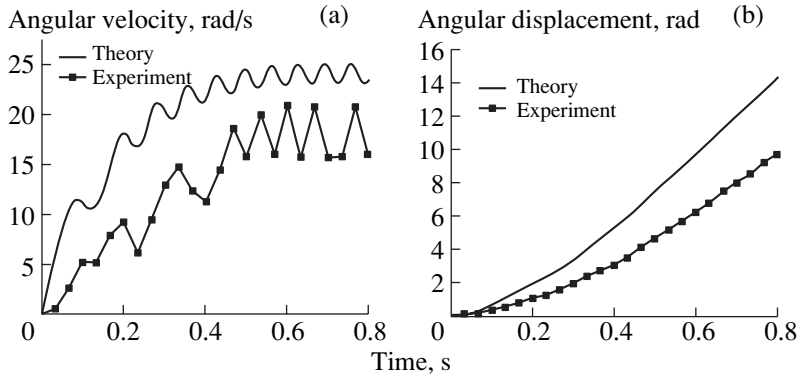

Fig. 5. Time evolution of (a) the angular velocity and (b) the angular displacement in both theoretical simulation and experiment for a two-ball rotor.

fore, the normal motion of the ball and the rotation of the rotor can be described as

$$m\frac{d^2y_{\text{ball}}}{dt^2} = N - mg, \tag{5a}$$

$$I\frac{d^2\theta}{dt^2} = 2\mu N\frac{R\left[\left(v - R\frac{d\theta}{dt}\sin\theta\right)\sin\theta - R\frac{d\theta}{dt}\cos\theta\cos\theta\right]}{\sqrt{\left(R\frac{d\theta}{dt}\cos\theta\right)^2 + \left(v - R\frac{d\theta}{dt}\sin\theta\right)^2}}, \tag{5b}$$

where N is the normal force of the ball, μ is the frictional factor of the rotor and the stator, and v is the tangential velocity of the particle motion of the stator where the ball contacts it. The rotary inertia I in Eqs. (4b) and (5b) consists of two parts: $I_1 = I_{\text{disk}}$ and $I_2 = 2mR^2$, where I_{disk} is the rotary inertia of the rotation disk to the axle. On the other hand, the experiments show that the balls hardly roll in the holes. Such unconventional motion may be dependent on the friction force between the balls and the holes of the rotor, in which the friction force is considered much smaller than mg and is neglected in Eqs. (4a) and (5a).

The normal contact force between the ball and the stator can be calculated by using Herzian contact theorem [7]:

$$N = \frac{4Er^{\frac{1}{2}}d^{\frac{3}{2}}}{3}, \quad E = \left(\frac{1-\sigma_1^2}{E_1} + \frac{1-\sigma_2^2}{E_2}\right), \tag{6}$$

where E_i and σ_i ($i = 1, 2$) are Young's modulus and Poisson's ratio, respectively; the index $i = 1, 2$, denotes the ball and the stator, respectively; and r is the radius of the steel ball. To calculate the time evolution of the angular velocity and the position of the rotor, the following Euler method is used:

$$\begin{cases} \theta^{n+1} = \theta^n + \left(\frac{d\theta}{dt}\right)^n \Delta t \\ y_{\text{ball}}^{n+1} = y_{\text{ball}}^n + \left(\frac{dy_{\text{ball}}}{dt}\right)^n \Delta t, \end{cases} \tag{7}$$

$$\begin{cases} \left(\frac{d\theta}{dt}\right)^{n+1} = \left(\frac{d\theta}{dt}\right)^n + \left(\frac{d^2\theta}{dt^2}\right)^n \Delta t \\ \left(\frac{dy_{\text{ball}}}{dt}\right)^{n+1} = \left(\frac{dy_{\text{ball}}}{dt}\right)^n + \left(\frac{d^2y_{\text{ball}}}{dt^2}\right)^n \Delta t, \end{cases} \tag{8}$$

where d^2y_{ball}/dt^2 and $d^2\theta/dt^2$ are derived from Eqs. (5a) and (5b).

NUMERICAL SIMULATION

Firstly, the rotor model with two balls is calculated. Figure 5 presents the theoretical and experimental results, where the angular velocity of the rotor is shown on the left side and the angular displacement is shown on the right. In the simulations, the time step Δt is 1 ns, which is enough, because the period of the SAW is about 100 ns. Based on our previous experiments [6], the dimensions and parameters of the stator and the rotor are shown in the table. It is clear that the results of simulation qualitatively reproduce the experimental features; i.e., the rotor experiences two phases: the acceleration phase in the first 0.3 s and the steady phase after 0.3 s. The angular velocity increases rapidly in the first phase, but displays oscillation in both phases. The oscillation can be considered to result from the variation of the driving moment as the arm of the force changes.

In the simulations of more balls, Eqs. (5), (6) become more complicated, since each pair of balls has two cases: contact and levitation. The numerical results

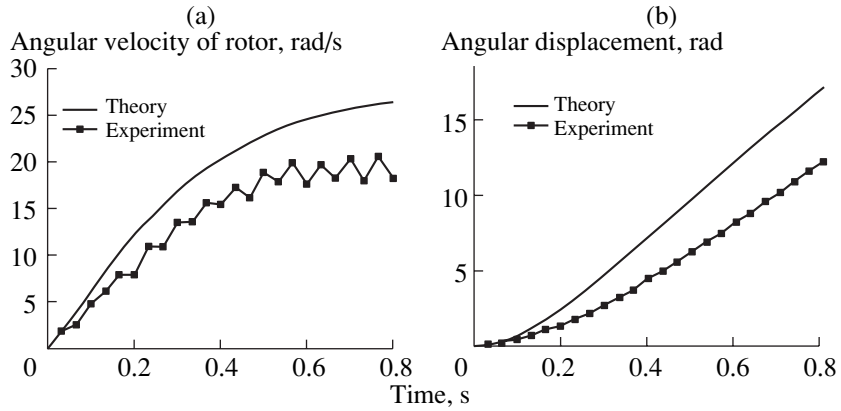

Fig. 6. Time evolution of (a) the angular velocity and (b) the angular displacement in both theoretical simulation and experiment for a four-ball rotor.

for four- or six-ball models are also calculated and compared with those of the experiments. As the second example, the numerical results for the four-ball model are shown in Fig. 6 and compared with the corresponding experiments. In addition to the similarities between the theory and the experiment, it is clearly seen that the four-ball rotor moves much more steadily than the two-ball rotor, since the variation of the moment force in the four-ball rotor is smaller than that of the two-ball rotor.

Further simulations with different normal vibration amplitude A indicate that the value of A, which is controlled by the driving voltage, does not considerably affect the acceleration in the first phase but has an enhancing effect on the steady velocity, as shown in Fig. 7. This result is naturally explained by the fact that greater amplitude corresponds to greater vibration velocity of the surface acoustic wave. It implies that a higher driving voltage produces a higher steady velocity.

In addition, the effect of the rotor radius R of the four-ball model is investigated, which is shown in Fig. 8. It is seen that, as R decreases, both the acceleration in the first phase and the steady velocity during the second phase become greater. It can also be seen that the steady velocity is negatively related to R. This can be deduced from Eq. (5b): the rotor inertia I_2 is proportional to R^2, and the moment is proportional to R; hence, as R decreases, I decreases faster than the driving moment, so that $d^2\theta/dt^2$ becomes greater.

Finally, it must be pointed out that a similar movement law is also available for other rotors with six or more balls.

DISCUSSION AND CONCLUSIONS

A simulation model is proposed to theoretically study the operation behavior of SAW rotary motors. Due to the complexity of the theory, some simplifica-

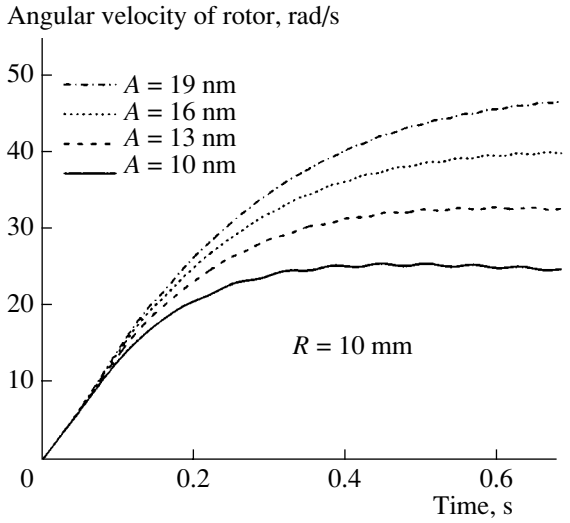

Fig. 7. Numerical simulation results for the time evolution of the angular velocity for the four-ball model in four different normal vibration amplitudes.

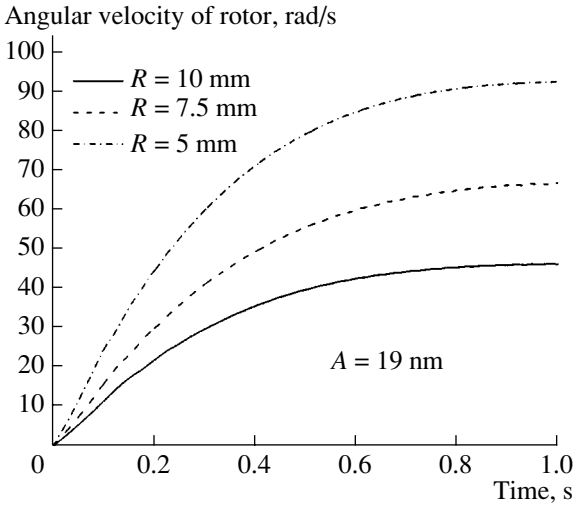

Fig. 8. Numerical simulation results for the time evolution of the angular velocity for the four-ball model in three different rotor radii (R).

Parameters used for simulations

Young's modulus of a steel ball, N/m^2	2.15×10^{11}
Young's modulus of $LiNbO_3$, N/m^2	1.73×10^{11}
Poisson's ratio of a steel ball	0.29
Poisson's ratio of $LiNbO_3$	0.245
Radius of a steel ball, mm	0.75
Weight of a steel ball, mg	12.6
Rotary inertia of the rotation disk to the axle, I_{disk}, kg m^2	7.0
Vibration amplitude of SAW (normal), nm	11
Vibration amplitude of SAW (horizontal), nm	0.7×11
Input voltage, V_{p-p}	102
Driving frequency, MHz	9.85
Friction factor	0.47

tions are adopted to make it solvable by simple equations. The simulations show that the numerical results are in good agreement with experiments, which verifies the validity of the theoretical model. Based on this model, the parameter dependence is investigated.

The numerical results can be formulated as follows:

(1) the rotors experience two phases: the acceleration phase and the steady phase;

(2) compared with a two-ball rotor, a multiball rotor rotates much more steadily. Further simulation indicates that the six-ball model behaves more steadily than the four-ball model;

(3) the normal vibration amplitude of an SAW does not significantly affect the acceleration (i.e., the slope of the acceleration phase) in the first phase; on the other hand, the amplitude has an enhancing effect on the steady velocity of the motor;

(4) as the rotor radius decreases, the acceleration and the steady velocity become greater. This feature of the rotary motor provides the possibility of miniaturizing it.

ACKNOWLEDGMENTS

This work was supported by the National Natural Science Foundation of China.

REFERENCES

1. H. Fujita, Sens. Actuators A **56**, 105 (1996).
2. M. Kurosawa, M. Takahashi, and T. Higuchi, Proc.–IEEE Ultrason. Symp., 535 (1994).
3. M. Kurosawa, M. Takahashi, and T. Higuchi, IEEE Trans. Ultrason. Ferroelectr. Freq. Control **38** (3), 901 (1996).
4. M. Kurosawa, M. Takahashi, and T. Higuchi, IEEE Trans. Ultrason. Ferroelectr. Freq. Control **45** (5), 1229 (1998).
5. T. Morita, M. Kurosawa, and T. Higuchi, IEEE Trans. Ultrason. Ferroelectr. Freq. Control **46** (4), 929 (1999).
6. G. M. Zhang, L. P. Cheng, S. Y. Zhang, *et al.*, Electron. Lett. **36** (16), 1437 (2000).
7. S. Timoshenko and J. Goodier, *Theory of Elasticity*, 3rd ed. (McGraw-Hill, New York, 1970).

Acoustical Physics, Vol. 49, No. 2, 2003, pp. 163–175. Translated from Akusticheskiĭ Zhurnal, Vol. 49, No. 2, 2003, pp. 199–214.

Fundamentals of the Direct Measurement of Sound Intensity and Practical Applications[1]

M. J. Crocker* and J. P. Arenas**

** Department of Mechanical Engineering, Auburn University, Alabama, 36849 USA*
e-mail: mcrocker@eng.auburn.edu
*** Institute of Acoustics, Universidad Austral de Chile, Valdivia, PO Box 567 Chile*

Received October 21, 2002

Abstract—Sound intensity is a measure of the magnitude and direction of the flow of sound energy. Developments in sound intensity measurement capabilities in the last quarter century have occurred because of several reasons. The main ones include the derivation of the cross-spectral formulation for sound intensity and developments in digital signal processing. This paper begins with a brief historical introduction of sound intensity measurements. Then elementary theory for sound intensity is presented. A section on sound intensity measurements is then included. The next section of the paper discusses sources of measurement error; the major sources of error are described in some detail. The paper continues with a discussion of the main applications of sound intensity measurements: sound power determination, noise source identification, and transmission loss measurements. The paper concludes with a discussion of ISO and ANSI intensity related standards and relevant references. © *2003 MAIK "Nauka/Interperiodica".*

1. INTRODUCTION

This article is dedicated to the memory of Leonid Mikhailovich Lyamshev, one of the giants of twentieth century acoustics. He made many contributions in acoustics and related fields: in particular, the scattering of sound from finite elastic thin plates and shells in a liquid, the scattering and radiation of sound in a moving medium, acoustics of controlled boundary layers, determination of the acoustics of moving media, thermooptical excitation by sound (sonoluminescence) and fractals in acoustics. But it is perhaps for one of his earliest contributions that Leonid Lyamshev is chiefly known in Western countries: his seminal studies and publications in the field of acoustical reciprocity.

Helmholtz first formulated the principles of acoustical reciprocity in the middle of the 19th century [1, 2]. In the 1870s acoustical measurements were in their infancy. O. Reynolds described the use of bells and the human voice and ear in his experimental studies of acoustical reciprocity in a letter to Lord Rayleigh in 1875 [3]. Soon after, in 1876, Lord Rayleigh used such devices as Tyndall's sensitive flames and smoke jets [4] in his acoustical reciprocity studies [5]. Just before the turn of the century, Lord Rayleigh presented a mathematical proof of the principle of reciprocity in acoustics for the case of discrete systems with a finite number of degrees of freedom [6], and just sixty years later Lyamshev presented a general mathematical proof of the principal of acoustical reciprocity for arbitrary continuous linear media containing an arbitrary number of elastic bodies [7]. It was a topic to which Lyamshev was to return several times again. See for instance his 1994 paper [8]. Hundreds of papers on the subject of acoustical reciprocity have been published since 1959, but Lyamshev's 1959 paper remains one of the most fundamental ones. Acoustical reciprocity has now been widely used in many practical problems including the radiation and transmission of sound from sources in aircraft, ships, tire/road interaction in vehicles, and other machinery sound sources by engineers and scientists such as Dowling, Heckl, Ver and Verheij, to name just a few. F.J. Fahy presents a review paper on this subject in the present issue of this journal.

In this current paper written in memory of L.M. Lyamshev, the authors deal with another important topic: the theory and measurement of sound intensity. The first author of this current paper had promised Professor Lyamshev for some time to write a paper on this topic for Acoustical Physics. Unfortunately it was not completed until after his passing, which we all now mourn. Although engineers and scientists have tried to measure sound intensity for over 120 years, it is only in the last 25 years that reliable practical sound intensity measurements have become possible. We know that several scientists including Mayer, Koenig, Helmholtz, and Rayleigh throughout the 1870s were concerned with the development of methods to measure the intensity of sound. However, it was not until 1882 that the first quantitative acoustical transducer was born in the form of the now famous Rayleigh disc. Surprisingly enough the design of the disc was conceived accidentally during Rayleigh's work on the absolute measurement of the ohm [9, 10]. Although the title of Rayleigh's papers suggest that the Rayleigh disc measures

[1] This article was submitted by the authors in English.

sound intensity, it is actually a device for measuring the mean square acoustic particle velocity, as has been shown by Koenig [11]. Rayleigh's disc was a great step forward in quantitative acoustical measurements, and it was for many years a standard instrument for acoustical calibration; however, it is hardly a practical instrument for "field" measurements.

The next important advance in acoustical measurements was the development of the telephone transmitter into a reliable electroacoustical transducer (microphone). Several researchers assisted in this development including Wente, Arnold, Crandall, and Fletcher [12]. Wente's papers in 1917 and 1922 describe a sophisticated device, which he called a condenser transmitter or electrostatic transmitter, from which modern condenser microphones are descended [13, 14]. Although Wente suggests in his titles and texts that the condenser microphone measures sound intensity, it is actually a device for measuring sound pressure (a scalar quantity). The sound intensity is, of course, a vector quantity and may be defined to be the time average rate of flow of sound energy through unit area (with the vector directed perpendicular to the area). Most intensity devices that have been proposed have required the use of two or more similar or different acoustical transducers. Unfortunately, until the last few years most of these intensity devices have appeared to suffer from calibration or other problems.

Olson in 1932 was probably the first to describe a device designed to measure the real sound intensity vector [15, 16]. Olson's device consisted of two closely-spaced pressure microphones. In 1941 Clapp and Firestone used a device consisting of two crystal pressure microphones combined with a ribbon velocity microphone [17]. Their device appeared to suffer from temperature instability and internal resonances of the ribbon. Bolt and Petrauskas in 1943 described an acoustical impedance meter using two microphones to measure the sound pressure sum and sound pressure difference [18]. This principle of operation is much the same as that used in most sound intensity devices today. In 1955 Baker described an acoustic intensity meter consisting of a hot-wire anemometer (to measure particle velocity) and a pressure microphone [19]. Because this device requires a steady airflow and is sensitive to undesired air movements, it appears unsuitable for practical applications. In 1954–1956 Schultz, during his doctoral research at Harvard University, used an intensity probe made from two electrostatic microphones mounted back-to-back [20]. Later in 1975 he discussed problems with intensity measurements in reverberant enclosures [21]. In 1973 Burger *et al.* and van Zyl and Anderson described sound intensity measurements with a probe made from a pressure sensitive microphone and a velocity sensitive microphone [22, 23].

The period 1975 to 1980 saw some rapid advances. In 1976 Hodgson and Erianne reported some of the first applications of digital signal processing to sound intensity measurements [24]. Their work involved the determination of the sound intensity from a sound pressure measurement with a microphone close to a vibrating surface and a simultaneous surface velocity measurement obtained from a surface-mounted accelerometer. Hodgson reported further such results in 1977 [25]. In 1977 Alfredson appears to be the first to report the use of an intensity probe made from two commercially available pressure microphones (Bruel & Kjaer type 4133) [26]. Alfredson used a face-to-face microphone arrangement and also employed digital signal processing techniques for the signal analysis. Alfredson also formulated an expression for the sound intensity obtained from the microphone signals, although he assumed that they were periodic in nature. He also presented some preliminary sound intensity measurements on a diesel engine. Then in 1977 and 1978, Fahy [27] and Chung [28, 29] independently made important formulations for sound intensity. They considered that the microphone signals were random and formulated the sound intensity in terms of the imaginary part of the cross-spectral density of the two microphone sound pressure signals. Lambert also later reported an independent but similar formulation.

Credit for first demonstrating in 1979 the reliability of the two microphone intensity technique for directly measuring the sound power of a large machine such as a diesel engine should perhaps go to Chung, Pope and Feldmaier [30]. Reinhart and Crocker published similar results in 1980 [31]. Also in 1980 Crocker *et al.* first demonstrated the use of the sound intensity method to measure the transmission loss (sound reduction index) of structures [32].

2. THEORETICAL BACKGROUND

Sound fields are usually described in terms of the sound pressure, which is the quantity we hear. However, sound fields are also energy fields, in which kinetic and potential energies are generated, transmitted, and dissipated. At any point in a sound field, the instantaneous intensity vector $I(t) = p(t)u(t)$ expresses the magnitude and direction of the instantaneous flow of sound energy, where $p(t)$ is the instantaneous sound pressure and $u(t)$ is the instantaneous particle velocity vector.

By combining the equation of mass continuity with the relation between the sound pressure and density changes, together with Euler's equation of motion (Newton's second law applied to a fluid), one can derive the equation of conservation of energy

$$\nabla I(t) + \frac{\partial w(t)}{\partial t} = 0, \tag{1}$$

where $\nabla I(t)$ is the divergence of the instantaneous sound intensity (that is the instantaneous net outflow of sound energy per unit volume) and $w(t)$ is the total instantaneous energy density [33, 34]. Equation (1)

expresses the simple fact that the rate of increase (or decrease) of the sound energy density at a given position in a sound field (represented by the second term) is equal to the rate of the flow of converging (or diverging) sound energy (represented by the first term). The global version of Eq. (1) is obtained using Gauss's theorem

$$\int_V \nabla I(t)dV = \int_S I(t)dS = -\frac{\partial}{\partial t}\int_V w(t)dV, \quad (2)$$

where S is the area of a surface around the source and V is the volume contained by the surface. The three terms above represents, respectively, the local net outflow of sound energy integrated over the volume, the total net outflow of sound energy through the surface, and the rate of change of the total sound energy within the surface. It can be seen that the rate of change of the sound energy within a closed surface is identical to the surface integral of the normal component of $I(t)$.

In practice the time-averaged intensity

$$I = \langle p(t)u(t)\rangle_t \quad (3)$$

is more important than the instantaneous intensity. Examination of Eq. (2) leads to the conclusion that the time average of the instantaneous net flow of sound energy out of a given closed surface is zero unless there is generation (or dissipation) of sound power within the surface; in this case the time average of the net flow of sound energy out of a given surface enclosing a sound source is equal to the net sound power of the source. In other words,

$$\int_S IdS = 0, \quad (4)$$

unless there is a steady source (or a sink) within the surface, irrespective of the presence of steady sources outside the surface, and

$$\int_S IdS = \Pi_a, \quad (5)$$

if the surface encloses a steady source that radiates the sound power Π_a, irrespective of the presence of other steady sources outside the surface.

If the sound field is simple harmonic with angular frequency $\omega = 2\pi f$, then the sound intensity in the r direction is of the form

$$I_r = \langle p\cos(\omega t)u_r\cos(\omega t + \varphi)\rangle_t = \frac{1}{2}pu_r\cos\varphi, \quad (6)$$

where φ is the phase angle between the sound pressure $p(t)$ and the particle velocity in the r direction $u_r(t)$. (For simplicity we consider only the component in the r direction here.) It is common practice to rewrite Eq. (6) as

$$I_r = \frac{1}{2}\mathrm{Re}\{pu_r^*\}, \quad (7)$$

where both the sound pressure p and the particle velocity here are complex exponential quantities, and u_r^* denotes the complex conjugate of u_r. The time averaging gives the factor 1/2. We note that the use of complex notation is mathematically very convenient and that Eq. (7) gives the same result as Eq. (6).

In the case of a plane progressive wave traveling without any reflections in the positive coordinate direction, the sound pressure and the particle velocity are always in phase and related by the characteristic impedance ρc as follows:

$$\frac{p}{u} = \rho c. \quad (8)$$

Thus for a plane wave traveling in the positive coordinate direction, the sound intensity is

$$I = \frac{p_{\mathrm{rms}}^2}{\rho c}. \quad (9)$$

In the case of a diffuse reverberant sound field, the sound intensity striking a plane surface from one side only, for example a wall, is given by

$$I = \frac{p_{\mathrm{rms}}^2}{4\rho c}. \quad (10)$$

In these two extreme cases in Eqs. (9) and (10), the sound intensity is simply related to the mean square sound pressure p_{rms}^2, which can be measured with a single microphone. In most practical cases, however, the sound intensity is not simply related to the sound pressure.

In general, in all steady sound fields (except the special case of plane progressive wave fields), the particle velocity may be divided into two components: one component in phase with the sound pressure, the other component out of phase with the sound pressure. The active sound intensity is the product of the sound pressure and the in-phase component of the particle velocity. The reactive sound intensity is the product of the sound pressure and the out-of-phase component of the particle velocity. We can write the sound intensity in the x direction as

$$I(x) = I_R(x) + jJ_I(x), \quad (11)$$

where I_R is the active component of intensity and J_I is the reactive component of intensity. Now, let us represent the sound pressure by $p(x, t) = P(x)\exp[j(\omega t + \phi_p(x))]$, where $P(x)$ is the sound pressure amplitude and $\phi_p(x)$ is the phase. Then, it can be shown that [34, 35]

$$I_R = \frac{-1}{2\omega\rho}P^2(x)\frac{\partial\phi_p(x)}{\partial x} \quad (12)$$

and

$$J_I = \frac{-1}{4\omega\rho}\frac{\partial P^2(x)}{\partial x}. \quad (13)$$

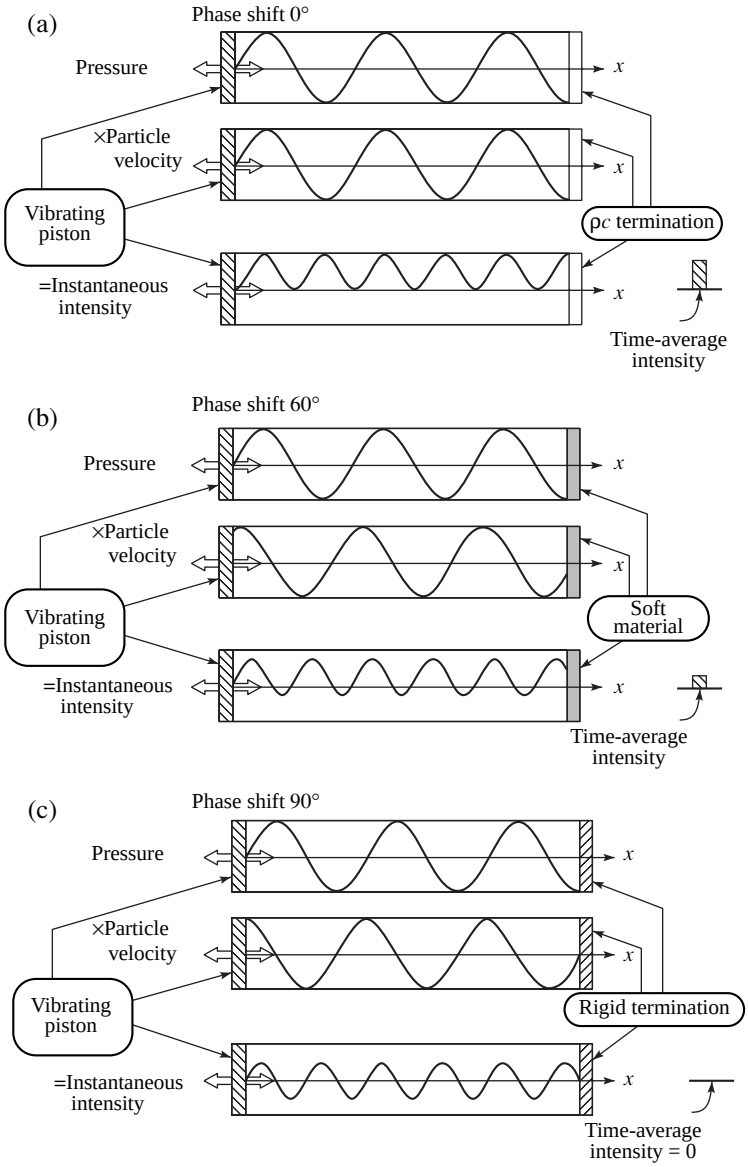

Fig. 1. Spatial distribution of instantaneous sound pressure, instantaneous particle velocity, instantaneous sound intensity, and time-average sound intensity for pure-tone one-dimensional plane wave in a tube. (a) Case with no reflection at right end of tube; sound pressure and particle velocity are in phase. (b) Case with partial reflection at right end of tube; sound pressure and particle velocity are 60° out of phase. (c) Case with rigid end at the right end of tube; there is a perfect reflection, and sound pressure and particle velocity are 90° out of phase; there is no time-average or active intensity—intensity is completely reactive.

Therefore, we see that the active component of the intensity is proportional to the phase gradient and the reactive part is proportional to the gradient of the mean square sound pressure.

Consider plane waves traveling along a hard-walled tube, as illustrated in Fig. 1; only a single frequency is present. The tube is terminated at the right end with a perfect sound absorber; therefore, there is no reflection of sound at the termination of the tube. Under these conditions, the pressure and particle velocity are in phase. In this case the sound intensity I is the product of the sound pressure p and particle velocity u. The intensity fluctuates in time and is always positive in a direction toward the termination (positive x) [36].

In Fig. 1b, the tube is terminated with material that is partially absorptive; here, the sound wave travels from left to right. There will be partial reflection at the termination in this example, so that a weaker wave returns from right to left. The two opposite traveling waves add together, giving the pressure distribution shown. For the material selected at the termination, the particle velocity distribution is 60° out of phase with the sound pressure. The two waves interact to give an active flow of intensity to the right that is less than that shown in Fig. 1a. There also is a small reactive compo-

nent, which flows back and forth from right to left (its magnitude depending on tube location x); the time-average of the reactive intensity is zero at any point in the tube [36].

In Fig. 1c, the tube is terminated with an infinitely hard material. Therefore the waves are perfectly reflected at the termination. In this case, the reflected waves traveling back to the left have the same amplitude as incident waves traveling to the right. These two traveling waves combine to give sound pressure and particle velocity spatial distributions, which are 90° out of phase. In this case, the time-average of the intensity is zero at any point in the tube; i.e., there is no active intensity flow; the sound intensity is completely reactive [36].

3. MEASUREMENT OF SOUND INTENSITY

As already discussed, many researchers have attempted to obtain quantitative measurements of sound intensity by different means in the last sixty years. The most successful measurement principle employs two closely spaced pressure microphones [37]. The particle velocity is obtained through Euler's relation

$$\nabla p(t) + \rho \frac{\partial u(t)}{\partial t} = 0, \tag{14}$$

or

$$u_r^{(e)}(t) = -\frac{1}{\rho}\int_{-\infty}^{t} \frac{p_2(\tau) - p_1(\tau)}{\Delta r} d\tau, \tag{15}$$

where p_1 and p_2 are the sound pressure signals from the two microphones, Δr is the microphone separation distance, and τ is a dummy time variable. The caret indicates the finite difference estimate obtained from the "two-microphone approach." The sound pressure at the center of the probe is estimated from

$$p^{(e)}(t) = \frac{p_1(t) + p_2(t)}{2}, \tag{16}$$

and the time-averaged sound intensity component in the axial direction is, from Eqs. (3), (15), and (16),

$$I_r^{(e)} = \frac{1}{2\rho\Delta r}\left\langle [p_1(t) + p_2(t)] \int_{-\infty}^{t} [p_1(\tau) - p_2(\tau)] d\tau \right\rangle. \tag{17}$$

All sound intensity measurement systems in commercial production today are based on the two-microphone method. Some commercial intensity analyzers use Eq. (17) to measure the intensity in one-third-octave frequency bands. Another type calculates the intensity from the imaginary part of the cross-spectrum G_{12} between the two microphone signals:

$$I_r^{(e)}(\omega) = -\frac{1}{\omega\rho\Delta r}\mathrm{Im}\{G_{12}(\omega)\}. \tag{18}$$

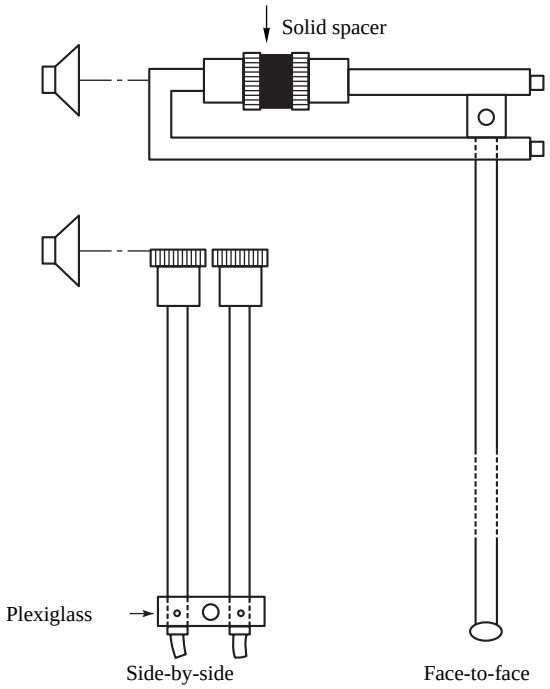

Fig. 2. Microphone arrangements used to measure sound intensity.

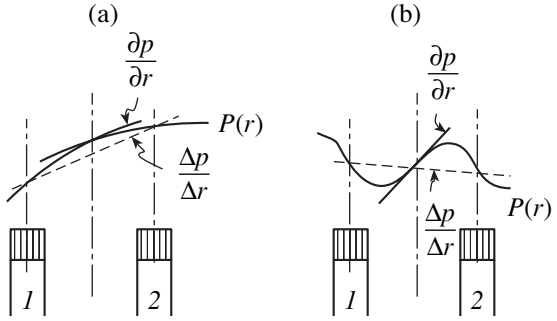

Fig. 3. Illustration of the error due to the finite difference approximation: (a) good approximation at a low frequency and (b) very poor approximation at a high frequency.

The time domain formulation and the frequency domain formulations, Eqs. (17) and (18), are equivalent. Equation (18), which makes it possible to determine sound intensity with a dual channel FFT analyzer, appears to have been derived independently by Fahy and Chung in the late 1970s [27, 28].

Figure 2 shows two of the most common microphone arrangements, "side-by-side" and "face-to-face." The side-by-side arrangement has the advantage that the diaphragms of the microphones can be placed very near a radiating surface, but it has the disadvantage that the microphones shield each other. At high frequencies the face-to-face configuration with a solid spacer between the microphones is claimed to be superior [38].

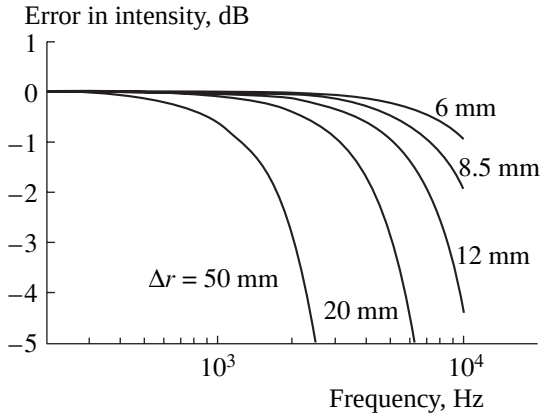

Fig. 4. Finite difference error of an ideal two-microphone sound intensity probe in a plane wave of axial incidence for different values of the separation distance.

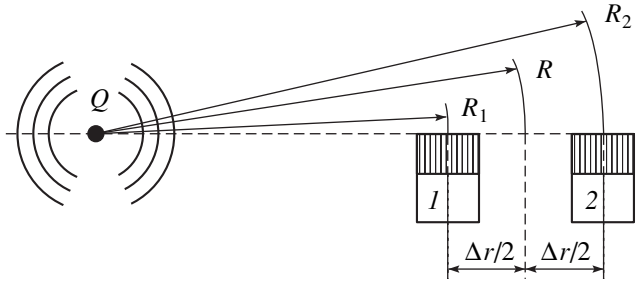

Fig. 5. Microphone probe in the sound field of a point source radiating into a free field.

4. MEASUREMENT LIMITATIONS

There are many sources of error in the measurement of sound intensity, and a considerable part of the sound intensity literature has been concerned with identifying and studying such errors, some of which are fundamental and others of which are associated with technical deficiencies [39–41]. The following is an overview of some of the sources of error in the measurement of sound intensity.

4.1. Finite Difference Approximation Errors

One of the obvious limitations of the measurement principle based on two pressure microphones is the frequency range. The high frequency error is sometimes called a *bias error* as it will result in the same error (in this case an underestimation) every time the sound intensity is measured. The two microphones approximate the gradient of a curve to a straight line between two points, as shown in Fig. 3. If the sound pressure changes too rapidly with distance, the estimate will be inaccurate. This will happen if the wavelength measured becomes small compared with the effective microphone separation Δr. For a plane wave of axial incidence propagating in free-field conditions, the finite difference error that is the ratio of the measured intensity $I_r^{(e)}$ to the true intensity I_r in decibels is

$$L_\varepsilon = 10\log\frac{I_r^{(e)}}{I_r} = 10\log\frac{\sin k\Delta r}{k\Delta r}, \qquad (19)$$

where k is the free field wavenumber. Equation (19) is plotted in Fig. 4 for different values of the microphone separation distance.

For a given effective microphone separation there will be a high frequency limit beyond which errors will increase significantly. Theoretically Eq. (19) and/or Fig. 4 predict that, for accuracy to within 1 dB, the wavelength measured must be greater than six times the spacer distance [42]. Note that in this simple theory the interference of the microphones on the sound field has been ignored. A recent numerical and experimental study of such interference effects has shown that the upper frequency limit of an intensity probe with the microphones in the usual face-to-face configuration is an octave above the limit determined by the finite difference error if the length of the spacer between the microphones equals the diameter, because the resonance of the cavities in front of the microphones gives rise to a pressure increase that to some extent compensates for the finite difference error [38]. An intensity probe, with two 12-mm-long half-inch microphones and with an optimum 12-mm long spacer, performs very well up to 10 kHz [38].

4.2. Near-Field Errors

Another error occurs if the intensity changes within the distance of the microphone spacing. This can happen if the source is comprised of multipoles of high order (e.g., a rotating propeller) or when the sound radiating surfaces vibrate with a small wavelength (e.g., thin plates). Under this condition, the approximation error is not only a function of the separation distance but also of the distance from the source to the probe. This inaccuracy is referred to as the near-field error. As an illustration, the geometry to calculate the error for a spherical wave from a monopole source is shown in Fig. 5. For simplicity in this example the probe is pointed directly at the center of the source. For this particular geometry, the error in decibels is given by [42]

$$L_\varepsilon = 10\log\left[\left(\frac{\sin k\Delta r}{k\Delta r}\right)\left(1-\frac{1}{4}\left(\frac{\Delta r}{r}\right)^2\right)^{-1}\right], \qquad (20)$$

where r is the distance from the source to the middle point between the microphones. From Eq. (20) we observe that the error is not only a function of $k\Delta r$ but also of $\Delta r/r$. It can be shown that, if $r > 2\Delta r$, this error is negligible, while for $r = \Delta r$, the error becomes an overestimation of approximately 1 dB. Thompson and Tree [43] and Elliot [44] have presented similar error formulas for dipole and quadrupole sources. From these functions it can be shown that if the distance

between the probe and the acoustic center of the different types of sources is greater than 2 to 3 times the microphone spacing, a proximity error of less than 1 dB is achieved.

4.3. Phase Mismatch Errors

The amount of phase mismatch between the two channels in the analyzing system determines the low frequency limit. Earlier, the term phase was used to describe the shift between pressure and particle velocity. Here it is used to describe the phase shift in a wave with time or distance. One wavelength can be expressed in terms of a rotation of 360°. The distance between the two microphones can be expressed as a fraction of a wavelength or equivalently as a change of phase between the two points. Sound intensity is directly related to this phase change; without a phase change there is no propagation and therefore no intensity [42].

This phase shift is also equivalent to the time taken for the wave to propagate over the spacer distance Δr. The time separation must be preserved to measure the correct intensity. However, in all analyzing systems there will be a small time delay between the two channels, which introduces a small phase change. This is called a *phase mismatch* error. For a good probe and analyzer combination, the maximum error might be ±0.3°. The phase mismatch error is a *bias* error and the intensity is under- or overestimated according to the sign of the phase mismatch. For accuracy to be within 1 dB, the phase change over the spacer distance should be more than five times the phase mismatch.

To obtain negligible high frequency error, the wavelength must be at least six times the spacer distance. Then the spacer corresponds to one sixth of a wavelength, and so the change in phase across the spacer distance for free field propagation along the probe axis is 60°. Obviously, a phase error of ±0.3° will then be insignificant. It we try to make measurements at a low frequency of, for example, 63 Hz, the wavelength is approximately 5.5 m and the change of phase over a 12 mm spacer is only 0.8°. So a phase mismatch of ±0.3° will cause a significant error in the intensity. Now let us try using a larger spacer. With a 50 mm (approximately four times 12 mm) spacer the phase change is 3.3° (approximately four times 0.8°), and so our results will be sufficiently accurate [45]. This is why a larger spacer is needed for sound intensity measurements at low frequencies. In general, the phase change will be reduced with increasing angle of incidence and in a reactive or diffuse sound field.

If sound is incident at an angle to the probe axis, the phase change to be detected is smaller. In other words, the effective spacer distance is reduced. The decrease in the phase change causes the measured sound intensity to be reduced by the $\cos\theta$ factor. But the pressure, a scalar quantity, is the same whatever the angle of incidence. Hence, there is a difference between the sound intensity and pressure levels and the phase mismatch error will become more significant and the measurement frequency range will be reduced.

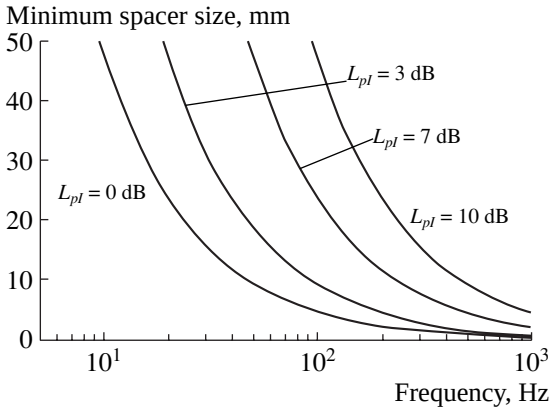

Fig. 6. Minimum spacer size for various sound-pressure indices assuming a system phase accuracy of 0.1°.

The difference between sound pressure and intensity also occurs in reactive and diffuse fields, as the intensity can be low even when the pressure is high. The term for this difference is the *pressure–intensity index*. This index is a very important indicator for the accuracy of a measurement. This is because it can be related to the phase change across the spacer. By measuring the pressure–intensity index, we can determine the phase change across the spacer and find out if the phase mismatch will make the measurement inaccurate. The phase change in degrees can be calculated from [45]

$$L_I - L_p + 10\log\frac{\rho c}{400} = 10\log\left(\frac{\lambda}{\Delta r}\frac{\phi}{360^\circ}\right), \qquad (21)$$

where $L_p - L_I$ is the measured pressure–intensity index (L_{pI}), ϕ is the phase change over the spacer distance Δr, λ is the wavelength, and $10\log(\rho c/400)$ is a small correction term which is usually negligible. Figure 6 shows the minimum spacer size for an accuracy of 1 dB as a function of frequency and for different pressure–intensity indices.

The pressure–intensity index L_{pI} describes the phase change over the spacer. Similarly, the phase mismatch can be described with the residual pressure–intensity index. If the same signal is fed to the two microphones, the analyzer should ideally measure zero intensity. However, any phase mismatch present causes a small phase difference between the two signals, which the analyzer interprets as intensity along the spacer. The intensity detected can be likened to a noise floor below which sound intensity measurements cannot be made. This intensity floor is not fixed. It varies with the pressure level. What is fixed is the difference between the pressure and intensity levels when the same signal is fed to both channels. The difference is defined as the

residual pressure–intensity index and can be related to phase mismatch in degrees using Eq. (21).

The residual pressure–intensity index can be measured with a small coupler that provides the same signal to both of the microphones. The phase change over the spacer distance must be five times the phase mismatch for the measurement accuracy to within 1 dB. This corresponds to the criterion that the pressure–intensity index must be 7 dB smaller than the residual pressure–intensity index. Therefore, we can subtract 7 dB from the residual pressure–intensity index to find the *dynamic capability*, which gives a limit to the pressure–intensity index that can be measured with accuracy [45].

Jacobsen has stated that under difficult measurement conditions the following methods can be used to improve the performance of a given sound intensity probe by using phase compensated measurements as follows [46]:

(1) one can determine the sound intensity from the geometric mean of two measured complex cross-spectra, the second one obtained with the microphones interchanged (or the probe reversed);

(2) one can correct the frequency response of one of the measurement channels;

(3) one can take the arithmetic mean of two measurements, the second one with the probe reversed; and

(4) one can add a correction that is proportional to the mean square pressure.

4.4. Off-Axis Measurement Error

The last source of intensity measurement error to be analyzed is that caused if the probe is aligned in the wrong direction. A sound intensity probe designed in accordance with IEC 1043 has an off-axis response characteristic that follows the cosine relationship

$$10\log\frac{I_\theta}{I_{0_\epsilon}} = 10\log(\cos\theta). \qquad (22)$$

When used for sound power measurements, the probe must be held relatively perpendicular to the measurement surface to prevent errors. If the probe axis is misaligned by 10°, the measured intensity will be wrong by only 0.07 dB. This is normally insignificant. However, a larger error is caused from intensity that is perpendicular to the measurement surface. This component of intensity should not make a contribution to the net intensity used in the sound power calculation. With a 10° misalignment, however, $\cos\theta$ goes from 0 at $\theta = 90°$ to 0.17 at $\theta = 80°$. This could cause an unwanted contribution from an off-axis source of noise. Although the null at 90° can cause errors in a sound power measurement, this characteristic is valuable when using sound intensity to locate a sound source precisely.

4.5. Errors Caused by Use of a Windscreen

When a sound intensity probe is exposed to unsteady airflow, the use of a windscreen is recommended. It reduces the noise in the microphone signals apparently without significantly affecting the acoustical measurements. The use of a windscreen protects the probe from mechanical and thermal damage, so windscreens are often used even in the absence of flow. Munro and Ingard have shown that the two-microphone technique cannot be extended to situations with airflow [47]. Strictly speaking, the measurement principle is simply not valid in the presence of mean flow. However, it can be shown that with a moderate flow velocity, say less than 15 m/s, the resulting errors are normally quite insignificant provided that the sound field is predominantly active. Under such conditions the noise generated by turbulence is likely to be a more serious source of error, and this noise will be reduced by use of a windscreen. In rotational, turbulent flow, it is, in principle, impossible to separate the fluctuating particle velocities associated with incompressible unsteady flow from those associated with the compressible acoustic field.

Jacobsen has examined the influence of windscreens made of porous foam on the performance of sound intensity probes [48]. He has shown that the use of windscreens can lead to a significant underestimation of the sound power of a source at low frequencies if the measurement is carried out in the reactive near field of the source, but it has no appreciable undesirable effect on the result if the measurement surface is further away from the source.

5. APPLICATIONS

Some of the most common practical applications of sound intensity measurements are now discussed briefly.

5.1. Sound Power Determination

One important application is the determination of the sound power of operating machinery. The sound power Π_a is given in terms of the intensity by Eq. (5), where the integration is made over an arbitrary measurement surface enclosing the sound source. Figure 7 illustrates a sound power measurement of a source using both hemispherical and rectangular measurement surfaces.

In practical applications the integration is normally replaced by a summation,

$$\Pi_a = \sum_{i=1}^{N} I_{ni}\Delta S_i, \qquad (23)$$

where N denotes the number of elemental areas into which the enclosing surface is divided and I_{ni} is the intensity measured normal to the ith elemental area ΔS_i.

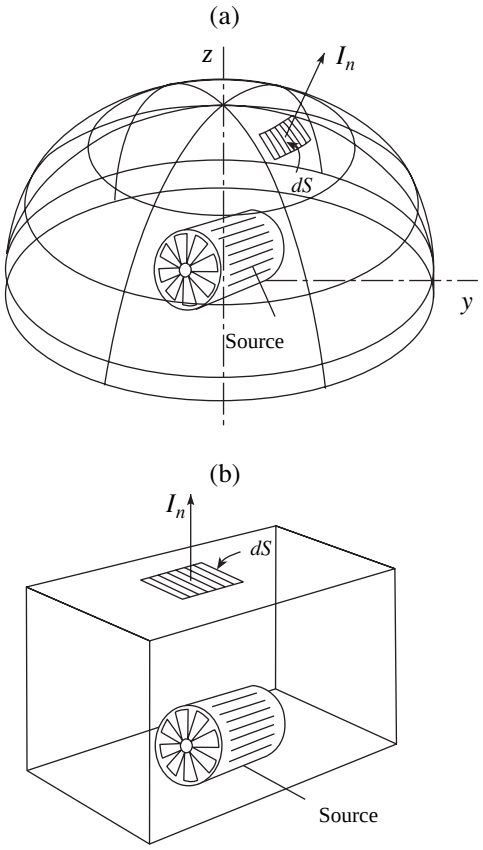

Fig. 7. Sound intensity measured on a segment of (a) a hemispherical measurement surface and (b) a rectangular measurement surface.

To ensure accurate results, the number of area elements N should be sufficiently large. In practice, the number of points at which the intensity needs to be measured can be reduced greatly by the so-called microphone sweeping or scanning technique, where a space-averaged value of I_n is determined by scanning the microphone probe over the surface ΔS during the data acquisition process. The scanning procedure, which was introduced in the late 1970s on a purely empirical basis, was regarded by some with much skepticism for more than a decade [49] but is now generally considered to be more accurate and far more convenient than the procedure based on the use of fixed points [50, 51]. A moderate scanning rate, say 0.5 m/s, and a "reasonable" scan line density should be used, say, 5 cm between adjacent lines if the surface is very close to the source, 20 cm if it is farther away. This measurement process can be achieved manually or with a robot. Hickling *et al.* have proposed guidelines for achieving good integration accuracy when using automated sound-intensity systems [52]. Hongisto *et al.* have recently developed an automatic scanning system for sound insulation measurements using the sound intensity method [53].

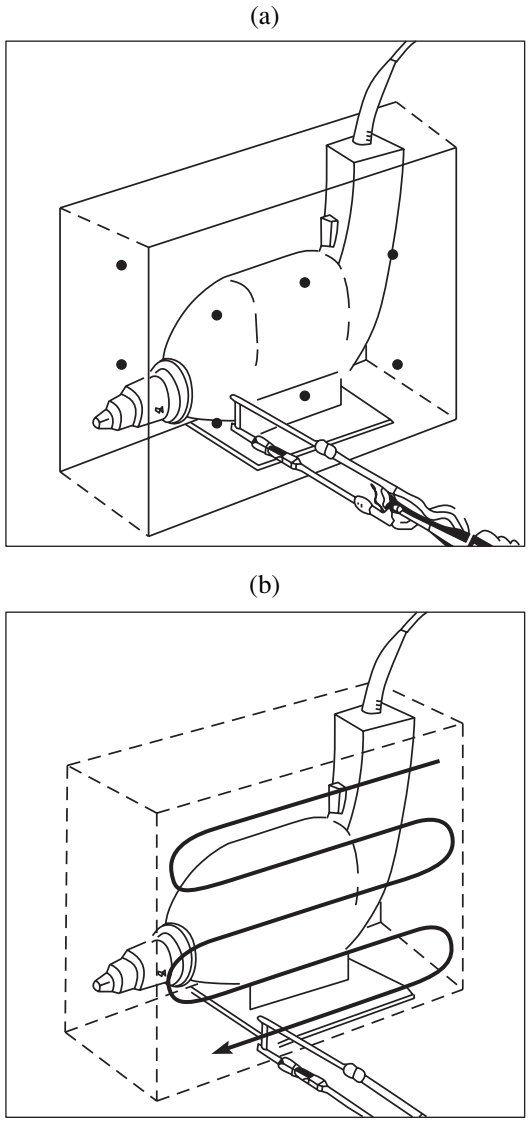

Fig. 8. Typical box surface used in sound power determination with the intensity method: (a) measurement at discrete points and (b) measurement path used in scanning measurement. (After Rasmussen [54].)

Figure 8 shows sound intensity measurements being made on a source using both the fixed point and the scanning techniques [54].

Recently, Crocker *et al.* presented the results of experimental studies on the noise of an air conditioning split unit [55]. Measurements of the normal sound intensity were made with a two-microphone intensity probe and space-averaged over surfaces enclosing different parts of the air conditioning unit. From these space-averaged measurements, the sound power level radiated from each surface was calculated. The sound power level was determined in this way for the metal cabinet, exhaust duct, and inlet duct of the air conditioning unit. For the measurement of the sound power radiated from the inlet and exhaust, care was taken to

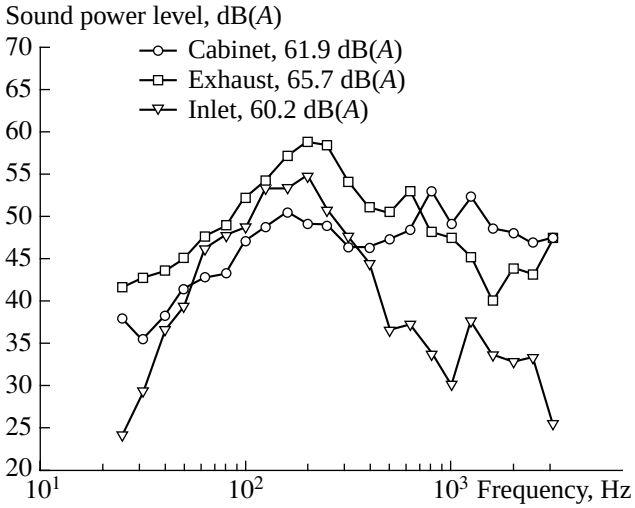

Fig. 9. One-third octave band *A*-weighted sound power levels for different parts of a split level residential air-conditioning system at a flow rate of 1.06 m^3/s. (After Crocker *et al.* [55].)

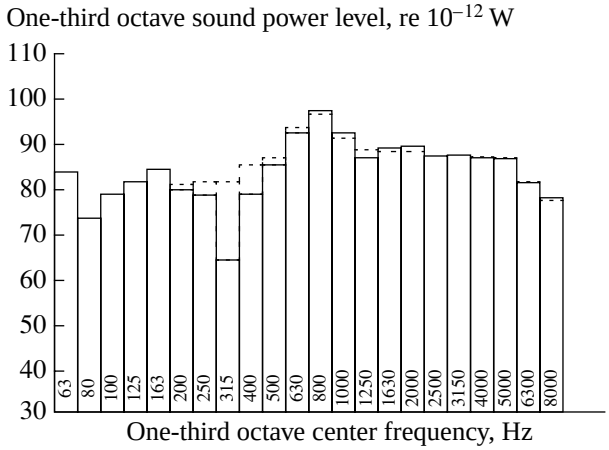

Fig. 10. The sound power of the oil pan of a diesel engine: (—) sound intensity method and (- - -) lead-wrapping results. (After Reinhart and Crocker [31].)

locate the intensity probe on an imaginary rectangular enclosing surface, which was situated just outside the flow. The length of each rectangular surface used for the inlet and exhaust sound power determination was about 4.5 times the duct diameter. Figure 9 shows the results for *A*-weighted one third-octave band sound power level measurements for the unit at the highest flow rate of 1.06 m^3/s. It is seen that the exhaust is the dominant source of sound power for the unit. The results confirm the subjective high frequency hissing character of the cabinet noise and the low frequency rumbling character of the inlet and exhaust noise.

5.2. Noise Source Identification

This is perhaps the most important application. Every noise reduction project usually starts with the identification and ranking of noise sources and sound transmission paths. In one study of diesel engine noise, the whole engine was wrapped in lead sheet. The various parts of the engine were then exposed, one at a time, and the sound power was estimated with single microphones at discrete positions on the assumption that the sound intensity could be approximated by Eq. (9). Sound intensity measurements make it possible to determine the partial sound power contribution of the various components directly. Figure 10 shows the sound power of the oil pan of the diesel engine determined with the sound intensity scanning approach compared to the result obtained from the lead wrapping approach [31].

In some applications such as identifying noise sources in rotating and reciprocating machinery, the use of the gated spectrum analysis technique can improve the results. By measuring the sound intensity for a certain interval of one cycle only and then repeating the process over many cycles, a sufficient number of averages can be taken to make the resulting signal appear stationary. The intensity measurement signal is usually triggered by a reflecting strip placed in a rotating part of the machine, which is sensed by a photoelectric probe. In this way it is possible to study just some part of the cycle only, for example the initiation of combustion in an engine or a particular event in a production process. This technique reveals more clearly the relationship between the various source mechanisms and the radiated sound [45]. Carletti and Vecchi applied this method to study the influence of gear meshing phenomena on global pump noise emission [56].

Difficulties of measurement arise when sound intensity measurements are used to localize or identify sound sources that are coherent (or partly coherent). The superposition principle of linear acoustics holds for field quantities such as pressure and velocities but not for powers and intensities. It is only for incoherent sound fields (where all cross-terms vanish) that energy and power happen to be additive.

Plots of the sound intensity measured on a measurement surface near to a machine can be used in locating noise sources. Sound intensity magnitude plots using arrows are useful in visualizing sound fields. By correlating pressure measurements close to a machine with measurements at reference points, it is possible to obtain a detailed picture of the sound field at the measurement plane and at another far away from the source. This technique is usually called near-field acoustic holography (NAH). However, the traditional sound intensity measurement technique cannot determine exactly the acoustic field at the surface of a source. This is because the sound intensity is measured at points relatively far from the source, and then the direction of the arrows is followed back to the source to imply the

sound source location. Broadband acoustic holography from intensity measurements (BAHIM) is a technique by which the two orthogonal components of the mean intensity tangential to a hologram plane are sampled at points on a grid and converted to distributions of sound pressure amplitude and phase by means of Eq. (12). From these results, the complete sound field can be reconstructed using the FFT technique to perform the spatial integration, subject to the limitation imposed by wavenumber aliasing. Mann and Pascal have applied the BAHIM technique with considerable success to the identification of the principal regions of sound power radiation from an industrial air compressor [57].

5.3. Transmission Loss of Structures

The conventional measure of the sound insulation of panels and partitions is the transmission loss (also called the sound reduction index), which is the ratio of the incident and transmitted sound powers expressed in logarithmic form. The traditional method of measuring this quantity requires a transmission suite consisting of two vibration-isolated reverberation rooms; the incident sound power is deduced from an estimate of the spatial average of the mean square sound pressure in the source room on the assumption that the sound is diffuse, and the transmitted sound power is determined from a similar measurement in the receiving room, where, in addition, the reverberation time must be determined. With the advent of reliable sound intensity measurements, the transmitted sound power can be measured directly using a sound intensity probe. In this case, it is not necessary that the sound field in the receiving room be diffuse, which means that only one reverberation room is necessary [32, 58]. An important advantage of the sound intensity approach over the conventional approach is that it also allows the evaluation of the transmission loss of individual parts of the partition. The sound intensity approach can also be used on structures in situ [59–61]. Weyna has applied this technique to identify the energy transmitted through different parts of composite panels and walls in ship cabin partitions [62].

Figure 11 shows the transmission loss of an aluminum panel determined with the intensity approach and with the conventional two-room method, and Fig. 12 shows measured and calculated transmission loss values of a composite panel, an aluminum aircraft panel with a Plexiglas window [58].

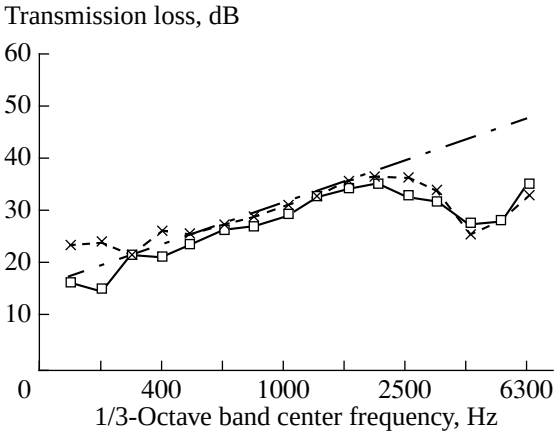

Fig. 11. Transmission loss of a 3.2-mm thick aluminium panel: (––) sound intensity method, (×–×–×) conventional method, and (–·–·–) mass law. (After Crocker *et al.* [58].)

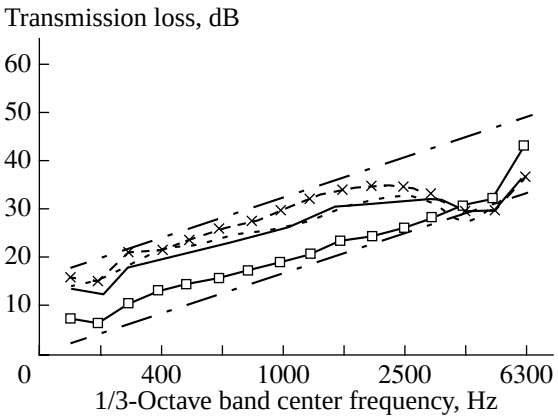

Fig. 12. Measured and calculated transmission loss of a composite aluminium–plexiglass panel. Measured values: (×–×–×) aluminium, (––) plexiglass, and (- - - -) total transmission loss. Calculated values: (–·–·–) mass law, aluminium; (-·-·-) mass law, plexiglass; and (—) total transmission loss. (After Crocker *et al.* [58].)

6. STANDARDS FOR SOUND INTENSITY MEASUREMENTS

There are several standards for the measurement of sound intensity that are completed or under development. These standards are being written both at the national and international levels.

In the United States, standards are being developed by the following ANSI and ASTM working groups:

(1) ANSI S12-21 “Determination of Sound Power Using Sound Intensity Measurements.” This committee began meeting in 1983 and in 1992 produced an engineering grade standard, which includes sound power measurement using *both* fixed points and scanning. This ANSI standard is entitled “Engineering Method for Determination of Sound Power Levels of Noise Sources Using Sound Intensity” and is numbered ANSI S12.12-1992.

(2) ANSI S1-12 “Measurements of Sound Intensity.” This committee was formed more recently than S12-21. The main charter of this committee was to determine methods of calibrating intensity measuring equipment and probes. The standard was completed in 1994 and is entitled “Instruments for the Measurement

of Sound Intensity" and it is numbered ANSI S1.9-1996.

The following standards have been developed internationally:

(3) ISO TC/SC1/WG25. This is the international counterpart to ANSI S12-21. Study group meetings have been held since 1982. Officially, meetings of ISO Working Group WG 25 commenced in 1984. The standards for the determination of sound power levels of noise sources using sound intensity were produced in 1993: ISO 9614-1: Sound Power Determination Using Sound Intensity Measurements: Measurement at Discrete Points and ISO 9614-2: Sound Power Determination Using Sound Intensity Measurements: Measurement by Scanning. More recently, Working Group WG 25 has produced a third standard, which is still in draft stage: ISO 9614-3: Sound Power Determination Using Sound Intensity Measurements: Precision Method for Measurement by Scanning.

(4) IEC/TC29/WG20. This is the international counterpart to ANSI S1-12. The Working Group WG 20 first met in Budapest in April 1985. In 1993 the committee produced the standard IEC 1043: Instruments for the Measurement of Sound Intensity.

(5) ISO 11205 (FDIS 2002). Emission sound pressure level is the sound pressure level obtained in a hemi-free field, which is an ideal environment for determining sound power using standards ISO 3744 or ISO 3745. The purpose of the draft ISO/DIS 11205 is to determine emission sound pressure level at the operator's position using sound intensity measurements under diffuse field conditions. Emission sound pressure levels are determined under a sound field corresponding to a hemi-free field. Sound intensity measurements enable one to determine emission sound pressure levels even under a reflecting acoustic environment, the levels corresponding to hemi-free field. However, these measurements can also be used to determine sound power levels using ISO 3744 and ISO 3745 [63].

(6) ISO 15186, Part 1: Determining Transmission Loss of Panels Using Sound Intensity Measurements. Laboratory Measurements.

(7) ISO 15186, Part 2: Determining Transmission Loss of Panels Using Sound Intensity Measurements. Measurements in the Presence of Flanking, in FDIS (First Draft International Standard) Stage Balloting.

(8) ISO 15186, Part 3: Determining Transmission Loss of Panels Using Sound Intensity Measurements. Low Frequency Measurements, Being Balloted as FDIS.

Also in the United States, ASTM is involved in the following:

(9) ASTM (American Society of Testing and Materials) is developing similar sound transmission loss standards along the lines of ISO 15186 Part 1 and Part 2.

7. CONCLUSIONS

In the last 25 years, the measurement of sound intensity has developed from a topic for research into a practical and useful measurement tool. Measurements of sound intensity are now fairly routinely made to determine the sound power of sources, machinery noise source identification, and the transmission loss (sound reduction index) of structures. There are a number of sources of measurement error including finite difference error, near-field effects, instrumentation phase mismatch, and the effects of background noise. These errors are now fairly well understood and can be overcome so that quite accurate sound intensity measurements can be made, even when environmental measurement conditions are nonideal or even "hostile." Several national and international standards now exist for the determination of the sound power of sources from sound intensity measurements. National and international bodies have also written documents for the calibration of sound intensity instrumentation.

REFERENCES

1. H. Helmholtz, Crelle, **57**, 1859; *Theory of Oscillations in Tubes with Open Ends* (1860).
2. H. Helmholtz, *Vorlesungen über die Mathematischen Prinzipien der Akustik* (Leipzig, 1898).
3. O. Reynolds to Lord Rayleigh (J. W. Strutt), unpublished letter on the reciprocity of sound (Fallowfield, Manchester, October 2, 1875).
4. J. Tyndall, in *Sound, a Course of Eight Lectures* (Longmans, Green, and Co., London, 1867), Lecture 6, pp. 217–254.
5. L. Rayleigh (J. W. Strutt), R. Soc. London **25**, 118 (1876); in *Acoustics: Historical and Philosophical Developments*, Ed. by R. B. Lindsay (Dowden, Hutchinson and Ross, Stroudsburg, Pa.), Paper 36, pp. 402–406.
6. L. Rayleigh (J. W. Strutt), *The Theory of Sound*, 2nd ed. (Macmillan, London, 1894 and 1897), Vols. 1 and 2.
7. L. M. Lyamshev, Dokl. Akad. Nauk SSSR **125**, 1231 (1959) [Sov. Phys. Dokl. **4**, 406 (1959)].
8. L. M. Lyamshev, in *Proceedings of Third International Congress on Air- and Structure-borne Sound and Vibration* (Montreal, 1994), p. 1839.
9. Lord Rayleigh (J. W. Strutt), Philos. Mag. **14**, 186 (1882).
10. Lord Rayleigh (J. W. Strutt) and A. Shuster, Proc. R. Soc. London **32**, 104 (1881).
11. *Acoustical Measurements–Methods and Instrumentation*, Ed. by H. B. Miller (Hutchinson and Ross, Stroudsburg, Pa., 1892), p. 237.
12. *Acoustical Measurements—Methods and Instrumentation*, Ed. by H. B. Miller (Hutchinson and Ross, Stroudsburg, Pa., 1892), p. 114.
13. E. C. Wente, Phys. Rev. **10**, 39 (1917).
14. E. C. Wente, Phys. Rev. **19**, 498 (1922).
15. H. F. Olson, U.S. Patent No. 1,892,644 (1932).
16. H. F. Olson, J. Audio Eng. Soc. **22**, 321 (1975).

17. C. W. Clapp and F. A. Firestone, J. Acoust. Soc. Am. **13**, 124 (1941).
18. R. H. Bolt and A. A. Petrouskas, J. Acoust. Soc. Am. **15**, 79(A) (1943).
19. S. Baker, J. Acoust. Soc. Am. **27**, 269 (1955).
20. T. J. Schultz, J. Acoust. Soc. Am. **28**, 693 (1956).
21. T. J. Schultz, P. W. Smith, and C. I. Malme, J. Acoust. Soc. Am. **57**, 1263 (1975).
22. J. F. Burger, G. J. J. van der Merwe, B. G. van Zyl, and L. Joffe, J. Acoust. Soc. Am. **53**, 1167 (1973).
23. B. G. van Zyl and F. Anderson, J. Acoust. Soc. Am. **57**, 682 (1975).
24. T. H. Hodgson and R. D. Erianne, in *Inter-Noise Proceedings* (1976), p. 13.
25. T. H. Hodgson, J. Acoust. Soc. Am. **61**, 2 (1977).
26. R. J. Alfredson, in *Noise-Conference 77 Proceedings* (1977), p. 307.
27. F. J. Fahy, J. Acoust. Soc. Am. **62**, 1057 (1977).
28. J. Y. Chung, J. Acoust. Soc. Am. **64**, 1613 (1978).
29. J. Y. Chung and J. Pope, in *Inter-Noise 78 Proceedings* (1978), p. 893.
30. J. Y. Chung, J. Pope, and D. A. Feldmaier, in *Proceedings of SAE Diesel Noise Conference* (SAE, 1979), Paper No. 790,502.
31. T. Reinhart and M. J. Crocker, Noise Control Eng. J. **18**, 84 (1982).
32. M. J. Crocker, B. Forssen, P. K. Raju, and A. Mielnicka, in *Inter-Noise 80 Proceedings* (1980), p. 741.
33. A. D. Pierce, *Acoustics: An Introduction to Its Physical Principles and Applications*, 2nd ed. (Acoust. Soc. Am., New York, 1989).
34. F. J. Fahy, *Sound Intensity*, 2nd ed. (Spon, London, 1995).
35. D. G. Crighton, A. P. Dowling, J. E. Ffowcs Williams, M. Heckl, and F. G. Leppington, *Modern Methods in Analytical Acoustics* (Springer, New York, 1992).
36. M. J. Crocker, in *Handbook of Acoustical Measurements and Noise Control*, Ed. by C. M. Harris (McGraw-Hill, New York, 1991), Chap. 14.
37. M. P. Waser and M. J. Crocker, Noise Control Eng. J. **22**, 76 (1984).
38. F. Jacobsen, V. Cutanda, and P. M. Juhl, J. Acoust. Soc. Am. **103**, 953 (1998).
39. F. Jacobsen, Int. J. Acoust. Vibr. **5**, 173 (2000).
40. M. Ren and F. Jacobsen, J. Sound Vibr. **128**, 247 (1991).
41. F. Jacobsen, J. Sound Vibr. **166**, 195 (1993).
42. S. Gade, in *Bruel and Kjaer Technical Review* (1982), No. 3, pp. 3–39.
43. J. K. Thompson and D. R. Tree, J. Sound Vibr. **75**, 229 (1981).
44. S. J. Elliot, J. Sound Vibr. **78**, 439 (1982).
45. *Sound Intensity* (Bruel and Kjaer Technical Publication, 1989).
46. F. Jacobsen, J. Sound Vibr. **174**, 140 (1994).
47. D. H. Munro and K. U. Ingard, J. Acoust. Soc. Am. **65**, 1402 (1979).
48. F. Jacobsen, Appl. Acoust. **42**, 41 (1994).
49. M. J. Crocker, Noise Control Eng. J. **27**, 67 (1986).
50. U. S. Shirahatti, M. J. Crocker, and P. K. Raju, J. Acoust. Soc. Am. **84**, 629 (1988).
51. U. S. Shirahatti and M. J. Crocker, Acustica **80**, 378 (1994).
52. R. Hickling, P. Lee, and W. Wei, Appl. Acoust. **50**, 125 (1997).
53. V. Hongisto, K. Nieminen, H. Koskela, *et al.*, Noise Control Eng. J. **45**, 85 (1997).
54. G. Rasmussen, Sound Vibr. **23**, 12 (1989).
55. M. J. Crocker, J. P. Arenas, and R. E. Dyamannavar, in *Proceedings of 9th International Congress on Sound and Vibration* (Orlando, FL, 2002), Paper 161.
56. E. Carletti and I. Vecchi, Noise Control Eng. J. **35**, 53 (1990).
57. J. A. Mann and J. C. Pascal, Noise Control Eng. J. **39**, 3 (1992).
58. M. J. Crocker, P. K. Raju, and B. Forssen, Noise Control Eng. J. **17**, 6 (1981).
59. K. E. Heitman, M. S. Atwal, and M. J. Crocker, J. Acoust. Soc. Am. **82**, 1342 (1987).
60. K. E. Heitman, M. S. Atwal, and M. J. Crocker, Noise Control Eng. J. **31**, 145 (1988).
61. Y. S. Wang and M. J. Crocker, Noise Control Eng. J. **19**, 80 (1982).
62. S. Weyna, Appl. Acoust. **44**, 341 (1995).
63. S. Keith and G. Krishnappa, Int. J. Acoust. Vibr. **6**, 162 (2001).

Acoustical Physics, Vol. 49, No. 2, 2003, pp. 176–183. Translated from Akusticheskiĭ Zhurnal, Vol. 49, No. 2, 2003, pp. 215–223.

Measurement of Wall Pressure Fluctuations in the Presence of Vibrations Induced by a Turbulent Flow

E. B. Kudashev

Space Research Institute, Russian Academy of Sciences, Profsoyuznaya ul. 84/32, Moscow, 117997 Russia
e-mail: eco@iki.rssi.ru
Received August 19, 2002

In memory of L.M. Lyamshev

Abstract—A systematic study of the methods of measuring wall pressure fluctuations against a background of intense vibrations is carried out. The method of separating the turbulent signal from noise on the basis of monitoring the level of vibration interference is considered. Active methods of vibration control are developed for a miniature receiver of turbulent pressure fluctuations. It is shown that the methods based on the spatial filtering of the noise field offer the greatest promise. The filtering properties of vibration-proof receivers and measuring systems are investigated. © *2003 MAIK "Nauka/Interperiodica".*

In the late 1950s and early 1960s, L.M. Lyamshev started his research into hydrodynamic flow noise. Numerous studies performed by Lyamshev at the boundary between acoustics and physical hydrodynamics, which resulted in the development of a new area of research—hydrodynamic acoustics—include a group of works that revealed the role of wall pressure fluctuations and viscous tangential stresses that arise in a turbulent boundary layer in the formation of the flow noise [1]. The problem of reducing the hydrodynamic flow noise was also investigated by Lyamshev, and, in this connection, he performed a series of studies concerned with the methods of controlling the characteristics of wall pressure fluctuations [2]. The problem of compensating the vibration interference in the measurements of wall pressure fluctuations is closely related to these studies.

In hydrodynamic acoustics, the wall pressure fluctuations in a turbulent boundary layer are studied by miniature receivers with the minimal possible receiving surface [3]. However, it is well known that this method of increasing the resolution of acoustic-hydrodynamic studies leads to an inevitable decrease in the sensitivity of the receiver and, hence, to low levels of the signals generated by the transducers measuring the turbulent pressures. In this situation, the effect of vibrations induced in the sensing element of the receiver by wall pressure fluctuations proves to be substantial. It should be noted that the effect of vibrations on miniature receivers of pressure fluctuations is typical of all experiments performed in actual conditions [4, 5]. Considerable interference is also caused by the acoustic noise arising in experimental measuring systems or test benches. In addition, it is necessary to take into account the effect of the wall temperature fluctuations on the measurement of the turbulent pressure fluctuations [6, 7].

Today, turbulent pressure measurements are carried out not only in laboratory conditions but also in full-scale conditions, where the effect of noise is enhanced. In the last few years, in connection with growing interest in nonstationary aerodynamic processes in power plants, the measurements of the wall pressure fluctuations have often been performed on objects of complex shape in conditions approaching full-scale ones. The aforementioned factors affect the results of measurements to one or another extent, and it is the effect of noise that is responsible for the disagreement between the results obtained from different test benches and measuring systems. In the case of aerodynamic test-bench experiments, the measured signals, in addition to the turbulent pressure component, contain the components caused by the vibration of the test bench and by the deformation of the sensing element of the receiver because of the nonstationary loading of its nonoperating surfaces, which do not directly perceive the pressure fluctuations. Our previous studies [7, 8] showed that, in these conditions, the most promising methods of noise control are the active methods based on spatial filtering.

The essence of the active method of vibration compensation consists in the introduction of an additional compensating sensing element into the measuring system, this element being identical to the main sensor in its characteristics. The compensating sensing element responds only to the field of the physical parameter responsible for the noise interfering with the measurements, and it generates an electric signal proportional to the instantaneous value of this physical parameter. The purpose of the additional sensing element is to

1063-7710/03/4902-0176$24.00

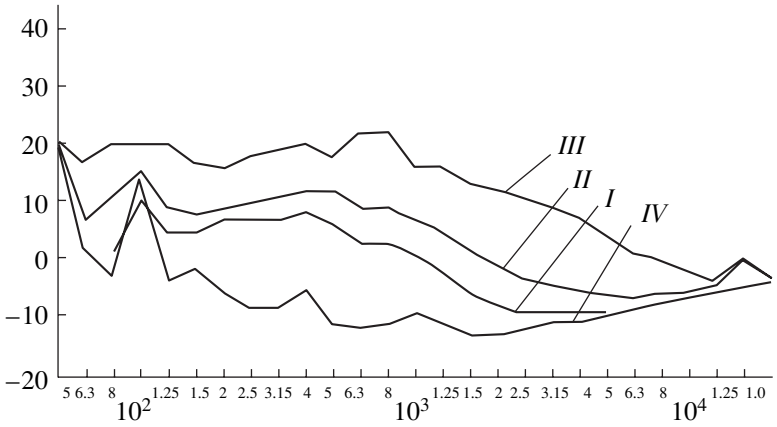

Fig. 1. Spectral levels of the turbulent pressure and the electric noise in a wind tunnel: (*I*) V_1 = 15 m/s, (*II*) V_2 = 20 m/s, (*III*) V_3 = 30 m/s, and (*IV*) V_4 = 0.

measure the noise field without any distortion. If, at any instant, the output signal of the compensating sensing element is identical with the noise component of the signal generated by the main sensing element, a counterconnection of these two sensing elements leads to the electric subtraction of the noise component from the total signal.

The practical implementation of the active compensation method encounters a number of problems (related to each other). They include the choice of the type of the compensating element and its position relative to the main sensing element, the determination of the limits of applicability of the resulting noise-immune measuring system, and the evaluation of the efficiency of the method of active noise control. Specific solutions to these problems depend on the characteristics of the acting noise field, the type of the receivers in use (the sensing elements), and the properties of the pressure field under study. Below, the problem of active noise control is considered in application to the measurements of wall pressure fluctuations in a turbulent boundary layer by miniature piezoelectric receivers against the background of vibrations.

METHOD OF SEPARATING THE TURBULENT SIGNAL FROM NOISE

To reduce the effect of vibrations on the piezoelectric receivers, the latter are placed in massive metal units, in specially vibration-damped pockets, the vibration levels of the frames of the experimental systems remaining considerable. The measurements performed on a vibration-testing machine with a transducer that had a sensing element of about 1 mm in size (the transducer was developed by the author of this paper) showed that, while the pressure sensitivity was $\gamma_p = 4$ μV/Pa, the vibration sensitivity was $\gamma_w = 0.2$ mV/(m/s^2).

For the measurements to be correct, it is necessary that the desired signal determined by the pressure fluctuations be at least ten times greater than the signal component related to noise (in the case under consideration, by vibrations W). Therefore, the following inequality should be satisfied:

$$\{\gamma_p p'/\gamma_w w'\} \geq 10,$$

where p' and w' are the characteristic values of the measured pressure fluctuations and vibrations, respectively. As applied to the aforementioned values of the sensitivities to pressure and acceleration for a standard vibration-damped receiver, this condition is reduced to the requirement $\{w'/p\} \leq 10^{-1}\gamma_p/\gamma_w$.

As an example satisfying this condition, Fig. 1 shows the frequency spectra of turbulent pressure fluctuations $P_T(f)$ and vibrations $W(f)$ measured in a turbulent boundary layer at the wall of the working section of a low-noise wind tunnel.

However, the condition of a multiple excess of the signal over the noise level is not always satisfied in the measurements of the frequency spectra of turbulent pressures. Hence, it is necessary to develop methods for separating the turbulent signal from noise.

Consider the method of separating the turbulent signal from noise on the basis of monitoring the level of the vibration interference [8]. A necessary element of vibration interference suppression in the turbulent pressure measurements is the comparative spectral analysis of the field of the turbulent signal $\Phi_T(w)$ and the vibration interference $\Phi_w(\omega)$, which allows one to determine the limits of the correct measurements of pressure fluctuations in the presence of vibration. The method is based on the direct measurement (monitoring) of the vibration spectrum in the region of pressure fluctuation measurements and on the calibration (determination in a special experiment) of the sensitivity of the electroacoustic transducer that measures the pressure fluctuations to vibrations.

The electric signal $\Phi_m(\omega)$ generated by the transducer can be represented in the form

$$\Phi_m(\omega) = \Phi_T(\omega) + \Phi_w(\omega). \quad (1)$$

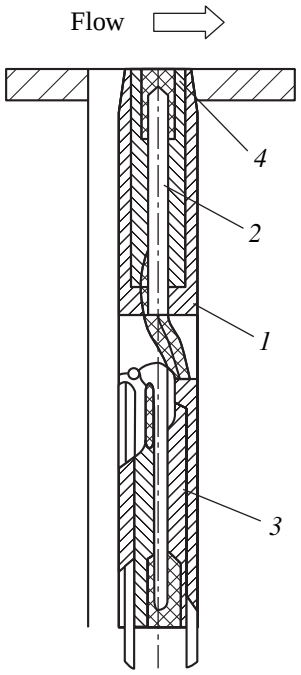

Fig. 2. Vibration-proof miniature transducer for turbulent pressure fluctuations: (*1*) casing, (*2*) main sensing element, (*3*) compensating sensing element, and (*4*) membrane.

Into the measurement equation (1), we introduce the sensitivity of the receiver to pressure in the case of a coherent action, γ_p, this sensitivity being obtained by acoustic calibration: $\gamma_p = \Phi_w/P_s(\omega)$. Then, Eq. (1) takes the form

$$P_m(f) = P_T(f) + P_{eq}(f), \quad (2)$$

where $P_{eq}(f) = \Phi_w/\gamma_p$ is introduced as the equivalent pressure induced by the effect of vibrations on the piezoelectric receiver. To calculate the vibration signal Φ_w, it is necessary to calibrate the fluctuation receiver on a vibration-testing machine and determine its frequency characteristic of sensitivity, $\gamma_w(f)$. Then, it is necessary to measure the spectrum of vibrations $w(f)$ acting on the receiver of pressure fluctuations by using an accelerometer with a known vibration sensitivity $\nu(f)$. Let the receiver detect the signal Φ_{acc}. In this case, the vibration spectrum is determined as

$$w(f) = \Phi_{acc}\nu(f).$$

From the vibration spectrum known from the experiment, one can obtain the vibration signal at the measuring transducer of turbulent pressures;

$$\Phi_W(f) = \gamma(w)W(f) = \Phi_{acc}\gamma_w(f)/\nu(f)$$

and determine the equivalent pressure P_{eq} induced by vibrations:

$$P_{eq}(f) = \Phi_W(f)/\gamma_p = \Phi_{acc}\gamma_W(f)/\gamma_p\nu(f). \quad (3)$$

Using Eq. (3), we represent the measurement equation (2) in the form

$$P_m(f) = P_T(f) + \Phi_{acc}\gamma_w(f)/\gamma_p\nu(f).$$

Performing the comparison of the spectra $P_T(f)$ and $P_{eq}(f)$ and using the condition

$$P_T(f) = 10\Phi_{acc}\gamma_w(f)/\gamma_p\nu(f), \quad (4)$$

it is possible to determine the limits for the correct measurements of turbulent pressure fluctuations in the presence of a vibration interference. However, if the turbulent pressures are studied in the presence of intense vibrations, condition (4) fails, and it is expedient to change to the methods of active compensation.

METHOD OF A VIBRATION-PROOF TRANSDUCER

In practical measurements of wall pressure fluctuations against the background of vibration interference, the situation when the signal and noise spectra almost coincide is rather common. This fact gave rise to the development of the method of compensation by the instantaneous value of interference and to the design of a series of miniature vibration-compensated transducers of turbulent pressure [2, 3, 5, 6]. In these transducers, the compensating sensing element is similar to the main working element in its characteristics, but, unlike the main element, it is insulated so as not to be directly affected by the flow.

Figure 2 shows a vibration-proof miniature transducer tested in practice. The transducer for measuring turbulent pressure fluctuations is mounted flush with the wall that is in contact with the flow. The sensing element *1* is a piezoelectric cylinder with a receiving surface of 1.3 mm in size and a height of 15 mm. To increase the sensitivity of the pressure fluctuation receiver, a membrane *4* is glued to the end of the piezoelectric cylinder. The transducer is enclosed in a brass casing, which has the form of a two-sided beaker. The vibration-proof receiver of pressure fluctuations operates in the following way. The working sensing element *2*, 15 mm in height, perceives the pressure fluctuations through membrane *4*. This element is enclosed in casing *1*, which is 4 mm in diameter. The compensating element *3* is represented by a similar piezoelectric element mounted under the main one in the same casing. When the transducer is in the flow (see Fig. 2), the pressure fluctuations act on only working element *2*, but the vibrations are perceived by both sensing elements. As a result, an electric potential is induced by vibrations at the electrodes of both sensing elements *2* and *3*. The vibration compensation is achieved by electrically connecting sensing elements *2* and *3* in opposite directions. The main piezoelectric element *2* is glued by a sealing compound along its lateral surface into brass casing *1*, which has the form of a two-sided beaker 4 mm in diameter. Under main element *2*, compensating element *3* is mounted in the same casing so that it lies out-

side the turbulent boundary layer and, hence, is not directly affected by pressure fluctuations.

The study and testing of the vibration-proof measuring systems based on the active compensation of vibration interference demonstrated the importance of carefully choosing identical piezoelectric elements from the PÉ-7T2 piezoelectric elements available from mass production. The working and compensating sensing elements should be identical in their capacitance and in the frequency characteristics of their pressure and vibration sensitivities. The identity is checked by testing the elements on a vibration-testing machine. The manufacture technology and the mounting technique used for the receiver of turbulent pressure fluctuations considerably affects the vibration compensation: it is necessary to provide identical conditions of mounting the working and compensating piezoelectric elements in the casing of the transducer from the point of view of the stiffness and resonance properties of the whole structure.

The natural scatter of both electric and structural parameters of piezoelectric elements in the mass production, as well as the technical problems and inaccuracies in the assembly of the receiver of pressure fluctuations, do not allow one to provide a complete identity of the deformations of the main and compensating elements under vibrations induced by the flow, as well as the identity of the operation of both sensing elements, and to obtain a complete vibration compensation. For example, in manufacturing a series of vibration-compensated receivers, two batches of 50 piezoelectric elements each were used to obtain 12 and 15 vibration-proof transducers. The efficiency of the compensation of vibration interference was proved in this case by testing the sensing elements and the vibration-compensated miniature transducers on vibration-testing machines and by the results of using them for studying turbulent pressure fluctuations in boundary layers and jet flows. Let us consider the typical frequency characteristics obtained for the sensitivity of the elements to acceleration from the studies on a vibration-testing machine (Fig. 3). From a comparison of the curves in Fig. 3, one can see that, after a thorough selection of identical sensing elements, the method of active compensation provides a reduction of the vibration interference level by 20–30 dB. Now, we consider the main result, namely, the resolution of the spectral amplitudes of turbulent pressure fluctuations against the vibration noise in the case of using vibration-proof miniature transducers for measuring turbulent pressure fluctuations in a turbulent boundary layer and in jet flows.

The measurements of turbulent pressure fluctuations by the vibration-compensated receivers developed by the author of this paper were performed in a wind tunnel at a flow rate of 300 m/s [9]. Figure 4 shows the measured spectra of the wall pressure fluctuations: curve *1* and spectrum *3* of vibration accelerations at the point of measurement. Curve *2* shows the spectral density of the electric signal generated by the receiver with the screened sensing element.

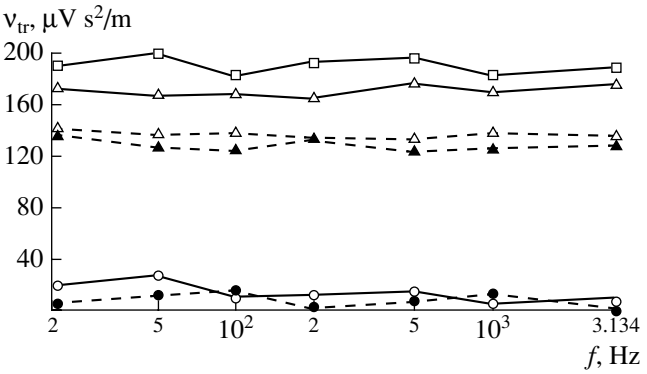

Fig. 3. Frequency characteristic of the vibration sensitivity of the transducer: (■□) the main element, (▲△) the compensating element, and (●○) the counterconnection of the elements.

The results of the experiment in the wind tunnel allow us to conclude that the miniature vibration-proof receiver developed provides the measurement of aerodynamic noise generated by the wall turbulence and the suppression of vibrations in the presence of intense vibration interference.

In engineering structures, in the case of a flow about objects of complex shape with inhomogeneities, turbulent pressure fluctuations induce complex multimode vibrations. At high frequencies, a considerable contribution to the vibration interference can be made by small-scale components of the vibration field. In this situation, the condition of the coherent action of vibration interference on the sensitive elements of the transducer considered above does not hold; hence, it is impossible to obtain the phase coincidence of the vibration signals s_{w_1} and s_{w_2} of the working and compensating sensing elements of the transducer. It should be also noted that the turbulent pressure fluctuations at the sensing surface are weakly correlated with the effect of vibration on the sensing elements.

In the case of the incoherent action of noise, the compensation of vibration interference by an instantaneous value is impossible, and it is expedient to use the method of vibration compensation by the mean square values.

METHODS OF COMPENSATING THE VIBRATION INTERFERENCE ON THE BASIS OF SPATIAL FILTERING

In practice, in the experimental acoustic-hydrodynamic studies of a turbulent boundary layer, it is not always possible to use the above-described methods of active compensation of vibration interference. For example, in the case of objects of complex shape, it is

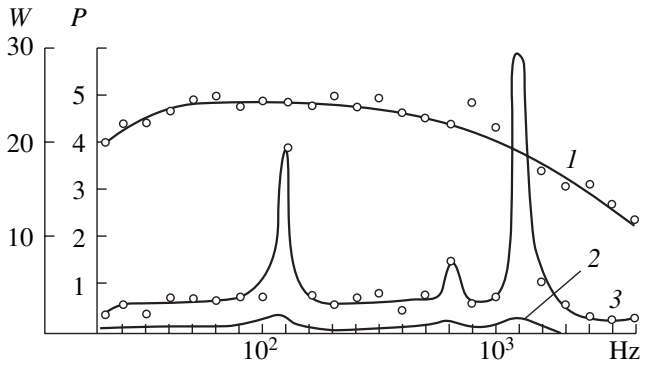

Fig. 4. Spectra of (*1*) the pressure fluctuations and (*2*) the vibrations; the spectra are measured by receivers with vibration compensation. (*3*) The levels of the electric noise of the measuring system.

impossible to use miniature receivers assembled in massive units. Often, a pressure fluctuation transducer is fixed in a relatively compliant element of the structure placed in the turbulent flow.

When turbulent pressures are measured on compliant elements of structures, the efficiency of the active method of vibration interference compensation can be reduced. This occurs because the vibration loading of the sensing elements mounted on compliant elements of the structure is caused by deformations whose inhomogeneity scales are determined by the energy-carrying components of the field of turbulent pressure fluctuations in the measurement region. A considerable part of the vibration interference proves to be correlated with the pressure fluctuations at the receiving surface. The scales of the turbulent pressure field in the range of significant frequencies of analysis are much smaller than the wavelengths of the strain waves propagating through the structure in the case of vibration without the flow, and these scales are comparable with the distance between the working and compensating sensing elements of the turbulent pressure transducer. Therefore, generally speaking, the instantaneous "vibration" signals s_{w_1} and s_{w_2} obtained from the main and compensating sensing elements in this case are different and cannot be considered as identical because of the difference in the instantaneous loads caused by vibrations.

In the conditions under discussion, one should use with caution the results of testing vibration-compensated transducers on vibration-testing machines in the case of estimating the compensation of the vibration interference in a real experiment, because the operating conditions of the sensing elements in a real flow may not coincide with the situation on the vibration-testing machine. One also has to take into account the effect of the relative positions of the main and compensating sensing elements on the compensation of the vibration interference.

Let us use the methods of spatial filtering to estimate the possibility of measuring the turbulent pressure fluctuations in the presence of vibration interference. The output signal of the working sensing element of a vibration-compensated transducer can be represented in the form of the sum

$$s_1(t) = \int_\infty K(\mathbf{x})\,p(\mathbf{x}, t)\,d\mathbf{x} + \int_\infty L_1(\mathbf{x})\,p(\mathbf{x}, t)\,d\mathbf{x} + W_1(t). \quad (5)$$

In expression (5), the first term represents the signal of the receiver of turbulent pressure fluctuations when the fluctuation field $p(\mathbf{x}, t)$ acts on the receiving surface of the sensing element. The second term is formed by analogy with the first one and represents the signal due to the deformations that occur in the structure placed in the flow because of the effect of turbulent pressure fluctuations in the vicinity of the point of measurement. This is the vibration interference component caused by the field of the desired signal, i.e., by the turbulent fluctuations. The last term $W_1(t)$ in Eq. (5) is the signal of the receiver that is caused by the vibrations that are unrelated to the fluctuating pressure in the region of measurement. The parameter L_1 takes into account the response of the working sensing element to the point excitation outside the receiving surface. Figure 5 shows the character of the amplitude distribution $L_1(\mathbf{x})$ in the region of measurement for a pressure transducer with vibration compensation in comparison with the amplitude distribution of the sensitivity to pressure, $K(\mathbf{x})$.

The signal from the additional compensating sensing element *2* of the pressure fluctuation receiver can be represented by analogy with Eq. (5) as the sum

$$s_2(t) = \int_\infty L_2(\mathbf{x})\,p(\mathbf{x}, t)\,dx + W_2(t), \quad (6)$$

where $L_2(\mathbf{x})$ is the response of the fluctuating pressure transducer to the excitation outside the receiving surface of the compensating sensing element. The spatial distribution of the parameter $L(\mathbf{x})$, which is the same for the main and compensating elements, is shown in Fig. 5.

In the case of full compensation for the "purely" vibrational signal, when the main and compensating sensing elements are counterconnected, the condition $W_1 = W_2$ is satisfied. Then, the resulting signal obtained from the vibration-compensated transducer has the form

$$\begin{aligned} s(t) &= s_1 - s_2 \\ &= \int_\infty [K(\mathbf{x}) + L_1(\mathbf{x}) - L_2(\mathbf{x})]\,p(\mathbf{x}, t)\,d\mathbf{x}. \end{aligned} \quad (7)$$

The analysis of Eq. (7) shows that, in this case, the vibration interference can strongly affect the resolution of the transducer measuring the turbulent pressure fluctuations.

Specific estimates of the effect of vibration on the measurement of pressure fluctuations by an electroacoustic transducer were obtained for a receiver with a

circular sensitive surface and a uniform amplitude distribution of sensitivity over the receiving surface:

$$K = \gamma/\pi R^2 \text{ at } |\mathbf{x}| \le R, \quad K = 0 \text{ at } |\mathbf{x}| > R, \tag{8}$$

where R is the radius of the circular receiving surface and γ is the sensitivity of the receiver to pressure. With allowance for the compliance of the surface contacting the flow, we set the parameter L_1 determining the sensitivity of the receiver to "extraneous" pressure fluctuations (outside the surface of the sensing element) in the form

$$L_1 = aK(x)e^{-(x/l)^2}, \tag{9}$$

where l is the size of the "effective" zone of sensitivity due to the effect of the extraneous pressure fluctuations with allowance for the compliance and a is the maximal value of the relative sensitivity of the receiver to vibrations: $a = L_{\max}(x)/K_{\max}(x)$.

If the compensating sensing element *2* introduced in the fluctuating pressure transducer is positioned, as usual, outside the region affected by turbulent fluctuations and is mounted behind the main working sensing element (see Fig. 5), the effect of pressure fluctuations on the signal of the compensating sensing element $s_2(t)$ in the measurement region proves to be negligibly small. Then, the parameter L_2 in Eq. (7) tends to zero. Let us construct an expression for the wave characteristic of the transducer by using the methods of spatial filtering. We define the wave characteristic of the receiver of pressure fluctuations as the frequency characteristic of the receiver in the $\boldsymbol{\kappa}$ space by using the Fourier transform of the transducer influence function $\theta(\varepsilon)$ [10].

The transducer influence function $\theta(\varepsilon)$, as the autocorrelation of the amplitude distributions of sensitivity, can be represented in the form

$$\theta(\varepsilon) = \int_\infty K(\mathbf{x})K(\mathbf{x}+\varepsilon)d\mathbf{x}. \tag{10}$$

Then, the spectrum of the influence function $\theta(\varepsilon)$ is

$$S(\mathbf{x}) = \int_\infty \theta(\varepsilon)e^{-i\mathbf{x}\varepsilon}d\varepsilon. \tag{11}$$

The wave characteristic of the vibration-compensated receiver of pressure fluctuations is expressed as

$$\begin{aligned} S(\mathbf{x}) &= \iint_\infty [K_1(\mathbf{x})K(\mathbf{x}+\varepsilon)]\exp(-i\mathbf{x}\varepsilon)d\varepsilon \\ &= \iint_\infty [K_1(\mathbf{x}) + L_1(\mathbf{x})][K_1(\mathbf{x}+\varepsilon) + L_1(\mathbf{x}+\varepsilon)] \\ &\quad \times \exp(-i\mathbf{x}\varepsilon)d\mathbf{x}d\varepsilon \\ &= \gamma^2\left[\frac{J_1(\boldsymbol{\kappa}R)}{\boldsymbol{\kappa}R/2} + a\left(\frac{l}{R}\right)^2\exp\left\{-\left(\frac{\boldsymbol{\kappa}l}{2}\right)^2\right\}\right]^2, \quad \kappa = |\boldsymbol{\kappa}|. \end{aligned} \tag{12}$$

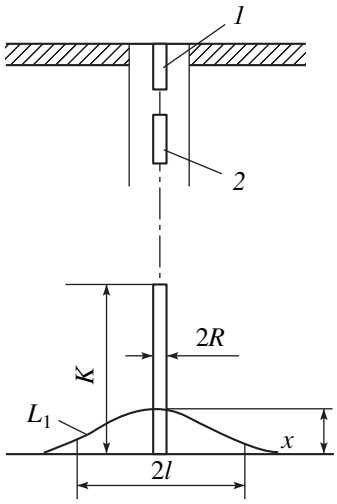

Fig. 5. Vibration-compensated transducer for turbulent pressure fluctuations: (*1*) the working sensing element and (*2*) the compensating sensing element.

Let us analyze the resulting expression (12).

In the region of energy-carrying scales of fluctuating pressures, we have $\kappa R \ll 1$; i.e., on the receiving surface of the transducer, $R \ll \lambda$ of a vortex. Then, evidently, for the first term in the brackets, we have $\dfrac{J_1(\kappa R)}{\kappa R/2} \longrightarrow 1$, and the wave characteristic of the transducer can be represented as

$$S(\kappa) = \gamma^2\left[1 + a\left(\frac{l}{R}\right)^2\exp\left\{-\left(\frac{\kappa l}{2}\right)^2\right\}\right]^2. \tag{13}$$

Now, we determine the output signal of the turbulent fluctuation transducer with vibration compensation by using the concept of spatial filtering:

$$\Phi_{ss}(\omega) = \int_\infty S(\mathbf{x})E_{pp}(\mathbf{x}, \omega)d\mathbf{x}, \tag{14}$$

where $E_{pp}(\boldsymbol{\kappa}, \omega)$ is the wave-vector–frequency spectrum of the wall pressure fluctuations, which characterizes the energy distribution of the two-dimensional field of turbulent pressures in the spatial scales (the wave vector $\boldsymbol{\kappa}$) and in the phase velocities $U_{\text{ph}} = \boldsymbol{\kappa}/\omega$ [10].

The analysis of expression (14) with allowance for Eq. (13) shows that, in addition to the wave-vector–frequency spectrum $E_{pp}(\boldsymbol{\kappa}, \omega)$ of pressure fluctuations, the factors that affect the signal measured by the transducer include such parameters of the structure as the relative vibration sensitivity, i.e., the parameter a (see Fig. 5), and the ratio between the size of the receiving surface of the transducer R and the effective radius l, which is the size of the zone affected by the extraneous pressure fluctuations. This ratio takes into account the compli-

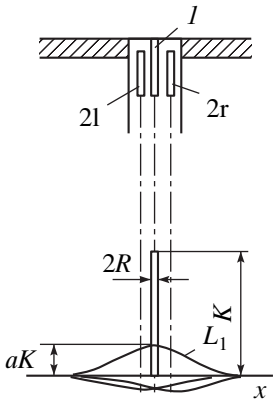

Fig. 6. Vibration-compensated system with two compensating elements: (*1*) the main sensing element and (2l) the left and (2r) the right compensating sensing elements.

ance of the structure placed in the flow and the relative positions of the working and compensating sensing elements of the transducer.

The calculation of the expression for the spectral density of the signal by Eq. (14) for a miniature vibration-compensated transducer with a compensating element positioned deeper than the working sensing element yields the following expression:

$$\Phi_{ss}(\omega) = \gamma^2 \iint_{\infty} \left[1 + a\left(\frac{l}{R}\right)^2 \exp\left\{-\left(\frac{\kappa l}{2}\right)^2\right\}\right]^2 E_{pp}(\boldsymbol{\kappa}, \omega)\, d\boldsymbol{\kappa}. \quad (15)$$

The effect of the vibration interference and the error introduced by the compliant surface can be estimated by comparing the spectral density (15), which characterizes the signal measured by the vibration-compensated receiver, with the power spectrum of the fluctuating pressure

$$\Phi_{pp}(\omega) = \iint_{\infty} E_{pp}(\boldsymbol{\kappa}, \omega)\, d\boldsymbol{\kappa}. \quad (16)$$

A comparison of Eqs. (15) and (16) shows that the reduction of the vibration compensation is related to the effect of the compliant surface. This is the effect of vibration induced by the pressure fluctuations. The analysis of Eq. (15) leads to the formulation of two conditions necessary for an efficient vibration compensation, which is achieved when the term $a(l/R)^2 \exp\{-\kappa l/2\}$ becomes equal to zero.

The first condition: the relative vibration sensitivity should be sufficiently small ($a \longrightarrow 0$) to satisfy the inequality

$$a(l/R)^2 \ll 1.$$

The second condition is satisfied when the size of the effective zone of influence l is sufficiently large. Then, in the region of the energy-carrying scales of pressure fluctuations, we have

$$\boldsymbol{\kappa} l \gg 1, \text{ i.e., } l \gg \lambda_T.$$

When this condition is satisfied, the self-suppression of the vibration signal takes place as a result of the incoherent summation of turbulent pressure fluctuations $p(\mathbf{x}, t)$.

If the conditions specified above fail because of a high relative vibration sensitivity or a small zone of influence, the suppression of the vibration interference may be ineffective.

Let us show that, in this case, it is expedient to use the modified method of measuring pressure fluctuations by using an array of compensating elements in the vibration-compensated transducer. The vibration-compensated measuring system presented in Fig. 6 includes the main working element and two compensating elements forming a compensating transducer for vibration interference. The compensating sensing elements are positioned symmetrically on both sides of the main working element, at a distance d from it, near the surface contacting the flow. Their positions are chosen in such a way that, in the course of measurements, they are located under the turbulent boundary layer outside the zone affected by pressure fluctuations. The compensating elements are electrically connected in series and counterconnected with the working element, so that the amplitude distribution of the vibration sensitivity is represented as

$$L_2 = L_{2l} + L_{2r},$$

where

$$L_{2l}(x) = \frac{1}{2}L_1(x + d), \qquad L_{2r}(x) = \frac{1}{2}L_1(x - d). \quad (17)$$

In the analysis of the vibration interference compensation, the functions of the sensitivity to extraneous pressure fluctuations are defined by analogy with L_1;

$$L_{2l}(x) = \frac{a}{2}K(x + d)\exp\left[-\left(\frac{x + d}{l}\right)^2\right], \qquad L_{2r}(x) = \frac{a}{2}K(x - d)\exp\left[-\left(\frac{x - d}{l}\right)^2\right], \quad (18)$$

but with a two times smaller coefficient of relative vibration sensitivity a.

It can easily be shown that the wave characteristic of the modified vibration-compensated measuring system is determined by the expression

$$S(\kappa) = \gamma^2\left[\frac{J_1(\kappa R)}{\kappa R/2} + a\left(\frac{l}{R}\right)^2 \exp\{-(\kappa l/2)^2\} \times (1 - \cos\kappa_\xi d)\right]^2, \quad (19)$$

which differs from the wave characteristic (13) of the transducer with a single compensating element by the presence of the factor $(1 - \cos\kappa_\xi d)$ in the second term. Here, κ_ξ is the projection of the wave vector on the axis of the array of elementary receivers (the working element and the two compensating elements). If we take into account the small size R of the receiver, which is common for the measurements of turbulent pressure fluctuations, and the small spatial separation of the array elements $d \sim R$, the wave characteristic of the system takes the form

$$S(x) = \gamma^2\left[1 + \frac{a}{2}\left(\frac{d}{R}\right)^2 (K_\xi l)^2 \exp\{-(\kappa l/2)^2\}\right]^2. \quad (20)$$

Then, the spectral density of the signal recorded by the modified measuring system is determined by the expression

$$\Phi_{ss}(\omega) = \gamma^2 \int\int_{\infty}\left[1 + \frac{a}{2}(d/R)^2(\kappa_\xi l)^2 \exp\{-(\kappa l/2)^2\}\right]^2 \times E_{pp}(\boldsymbol{\kappa}, \omega)\, d\boldsymbol{\kappa}. \quad (21)$$

From relation (21), it follows that, in the modified method of compensating the vibrations induced by the fluctuating pressure outside the receiving surface of the transducer, the relative effect of vibration interference is limited by a value of the order of a ($S(\kappa) \longrightarrow 1$), because, according to estimates, the factor multiplying a is of the order of unity. This level of vibration interference is usually acceptable for the measurements of turbulent pressures [8].

ACKNOWLEDGMENTS

I am grateful to L.R. Yablonik for long-term fruitful cooperation and to J.D. Verbitskii (from the Mendeleev All-Russian Research Institute of Metrology) for the participation in the experiments.

This work was supported by INTAS (project no. INF0-00-089) and the Russian Foundation for Basic Research (project nos. 01-07-90008 and 02-07-90092).

REFERENCES

1. L. M. Lyamshev, Vestn. Akad. Nauk SSSR, No. 7, 22 (1973).
2. L. M. Lyamshev, B. I. Chelnokov, and A. G. Shustikov, Akust. Zh. **29**, 806 (1983) [Sov. Phys. Acoust. **29**, 477 (1983)].
3. A. V. Smol'yakov, Akust. Zh. **47**, 264 (2001) [Acoust. Phys. **47**, 218 (2001)].
4. W. K. Blake, *Mechanics of Flow-Induced Sound and Vibration*, Vol. 2: *Complex Flow-Structure Interactions* (Academic, New York, 1986).
5. N. K. Andreev and A. A. Veĭp, in *Experimental Methods and Equipment for Turbulence Studies* (Inst. Teplofiz., Sib. Otd. Akad. Nauk SSSR, Novosibirsk, 1980), pp. 77–82.
6. E. B. Kudashev and L. R. Yablonik, in *Proceedings of Ninth European Turbulence Conference: Advances in Turbulence IX*, Ed. by I. P. Castro, P. E. Hancock, and T. G. Thomas (2002), p. 896.
7. E. B. Kudashev and L. R. Yablonik, Akust. Zh. **32**, 127 (1986) [Sov. Phys. Acoust. **32**, 78 (1986)].
8. E. B. Kudashev and L. R. Yablonik, in *Proceedings of 5th International Symposium on Fluid-Structure Interactions, Aeroelasticity and Flow-Induced Vibrations and Noise* (New Orleans, 2002).
9. E. B. Kudashev and L. R. Yablonik, Izv. Vyssh. Uchebn. Zaved. Énerg., No. 2, 72 (1986).
10. E. B. Kudashev and L. R. Yablonik, Akust. Zh. **23**, 615 (1977) [Sov. Phys. Acoust. **23**, 351 (1977)].

Translated by E. Golyamina

Acoustical Physics, Vol. 49, No. 2, 2003, pp. 184–188. Translated from Akusticheskiĭ Zhurnal, Vol. 49, No. 2, 2003, pp. 224–228.

Amplitude Modulation of Underwater Noise Produced by Seagoing Vessels[1]

A. A. Kudryavtsev[†], K. P. Luginets, and A. I. Mashoshin

Laboratory of Applied Acoustic Research, a/ya 10, Pushkin-4, St. Petersburg, 189620 Russia

e-mail: mai@lpai.spb.ru

Received June 16, 2001

Abstract—Data obtained from the processing of records of underwater noise produced by seagoing vessels are used to refine the model of the noise amplitude modulation caused by the rotation of the propeller shaft and ship roll and pitch in a seaway. Specifically, the width of the frequency band of the modulation process, the value of the modulation coefficient, and the distribution of the magnitude and phase of the modulation coefficient over the carrier frequency spectrum are investigated. © *2003 MAIK "Nauka/Interperiodica".*

The amplitude modulation of underwater noise produced by seagoing vessels is widely used in practice for the classification of ships [1–5]. The purpose of this paper is to describe the results of the experimental study of a model of the amplitude-modulated underwater noise produced by a ship in application to two types of modulation:

—modulation caused by the rotation of the propeller shaft (shafts) and the screw-propeller (propellers) (in what follows, we will call it shaft–blade modulation; the origin of this term will be explained below) and

—modulation caused by ship roll and pitch in a seaway (we will call it roll–pitch modulation).

Since the model is intended for solving the problem of target classification, we do not consider here other problems connected with these types of amplitude modulation, specifically, the mechanism of their generation.

In the most general form, the model of amplitude-modulated noise emitted by a ship can be presented as follows:

$$A_{\mathrm{AMN}}(f, t) = [1 + U_{\mathrm{SBM}}(f, t) + U_{\mathrm{RPM}}(f, t)]A_{\mathrm{N}}(f), \quad (1)$$

where $A_{\mathrm{AMN}}(f, t)$ is the instant amplitude spectrum [6] of the amplitude-modulated noise of a ship, f is the frequency, t is the running time, $A_{\mathrm{N}}(f)$ is the instant amplitude spectrum of the nonmodulated quasi-stationary carrier of the noise, $U_{\mathrm{SBM}}(f, t)$ is the normalized modulation process characterizing the shaft–blade modulation of the noise carrier in a narrow frequency band with the central frequency f, and $U_{\mathrm{RPM}}(f, t)$ is the normalized modulation process characterizing the roll–pitch modulation of the noise carrier in a narrow frequency band with the central frequency f.

It is necessary to note that, in the calculation of the spectrum given by Eq. (1), the frequency band of the spectral analysis must be much greater than the frequencies of the shaft–blade and roll–pitch modulations.

Thus, the above-stated purpose of this paper is specified to consist in the refinement of the form and parameters of the functions $U_{\mathrm{SBM}}(f, t)$ and $U_{\mathrm{RPM}}(f, t)$ representing the models of the shaft–blade and roll–pitch modulations, respectively.

We start with the refinement of the model of the shaft–blade modulation. From papers [1–5] concerned with this type of modulation, the following data are known.

(i) Shaft–blade modulation is a consequence of the rotation of the propeller shaft and the screw-propeller. The corresponding modulation coefficient strongly depends on the rotation rate. In the case of a small (precavitation) rate of rotation, the modulation coefficient is fairly small, which usually prevents the detection of the shaft–blade modulation in the received signals of noise emission from ships at an insufficiently high signal-to-noise ratio. A sharp growth of the modulation coefficient begins from the rate corresponding to the appearance of cavitation at the screw-propeller. This rate of shaft rotation (as well as the ship speed corresponding to it) is called the critical rotation rate (the critical speed).

(ii) In the course of the rotation of the propeller shaft and the screw-propeller, the modulation of noise occurs at two discrete frequencies, namely, at the frequency of the shaft rotation (the shaft frequency) and at the frequency equal to the product of the frequency of shaft rotation and the number of blades of the screw-propeller (the blade frequency). This is the reason why this type of modulation is called shaft–blade modulation. The shaft frequencies of seagoing vessels lie within the interval 2–6 Hz, and the blade frequencies, within 6–24 Hz. Due to the nonlinear effects accompanying the

[†] Deceased.

[1] The paper is dedicated to the memory of Aleksandr Aleksandrovich Kudryavtsev.

radiation, the discrete spectrum of shaft–blade modulation usually contains the harmonics of the shaft and blade frequencies, which form a combined shaft–blade sound series with the fundamental equal to the shaft frequency. The shaft–blade sound series may extend to 100 Hz or more, but in most cases, it does not go beyond 25 Hz. In some cases, the shaft frequency and its harmonics cannot manifest themselves and the spectrum of the shaft–blade modulation contains only the blade sound series.

Taking this into account, the model of the shaft–blade modulation can be represented in the form [2]

$$U_{\mathrm{SBM}}(f,t) = \sum_{i=1}^{N_{\mathrm{SBSS}}} m_{\mathrm{SBM}_i}(f)\cos[2\pi(F_{\mathrm{SBM}_i}t + \delta F_{\mathrm{SBM}_i}(t)/F_{\mathrm{SBM}_i}) + \varphi_{\mathrm{SBM}_i}(f)], \quad (2)$$

where N_{SBSS} is the number of harmonics in the shaft–blade sound series, F_{SBM_i} is the middle frequency of the ith harmonic in hertz, $\delta F_{\mathrm{SBM}_i}(t)$ is the centered normal process describing the frequency fluctuations of the ith harmonic, $m_{\mathrm{SBM}_i}(f)$ is the frequency dependence of the modulation coefficient of the modulated process for the ith harmonic of the shaft–blade sound series, and $\varphi_{\mathrm{SBM}_i}(f)$ is the frequency dependence of the initial phase of modulation of the modulated process for the ith harmonic of the shaft–blade sound series.

(iii) A device whose flowchart is given in Fig. 1 is used to separate shaft–blade modulation [2, 8]. An amplitude-modulated signal is fed to the input of this device. A band-pass filter provides an opportunity to select the carrier frequency band, where the amplitude envelope is separated. An automatic gain control provides a constant level of amplitude-modulated signal at the filter output. The envelope is separated by using an amplitude detector. As a rule, the latter is represented by a full-wave linear detector realized by ignoring the sign of the output process. This detector provides a certain advantage over other detectors [7]. A low-pass filter limits the frequency range of the envelope by the band containing a discrete spectrum of the shaft–blade modulation. A narrow-band spectrum analyzer calculates the accumulated narrow-band energy spectrum of the envelope of the shaft–blade modulation, in which it manifests itself as a shaft–blade sound series, as has been mentioned above. A computing device connected to the output of the spectrum analyzer serves to separate this shaft–blade sound series.

The noise immunity of the device pictured in Fig. 1 is described by the formula [8]

$$Q_{\mathrm{out}_i} = \sqrt{N_{\mathrm{SA}}}\frac{\Delta f_{\mathrm{BF}}}{\max(\Delta F_{\mathrm{SA}}, \Delta F_{\mathrm{SBM}_i})} m_{\mathrm{SBM}_i}^2 \frac{q_{\mathrm{in}}^2}{(q_{\mathrm{in}}+1)^2}, \quad (3)$$

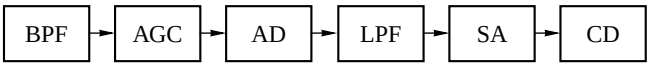

Fig. 1. Flow chart of the device for the separation of the amplitude modulation of broadband noise produced by marine objects (BPF is a band-pass filter, AGC is a device of automatic gain control, AD is an amplitude detector, LPF is a low-pass filter, SA is a narrowband spectrum analyzer, and CD is a computing device).

where Q_{out_i} is the output signal-to-noise ratio equal to the ratio of the excess of the ith harmonic of the shaft–blade sound series observed in the energy spectrum of the envelope over the average level of the background in its vicinity to the value of the rms fluctuation of the background in the same vicinity; $\Delta F_{\mathrm{SBM}_i}$ is the bandwidth of the frequencies of the modulating process corresponding to the ith harmonic of the shaft–blade sound series in hertz; m_{SBM_i} is the modulation coefficient corresponding to the ith harmonic of the shaft–blade series, which is equal to the ratio of the modulating process amplitude to the carrier amplitude; Δf_{BF} is the filter band in hertz; q_{in} is the input ratio of the power of the amplitude-modulated signal to the power of noise at the filter output; ΔF_{SA} is the band of the spectral analysis in hertz; and N_{SA} is the number of the acts of energy spectrum storage.

To refine the model of shaft–blade modulation, a processing of the noise records obtained from the output of an omnidirectional hydrophone with a transmission band from 10 Hz to 10 kHz was carried out. The hydrophone was cast from a ship drifting near navigation routes (in various regions of the ocean) to a depth of 50–200 m, which provided the best conditions for the reception of underwater noise from a ship passing by.

The noise was recorded by a measuring tape recorder with an operational frequency band of 5 Hz to 10 kHz. Each record began when a ship was visually detected, on the condition that its noise level exceeded the level of ambient sea noise by no less than 10 dB. The length of records was from 5 to 30 min, depending on the observation conditions. Each record was complemented by characteristic information containing the type and name of the ship, its speed, the time dependence of the record of its relative bearing (aspect angle), the records of marine noise before and after the ship's passage, and the degree of sea roughness.

In total, 189 noise records were obtained, including 67 records from tankers, 39 records from dry cargo carriers, 31 records from trawlers, 23 records from passenger vessels, and 29 records of noise from ships of other types.

The distribution of the width of the frequency band of the modulating process was determined first of all.

The experimental technique proceeded from the fact [see Eq. (3)] that if the inequality

$$\Delta F_{\mathrm{SA}} > \Delta F_{\mathrm{SBM}_i} \tag{4}$$

is satisfied (i.e., the band of analysis exceeds the width of the frequency band of the modulating process), a decrease in the band of analysis ΔF_{SA} will be accompanied by a proportional increase in the output signal-to-noise ratio Q_{out}. This growth stops only when Eq. (4) becomes invalid. Taking this fact into account, the technique used for the record processing was chosen to be as follows. Each record of underwater noise, being multiply reproduced by the tape recorder, was fed to the input of the processing device whose flowchart is given in Fig. 1. The processing of each record was performed twice. At first, the one-third-octave band of the filter was determined within the range 50 Hz–10 kHz, at the output of which the output value of the signal-to-noise ratio Q_{out} was maximal. All other parameters of the device were fixed: the cutoff frequency of the low-pass filter was 25 Hz, the band of analysis was ΔF_{SA} = 0.05 Hz, and N_{SA} = 4. Then, the selected one-third-octave band corresponding to the maximum of the signal-to-noise ratio was set as the filter band, and only the band ΔF_{SA} was reduced from 0.1 Hz down to the value at which the growth of the output signal-to-noise ratio Q_{out} terminated for all harmonics of the shaft–blade sound series. In this process, for each harmonic of the shaft–blade sound series, the band ΔF_{SA} was fixed, at which the growth of the output signal-to-noise ratio for this harmonic terminated. This band was taken as the width of the frequency band of the modulating process $\Delta F_{\mathrm{SBM}_i}$ for this harmonic.

The results obtained after processing all the records were analyzed, and this analysis led to the following conclusions. The bandwidth of the modulating process in the case of shaft–blade modulation depends most strongly on the number of harmonic and on the degree of sea roughness. The dependence on the harmonic number is a directly proportional one, and, therefore, the relative (with respect to the middle frequency of the harmonic) band of the modulating process essentially depends on only the degree of sea roughness according to the empirical formulas

$$M\left\{\frac{\Delta F_{\mathrm{SBM}_i}}{F_{\mathrm{SBM}_i}}\right\} = (3 + 0.25W^3) \times 10^{-3},$$
$$\sigma\left\{\frac{\Delta F_{\mathrm{SBM}_i}}{F_{\mathrm{SBM}_i}}\right\} = \max[2.5;\ 2.5 + 5(W - 2)] \times 10^{-3}, \tag{5}$$

where $M\{X\}$ and $\sigma\{X\}$ are the sample mathematical expectation and the rms deviation of the random quantity X, and W is the degree of sea roughness (number on the Beaufort scale).

From Eqs. (5), it follows in particular that, in the case of small sea roughness (up to Beaufort 3 inclusive), the relative bandwidth of the modulating process of the shaft–blade modulation is no greater than 1%.

The distribution of the shaft–blade modulation coefficient and the dependence of the modulation coefficient on the frequency of the modulated carrier were studied using the same device (Fig. 1). The technique used for the record processing was as follows. Of all the noise records available, 149 were chosen to correspond to the sea roughness up to Beaufort 3 inclusive. All the device parameters, except for the filter band, were fixed (the cutoff frequency of the low-pass filter was 25 Hz, ΔF_{SA} = 0.05 Hz, and N_{SA} = 8). Each selected noise record was multiply reproduced by the tape recorder and fed to the device input, each time with a new filter band value. Simultaneously, both the central frequency and the filter bandwidth were changed: the central frequency was tuned from 50 Hz to 10 kHz and the relative filter width was 22% for the central frequencies within the range 50–500 Hz, 10% within the range 0.5–1 kHz, 5% within the range 1–2 kHz, 3% within the range 2–4 kHz, and 1.5% within the range 4–10 kHz. The input signal-to-noise ratio q_{in} was calculated for each of these bands (as the ratio of the power of the amplitude-modulated signal to the noise power at the filter output). Then, the harmonics of the shaft–blade sound series were separated from the envelope spectrum, and the output signal-to-noise ratio Q_{out_i} was calculated for each of them (as the ratio of the excess of the ith harmonic of the shaft–blade sound series over the average background level in its vicinity to the value of the rms fluctuation of the background in the same vicinity). After that, the modulation coefficient was calculated for each harmonic of the shaft–blade sound series according to the formula

$$m_{\mathrm{SBM}_i} = \sqrt{\frac{Q_{\mathrm{out}_i}}{\sqrt{N_{\mathrm{SA}}}\dfrac{\Delta f_{\mathrm{BPF}}}{\Delta F_{\mathrm{SA}}}\dfrac{q_{\mathrm{in}}^2}{(q_{\mathrm{in}} + 1)^2}}}, \tag{6}$$

which was obtained from Eq. (3) with condition (4) (according to the results of processing, this condition is satisfied in the case of small sea roughness with the selected band of analysis of 0.05 Hz).

The analysis of the processing results obtained for all records led to the following conclusions.

—In the case of ship movement with over-critical speed, all studied carrier frequencies (50 Hz–10 kHz) are subjected to shaft–blade modulation;

—The dependence of the modulation coefficient on the carrier frequency for each noise record has a complex form characterized as a rule by the presence of so-called cavitation peaks. The form of this dependence is repeated for all harmonics of the shaft–blade series. It was impossible to determine the connection of the peak positions with the type, speed, and aspect angle of ships. The result of averaging the dependences of the modulation coefficient on the carrier frequency over all

processed noise records is an almost straight line parallel to the frequency axis. In view of this result, when synthesizing an algorithm for target classification, it is expedient to proceed from a uniform distribution of the coefficient of shaft–blade modulation over the modulated carrier frequencies. The shaft–blade modulation coefficient that corresponds to the maximal harmonic of the shaft–blade sound series with respect to the output signal-to-noise ratio lies within the interval 0–0.15 with a probability of 0.95, and single peaks reach a value of 0.4. The distribution of this shaft–blade modulation coefficient obeys a limited ($m_{\mathrm{SBM}} \geq 0$) normal law with a mathematical expectation of 0.06 and an rms deviation of 0.035.

To study the distribution of the initial phase of the shaft–blade modulation process over the modulated carrier frequencies of noise, the device shown in Fig. 1 was transformed into the device shown in Fig. 2. The device became a two-channel one, and the spectrum analyzer began to operate in the mode of calculation of the amplitude and phase cross-spectra. The values of the phase cross-spectrum at the frequency of each harmonic of the shaft–blade sound series were determined by the computing device, together with the separation of the harmonics of the shaft–blade sound series in the amplitude spectrum. The technique used for the record processing was as follows. The band-pass filters BPF-1 and BPF-2 were tuned to the nonoverlapping frequency bands from the band set realized in the preceding experiment. Other parameters of the device were also taken from the preceding experiment. The noise record played back by the tape recorder was fed simultaneously to both inputs of the processor. The phase differences of the modulating processes corresponding to each harmonic of the shaft–blade sound series that was separated from the cross-spectrum of the amplitude envelopes detected in the nonoverlapping bands of the carrier were determined.

An analysis of the results of processing all the records by this technique when different nonoverlapping bands of the carrier are chosen led to an expected conclusion: the phase difference of like processes (i.e., corresponding to the same harmonics of the shaft–blade sound series) modulating different bands of the carrier is equal to zero in all cases correct to the measurement error of the phase spectrum; i.e., the modulation of all carrier frequencies is performed in phase. This fact could be predicted proceeding from the unified mechanism of formation of the shaft–blade modulation. Our experiments confirm this hypothesis. Moreover, the conclusion that the modulation of all carrier frequencies is in phase is very important, since it provides an opportunity to substantiate such an important parameter of the device separating the shaft–blade modulation as the preselector band.

The initial phase of the modulating process $\varphi_{\mathrm{SBM}_i}(f)$ in Eq. (2) does not depend on frequency due to the in-phase character of the modulation of all carrier frequencies of the ship noise, and, furthermore, it can be assumed to be equal to zero for all harmonics of the shaft–blade sound series without any loss for the problem.

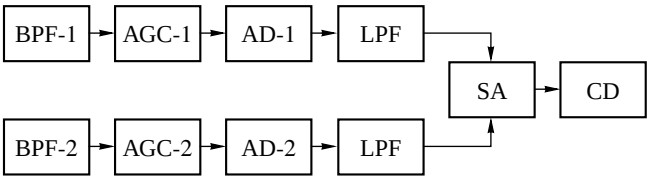

Fig. 2. Flow chart of the device for the determination of the distribution of the initial phase of a modulating process over the carrier frequency spectrum. (Notation is the same as in Fig. 1.)

The same technique of record processing as in the case of the determination of the value of the modulation coefficient was used to answer the question of whether the discrete (i.e., narrow-band) components of the noise spectrum, which are caused by the operation of mechanisms aboard a ship and have frequencies exceeding the frequencies of the harmonics of the shaft–blade sound series, are subjected to shaft–blade modulation. The exception was the fact that the band-pass filter was tuned to the frequency and band of one of the discrete components of the carrier spectrum at the frequencies above 50 Hz. A second spectrum analyzer operating in the mode of calculation of the energy spectrum was connected to the output of the tape recorder in parallel with the band-pass filter to reveal such components and to measure their frequencies and bands. The records with the spectrum containing the discrete components not belonging to the shaft–blade series and exceeding the continuous part of the spectrum by no less than 10 dB were chosen for the experiment. There were 48 such records. Their processing by the technique described offered the following conclusions. The modulation of discrete components that coincided in frequency with one of the frequencies of the shaft–blade sound series was revealed in 40% of the selected noise records. Another 40% of the selected records revealed modulation with frequencies that differed from the frequencies of the shaft–blade sound series. The modulation of discrete components was not revealed in 20% of the selected records despite the fact that the excess of the discrete components over the continuous part of the spectrum reached 15 dB or more. The shaft–blade modulation was separated by processing all selected records with the help of one-third-octave filters. This fact testifies that the amplitude modulation of the discrete components produced by the operation of mechanisms is not always connected with the operation of the screw-propeller.

Now, let us proceed to the refinement of the model of noise modulation by the roll and pitch of the ship.

The following data are known from earlier papers.

(i) The spectrum of ship noise can be modulated in amplitude by ship roll or pitch (and in rare cases, by both of them together).

(ii) The frequency of ship roll lies within the interval 0.03–0.2 Hz and the frequency of ship pitch, within the interval 0.12–0.4 Hz, depending on the type and tonnage of a ship.

(iii) The coefficient of modulation by roll and pitch increases monotonically with the growth of the degree of sea roughness.

Taking these facts into account, the noise modulation by roll and pitch can be represented in a form analogous to the model of the shaft–blade modulation [Eq. (2)]:

$$U_{\mathrm{RPM}}(f,t) = m_{\mathrm{RPM}}(f)\cos[2\pi(F_{\mathrm{RPM}}t + \delta F_{\mathrm{RPM}}(t)/F_{\mathrm{RPM}}) + \varphi_{\mathrm{RPM}}(f)], \quad (7)$$

where F_{RPM} is the average frequency of the ship roll or pitch in hertz, $\delta F_{\mathrm{RPM}}(t)$ is the centered normal process describing the frequency fluctuations of roll or pitch, $m_{\mathrm{RPM}}(f)$ is the frequency dependence of the coefficient of modulation by roll or pitch, and $\varphi_{\mathrm{RPM}}(f)$ is the frequency dependence of the initial phase of modulation by roll or pitch.

To separate this type of modulation, the same device was used as for the separation of shaft–blade modulation (Fig. 1). The processing of magnetic records of ship noise for studying the parameters of modulation by roll and pitch was conducted using the same technique (with the corresponding changes in the frequency range).

The analysis of the processing results led to the following conclusions.

—The frequency bandwidth of the modulating process in the case of modulation by roll and pitch lies within the interval 0.01–0.12 Hz. It was impossible to determine the dependence of the width of the modulating process on the sea roughness and the ship type.

—All frequencies of the studied frequency range 50 Hz–10 kHz are subjected to modulation by roll and pitch. The coefficient of modulation by roll and pitch strongly depends on the sea roughness and the carrier frequency.

—In the case of sea roughness within Beaufort 3–6, the mathematical expectation of the frequency dependences of the coefficient of modulation by roll and pitch and its rms deviation is well approximated by the dependences

$$M\{m_{\mathrm{RPM}}(f)\} = [9.5 + 15.5\log(f_{\mathrm{kHz}})]\times 10^{-2},$$
$$0.05 < M\{\sigma_{\mathrm{RPM}}(f)\} < 0.07.$$

—In the carrier frequency band 0.5–8 kHz, the mathematical expectation of the coefficient of modulation by roll and pitch and its rms deviation depending on sea roughness have the form

$$M\{m_{\mathrm{RPM}}(W)\} = 0.043W,$$
$$0.04 < M\{\sigma_{\mathrm{RPM}}(W)\} < 0.06.$$

—The modulation of all carrier frequencies by roll and pitch occurs in phase, which allows one to set the term $\varphi_{\mathrm{RPM}}(f)$ in Eq. (7) equal to zero.

REFERENCES

1. R. J. Urick, *Principles of Underwater Sound* (McGraw-Hill, New York, 1975; Sudostroenie, Leningrad, 1978).
2. A. K. Novikov, *Statistical Measurements in Ship Underwater Acoustics* (Sudostroenie, Leningrad, 1985).
3. W. S. Burdic, *Underwater Acoustic System Analysis* (Prentice Hall, New York, 1984; Sudostroenie, Leningrad, 1988).
4. J. G. Lourence and M. W. Coetzer, in *Proceedings of ICASSP-87* (IEEE, 1987).
5. J. G. Lourence, in *Undewater Acoustic Data Processing*, Ed. by Y. T. Chan (NATO Adv. Study Inst., 1989).
6. P. T. Arveson and D. J. Vendittis, J. Acoust. Soc. Am. **107**, 118 (2000).
7. A. A. Kharkevich, *Spectra and Analysis* (Nauka, Moscow, 1973).
8. V. I. Bunimovich, *Fluctuation Processes in Radio Receivers* (Sovetskoe Radio, Moscow, 1951).
9. L. M. Gel'man, Radiotekhnika (Moscow) **36** (1), 74 (1981).

Translated by M. Lyamshev

Acoustical Physics, Vol. 49, No. 2, 2003, pp. 189–192. Translated from Akusticheskiĭ Zhurnal, Vol. 49, No. 2, 2003, pp. 229–232.

Sound Velocity Dispersion and Second Viscosity in Media with Nonequilibrium Chemical Reactions

N. E. Molevich

Korolev State Aerospace Institute, Moskovskoe sh. 34, Samara, 443086 Russia

e-mail: molevich@mb.ssau.ru

Received December 29, 2000

Abstract—Propagation of acoustic waves in chemically nonequilibrium media is considered. It is demonstrated that the inversion of both sound velocity dispersion and second viscosity is possible in these media.

It is common knowledge that, in media with chemical reactions, the equilibrium velocity of sound u_0 differs from the "frozen" one u_∞. The dispersion of sound in media with reversible equilibrium reactions has been much investigated [1–4], and it was found that such media always satisfy the inequality $u_0 < u_\infty$. The same conclusion immediately follows from the Le Chatelier principle [5]. The formula for the equilibrium velocity of sound was derived in [6, 7]. The absorption of sound of frequency ω in such media is characterized by the damping decrement

$$\alpha = \frac{\omega^2 \mathrm{Re}\xi(\omega)}{2\rho_0 u_S^3(\omega)}, \tag{1}$$

where ρ_0 is the stationary density of the medium, ξ is the complex second viscosity due to the chemical "relaxation" process [5], u_S is the velocity of sound, and $\mathrm{Re}\xi$ is the real part of ξ. In Eq. (1) and in the following computations, the contributions of other dissipative processes, i.e., processes associated with the presence of shear viscosity and heat conduction in the medium, to the damping decrement are ignored.

By contrast, media with highly nonequilibrium (irreversible) reactions are known to be acoustically active with $\alpha < 0$ [8–12]. The present paper determines the sound velocity dispersion and the second viscosity for the simplest model of a medium with a nonequilibrium chemical reaction of the $A \longrightarrow B$ type. According to [11], this model can also be used for describing the acoustic properties of reacting media with more complex, branching reactions. The acoustic activity of such a medium corresponds to the inversion of the second viscosity: $\mathrm{Re}\xi < 0$. Earlier, the conditions of the second viscosity inversion were determined for a vibration excited gas [13–16], a medium with several relaxation processes [17, 18], a nonisothermic plasma [19], and a medium with a volume heat source depending on the temperature and density of the medium [20].

The initial system of gas dynamics equations has the form

$$\begin{gathered}\frac{dY}{dt} = -\frac{W}{\rho}, \quad P = \frac{\rho T}{m}, \quad \frac{d\rho}{dt} + \rho \mathrm{div}\mathbf{V} = 0, \\ \rho\frac{d\mathbf{V}}{dt} = -\nabla P, \quad C_{V\infty}\frac{dT}{dt} - \frac{T}{\rho}\frac{d\rho}{dt} = Q,\end{gathered} \tag{2}$$

where $d/dt = \partial/\partial t + \mathbf{V}\nabla$; Y is the mass fraction of the reagent A; W is the volume rate of formation of the reaction product B; $Q = HmW/\rho$ is the heat power produced in the medium (per one molecule); H is the reaction enthalpy (per unit mass of the reagent A); m is the average molecular mass; $\mathbf{V}$, T, ρ, and P are the velocity, temperature (in energy units), density, and pressure in the medium; and $C_{V\infty}$ is the frozen heat capacity at constant volume. In what follows, we assume that the stationary conditions in the medium (Y_0, T_0, P_0, ρ_0) are maintained by a transverse pumping; i.e., in the longitudinal direction (along the X axis), the stationary medium is assumed to be homogeneous, and we consider the propagation of a one-dimensional sound wave of the form $\sim\exp(ikx - i\omega t)$, where k is the wave number. Note that, when a sound wave propagates in a longitudinally inhomogeneous stationary medium, the form of the increment changes [21] and the sound velocity becomes a nonmonotone (oscillating) function of x [22]. Similar effects can also be observed in homogeneous nonstationary media [8], their role increasing for low-frequency sound.

Applying the linearization procedure to system (2), we arrive at a linear relationship between the perturbations Y', T', and ρ' in an acoustic wave

$$\frac{Y'}{Y_0} = -\frac{Q_T T'/T_0 + Q_\rho \rho'/\rho_0}{Q_Y(1 - i\omega\tau_C)} \tag{3}$$

and at a simple dispersion relation

$$\frac{\omega^2}{k^2} = \frac{T_0 C_P}{mC_V}, \tag{4}$$

where

$$C_V = \left(\frac{\partial u}{\partial T}\right)_V = C_{V\infty} + mH\left(\frac{\partial Y}{\partial T}\right)_V = \frac{C_{V0} - i\omega\tau_C C_{V\infty}}{1 - i\omega\tau_C}, \tag{5}$$

$$C_P = \left(\frac{\partial h}{\partial T}\right)_P = C_{P\infty} + mH\left(\frac{\partial Y}{\partial T}\right)_P = \frac{C_{P0} - i\omega\tau_C C_{P\infty}}{1 - i\omega\tau_C} \tag{6}$$

are the complex heat capacities of the reacting medium at constant volume and at constant pressure; u and $h = u + P/\rho$ are the internal energy and enthalpy of the medium per one molecule; $\tau_C = \rho_0 Y_0/WQ_Y$ is the characteristic time of the chemical reaction; $C_{P0} = C_{P\infty} + Y_0 Hm(Q_\rho - Q_T)/T_0 Q_Y$ and $C_{V0} = C_{V\infty} - Y_0 HmQ_T/T_0 Q_Y$ are the equilibrium (low-frequency) heat capacities in the chemically reacting medium;

$$Q_T = \partial \ln Q/\partial \ln T; \quad Q_\rho = \partial \ln Q/\partial \ln \rho; \quad Q_Y = \partial \ln Q/\partial \ln Y.$$

Dispersion relation (4) allows us to determine the sound velocity $u_S = \omega/k'$ and the damping decrement $\alpha = k''$, where k' and k'' are the real and imaginary parts of the wave number k. When the absorption within the wavelength is small ($k'' < k'$), Eqs. (4)–(6) yield expression (1), in which the second viscosity and the sound velocity have a form that is conventional for a medium with a single relaxation process [5, 17, 23, 24]:

$$\xi = \frac{\xi_0}{1 - i\omega\tau_C C_{V\infty}/C_{V0}}, \tag{7}$$

$$u_S^2 = \frac{C_{V0}^2 u_0^2 + \omega^2 \tau_C^2 C_{V\infty}^2 u_\infty^2}{C_{V0}^2 + \omega^2 \tau_C^2 C_{V\infty}^2}. \tag{8}$$

Here,

$$\xi_0 = \frac{C_{V\infty}\tau_C(u_\infty^2 - u_0^2)\rho_0}{C_{V0}} \tag{9}$$

is the low-frequency second viscosity; $u_\infty^2 = \gamma_\infty T_0/m$; $u_0^2 = \gamma_0 T_0/m$; and $\gamma_\infty = C_{P\infty}/C_{V\infty}$ and $\gamma_0 = C_{P0}/C_{V0}$ are the frozen and equilibrium adiabatic exponents.

According to Eqs. (1) and (7)–(9), the condition of sound amplification $\alpha < 0$ is satisfied when $\xi_0 < 0$, i.e., when

$$H(C_{V\infty}Q_\rho + Q_T) > 0. \tag{10}$$

As shown in [17], the latter condition means the presence of positive feedback between the acoustic perturbation and the nonequilibrium volume heat release.

If $C_{V0} > 0$ and condition (10) is satisfied, the equilibrium sound velocity u_0 is higher than the frozen one u_∞. The possible existence of conditions with $u_0 > u_\infty$ in a chemically active medium was first mentioned in [10], but the dispersion characteristics of the medium were not adequately investigated in the cited publication.

As a rule, chemical reactions are accompanied by a nonequilibrium excitation of the internal degrees of freedom of molecules. In view of this fact, we consider the acoustics of a medium in which two relaxation processes take place: a chemical process with a relaxation time τ_C [which is taken into account by the first equation of Eqs. (2)] and a vibration process

$$\frac{dE_v}{dt} = \frac{E_v^E - E_v}{\tau_v(T, \rho)} + \delta Q(Y, \rho, T), \tag{11}$$

where τ_v is the vibration relaxation time, E_v and E_v^E are the vibration energy and its equilibrium value (per molecule), and δ is the fraction of the chemical reaction energy that contributes to the vibrational states of molecules.

We supplement the system of gas dynamics equations (2) with Eq. (11) and represent the last equation of Eqs. (2) in the form

$$C_{V\infty}\frac{dT}{dt} + \frac{dE_v}{dt} - \frac{T}{\rho}\frac{d\rho}{dt} = Q.$$

Linearizing the resulting new system of equations with respect to the previously determined perturbations, we obtain dispersion relation (4) with complex heat capacities, which are expressed as

$$C_V = \left(\frac{\partial u}{\partial T}\right)_V = C_{V\infty} + \left(\frac{\partial E_v}{\partial T}\right)_V + mH\left(\frac{\partial Y}{\partial T}\right)_V = \frac{C_{V0} - i\omega\tau_v C_{VC} - i\omega\tau_C C_{Vv} - \omega^2\tau_C\tau_v C_{V\infty}}{(1 - i\omega\tau_v)(1 - i\omega\tau_C)}, \tag{12}$$

$$C_P = \left(\frac{\partial h}{\partial T}\right)_P = C_{P\infty} + \left(\frac{\partial E_v}{\partial T}\right)_P + mH\left(\frac{\partial Y}{\partial T}\right)_P = \frac{C_{P0} - i\omega\tau_v C_{PC} - i\omega\tau_C C_{Pv} - \omega^2\tau_C\tau_v C_{P\infty}}{(1 - i\omega\tau_v)(1 - i\omega\tau_C)}. \tag{13}$$

Here, $C_{Vv} = C_{V\infty} + C_v + S\tau_T$ and $C_{Pv} = C_{P\infty} + C_v + S(\tau_T - \tau_\rho)$ are the heat capacities of vibrationally excited gas [13] that are frozen with respect to the chemical equilibrium; $S = \delta Q\tau_v/T_0$ is the degree of vibrational nonequilibrium;

$$C_v = \partial E_v^E/\partial T; \quad \tau_T = \partial \ln \tau_v/\partial \ln T; \quad \tau_\rho = \partial \ln \tau_v/\partial \ln \rho;$$

$$C_{V0} = C_{Vv} - mHY_0Q_T/T_0Q_Y,$$
$$C_{P0} = C_{Pv} + mHY_0(Q_\rho - Q_T)/T_0Q_Y$$

are the equilibrium heat capacities of the chemically active medium under consideration; and

$$C_{VC} = C_{V\infty} - mHY_0(1-\delta)Q_T/T_0Q_Y,$$
$$C_{PC} = C_{P\infty} + mHY_0(1-\delta)(Q_\rho - Q_T)/T_0Q_Y$$

are the heat capacities of the chemically active medium that are frozen with respect to the vibration excitation.

Using Eqs. (12) and (13), we determine the damping decrement $\alpha = k''$ in the form of Eq. (1) (for the case of $k'' \ll k'$), in which

$$\begin{aligned}\mathrm{Re}\xi = P_0\{&\tau_v(C_{V0}C_{PC} - C_{P0}C_{VC}) \\ &+ \tau_C(C_{V0}C_{Pv} - C_{P0}C_{Vv}) \\ &+ \omega^2\tau_C\tau_v[\tau_C(C_{P\infty}C_{Vv} - C_{V\infty}C_{Pv}) \\ &+ \tau_v(C_{P\infty}C_{VC} - C_{V\infty}C_{PC})]\}/Z,\end{aligned} \tag{14}$$

$$\begin{aligned}u_S^2 = \frac{T_0}{m}[&(C_{P0} - C_{P\infty}\omega^2\tau_C\tau_v)(C_{V0} - C_{V\infty}\omega^2\tau_C\tau_v) \\ &+ (C_{PC}\omega\tau_v + C_{Pv}\omega\tau_C)(C_{VC}\omega\tau_v + C_{Vv}\omega\tau_C)]/Z,\end{aligned} \tag{15}$$

$$Z = (C_{V0} - C_{V\infty}\omega^2\tau_C\tau_v)^2 + \omega^2(C_{VC}\tau_v + C_{Vv}\tau_C)^2.$$

In the high-frequency limit ($\omega^2\tau_C\tau_v \gg 1$) at $\delta \approx 1$, expressions (14) and (15) are simplified:

$$\mathrm{Re}\xi = \frac{C_{Vv}(u_\infty^2 - u_v^2)\rho_0}{C_{V\infty}\omega^2\tau_v}, \tag{16}$$

$$u_S = u_\infty, \tag{17}$$

where $u_v = (C_{Pv}T_0/C_{Vv}m)^{1/2}$.

According to Eqs. (16) and (17), high-frequency sound propagates with a velocity that is frozen with respect to both chemical equilibrium and vibration excitation. The amplification condition for this sound ($\alpha < 0$) is realized when $\mathrm{Re}\xi < 0$, i.e., when $S(C_{V\infty}\tau_\rho + \tau_T) + C_v < 0$. In this case, the effect of the chemical reaction on the acoustics of the medium manifests itself only through the degree of vibrational nonequilibrium S.

In the opposite limit ($\omega^2\tau_C\tau_v \ll 1$), sound propagates with the equilibrium velocity u_0, and the damping decrement is expressed as

$$\alpha = \frac{\omega^2\xi_{0\Sigma}}{2\rho_0 u_0^3}.$$

Here, the coefficient $\xi_{0\Sigma}$ is the sum of two low-frequency second viscosities formed by the chemical and vibrational relaxation processes:

$$\begin{aligned}\xi_{0\Sigma} &= \xi_{0v} + \xi_{0C} \\ &= \frac{\rho_0\tau_vC_{V\infty}(u_\infty^2 - u_0^2)}{C_{V0}} + \frac{\rho_0\tau_CC_{Vv}(u_v^2 - u_0^2)}{C_{V0}}.\end{aligned}$$

The inversion of the coefficients ξ_{0v} and ξ_{0C} occurs when the following conditions are satisfied:

$$S(C_{V\infty}\tau_\rho + \tau_T) + C_v - \frac{mHY_0}{T_0Q_Y}(C_{V\infty}Q_\rho + Q_T) < 0,$$

$$H[Q_T(C_{Pv} - C_{Vv}) + C_{Vv}Q_\rho] > 0,$$

respectively.

The dispersion characteristics obtained above for media with highly nonequilibrium chemical reactions testify that these media have essentially new acoustic properties, as compared to equilibrium media. Presumably, it is just the presence of nonequilibrium relaxation processes that is responsible for the discrepancy revealed in [25] between the high experimental value of the equilibrium velocity of the sound wave following a detonation wave and the theoretical value of u_0 calculated by the method described in [7].

ACKNOWLEDGMENTS

I am grateful to L.G. Gvozdeva for discussing this paper.

REFERENCES

1. A. Einstein, *Sitzungsberichte* (Akad. Wiss., Berlin, 1920).
2. Ya. Zel'dovich, Zh. Éksp. Teor. Fiz. **16** (4), 365 (1946).
3. W. W. Wood and J. G. Kirkwood, J. Appl. Phys. **28** (4), 395 (1957); in *Gas Dynamics and Heat Transfer in The Presence of Chemical Reactions*, Ed. by V. P. Motulevich and V. P. Ionov (Inostrannaya Literatura, Moscow, 1962).
4. J. F. Clarke and M. McChesney, *The Dynamics of Real Gases* (Butterworths, London, 1964; Mir, Moscow, 1967).
5. L. D. Landau and E. M. Lifshitz, *Course of Theoretical Physics*, Vol. 6: *Fluid Mechanics* (Nauka, Moscow, 1986; Pergamon, New York, 1987).
6. P. S. Epshteĭn, *Course of Thermodynamics* (OGIZ, Moscow, 1948).
7. E. V. Stupochenko, I. P. Stakhanov, E. V. Samuĭlov, *et al.*, in *Physical Gas Dynamics* (Akad. Nauk SSSR, Moscow, 1959), pp. 3–38.
8. T.-Y. Toong, Combust. Flame **18** (2), 207 (1972).
9. C. A. Garris, T.-Y. Toong, and J.-P. Patureau, Acta Astron. **2**, 981 (1975).
10. A. A. Borisov, in *Research in Hydrodynamics and Heat Transfer* (Inst. Teor. Fiz. Sib. Otd. Akad. Nauk SSSR, Novosibirsk, 1976), pp. 94–95.
11. G. E. Abouseif, T.-Y. Toong, and J. Converti, in *Proceedings of 17th International Symposium on Combustion* (Univ. of Leeds, England, 1978), p. 1341.

12. R. M. Detsch and H. E. Bass, J. Acoust. Soc. Am. **77**, 512 (1985).
13. E. Ya. Kogan and N. E. Molevich, Zh. Tekh. Fiz. **56** (5), 941 (1986) [Sov. Phys. Tech. Phys. **31**, 573 (1986)].
14. A. I. Osipov and A. V. Uvarov, Vestn. Mosk. Univ., Ser. 3: Fiz., Astron. **28** (6), 52 (1987).
15. V. N. Malnev, Preprint No. ITP-92.21E (ITP, Kiev, 1992).
16. V. N. Malnev and A. V. Nedospasov, in *Perspectives of MHD Plasma Technologies in Aerospace Applications* (Inst. Vys. Temp. Ross. Akad. Nauk, Moscow, 1999), pp. 128–130.
17. N. E. Molevich and A. N. Oraevskiĭ, Tr. Fiz. Inst. im. P.N. Lebedeva, Akad. Nauk SSSR **222**, 45 (1992).
18. N. E. Molevich and V. E. Nenashev, Akust. Zh. **46**, 520 (2000) [Acoust. Phys. **46**, 450 (2000)].
19. I. P. Zavershinskiĭ, E. Ya. Kogan, and N. E. Molevich, Akust. Zh. **38**, 702 (1992) [Sov. Phys. Acoust. **38**, 387 (1992)].
20. N. E. Molevich and A. N. Oraevskiĭ, Zh. Éksp. Teor. Fiz. **94** (3), 128 (1988) [Sov. Phys. JETP **67**, 504 (1988)].
21. N. E. Molevich, Akust. Zh. **47**, 96 (2001) [Acoust. Phys. **47**, 102 (2001)].
22. N. Cretu, P. P. Delsanto, G. Nita, *et al.*, J. Acoust. Soc. Am. **104**, 57 (1998).
23. Ya. B. Zel'dovich and Yu. P. Raĭzer, *Physics of Shock Waves and High-Temperature Hydrodynamic Phenomena* (Nauka, Moscow, 1963; Academic, New York, 1966 and 1967), Vols. 1 and 2.
24. M. A. Isakovich, *General Acoustics* (Nauka, Moscow, 1973).
25. T. V. Bazhenova, L. G. Gvozdeva, Yu. P. Lagutov, V. N. Lyakhov, Yu. M. Faresov, and V. P. Fokeev, *Nonstationary Interactions of Shock and Detonation Waves in Gases* (Nauka, Moscow, 1986).

Translated by E. Golyamina

Acoustical Physics, Vol. 49, No. 2, 2003, pp. 193–202. Translated from Akusticheskiĭ Zhurnal, Vol. 49, No. 2, 2003, pp. 233–244.

Adaptive Neuro-Fuzzy and Fuzzy Decision Tree Classifiers As Applied to Seafloor Characterization[1]

A. Stepnowski, M. Moszyński, and Tran Van Dung

Department of Remote Sensing Systems, Gdańsk University of Technology, ul. Narutowicza 11/12, Gdańsk, 80-952 Poland

e-mail: astep@pg.gda.pl

Received October 21, 2002

This paper is dedicated to the memory of the outstanding Russian acoustician and my dear friend and colleague Professor Leonid M. Lyamshev.

Abstract—This paper investigates the influence of various backscattered echo parameters collected at an echosounder frequency of 200 kHz on the performance of the neuro-fuzzy and fuzzy decision tree classifiers of a seabed. In particular, the wavelet coefficients of the bottom echo were investigated along with other echo parameters like energy, amplitude, slope of the falling part of the echo, etc. The data were processed in an Adaptive Neuro Fuzzy Inference System (ANFIS), which was implemented in two multistage structures, viz.; Incremental Fuzzy Neural Network (IFNN) and Aggregated Fuzzy Neural Network (AFNN). The number of input parameters for the networks was reduced by using the Principal Component Analysis (PCA). A fuzzy decision tree algorithm was developed and used directly (without PCA data reduction) in the classification procedure utilizing the same data. The performances of both approaches were analyzed and compared. © *2003 MAIK "Nauka/Interperiodica"*.

INTRODUCTION

In the last two decades, acoustic methods for seafloor classification, as they are non-invasive, faster, and more cost effective than other methods, have become well-recognized and useful tools in rapid geological analysis and bottom sediment mapping. Creating automatic methods of bottom typing based on analysis of sea-bed echoes has become one of the main challenges in this field. In recent years, the most advanced acoustic techniques that use swath-beam geometry (side-scan sonar [1] and multibeam sonar [2]) have been successfully introduced for imaging and classifying the bottom. However, the conventional methods of normal incidence, which utilize the bottom backscatter from a single-beam echosounder, are still in use due to their simplicity and versatility. These methods can be roughly categorized as follows:

—measurement of the first and second bottom echo (Roxann) [3];

—comparison of bottom echo shape with patterns obtained from backscatter theoretical models [4];

—techniques using wideband (chirp) signals and parametric arrays [5–7];

—analysis of various parameters of the bottom echo (spectral, statistical, time-frequency, wavelet coefficients, fractal dimension, etc.) [4, 8, 9, 10, 22];

—analysis of the bottom echo using expert systems and neural networks [6, 11].

In general, the performance of the methods and their generalization ability increases concurrently with the number of input parameters or dimensionality of the input vector space [11, 12]. This feature is specifically characteristic of the class of artificial intelligence methods and, in particular, neuro-fuzzy methods [11], which were successfully adapted to seabed recognition systems in recent years.

In such a context, one of the objectives of the paper was to investigate the possibility of reducing the redundant number of input parameters without decreasing the quality of the seafloor classification from acoustic echoes.

This sort of feasibility study was carried out using two neuro-fuzzy structures, viz., IFNN and AFNN. These neuro-fuzzy classifiers processed the set of data consisting of wavelet coefficients derived from the bottom echoes along with several other echo parameters. As was shown in [10], the performance of such an approach in the classification schemes is better than that of conventional time-domain methods. The redundancy of the input parameter's vector space was reduced by applying the Principal Component Analysis (PCA).

Decision trees are one of the most popular choices for learning and reasoning from feature-based examples. They have undergone a number of alterations to

[1] This paper was submitted by the author in English.

1063-7710/03/4902-0193$24.00 © 2003 MAIK "Nauka/Interperiodica"

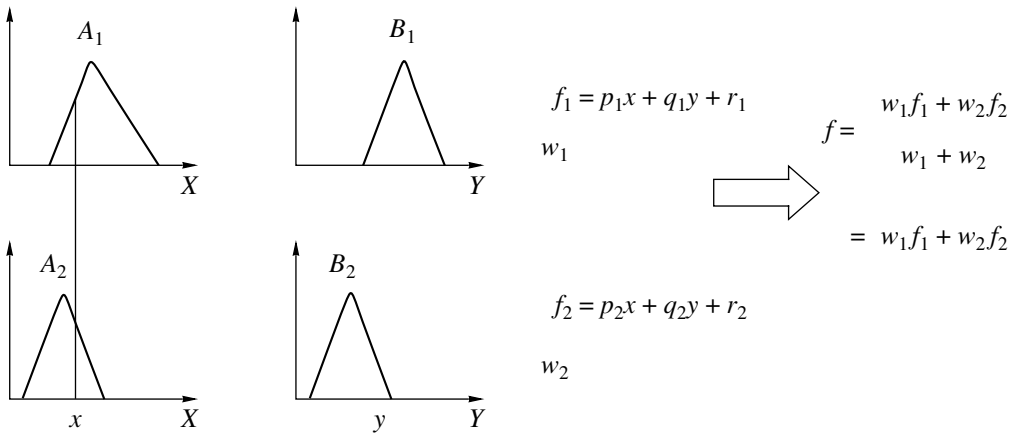

Fig. 1. The membership function and the rules of the Sugeno fuzzy model.

deal with language and measurement uncertainties. The paper presents another modification aimed at combining symbolic decision trees with the approximate reasoning offered by fuzzy representation. The intent is to exploit complementary advantages of both: the popularity in applications to learning from examples and the high knowledge comprehensibility of decision trees and the ability to deal with inexact and uncertain information of fuzzy representation [21]. Fuzzy decision trees combine approximate reasoning and fuzzy functions. The fuzzy decision tree constructed makes use of the information contained in the tree to deal with new samples presented for classification.

A special fuzzy decision tree algorithm was developed for seafloor characterization from acoustic echoes as an alternative to the neuro-fuzzy approach. The performances of both approaches were investigated concurrently.

ADAPTIVE NEURO-FUZZY INFERENCE SYSTEMS

The Adaptive Neuro-Fuzzy Inference System (ANFIS) [17] investigated in the paper is based on the Sugeno fuzzy model, which was proposed in an effort to develop a systematic approach to generating fuzzy rules from a given input–output data set that has a fuzzy rule of the form

$$\text{if } x \text{ is } A \text{ and } y \text{ is } B, \text{ then } z = f(x, y), \qquad (1)$$

where $z = f(x, y)$ is a classical function in a consequent of the rule. Usually $f(x, y)$ is a polynomial in the input variables x and y. When $f(x, y)$ is a first-order polynomial, the resulting fuzzy inference system (FIS) is called a first-order Sugeno fuzzy model [16], whose membership function and rules are depicted in Fig. 1. Since each rule has a crisp output (by contrast to the fuzzy output), the overall output is obtained via a weighted average.

The ANFIS system is a generalization of the FIS, which is able to derive the optimal shapes of membership functions and a number of fuzzy rules from the given data sets. The structure of this neuro-fuzzy version is "hidden" in the neural network, and, therefore, the system adapts its parameters in the learning process. An example of the two-input Sugeno ANFIS model architecture is shown in Fig. 2.

In Sugeno ANFIS architecture, consecutive layers are dedicated to different tasks. Layers 1 and 2 realize promises of rules, layer 3 a part of inferences, and layers 4 and 5 a process of sharpening. The parameters of fuzzy sets A_1, A_2, B_1, B_2 in layer 1 and the parameters of inferences in layer 3 are modified in the process of learning.

The characteristic feature of the Sugeno ANFIS model is that the output is calculated by combining the firing strengths of the consequence. Therefore the process of defuzzification is not needed, as the output value is represented by a crisp number and not a fuzzy set. In multistage systems, it leads to additional computations, as the intermediate results of one stage, expressed as crisp values, must firstly be fuzzified before passing to the next classifier's stage.

The basic IFNN structure is depicted in Fig. 3. The input variables have been divided into M sets, and each of them is fed to an individual reasoning stage (module), which corresponds to a single-stage ANFIS. Therefore, there are totally M single-stage ANFIS models involved in a serial manner, and the fuzzy inference is carried out stage by stage [18]. The variable $y^{(k)}$ ($k < M$) is the intermediate variable that represents the output from stage k, as well as the input to stage $k + 1$. All the intermediate variables are located in the same universe of discourse as the output variable $y^{(M)}$. The decision is later fine-tuned by considering more and more factors, until the final decision corresponding to the output variable is undertaken.

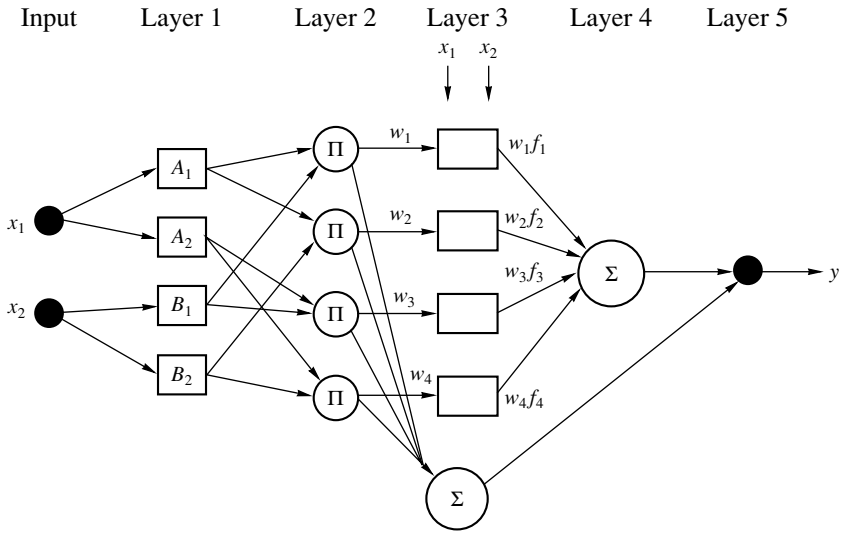

Fig. 2. ANFIS architecture for a two-input first-order Sugeno fuzzy model.

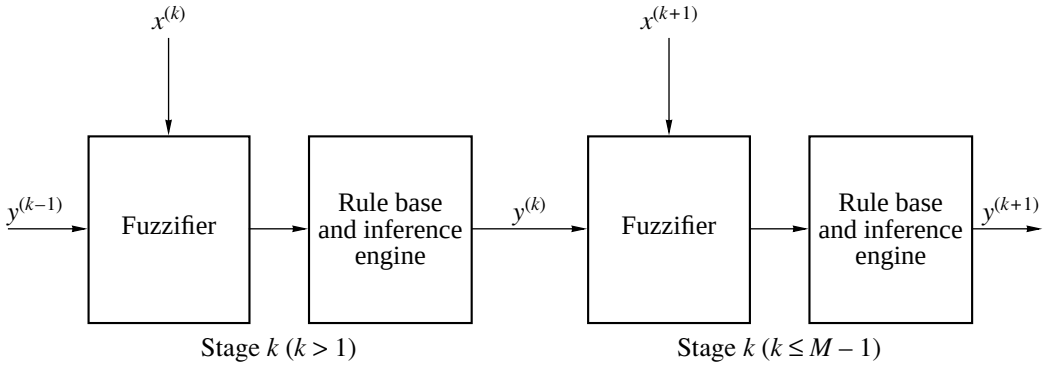

Fig. 3. IFNN architecture adopted for a multistage system, as applied for bottom typing.

As this model is based on the Sugeno ANFIS model, the jth fuzzy rule in stage $k > 1$ has the following form [17]:

$$\text{Rule}_j^k\text{: If } (x_1^{(k)} \text{ is } A_{1,j}^{(k)}, \ldots, \text{and } x_{n_k}^{(k)} \text{ is } A_{n_k,j}^{(k)})$$

$$\text{and } (y^{(k-1)} \text{ is } B_j^{(k-1)}), \qquad (2)$$

$$\text{then } y^{(k)} = c_{n_k+1,j}^{(k)} y^{(k-1)} + \sum_{i=1}^{n_k} c_{i,j}^{(k)} x_i^{(k)} + c_{0,j}^{(k)},$$

where $x_i^{(k)}$ is the ith input variable in stage k, $A_{i,j}^{(k)}$ is the linguistic label of the ith input variable appearing in the jth rule of stage k, n_k is the number of input variables used in stage k, $y^{(k)}$ is the single output variable in stage k, $B_j^{(k-1)}$ is the fuzzy term of $y^{(k-1)}$ in the jth rule of stage k, and $c_{i,j}^{(k)}$ are the consequent parameters in stage k.

DECISION TREES AND FUZZY DECISION TREES

In classical and fuzzy decision trees, samples with a known classification are used to build a tree. A decision tree has a root, nodes, and leaves (one leaf indicates one class). A decision node is a leaf or specifies some test to be carried out on a single attribute value, with one branch. The tree building is based on recursive partitioning. The most popular partitioning algorithms are ID3 [19] and CART [20]. In ID3, the attribute that has the maximal information gain is selected to split a node. A new sample is classified according to the classification of the leaf that it reaches. In a classical (not fuzzy) decision tree, a training example's membership in a node is binary.

A fuzzy tree may have leaves with nonunique classifications of its examples. Fuzzy trees make use of membership functions for attributes. The membership function of a classical set for a selected argument has a value of 0 or 1, whereas the membership function of a

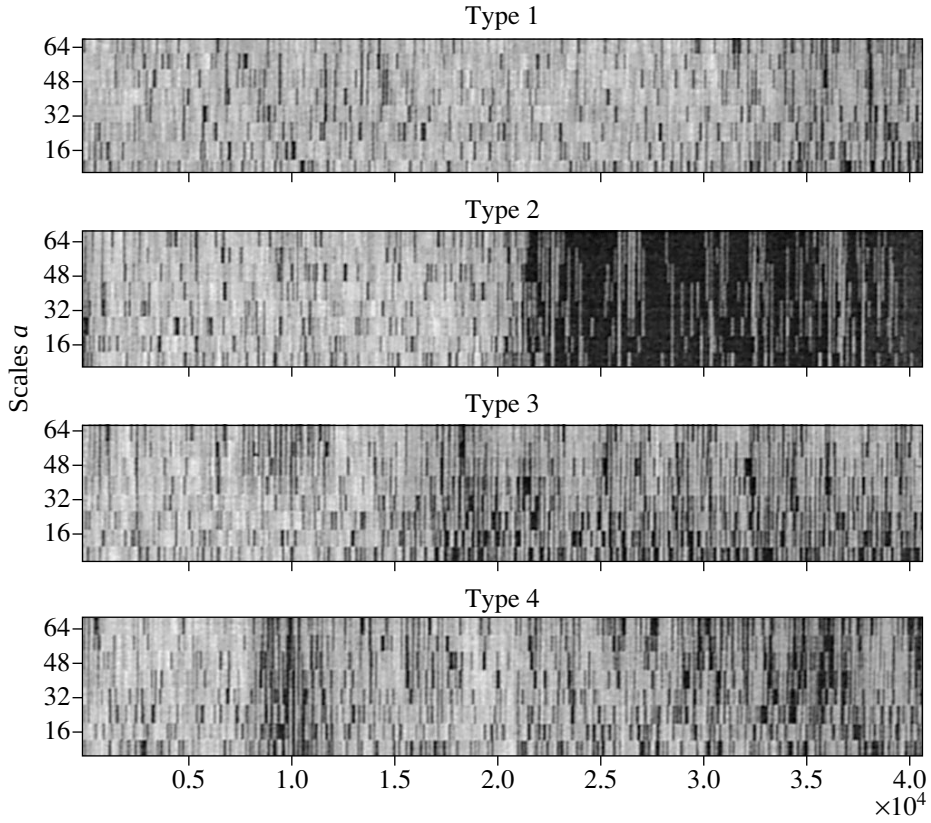

Fig. 4. Continuous Wavelet Transform of 160 consecutive echoes from four different bottom types.

fuzzy set has a value between 0 and 1. In practice, these functions are trapezoidal- or triangular-shaped. In this paper, we use triangular-shaped membership functions for attributes. To build a fuzzy decision tree and a decision procedure for dealing with new samples presented for classification, the procedure proposed in [21] was used. Splitting a node into subnodes uses fuzzy functions and fuzzy logic. As in classical trees, the maximal information gain criterion is selected to split a node. Example counts uses the function that determines the degree of satisfaction of a consequent. Memberships for subnodes are computed using fuzzy functions. The decision procedure for dealing with new samples makes use of fuzzy decision trees. Inferences using fuzzy logic based on the information contained in leaves whose restrictions are satisfied by the sample were applied.

DATA PREPROCESSING

Generally, the data used in the bottom classification constitutes the sets of seabed echoes acquired during the acoustical survey. However, in order to achieve a compact representation of the echoes, some parameters are extracted from the waveforms. In particular, by using Wavelet Transform, the Wavelet coefficients are obtained. All the parameters are subjected to further data processing by applying the Principal Component Analysis (PCA) in order to obtain a data reduction.

Wavelet Analysis

The well-known techniques for signal analysis are based on Fourier or Fourier-derived transforms, which convert the signal waveform in the time domain to its spectrum in the frequency domain. For a broad class of signals, Fourier analysis is extremely useful, because the frequency content of the signal is of great importance. However, when transforming to the frequency domain, the time information is lost. Many interesting signals contain numerous nonstationary or transient characteristics, which are the most important part of the signal, and Fourier analysis is not suited to detecting them. To overcome this deficiency, the technique based on windowing a small section of the signal at a time may be used. The wavelet analysis represents a particular windowing technique that uses variable-sized regions, which allows us to use longer time intervals for more precise extraction of low-frequency information and shorter intervals for high-frequency information. Mathematically, the continuous wavelet transform (CWT) of the signal $x(t)$ is defined as a projection of a signal x on a family of zero-mean functions derived

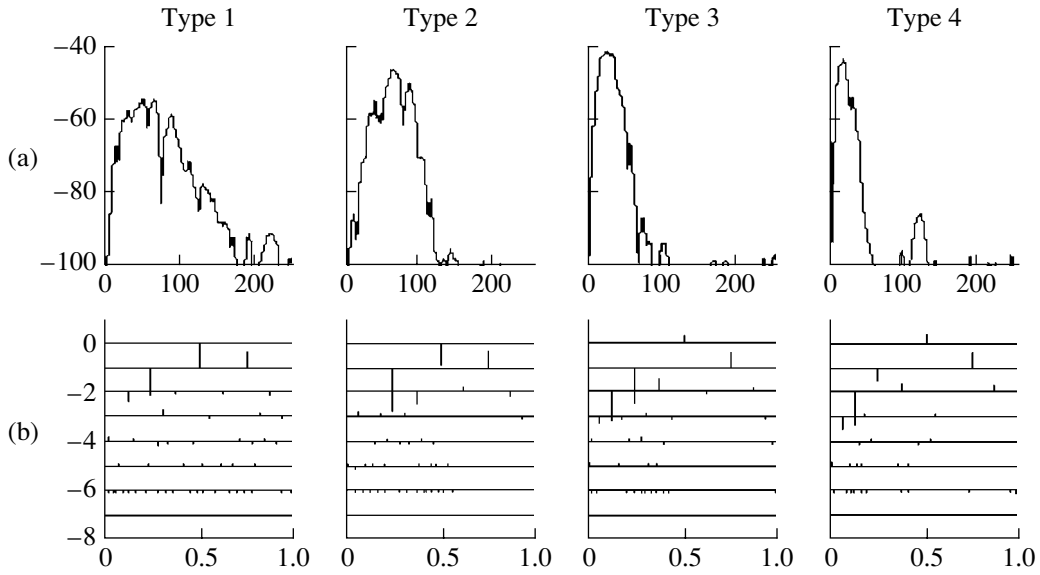

Fig. 5. (a) Sample echo envelopes of four bottom types and (b) their corresponding wavelet coefficients.

from an elementary function (mother wavelet) by translations and dilations [13, 14]:

$$C(a, b) = \int_{-\infty}^{\infty} x(t)\psi(a, b, t)dt, \quad (3)$$

where $C(a, b)$ is the set of wavelet coefficients, $\psi(a, b, t) \equiv \frac{1}{\sqrt{a}}\psi\left(\frac{t-b}{a}\right)$ is the wavelet function, a is a variable representing the scale, and b is a variable representing the position. By definition, the wavelet transform is more a time-scale than time-frequency representation. However, for wavelets that are well localized around a non-zero frequency f_0 at a scale $a = 1$, a time-frequency interpretation is possible due to the formal identification $f = f_0/a$.

The Wavelet Transform demonstrates its usefulness in a variety of applications [13, 14]. It seems to be also a well suited and attractive tool for the recognition of seabed type from acoustic echoes. Figure 4 represents the CWT of echoes from the data set representing four different bottom types received from an echosounder operating at 200 kHz.

The Continuous Wavelet Transform is a time consuming operation, so, for actual implementation, the discrete version of this transform can be used. The Discrete Wavelet Transform (DWT) is defined similarly as

$$C(j, k) = \sum_{n=0}^{N-1} x(n)\psi_{j,k}(n), \quad (4)$$

where $C(j, k)$ is the set of discrete wavelet coefficients, $\psi_{j,k}(n) \equiv 2^{-j/2}\psi(2^{-j}n - k)$ is a wavelet filter constructed from the wavelet function $\psi(\cdot)$, and N is the signal length. Note that, in this definition, the variables a and b, representing the position and scale from Eq. (3), are replaced by the indices j and k related to these variables by dyadic relations: $a = 2^j$ and $b = k2^j$. Sample results of the discrete Wavelet Transform in the computations of Wavelet coefficients are presented in Fig. 5 in the form of echo envelopes for four bottom types (Fig. 5a) and the corresponding four sets of discrete wavelet coefficients (Fig. 5b).

Principal Component Analysis

To select which of the above-mentioned parameters of the echoes backscattered from the seabed is most useful in the classification process as the input parameter, we applied the Principal Component Analysis (PCA) [9]. The PCA is especially useful for simplifying the interpretation of highly multivariate data sets by reducing the number of variables.

The defining characteristic of this method is that it aims to understand a data set by considering a group of variables together rather than focusing on only one variable at a time. The method generates a new set of variables (principal components), each of which is a linear combination of the original variables. All the principal components are orthogonal to each other, so that there is no redundant information.

Mathematically, Y_1 and Y_2 are the first and second principal components of the variable vector X if $Y_1 = a_1^T X$ and $Y_2 = a_2^T X$. The vector a_1 is the solution to the equation $a_1^T Sa_1 = \max a^T Sa$, where $a^T a = 1$, and a_2 is the

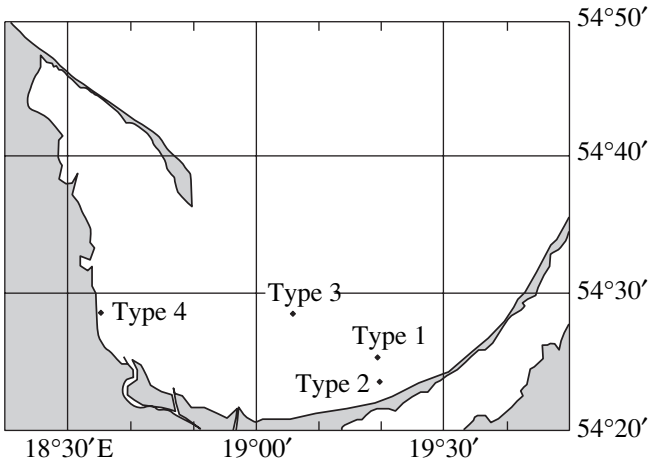

Fig. 6. Map of the Gulf of Gdansk with the sites of acquired acoustic data.

solution of equation $a_2^T Sa_2 = \max a^T Sa$, where $a^T a = 1$ and $a^T Sa_1 = 0$.

In this case, $S = \frac{1}{n}\sum_{i=1}^{n}(x_i - \bar{x})(x_i - \bar{x})^T$ is a covariance matrix of the vector X, and a_1 and a_2 are the eigenvectors of the 1st and 2nd principal values. It appears that the first principal component is a single axis in space. When one projects each observation on this axis, the resulting values form a new variable. The variance of this variable is the maximum among all possible choices of the first axis. The PCA can evaluate the degree of importance of each input variable by weights in the first column (1st principal component). The input variable, which has the largest weight, contains the most information.

RESULTS

The experimental data were acquired from the acoustic surveys carried out in the Southern Baltic using a single-beam digital echosounder DT4000. The echosounder was operating at a frequency of 200 kHz with a pulse duration of 0.3 ms. The acquisition sampling rate for this system was 41.66 kHz, which was equivalent to acquiring around 56 samples per meter. The 3-dB beamwidth of the transducer was 6°. The echosounder was equipped with a digital Time Varied Gain (TVG) feature that had standard "20logR" and "40logR" characteristics. For the experiment, only data obtained from the anchored vessel in the same location for each bottom type and each frequency was further investigated in order to assure more reliable groundtruthing information. To make sure that the data collected at different frequencies came from the same sites, so that the echoes corresponded to identical types of sediment, the geographical position of the vessel recorded by GPS was carefully checked. The ground truth was obtained by a camera. Four types of sediments were represented in the collected data and called as follows: type 1 for mud, type 2 for fine- and medium-grained sand, type 3 for medium-grained sand and type 4 for gravel, hetero-grained sand, and rock.

Figure 6 presents the sample chart of the Gulf of Gdańsk, where the acoustic surveys were carried out, with sampling sites for each bottom type. Figure 7 represents a sample of the bottom echo envelope acquired by the DT4000 echosounder from a type-l bottom in a screen dump of the VBT Seabed Classifier system developed by the authors.

A set of parameters was extracted from each digitized bottom echo:

(1) eight first wavelet coefficients C_i;

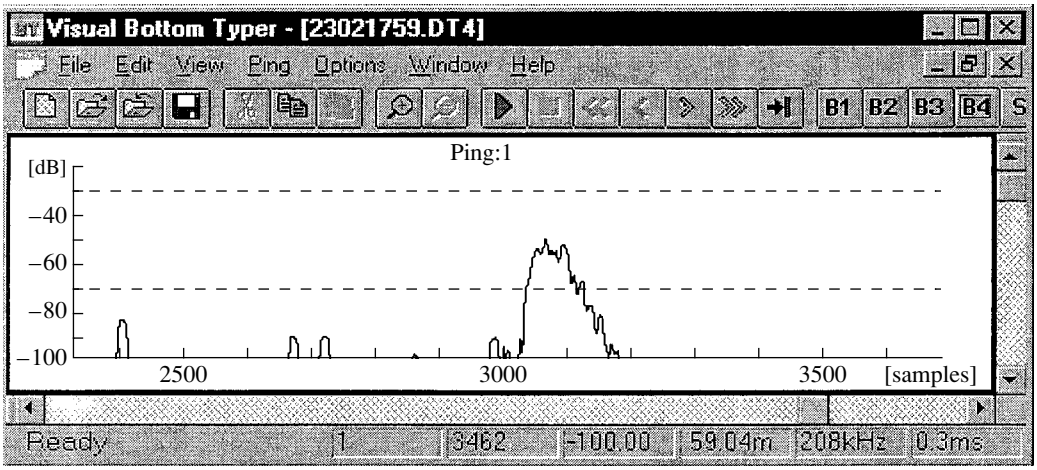

Fig. 7. Screen dump of the Seabed Classifier software with the sample bottom echo envelope.

(a)

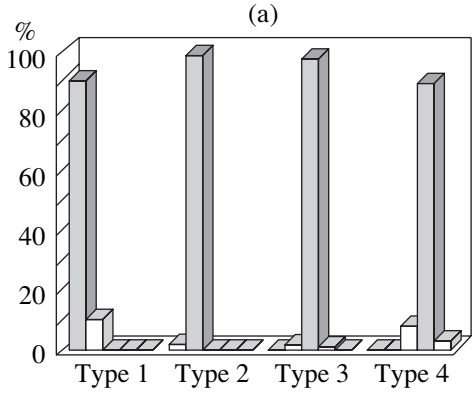

(b)

True class	Classified to *x*				
	Type 1	Type 2	Type 3	Type 4	Not known
Type 1	89.8%	10.2%	0%	0%	0%
Type 2	1.8%	98.2%	0%	0%	0%
Type 3	0%	1.7%	97.2%	1.1%	0%
Type 4	0%	0%	8%	88.9%	3.1%

Fig. 8. (a) Box diagram and (b) confusion matrix of the testing results after the 2nd stage of the IFNN system (the echo duration); the percentage of echoes correctly classified in total is 94.71%.

(a)

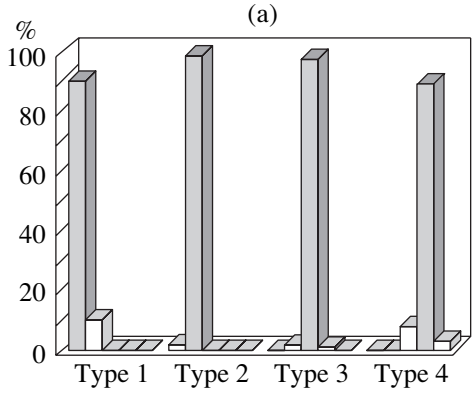

(b)

True class	Classified to *x*				
	Type 1	Type 2	Type 3	Type 4	Not known
Type 1	90.7%	9.3%	0%	0%	0%
Type 2	2.4%	96.4%	0.8%	0%	0.4%
Type 3	0.3%	1.1%	97.5%	0.8%	0.3%
Type 4	0%	0%	8%	90.7%	1.2%

Fig. 9. (a) Box diagram and (b) confusion matrix of the testing results after the 2nd stage of the AFNN system; the percentage of echoes correctly classified in total is 94.56%.

(2) sums of the absolute values of wavelet coefficients of the *i*th level, S_i;

(3) energy of the leading part of the echo, E';

(4) energy of the falling part of the echo, E';

(5) amplitude of the echo, A;

(6) echo duration, T;

(7) number of echo envelope maxima, N.

In this way, 20 parameters were extracted from the echo, where eight parameters come out from the eight first wavelet coefficients, seven parameters come out from the sums of the absolute values of wavelet coefficients (the sum of the absolute values of wavelet coefficients of the first level $S1$ is equal to the second wavelet coefficient) and five other parameters representing the echo features, as listed above. These parameters were processed from individual sea bottom echoes.

The results of the PCA are presented in the table. The PCA shows that the fifth wavelet coefficient $C5$ has the largest first principal component, and the first wavelet coefficients $C1$ have the value of the first principal component that is comparable with the echo duration T. Therefore, these parameters were chosen for further investigation.

The classifiers developed were trained on a learning set of data, and its generalization ability was checked on testing data. The learning set counted 182 records, and the testing set had 1361 records.

In the experiment, a two-stage ($k = 2$) IFNN system was built. On the bases of the parameters selected by the PCA, the coefficient $C5$ was supplied to the first stage, and, in the second stage, we experimented with feeding the system with the parameters $C1$ and T. This experiment showed that the network with T as one of the input parameters gives better results in spite of the comparable first principal component values. These results are represented as follows: In the learning process, the percentages of correctly classified echoes achieved after the 1st and 2nd stage of the classifier were 75.82 and 96.70%, respectively. In the testing phase, the percentages of correctly classified echoes obtained were 75.02% after the 1st stage and 94.71% after the 2nd stage (Fig. 8).

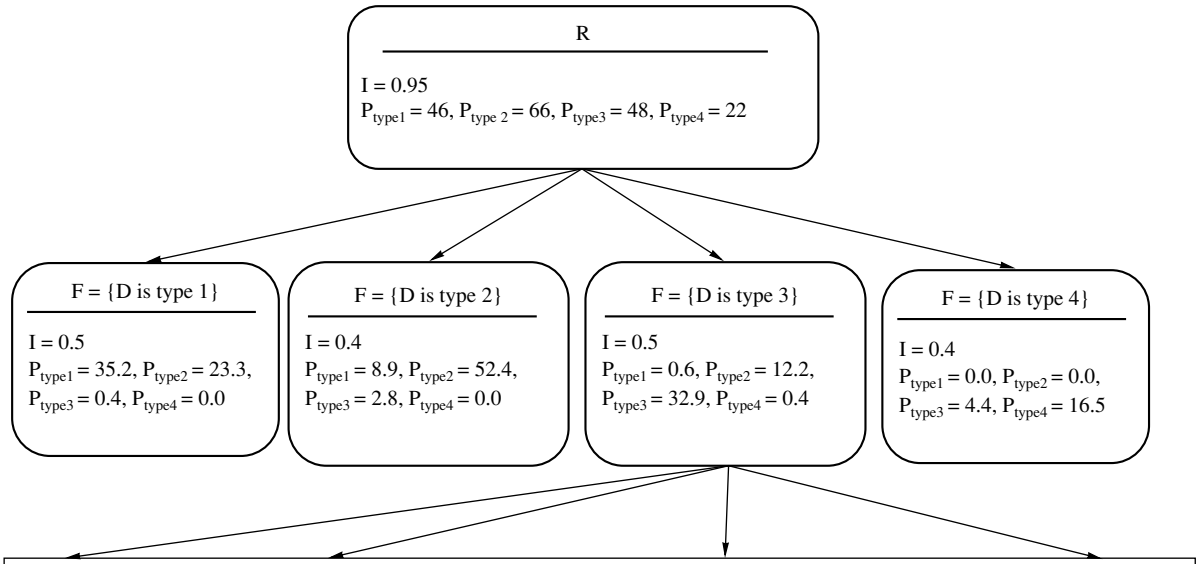


```
[] Root NumOfSplits = 1 IN = 0.95 PN = 182.00 : type1 = 46.0  type2 = 66.0  type3 = 48.0  type4 = 22.0
|**Split number: 1  Info gain: 0.5
|--[D = lingVal1]  <leaf>  IN = 0.5  PN = 59.0 : type1 = 35.2  type2 = 23.3  type3 = 0.4  type4 = 0.0
|--[D = lingVal2]  <leaf>  IN = 0.4  PN = 64.0 : type1 = 8.9  type2 = 52.4  type3 = 2.8  type4 = 0.0
|--[D = lingVal3]  NumOfSplits = 1  IN = 0.5  PN = 46.0 :  type1 = 0.6  type2 = 12.2  type3 = 32.9  type4 = 0.4
| |**Split number : 1  Info gain: 0.4
| |--[D = lingVal3] [C1 = lingVal1]  <leaf>  IN = 0.2  PN = 12.5 : type1 = 0.6  type2 = 11.7  type3 = 0.3  type4 = 0.0
| |--[D = lingVal3] [C1 = lingVal2]  <leaf>  IN = 0.2  PN = 12.1 : type1 = 0.6  type2 = 11.4  type3 = 0.1  type4 = 0.0
| |--[D = lingVal3] [C1 = lingVal3]  NumOfSplits = 1  IN = 0.1  PN = 29.8 : type1 = 0.0  type2 = 0.0  type3 = 29.3  type4 = 0.4
| | |**Split number : 1  Info gain: 0.0
| | |--[D = lingVal3] [C1 = lingVal3] [C2 = lingVal1]  <leaf>  IN = 0.0  PN = 26.7 : type1 = 0.0  type2 = 0.0  type3 = 26.7  type4 = 0.0
| | |--[D = lingVal3] [C1 = lingVal3] [C2 = lingVal2]  <leaf>  IN = 0.1  PN = 2.7 : type1 = 0.0  type2 = 0.0  type3 = 2.7  type4 = 0.0
| | |--[D = lingVal3] [C1 = lingVal3] [C2 = lingVal3]  <leaf>  IN = 0.0  PN = 26.6 : type1 = 0.0  type2 = 0.0  type3 = 26.5  type4 = 0.0
| | \--[D = lingVal3] [C1 = lingVal3] [C2 = lingVal4]  <leaf>  IN = 0.0  PN = 0.4 : type1 = 0.0  type2 = 0.0  type3 = 0.0  type4 = 0.4
| \--[D = lingVal3] [C1 = lingVal4] NumOfSplits = 1  IN = 0.1  PN = 27.1 : type1 = 0.0  type2 = 0.0  type3 = 26.6  type4 = 0.4
|    |**Split number : 1  Info gain: 0.1
|    |--[D = lingVal3] [C1 = lingVal4] [C2 = lingVal1]  <leaf>  IN = 0.0  PN = 24.2 : type1 = 0.0  type2 = 0.0  type3 = 24.2  type4 = 0.0
|    |--[D = lingVal3] [C1 = lingVal4] [C2 = lingVal2]  <leaf>  IN = 0.0  PN = 1.4 : type1 = 0.0  type2 = 0.0  type3 = 1.4  type4 = 0.0
|    |--[D = lingVal3] [C1 = lingVal4] [C2 = lingVal3]  <leaf>  IN = 0.0  PN = 24.2 : type1 = 0.0  type2 = 0.0  type3 = 24.2  type4 = 0.0
|    \--[D = lingVal3] [C1 = lingVal4] [C2 = lingVal4]  <leaf>  IN = 0.0  PN = 0.4 : type1 = 0.0  type2 = 0.0  type3 = 0.0  type4 = 0.4
\--[D = lingVal4]  NumOfSplits = 1  IN = 0.4  PN = 20.9 : type1 = 0.0  type2 = 0.0  type3 = 4.4  type4 = 16.5
   |**Split number : 1  Info gain: 0.3
   |--[D = lingVal4] [C2 = lingVal1]  <leaf>  IN = 0.1  PN = 3.9 : type1 = 0.0  type2 = 0.0  type3 = 3.7  type4 = 0.2
   |--[D = lingVal4] [C2 = lingVal2]  <leaf>  IN = 0.0  PN = 0.3 : type1 = 0.0  type2 = 0.0  type3 = 0.3  type4 = 0.0
   |--[D = lingVal4] [C2 = lingVal3]  <leaf>  IN = 0.0  PN = 3.2 : type1 = 0.0  type2 = 0.0  type3 = 3.2  type4 = 0.0
   \--[D = lingVal4] [C2 = lingVal4]  <leaf>  IN = 0.0  PN = 14.6 : type1 = 0.0  type2 = 0.0  type3 = 0.0  type4 = 14.6

TOTAL 16 leaves
```

Fig. 10. Fuzzy decision tree scheme obtained from the FID4.0 program.

As shown in Fig. 8, the IFNN system works satisfactorily, and only two stages implemented in this system allows for archiving good classification results.

Concurrently with the incremental structure (IFNN), where all input parameters were processed sequentially, the aggregated structure (AFNN) was also investigated [12]. In the AFNN architecture, all input parameters are divided into *M* subsets, which are further fed to an individual substage of the first stage. The classification rule takes into account all possible answers obtained at the outputs of the first stage. As seen from Fig. 9, the performance of an AFNN classifier was similar to those obtained from an IFNN structure.

For comparison, concurrently with the Adaptive Neuro Fuzzy Inference System (ANFIS), the fussy decision tree algorithm was also investigated [20]. The software package FID4.0 [21] was used to build up the fuzzy decision trees. These trees were trained on a learning set of data, and their generalization ability was

(a)

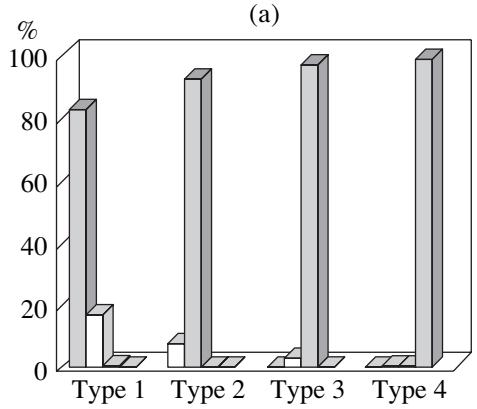

(b)

True class	Classified to *x*			
	Type 1	Type 2	Type 3	Type 4
Type 1	82.8%	16.9%	0.3%	0%
Type 2	7.5%	92.5%	0%	0%
Type 3	0%	3%	97%	0%
Type 4	0%	0.6%	0.6%	98.8%

Fig. 11. (a) Box diagram and (b) confusion matrix of the testing results of the fuzzy decision tree; the percentage of echoes correctly classified in total is 92%.

checked on a testing data set. The fuzzy decision tree schemes are shown in Figs. 11 and 12.

As was shown in Fig. 11, the decision tree algorithm works satisfactorily and allows one to achieve good classification results. In the testing process, the percentage of correctly classified echoes was 92%.

First Principal component coefficients for twenty input parameters

Parameter	1st principal component coefficient
*C*1	0.28194719
*C*2	−0.29078707
*C*3	−0.23517729
*C*4	0.19610819
*C*5	0.29887814
*C*6	−0.26130776
*C*7	0.25796993
*C*8	−0.29753704
*S*2	0.25250084
*S*3	−0.29503467
*S*4	−0.16163937
*S*5	0.018061612
*S*6	−0.077405941
*S*7	−0.056001851
*S*8	−0.18929400
E'	−0.12514390
E	−0.12889548
A	−0.18965035
T	0.27821713
N	0.24825874

CONCLUSIONS

This paper investigates the application of two approaches to seafloor classification, namely; the neuro-fuzzy system and fuzzy decision trees. To verify the idea and practical utility of the proposed methods, four sites of known and different bottom types, which also have comparable bottom depths, were selected. Such an approach simplifies the investigation, since it allows us to some extent to neglect the problem of echo envelope dependence on depth.

The wavelet coefficients used in both methods were derived from the Discrete Wavelet Transform (DWT) and combined with several selected echo parameters, viz., energy, amplitude, echo duration, etc. These combined parameters were subsequently analyzed by means of the principal component analysis (PCA) in order to extract those most significant for classification purposes. The PCA reduced the number of the input parameters to only the two most significant ones, viz., the fifth wavelet coefficient and the echo duration, which appeared to be sufficient for achieving good classification results. The performance of the fuzzy classification schemes developed, which use wavelet coefficients, appeared to be better than those using "conventional" time-domain parameters. This is due to the application of the Wavelet Transform, which represents the time–frequency approach and introduces both temporal and spectral characteristics of echo features in the classification procedure.

The results show that the neuro-fuzzy multistage classification system introduced seems to be a promising tool in seabed classification techniques. Due to the IFNN's incremental architecture, its classification algorithm is improved in successive stages by reinforcement from preceding stages. This results in a rather high classification accuracy (94.7%), and, generally, it

also reduces the computation power required. Although the method has been verified only in two experiments (viz., one in the Southern Baltic presented in this paper and the second referred to in [12]) and in privileged conditions of similar bottom depth, it seems to be quite probable that the proposed method will demonstrate its usefulness also in other conditions. Such a neuro-fuzzy system, similarly to an artificial neural network, has adaptive properties, which means that it allows for the modification of its internal parameters during the learning stage. As a consequence, optimal membership functions and optimal decision rules are obtained. However, it seems to be quite possible that the method could be generalized by extending the set of input parameters by adding the bottom depth to the set.

A fuzzy decision tree can be used to create if–then rules that classify new cases. It provides nearly the same performance as a neuro-fuzzy system. However, it has additional advantages when compared with neuro-fuzzy systems, namely, a shorter computation time and a less complex algorithm. The results show that the proposed fuzzy decision tree classifier with wavelet coefficients also seems to be a promising simple tool in seabed classification techniques.

REFERENCES

1. J. E. Hughes Clarke, B. W. Danforth, and P. Valentine, in *SACLANTCEN Conference Proceedings Series CP-45, High Frequency Acoustics in Shallow Water* (La Spezia, 1997), p. 243.
2. X. Lurton, J. M. Augustin, S. Dugelay, *et al.*, in *SACLANTCEN Conference Proceedings Series CP-45, High Frequency Acoustics in Shallow Water* (La Spezia, 1997), p. 313.
3. R. C. Chivers, N. Emerson, and D. R. Burns, Hydrograph. J., No. 56, 9 (1989).
4. E. Pouliquen and X. Lurton, in *Proceedings of the European Conference on Underwater Acoustics* (Elsevier, London and New York, 1992), p. 535.
5. L. R. Le Blanc, L. Mayer, M. Rufino, *et al.*, J. Acoust. Soc. Am. **91**, 107 (1992).
6. P. Andrieux, P. Delachartre, D. Vray, and G. Giménez, J. Acoust. Soc. Am. **98**, 552 (1995).
7. M. Gensane and H. Tarayre, Acoust. Lett. **16** (5), 110 (1992).
8. C. S. Maroni and A. Quinquis, in *SACLANTCEN Conference Proceedings Series CP-45, High Frequency Acoustics in Shallow Water* (La Spezia, 1997), p. 347.
9. R. A. Calvo, M. G. Partridge, and M. A. Jabri, in *Proceedings of the 9th Australian Conference on Neural Networks* (Brisbane, QLD, 1998).
10. M. Moszynski, A. Stepnowski, and Z. Lubniewski, in *Proceedings of the 2nd EAA International Symposium on Hydroacoustics* (Gdańsk, 1999), p. 85.
11. A. Stepnowski, J. Maciolowska, and T. V. Dung, Arch. Acoust. **24** (3), 365 (1999).
12. T. V. Dung and A. Stepnowski, Acta Acust. (China) **86**, 830 (2000).
13. C. K. Chui, *Wavelet: A Tutorial in Theory Applications* (Academic, San Diego, 1992).
14. M. Moszynski, in *Proceedings of the 4th European Conference on Underwater Acoustics* (Rome, 1998), p. 205.
15. L. A. Zadeh, Inf. Control., No. 8, 338 (1965).
16. J. S. R. Jang, C. T. Sun, and E. Mizutani, *Neuro-Fuzzy Soft Computing: A Computational Approach to Learning Machine Intelligence* (Prentice Hall, Upper Saddle River, NJ, 1997).
17. J.-S. R. Jang, IEEE Trans. Syst. Man Cybern. **23** (3), 665 (1993).
18. J. S. Duan and F. L. Chung, in *Proceedings of the IEEE World Congress on Computational Intelligence* (Fuzzy IEEE, Anchorage, Alaska, 1998), p. 1253.
19. R. J. Quinlan, Mach. Learn. **1**, 81 (1986).
20. L. Breiman, J. H. Friedman, R. A. Olsen, and C. J. Stone, *Classification and Regression Trees* (Wadsford, Belmont, Cal., 1984).
21. C. Z. Janikow, IEEE Trans. Syst. Man Cybern. **28** (1), 1 (1998).
22. L. M. Lyamshev and A. Stepnowski, *Fractal Laws of Sound Backscattering by Sea Surface and Bottom Hydroacoustics* (Gdynia, 2001), Vol. 4.

Acoustical Physics, Vol. 49, No. 2, 2003, pp. 203–206. Translated from Akusticheskiĭ Zhurnal, Vol. 49, No. 2, 2003, pp. 245–249.

Approximation of the Basic Characteristics of the Auditory Analyzer

I. A. Stefanova

Volga Regional State Academy of Telecommunication and Informatics, Moskovskoe sh. 77, Samara, 443090 Russia

e-mail: aistvt@mail.ru

Received October 1, 2001

Abstract—Empirical approximating formulas describing the most important psychophysiological properties of the human auditory analyzer are derived. © *2003 MAIK "Nauka/Interperiodica".*

Experimental studies of the subjective perception of sound signals have revealed a vast variety of the properties of hearing [1–3]. The most important ones are (1) the grouping of the frequency components of sound into certain frequency bands, (2) the masking (suppression of aural perception) of low-level tones by a higher-level tone, and (3) the threshold perception of the change in the tone frequency.

A band series based on experimental data was proposed in [1]. In this case, the group located within the middle-frequency range with the width measured to the highest precision was adopted as the reference point. However, it was noted that the ear can form frequency groups at any interval of the frequency scale, the group width depending only on the value of its central frequency. Therefore, an arbitrary choice of the starting point of the band series formation may lead to its distorted representation. Moreover, the proposed series is bounded from above by a frequency of 16 kHz. This fact is explained by the large scatter of hearing sensitivity among different people in the frequency range higher than 16 kHz, where it is fundamentally impossible to provide the necessary precision of measurements. On the other hand, transmitting systems for sound signals within the frequency band not smaller than 20–20 000 Hz are currently under development [4, 5]. It seems that both these problems can be solved only with the help of an analytical expression describing the dependence of the width of a frequency group on the frequency of the tone generating it. Regretfully, such a description is absent, at least in the available literature.

The effect of masking characterizes the hearing ability within a frequency group (and at certain conditions, beyond it as well) not to respond to those frequency components of the sound signal whose level lies lower than a certain threshold. The use of this property, for example in the process of compression of sound signals, provides an opportunity to reduce the number of the transmitted frequency components of the initial sound signal [6]. However, it is very difficult to apply this property in practice because of the absence of the corresponding mathematical description, which is apparently caused by the lack of an explicit expression for describing the frequency dependence of the masking curves.

The threshold values of the change of a tone frequency are the minimal changes of the sound frequency that can be perceived by hearing. This property may be very useful for utilization in systems sensitive to phase and frequency changes of sound signals.

One should note that a sufficiently precise mathematical description of the basic psychophysiological properties of the auditory analyzer is needed to apply these properties in practice.

Let us first analyze the integrating abilities of hearing in the frequency domain. We use experimental data obtained for people with different hearing sensitivities [1] to determine the analytical dependence of the width of the frequency group ΔF on the frequency of the tone f_m forming it.

The problem is solved by comparing a certain function $\Delta Fc(f_m)$ with the experimental results. It is convenient to use one of the techniques of regression analysis, namely, the linear regression of a general form [7, 8]. In this case, the correlation coefficient R^2 is taken as the criterion of accuracy of the function approximation to the average behavior of statistical data: the closer R^2 is to unity, the more accurate the approximation is.

The following function was obtained as a result of using the regression of a general form:

$$\Delta Fc(f_m) = 10^{-5.1} f_m^2 + 0.114 f_m + 68, \qquad (1)$$

where f_m is the frequency in hertz. The function given by Eq. (1) corresponds exactly ($R^2 = 1$) to the center of the "cloud" of statistical data.

The array of data can be considered as a family of parabolas corresponding to certain hearing sensitivities. However, in this case, the parabola going along the lower boundary of the data array corresponds to high

1063-7710/03/4902-0203$24.00

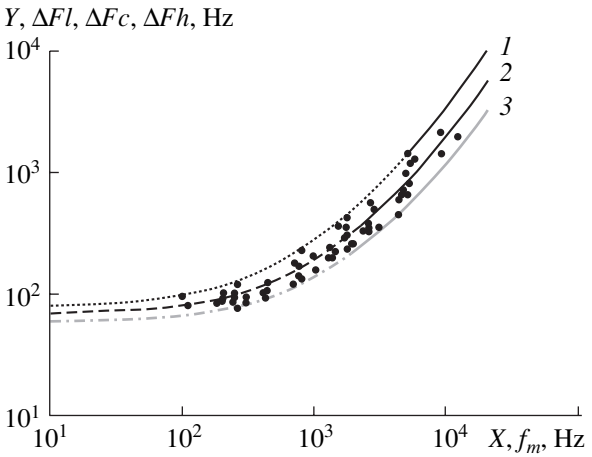

Fig. 1. Dependence of the width of frequency groups ΔF on the central frequency f_m at different frequency sensitivities. The experimental points for $Y(X)$ are taken from [1].

selectivity and the parabola going along the corresponding upper boundary, to low selectivity.

It is necessary to note one important feature of the experimental results, namely, the fact that the width of the data distribution along the vertical axis decreases with a decrease in frequency and increases with its increase. This means that the extreme parabolas must diverge with respect to the medium one in the upper frequency range and converge in the lower frequency range.

Taking into account the above considerations, with the help of the same regression analysis, we obtain the functions for hearing of low $\Delta Fl(f_m)$ and high $\Delta Fh(f_m)$ sensitivities:

$$\Delta Fl(f_m) = 10^{-4.8} f_m^2 + 0.165 f_m + 78, \quad (2)$$

$$\Delta Fh(f_m) = 10^{-5.4} f_m^2 + 0.076 f_m + 58. \quad (3)$$

Figure 1 presents the experimental data and the parabolas calculated according to Eqs. (1)–(3). Curves *1–3* correspond to low, medium, and high hearing sensitivities, respectively.

The expressions obtained above provide an opportunity to estimate the number and width of frequency groups for the case of a broadband sound signal for people perceiving different frequency ranges. In this case, it is possible to use the following technique.

Number of frequency groups for some frequency bands

Frequency range, Hz	Different hearing sensitivity		
	low	average	high
	Number of frequency groups		
20–20000	–	–	36
30–15000	–	24	34
50–10000	14	22	31

It is known [1] that a single tone forms a frequency group centered at it. In this case, setting the left boundary (corresponding to the lower frequency of the preset band, e.g., 20 Hz) of the first frequency group for a tone of arbitrary frequency from Eqs. (1), (2), or (3), we determine the width of the corresponding group and its central frequency. If the left boundary of this group is lower than the left boundary of the first group, the tone is shifted to the right. Next, the width of a new group is determined. If the left boundary of this new group is higher than the left boundary of the first group, the tone is shifted to the left. The procedure described is performed until the left boundary of the shifted tone group coincides with the left boundary of the first group. The boundaries of all other groups of the given frequency range are determined in a similar way.

The results of calculating the number of groups for a broadband signal for the people perceiving some of the possible frequency ranges are given in the table. The results agree well with the probabilistic approach to the evaluation of the maximal number of audible groups (about 30 [1]) on the basis of experimental data.

In the audible frequency band (20–20000 Hz), human hearing perceives sounds with levels lying between the hearing threshold and the pain threshold. The experimental curves for the change of the hearing threshold under the interfering effect of narrowband noise with a medium frequency of 1 kHz, a bandwidth of 160 Hz, and with levels E_n equal to 100, 80, 60, 40, and 20 dB were obtained in [1]. All five curves for the hearing threshold in the case of masking (masking curves) are asymmetric and have a distinct peak at the middle frequency of the noise band. The masked tone becomes audible at the peak points only at the level *Et* smaller than the noise intensity E_n by a_m dB. In the case of masking by a pure tone, the character of the masking curves is the same as in the case of masking by narrowband noise.

Furthermore, the masking curves for a tone at different medium frequencies of narrowband noise (250, 1000, and 4000 Hz), but at the same noise level E_n = 60 dB, are given in [1]. In this case, it is interesting that the peak points of the masking curves are shifted towards smaller levels when the frequency increases.

We reduce the curves to a single maximum of 60 dB by shifting them upwards, parallel to themselves, to a_m = 2.3 and 4.5 dB, respectively, to obtain an analytical description of the masking curves (Fig. 2). The masking curves are shifted towards smaller levels just by these values, according to the law displayed in Fig. 3 [1].

Then, we take

$$F = \frac{f - f_m}{\Delta F} \quad (4)$$

as the argument of the desired empirical function, where f is the current frequency with respect to the

tone with the frequency f_m, which forms a frequency group with the width ΔF. As a result, all three masking curves almost coincide, which confirms the unified character of their change, and an opportunity to obtain the desired functional relation with constant coefficients appears.

We again use the linear regression of a general form to approximate such a generalized masking curve. As a result of approximation, it becomes possible to determine with a high accuracy ($R^2 = 0.9997$) an empirical formula for describing the masking curves within the limits of the tripled width of the frequency group:

$$\begin{aligned} Et(F) &= 6.4\cos(F + 0.013)^4 - 1.1\sin(F + 0.013)\pi \\ &+ 5.26(F + 0.013) - 10.7(|F + 0.013|)^{\pi/2} \\ &- 6.4 + E(f_m) + a_m, \text{ dB}, \end{aligned} \quad (5)$$

where $Et(F)$ is the tone intensity at the value F of the argument, $E(f_m)$ is the intensity of the tone with the frequency f_m forming the masking curve, and a_m is the masking coefficient of the frequency group that compensates the aforementioned shift of the masking curves and depends on the frequency f_m.

Equation (5) is simplified within a single width of the frequency group. In this case, the masking curves are approximated to a high accuracy ($R^2 = 1$) by a third-degree polynomial:

$$\begin{aligned} &Et(F) \\ &= 9.85F^3 - 27.68F^2 + 1.12F + E(f_m) + a_m, \text{ dB}. \end{aligned} \quad (6)$$

The quantity a_m (Fig. 3) does not depend on the level of sound pressure, and, therefore, it adequately characterizes the properties of human hearing [1]. Using the polynomial regression, the desired approximating dependence of the value of a_m on frequency is determined to a high precision ($R^2 = 0.999$) in the form

$$\begin{aligned} a_m(f) &= -1.45 \times 10^{-12} f^3 + 6.135 \times 10^{-8} f^2 \\ &- 8.49 \times 10^{-4} f - 1.98. \end{aligned} \quad (7)$$

Equations (5)–(7) provide an opportunity to use the properties of masking, in particular, in the case of compression of sound signals.

The frequency and amplitude change in time for the majority of sound tones. To judge these changes, it is necessary to know what minimal changes in the frequency and level can be perceived by hearing.

The minimal changes of tone frequencies that are still perceived by hearing can be interpreted as the still audible minimal deviation Δf at the frequency modulation performed according to a sinusoidal law [1]. The value of the still audible minimal frequency deviation depends on the modulation frequency f_{mod}, the frequency of the tone studied f, and its level. As it is determined experimentally [1], the sensitivity of hearing to frequency changes is maximal at a modulation frequency of 4 Hz. The threshold deviation for this frequency Δf at different tone frequencies lies within the range from 1.5 to 50 Hz.

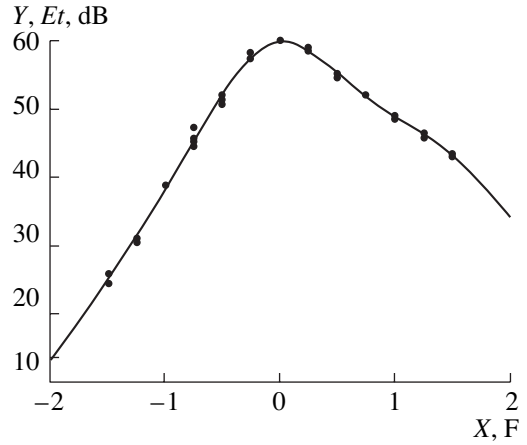

Fig. 2. Approximating masking curve $Et(F)$ within the limits of the triple width of a frequency group. The experimental points for $Y(X)$ reduced to a single maximum are taken from [1].

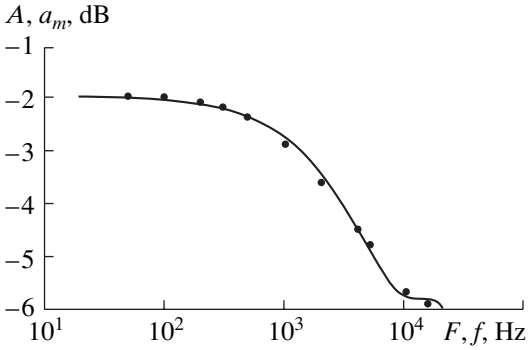

Fig. 3. Approximating curve for the dependence of the value of a_m on the frequency f. The experimental points for $A(F)$ are taken from [1].

The dependence of the threshold deviation on the frequency of the modulating tone at a sound pressure level of 70 dB is given in Fig. 4 (curve *2*). The dots indicate the results of measurements [1]. The curve divides the regions of the audible (the region above the curve) and inaudible (the region below the curve) oscillations of the pitch. In the region of frequencies lower than 500 Hz, the threshold deviation almost does not depend on the modulating frequency. At frequencies higher than 500 Hz, it increases proportionally to frequency. As one can see, the character of the curve is the same as that of the dependence of the width of the frequency group on the middle frequency of narrowband noise (Fig. 1). One of the most important properties of hearing manifests itself in this coincidence.

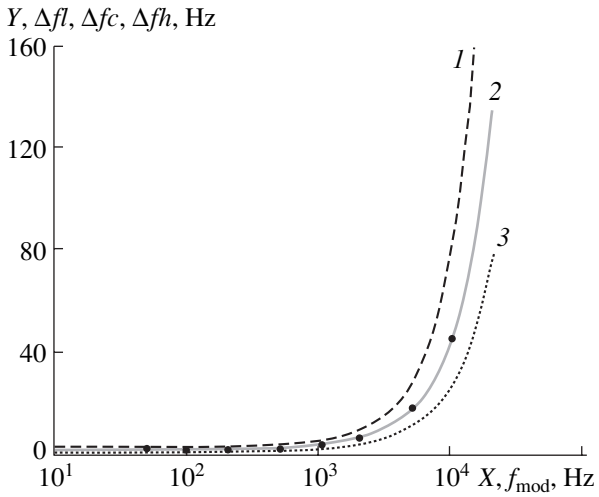

Fig. 4. Dependence of the threshold deviation Δf on the frequency of a modulating tone f_{mod}. The experimental points for $Y(X)$ are taken from [1].

As a result of the approximation of this curve, it turned out that it is described to a high accuracy ($R^2 = 1$) by the expression

$$\Delta fc(f_{\text{mod}}) = 2.253 \times 10^{-7} f_{\text{mod}}^2 + 2.124 \times 10^{-3} f_{\text{mod}} + 1.32. \quad (8)$$

It is logical to assume that this curve corresponds to the average sensitivity of hearing, and, by analogy with the integrating capability of hearing, it is possible to obtain expressions and plot curves for the dependence of the threshold deviation on the frequency of the modulating tone for people with different hearing sensitivity. These dependences for hearing of low $\Delta fl(f_{\text{mod}})$ and high $\Delta fh(f_{\text{mod}})$ sensitivity have the forms

$$\Delta fl(f_{\text{mod}}) = 2.2 \times 10^{-6.6} f_{\text{mod}}^2 + 2.36 \times 10^{-3} f_{\text{mod}} + 2.32, \quad (9)$$

$$\Delta fh(f_{\text{mod}}) = 2.2 \times 10^{-7.3} f_{\text{mod}}^2 + 1.6 \times 10^{-3} f_{\text{mod}} + 1.22. \quad (10)$$

Figure 4 presents curves *1–3* calculated according to Eqs. (8)–(10) for low, average, and high sensitivities of hearing, respectively.

Thus, the results of this study offer the following conclusions.

(1) It is confirmed that the dependence of the width of a frequency group on the position of the tone generating it on the frequency axis is close to quadratic.

(2) Empirical analytical expressions describing the dependence of the width of a frequency group on the position of its generating tone on the frequency axis are obtained for hearing with different frequency sensitivities. Thus it seems possible to evaluate with a high accuracy the band series for people perceiving different frequency ranges.

(3) Analytical expressions describing with a high accuracy ($R^2 \longrightarrow 1$) the masking curves within the limits of both single and a triple widths of a frequency group are obtained, which provides an opportunity to design highly efficient algorithms of sound signal compression.

(4) Empirical approximating expressions describing with a high accuracy ($R^2 \longrightarrow 1$) the dependence of the threshold deviation on the frequency of the modulating tone are obtained, which provides an opportunity to evaluate the minimal changes in frequency that still can be perceived by hearing with different frequency sensitivities.

REFERENCES

1. E. Zwicker and R. Feldtkeller, *Das Ohr als Nachrichtenempfänger* (Hirzel, Stuttgart, 1967; Svyaz', Moscow, 1971; Acoust. Soc. Am., New York, 1999).
2. E. Zwicker, *Psychoacoustics* (Springier, Berlin, 1982), p. 390.
3. T. Painter and A. Spanias, Proc. IEEE **88** (4), 451 (2000).
4. U. Gbur, M. Dietz, B. Teichmann, *et al.*, FRG Patent No. 19,628,292 (12 July 1996).
5. C. C. Todd, U.S. Patent No. 5,581,653 (31 April 1993).
6. H. L. Vu, Period. Polytech. Electr. Eng. **41** (1), 75 (1997).
7. E. Förster and B. Rönz, *Methoden der Korrelations- und Regressionsanalyse: Grundlagen, Methoden, Beispiele* (Gabler, Wiesbaden, 1992; Finansy i Statistika, Moscow, 1983).
8. N. Draper and H. Smith, *Applied Regression Analysis* (Wiley, New York, 1966; Finansy i Statistika, Moscow, 1996).

Translated by M. Lyamshev

Acoustical Physics, Vol. 49, No. 2, 2003, pp. 207–216. Translated from Akusticheskiĭ Zhurnal, Vol. 49, No. 2, 2003, pp. 250–261.

Intensity and Space–Time Characteristics of the Sound Field in the Underwater Sound Channel of the Black Sea

N. V. Studenichnik

Andreev Acoustics Institute, Russian Academy of Sciences, ul. Shvernika 4, Moscow, 117036 Russia

e-mail: bvp@akin.ru

Received March 25, 2001

Abstract—Experimental data are presented on the intensity and space–time characteristics of the sound field generated by explosions in underwater and surface sound channels of the Black Sea. The fine field structure is studied as a function of distance and positions of the source and the receiver. The discreteness of the field structure governed by the deterministic nature of the waveguide is revealed, and the destruction of this structure under the effect of the instability of the waveguide parameters is demonstrated. The effect of the rough sea surface on the sound field in the surface channel is studied, and the diffraction-caused propagation loss is estimated. The mechanism of the forerunner formation is considered. The experimentally observed sound field features are compared with the calculations. A possibility for solving the inverse problem is indicated, and the main parameters that are used in the ray method of determining the source coordinates in the underwater channel (i.e., the method earlier proposed by the author on the basis of the intrinsic structure of the sound field) are pointed out. © *2003 MAIK "Nauka/Interperiodica".*

Studies of sound propagation in underwater waveguides are the subject of numerous publications. The results of these studies are well known. Geographically, they cover nearly all regions of the ocean all over the world. However, the majority of the publications contain either purely theoretical considerations based on idealized classical waveguide models or experimental data averaged and generalized to the extent that it does not allow one to obtain information on the intrinsic structure of the sound field. The main disadvantage of these studies is the absence of identification and analysis of the sound field components and their governing physical mechanisms determined by the actual oceanic conditions. This disadvantage does not allow one to correctly compare theoretical models with experimental data.

This paper, in view of the aforementioned factors, studies the general structure of the sound field governed by deterministic environmental conditions and the destruction of the field components in space and time due to the instability of the waveguide. The experimental data are compared with the calculations based on the theory of waves in layered media [1]. The features established for the deterministic conditions, namely, the strict discreteness and the space–time stability of the field components, along with the destruction limits determined for this stability in inhomogeneous waveguides, can serve to estimate the domain where the direct and inverse problems have physically justified and correct solutions in both fundamental and applied ocean acoustics. In addition to considering the general features of the regular field components, the properties of the fluctuating components are discussed that lead to the phenomenon of prereverberation, whose main characteristics, mechanisms, and theoretical analysis can be found in [2–8]. The fine structure of the sound field is considered in [9], where the theoretical and experimental data on the filtering of normal waves in both shallow and deep seas with near-bottom and surface sound channels are presented. The effect of the bubble layer on the enhancement of the sound field due to the interaction of the rough sea surface with the bubble layer is described in [10].

We performed our experiments in autumn in the deep-water basin of the Black Sea, 100–300 km southeast of the Crimea peninsular. The sea depth on the paths was 1900–2100 m. The bottom was silty and smooth. Two research vessels that freely drifted during the measurements were used in the experiments. One of the vessels that drifted at the western point of the path carried receiving and recording equipment. From the second vessel, explosive charges were dropped that served as the sound sources. In total, 160 charges were exploded on the two 180-km paths: 150 charges of 25 kg and 10 of 135 kg. The headings of the transmitting vessel were 105° and 285° on the direct and inverse tacks, respectively. The water temperature was 18°C near the surface and 7–9°C in deeper layers, with a salinity of 18.5–24‰. The wind speed was 3–6 m/s, the sea state was Beaufort 1–3. At the time of the experiment, fully developed sound channels were present in the sea: the underwater channel with the axis at a depth of 60 m and the surface channel 24–27 m in thickness. The thickness of the discontinuity layer was 2–4 m. The sound speed was 1464 m/s at the channel axis, 1472 m/s at a depth of 35 m, and 1500 m/s at the sur-

1063-7710/03/4902-0207$24.00 © 2003 MAIK "Nauka/Interperiodica"

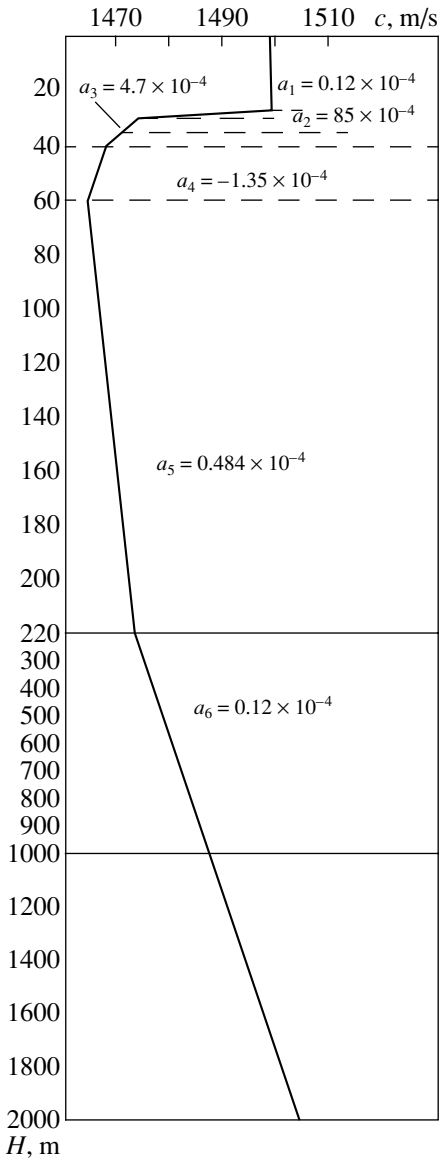

Fig. 1. Sound speed profiles in the region of the experiment; a_n represents the relative gradient of the sound speed in the nth layer.

face. Figure 1 shows the vertical distribution of the sound speed. In accordance with the sound speed profile, the transmission and reception depths were chosen to be 20, 35, and 60 m. True depths of the explosions could differ by 1–5 m from the expected ones, these differences being determined by the oscillation periods of the gas bubble. The signals were received by hydrophones without preamplifiers and recorded by a photorecorder after band-filtering within a 20% window. The data were recorded at film transport rates of 326 and 107 mm/s. Simultaneously, the signals were stored with the MZ and MIZ magnetic-tape recorders and light-beam oscilloscopes within a broad frequency band from 1–2 Hz to 15 kHz.

Below, we analyze the structure of the sound field with the following aims:

(i) to reveal the fine structure of the field and the mechanism governing its formation;

(ii) to study the effects of the underwater and surface sound channels on the intensity and space–time characteristics of the field for different combinations of the source and receiver positions; and

(iii) to determine the role of the waveguide inhomogeneities in the formation of the fine structure of the field and its stability in space and time.

At a 35-m depth of transmission, the zone of direct visibility was no longer than 0.5–1 km. The shadow zone covered depths down to 160 m and was limited by the distance of secondary signal arrival at the transmission horizon, which was equal to 4.5 km. At longer ranges, the zone of full insonification was formed. The surface channel was an exception: much like the shadow zone, it was insonified by the bottom–surface reflections and the components of the diffracted field. The initial convergence zones and the corresponding caustics formed by the first cycles of the diffracted signals ranged from 4.5 to 34 km and concentrated within the discontinuity layer, at the depths 35 to 27 m. The difference in the sound speeds near the bottom and the surface (+5 m/s) made the deep rays arrive at the surface at distances of 34–40 km, with grazing angles of 0°–5° and a difference of ±2° in the departure angles. At a 20-m transmission depth in the surface channel, the lengths of the horizontally leaving ray and the limiting ray were 3650 and 4650 m, respectively. Their grazing angles were 1.26° and 1.47° near the surface. The channel captured the rays with angles of ±0.2°. The total capacity of the channel was ±1.47°. The critical frequency was 815 Hz.

Figures 2–4 show the forms of individual components and the total field structure for different positions of the sources and the receivers at distances from 130 m to 180 km. In the zone of direct visibility, at a distance of 130 m with transmission and reception depths of 35 m, two signals produced by the shock wave (they are limited in their amplitudes to 20–22 dB) and two signals produced by the first gas-bubble oscillation can be seen. The period of the oscillation is T = 255 ms. The first arrivals in the recorded signal pairs are the refracted components, and the second arrivals are the surface reflections. The level of the sound field backscattered by the volume inhomogeneities and in the bubble layer is –35 to –40 dB. The loss in the component specularly reflected by the surface is 7 dB, and the level of the reflected sound field is –30 to –35 dB. At a distance of 700 m, the following signals are clearly pronounced: the direct signal, the forerunner with a 3-ms time advance and a level of –22 to –25 dB, and the signal of the first gas-bubble oscillation (T = 240 ms) with a level of –25 dB. The level of the signals scattered by the surface at the grazing angles 3°–4° is –35 to –40 dB or even lower. In the shadow zone (at a distance of

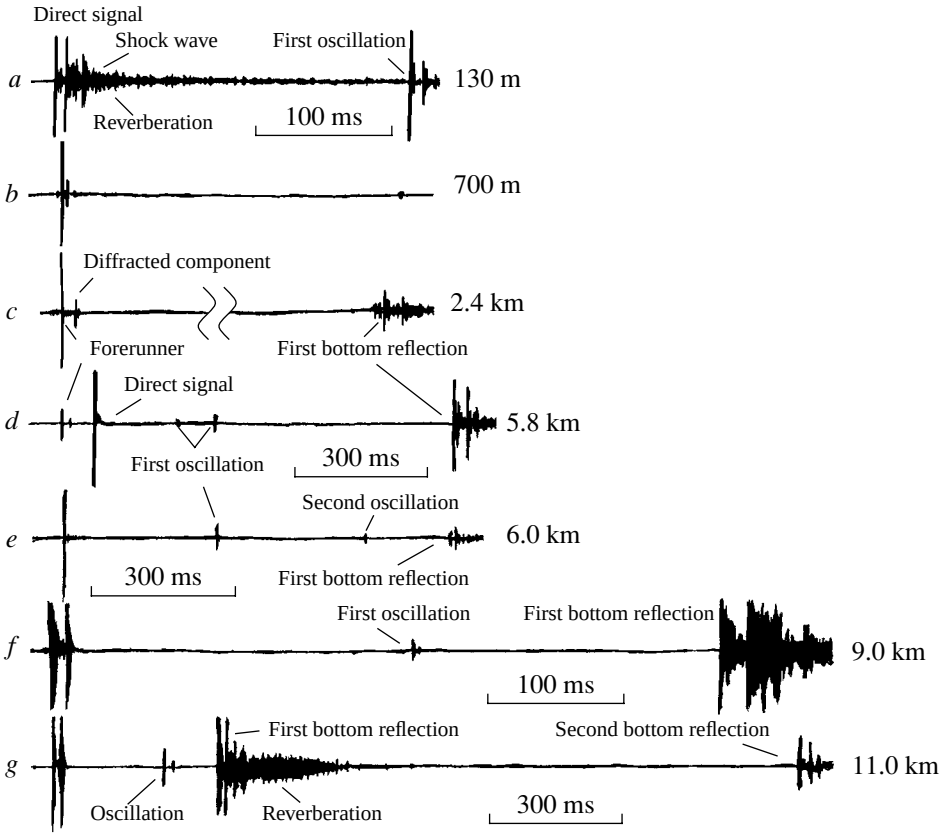

Fig. 2. Field structure in the near zone at distances between 130 m and 11 km for different source and receiver depths. The parameters of the records are as follows (the first number is the distance in km, the second number is the source depth in m, the third number is the receiver depth in m, and the fourth number is the film-transport rate in mm/s): (*a*) 0.13, 35, 35, 326; (*b*) 0.7, 35, 35, 326; (*c*) 2.2, 35, 35, 107; (*d*) 5.8, 35, 35, 326; (*e*) 6.0, 20, 20, 107; (*f*) 9.0, 35, 35, 326; and (*g*) 11.0, 35, 35, 107.

2.2 km), two diffracted signals and bottom–surface reflections are present. The first arrival is the forerunner. It is produced by the field component captured by the surface channel after its reflection from the rough sea surface; it is then propagated in the channel, captured by the channel again after secondary reflections, and, finally, scattered into the water bulk below the discontinuity layer. The propagation velocity of this component is close to the sound speed in the surface channel. The second signal, with an amplitude that is 10 dB lower and with the delay time Δt = 33 ms, is the diffracted component. Its propagation velocity is close the sound speed at the transmission horizon. The bottom–surface reflections (Δt = 1475 ms) with grazing angles of 63° have the form of a scattered field without any pronounced specular component. As the distance increases, the diffracted component completely vanishes. The forerunners are retained up to 180 km.

In the first convergence zone of the zero-angle ray at a distance of 5.8 km, the first arrival is the forerunner (Δt = 80 ms), the second is the main field component, and the third is the group of bottom–surface reflections (Δt = 780 ms). The diffracted component is absent. The amplitude of the forerunner is by as little as 16–20 dB lower than that of the main signal (focused up to 6–7 dB). In contrast to the previous record, the bottom–surface reflections include well-resolved specular signal pairs (Δt = 30 ms) with a level that is 10–20 dB higher than the level of the scattered signals. Their grazing angles are 34°. In the surface channel at a distance of 6 km with transmission and reception depths of 20 m, only one direct signal and a pair of the bottom-surface reflections (Δt = 15 ms) are observed. The periods of the two oscillations are 326 and 316 ms. At distances of 9 and 11 km with transmission and reception depths equal to 35 m, the second refracted signals appear with differences of 11 and 15 ms in their arrival times. The first signals of this group produced one full cycle, while the second ones produced two full cycles. The difference in their levels decreased from –20 or –25 to –10 dB as the distance changed by 2 km. At longer distances, the number of the signals refracted in the underwater channel increases, but the number of those refracted in the surface channel is retained: there is one deep-water signal and one forerunner. Overlapping of the insonification zones and the appearance of two deep-water signals are possible starting from a distance of 200 km.

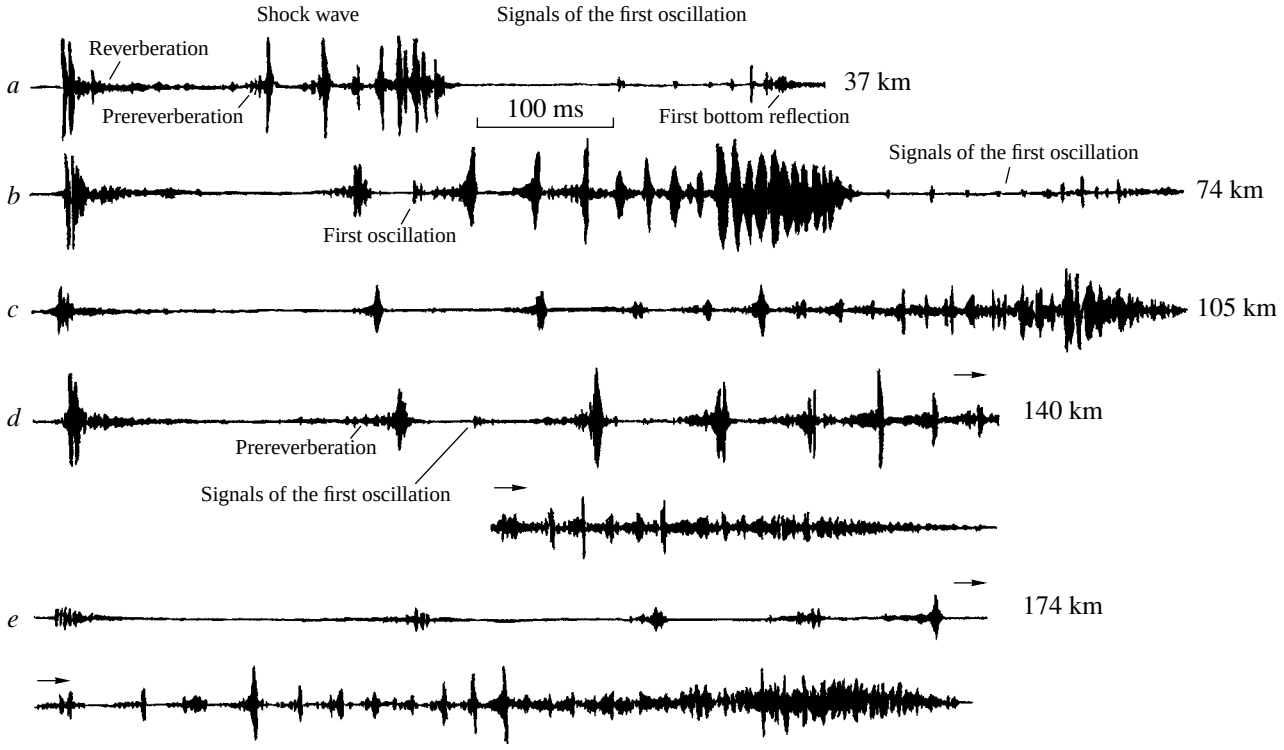

Fig. 3. Field structure in the underwater sound channel at distances of (*a*) 37, (*b*) 74, (*c*) 110, (*d*) 140, and (*e*) 174 km. The source and receiver depths are 35 m; the film-transport rate is 326 mm/s.

Figure 3 shows the field structure at distances of 37–175 km for the transmitter and receiver positions near the channel axis. At a 37-km distance, the whole set of the refracted components that can be guided in this case arrives at the receiver after having produced one or more full cycles. Two systems of components identical in propagation times and amplitude ratios can be distinguished. These systems are produced by the shock wave and the first gas-bubble oscillation (T = 260 ms). The difference in their amplitudes is 25 dB. The maximal time of signal elongation is 273 ms. The initial and terminal components of the oscillation overlap with the near-axis components of the shock wave and with its twofold bottom–surface reflections. The grazing angles of these components are 7°–8°. When the components that have lower characteristic angles (that is, angles at which the rays cross the channel axis) begin to arrive, the signals become closer in time, and the difference in the delay times tends to zero. The time relations and the levels of the regular components agree well with the calculations. The first arrival produced by the surface reflections exhibits a sharp increase in the wave front, a time splitting of the signal pairs (Δt = 5 ms), and a high level of the scattered components (reverberation). Their reverberation time exceeds 300 ms. Later arrivals do not reach the surface and are not accompanied by such high-level reverberation. They are purely refracted and have a form close to mirror-like with respect to the first arrival. Their leading edge is smeared and the trailing edge is steeper. The smearing of the wave front is caused by prereverberation [2–6]. The levels of the prereverberation produced by the forward scattering of the regular field components from the channel inhomogeneities are nearly as high as those of the reverberation signals backscattered by the surface. The prereverberation components (propagating in the forward direction) may also arrive after the regular component and look like reverberation components (backscattered by the surface). Such a delayed prereverberation can be produced by the sound scattering in the azimuth plane. In this case, the components can be nearly symmetrical. The first arrivals in initial cycles and the signals arriving along the rays touching the bottom in the subsequent cycles cannot be accompanied by prereverberation.

At long ranges, when the sources and receivers are under the discontinuity layer, at depths of 30–60 m near the channel axis, the duration of the set of signals and the number of signal components increase proportionally to the distance (if the characteristic angles are fixed). The structure of the arrival times and the angles of the components change according to the distance. The accumulation of the prereverberation components (in their duration and amplitude) manifests itself more clearly. The records demonstrate the reverberation from two initial surface-reflected arrivals and the prerever-

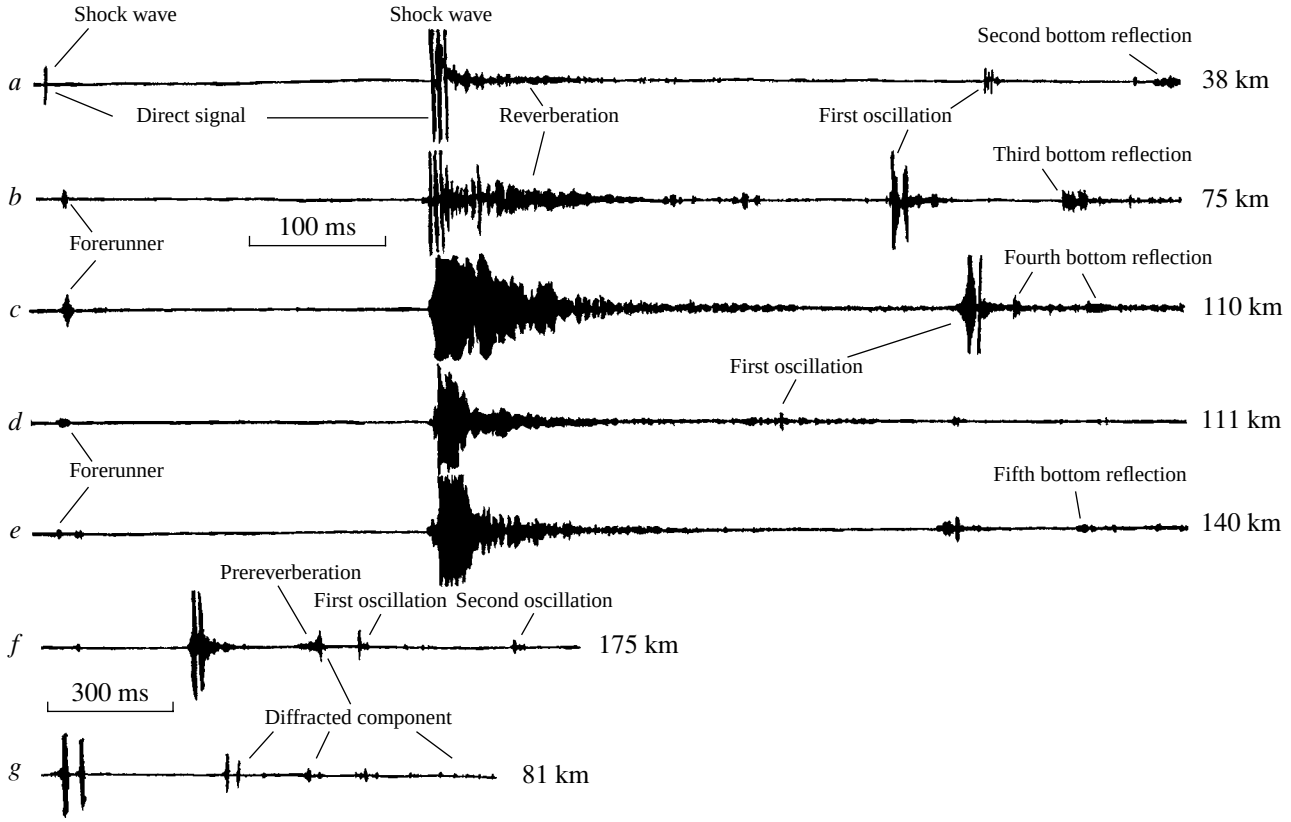

Fig. 4. Field structure at distances of 38–180 km with the source and receiver in the surface channel and with their symmetric positions relative to the discontinuity layer: (*a*) 38, 20, 20, 326; (*b*) 75, 35, 35, 326; (*c*) 110, 20, 20, 326; (*d*) 111, 43, 20, 326; (*e*) 141, 35, 20, 326; (*f*) 180, 22, 35, 107; (*g*) 81, 60, 30, 326. Here, the numbers mean the same as in Fig. 2.

beration from other components scattered by the volume inhomogeneities. These features are most pronounced in the record obtained at a 140-km distance. The levels of surface reverberation and volume prereverberation are comparable. The existence of the prereverberation components before each of the first components indicates that they arrive along the rays that are not limiting ones but rather refracted above the bottom. In the signal sets, the discreteness in the arrivals of the components is quite pronounced, this discreteness being governed by the deterministic characteristics of the channel. The time intervals between the arrivals decrease from 200–250 ms to zero. At the terminal parts of the records, when the near-axis components arrive, the prereverberation causes full overlapping of the coherent and incoherent components, which are equal in their amplitudes. A continuous noiselike sound field is formed with a uniform probability distribution of the amplitudes and phases in the near-axis components.

Figure 4 presents the field structure for the source and receiver positioned in the surface waveguide at different depths relative to the discontinuity layer. At a distance of 38 km with source and receiver depths of 20 m, the field structure is formed by signals of three different types. The first one is the direct signal propagating in the surface channel with $\Delta t = 264$ ms. The second type (along with the gas-bubble oscillation at $T = 382$ ms) is represented by the deep-water signals that arrive at the surface and form the terminal part of the first convergence zones at the limiting distance. Their characteristic angles are 12.2°–14.2°. The third signal group consists of the twofold bottom–surface reflections. The associated grazing angles are 13°, and the delay times are 500 ms. A scattered field with a level of –35 to –40 dB can be observed within 200–300 ms. In the deep-water signals, the temporal resolution of the specular components is retained at $\Delta t = 1.5$ ms. Their amplitudes are nearly equal and exceed the level of the direct signal by 20–22 dB. The high loss in the surface channel (in comparison with that of the deep-water components) is determined by the scattering and absorption at the surface and in the bubble layer and, as the most probable main mechanism, by the diffraction-caused energy leakage below the discontinuity layer. At long distances, independently of the source and receiver positions, the field structures include a single forerunner created by the penultimate cycles of the deep-water signals in their reflections by the surface. For all cycles, their advance times are 252–257 ms, which correspond to the difference in the propagation times within a single deep-water ray cycle. There are no direct signals

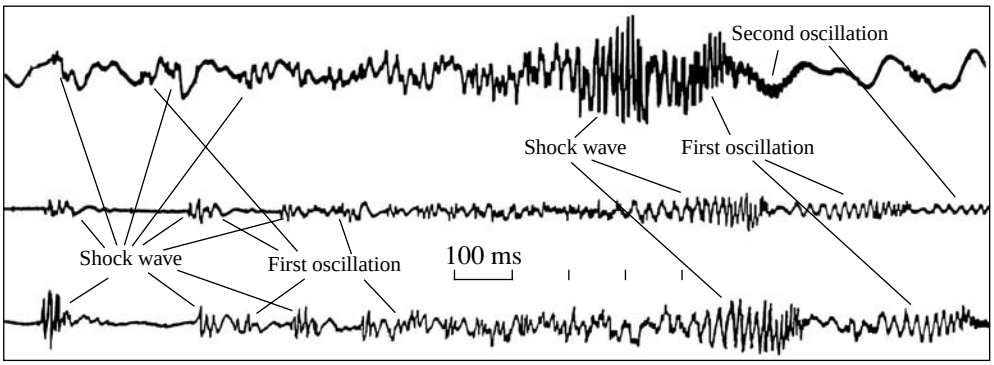

Fig. 5. Field structure in the underwater sound channel in a broad frequency band (1–300 Hz). The distances are (a) 165, (b) 174, and (c) 180 km. The explosion depths are 60, 35, and 20 m. The reception depth is 35 m. The transport rate is 160 mm/s.

and forerunners whose trajectories lie in the surface channel for two or more cycles. In our experiments of 1963 in the Atlantic Ocean (southwest of the Madera Islands), with a surface channel of 30–40 m in thickness and a sea state of Beaufort 3–4 at frequencies of 800–1200 Hz, we observed up to two to three forerunners with advance times of 2–3 s. Several forerunners were also observed in other ocean regions. In particular, in the experiments in the central part of the Pacific Ocean, southwest of the Hawaii Islands, the forerunners were observed at frequencies of 500–800 Hz with a 60–70-m thickness of the surface channel. The differences between the levels of the forerunners and the refracted components weakly depend on the number of surface reflections and are within –35 to –40 dB. These values indicate only slight changes in the parameters of the surface channel and testify to a universal mechanism of the forerunner generation. If the positions of the source and receiver are interchanged relative to the discontinuity layer, the structure of the sound field remains nearly unchanged. The discontinuity layer behaves as a relatively powerful potential barrier whose screening effect reaches 40–60 dB. At distances of 110 and 140 km, the signals produced by four- and fivefold bottom–surface reflections are observed with amplitudes of between –40 and –45 dB. Their effective reflection coefficient ranges from 0.28 to 0.32 at angles of 4°–4.5°.

At a distance of 180 km with the source in the surface channel (at a depth of 20 m) and the receiver under the discontinuity layer (35 m), the field structure, in addition to the main deep-water signal (which is surface-reflected and limited by 10 dB in its amplitude), includes another guided signal with an amplitude of –20 dB, which does not reach the surface and produces one additional ray cycle. Its delay time is 270 ms. It is advanced by a considerable level of prereverberation and is followed by a short-time reverberation. According to ray-theory considerations, no such component can exist in the field structure. Its presence at a depth of 35 m can be explained by nothing but the diffraction-caused penetration of part of the energy below the discontinuity layer and the subsequent propagation in the channel at lower characteristic angles. Again, the forerunner and two gas-bubble oscillations can be noticed with periods of 355 and 327 ms.

With the source at the channel axis (60 m) and the receiver under the discontinuity layer (28–30 m), at a distance of 81 km, the field is formed by the signals with decreasing amplitudes, which are caused by the refracted (two initial pairs) and diffracted components. The turning points of their trajectories are 2–5 m off the reception horizon. The level of the diffracted components is by 20–40 dB lower than that of the refracted components. Between the second and third arrivals, one can see the signals caused by the first gas-bubble oscillation (T = 165 ms) and by threefold bottom–surface reflections that arrive simultaneously. The amplitude difference in the first arrival and the bottom reflections is 22 dB.

The above analysis of the fine structure of the acoustic field in the underwater and surface sound channels shows that the experimental data agree well with the ray-theory calculations. However, in some cases, there is a considerable disagreement caused by the channel inhomogeneities (prereverberation) and wave processes (leakage of the acoustic energy through the discontinuity layer). In particular, the strong attenuation observed in the surface channel at a frequency of 3 kHz, which is nearly two octaves higher than the critical frequency (not to mention the lower frequencies), can hardly be explained by only the loss due to the scattering from the surface and from the bubble layer: one cannot neglect the wave effects and the diffraction-caused sound penetration below the discontinuity layer. The latter loss mechanisms, which are ignored by the ray approximation, can lead to false conclusions in interpreting the experimental data and predicting the sound field structure, even when the validity conditions for the ray theory are met.

As an example, Fig. 5 shows the field structure observed in a broad low-frequency band (1–300 Hz) at distances of 165, 174, and 180 km with the sound sources positioned at the channel axis (at a depth of

60 m) under the discontinuity layer (35 m) and in the surface channel (20 m). The receiver was near the channel axis at a depth of 35 m. The records are obtained with the use of a light-beam oscilloscope at a transport rate of 160 mm/s. The data presented in Fig. 5 show that, in the infrasound and low-frequency sound regions, the space–time structure of the sound field remains unchanged, independently of the depth of the sound source. The only difference in the field structures consists in the relative levels of the field components. Thus, at a 60-m source depth, the near-axis components have a level which is 14–18 dB higher than that of the initial arrivals. These levels differ by 2–6 dB at a 35-m horizon, and, at a 20-m depth, the components of the entire signal, including the region of the developed dispersion and quasi-in-phase summation, are nearly equal. At low frequencies, up to 300 Hz, the upper part of the sound speed profile has no effect on the sound field in the channel and, hence, can be neglected. No ray considerations can explain these experimental data: ray-theory calculations are useless at frequencies from several hertz to several hundreds of hertz. For this frequency band, the underwater waveguide degenerates into a strong surface channel 2000 m in thickness. As to the deeper part of the channel, it determines the intensity and space–time characteristics of the refracted components at frequencies that are higher than the critical one of the entire channel (1.8 Hz). At lower frequencies, the whole waveguide degenerates into a uniform layer with characteristics of a shallow sea. In the signal sets, independently of the source depth, a pronounced dispersion structure can be seen at frequencies of 300 to 30–50 Hz. The dispersion is equally characteristic of the signals from the gas-bubble oscillations. The amplitude differences in the shock wave and in the two initial oscillations are 6 and 10 dB at frequencies of 80–150 Hz and 20–25 and 30 dB at 3 kHz. At explosion depths of 60, 35, and 20 m, the periods of the first oscillations are 170, 250, and 340 ms, respectively.

To conclude with analyzing the structure of the sound field in the underwater channel, let us take a closer look at its aforementioned specific features, which are related to the space–time behavior of the field structure and to the prereverberation and which had been rather poorly investigated until the present time. At all distances, independently of the source position, the first arrivals have a sharp leading edge and a monotonically decreasing reverberation background. The following arrivals are strictly quantized in their arrival times and grazing angles and include additional components that precede the main components and form the prereverberation. At short distances, their amplitudes are much lower than those of the main components. As the distance increases, their levels become higher and reach 0.3–1 of the amplitudes of the deterministic components. For the volume inhomogeneities, the estimated angular width of the forward-scattering diagram is +0.5° or less at a level of 30–35 dB. With fully-developed prereverberation, in the terminal part of the signal set, the elementary signals arrive more frequently, the amplitudes of the coherent and incoherent components become equal, and they fully overlap. As a result, the near-axis components exhibit the properties of a noise-like diffuse process with a uniform amplitude and phase distributions of all the arriving components. These features, which are specific to a natural waveguide, can be described by neither ray nor wave approximations and cannot be explained by the classical theory of sound propagation in stratified waveguides [1]. At high frequencies, the coherent components lose their governing role in long-range energy transport, and this fact restricts the possibility of using the phase methods for sound field calculations. In addition, the informative capacity and efficiency of using the intrinsic field structure becomes low when applied to phase methods of signal processing in both direct and inverse problems of ocean acoustics. The same is also true for the technique based on using wide-aperture vertical arrays. At low frequencies, the ocean inhomogeneities have a weaker effect on the wave front and even on its phase, so that a stable in-phase summation is possible and a quasi-normal wave with pronounced dispersion properties can be formed (Fig. 5).

In Fig. 6, the calculated (curves and straight lines) and experimental (crosses) space–time structures are presented for the sound field in the underwater channel. The abscissa axis represents the distance. The ordinates represent the advance times for the refracted signal components propagating along the channel axis. The parabola-like curves are the angular dependences of the advance times for individual components and for the whole sequence of the cycles determined by the distance, the source and receiver positions, and the waveguide parameters. The straight lines emerging from the origin of coordinates show the mean horizontal velocities of the signals at fixed departure angles and the advance times as functions of the distance. The set of curves originating from the turning points of the parabolic curves indicate the advance and delay times for the signals reflected by the bottom and the surface. In the upper part of Fig. 6, the lines represent the advance times for the direct signals and forerunners that fully (straight line *1*) or partially (straight line *2*) propagate in the surface channel and penetrate below the discontinuity layer. Near lines *1* and *2*, the mean propagation velocities of the forerunners are indicated. The data presented in this figure clearly show the features of the regular components, namely: the discreteness of the arrivals and the strict dependences of the differences in the arrival times for all signal sequences at different ranges, the nonmonotonicity of the increase in the signal duration as a function of distance, and a good agreement between the experimental and calculated data. The chart presented allows one to determine the general structure of the sound field at an arbitrary point of space, at any distance, and at any depth. The vertical cross section of the chart yields the number of arriving signals at a given distance, along with their angular and

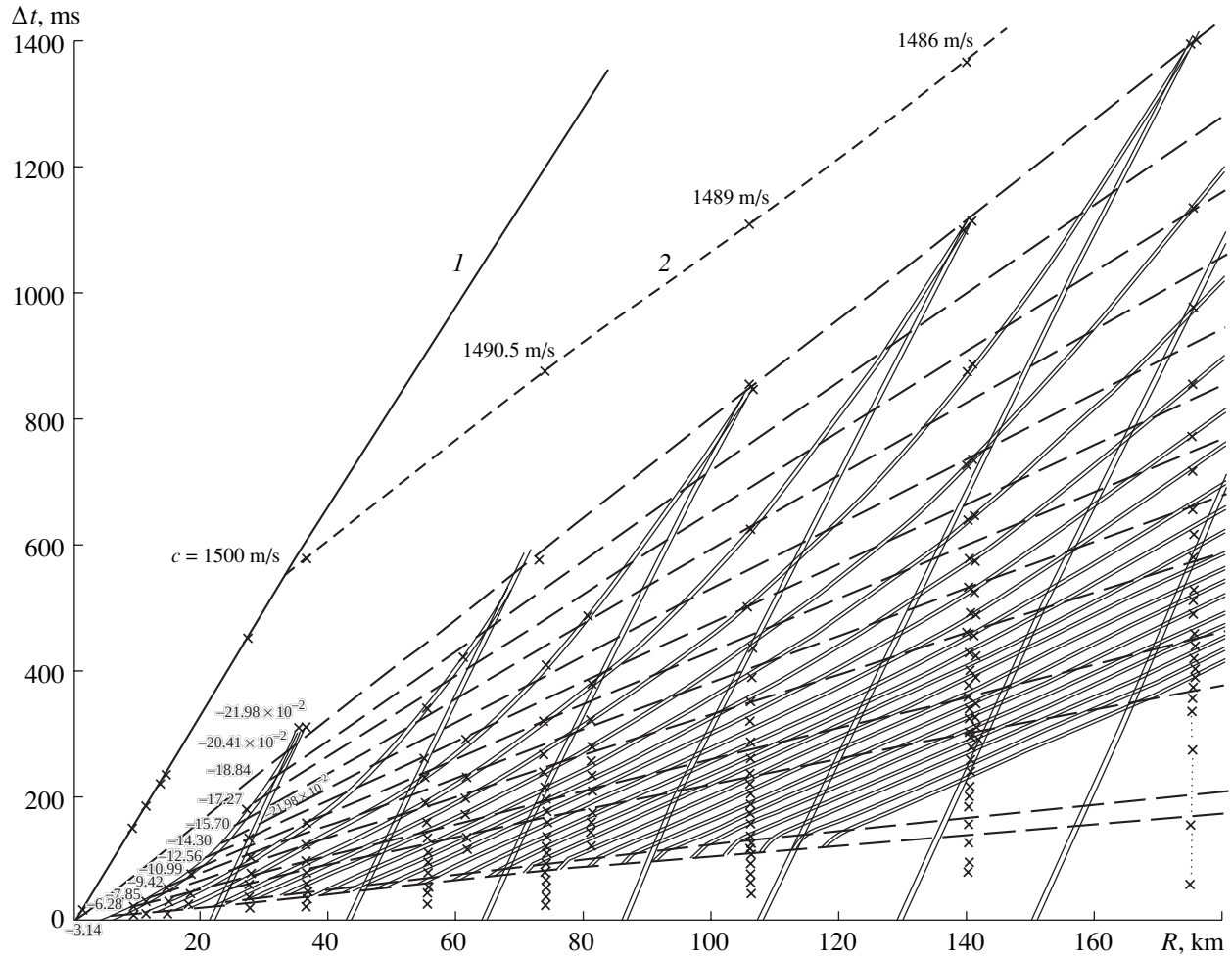

Fig. 6. Space–time characteristics of the sound field in the underwater sound channel. The source and receiver depths are 35 m. The parabola-like curves and the approximating straight lines are obtained by calculation, and the crosses indicate the experimental data.

time spectra, the number of produced ray cycles, the cycle lengths at the given characteristic angles, and the deformation of the signal structure with varying source and receiver positions. When the reception point moves off the channel axis, the number of arriving signals decreases and the total duration of the signal set becomes shorter, in accordance with the isospeed profiles. The chart also allows one to determine the critical frequency of the whole waveguide (1.8 Hz in our case) and the critical frequencies for the waveguide layers of an arbitrary thickness, from several meters to the ultimate sea depth. On the basis of the chart, one can plot the dispersion curve, determine the structure of the field produced by the first normal wave for the whole frequency band, estimate the validity limits for ray and wave techniques to be applied to analyzing and calculating the sound field, and find the extent to which the channel is filled with the refracted sound field at different frequencies. The good agreement between the experimental and calculated space–time and space–angular field structures allows one to correctly formulate and successfully solve inverse problems for the underwater sound channel. Thus, with the known waveguide parameters (the space–time and space–angular characteristics), the determination of the coordinates of the sound source becomes feasible. Equally, one can reconstruct the waveguide parameters from the measured characteristics of the sound field if the source and the receiver positions are known. In our case, an accuracy of 1–4% can be attained in estimating the distance from the source, which is comparable with the accuracy of other methods.

The author of this paper has developed a ray method for determining the source coordinates. This method is based on the data of the aforementioned type, on the established basic features of the sound field in different waveguides, and on numerous calculations of time and angular structures of the sound field in moderate-latitude and tropical regions of the Atlantic, Pacific, and Indian Oceans, including the Mediterranean, Norwegian, and other seas, with source and receiver depths varying from 5 to 1000 m. The method is patented (in cooperation with V.A. Kakalov) with the priority from

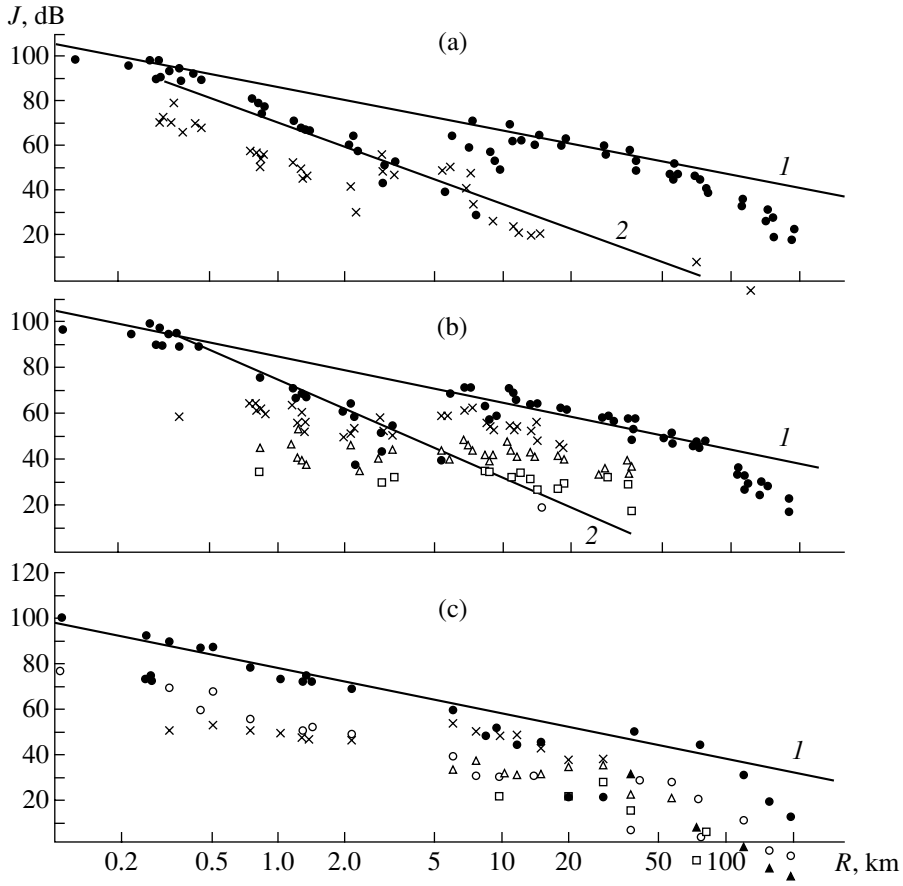

Fig. 7. Decays of the sound levels for the source and receiver depths (a, b) 35 and (c) 20 m. The dots indicate the mean levels of the refracted sound field. The straight lines correspond to the laws (*1*) $J \approx r^{-2}$ and (*2*) $J \approx r^{-4}$; (a) the crosses mean forerunners; (b) the crosses, triangles, rectangles, and circles indicate single, twofold, triple, and fourfold bottom–surface reflections, respectively; (c) the crosses, empty triangles, and rectangles indicate single, twofold, and triple bottom–surface reflections, respectively, and the full triangles show the forerunners.

1969. The description of the method is supplemented with the necessary and sufficient conditions for the problem to be solved. Also, the unambiguity of the solution is studied, and the required specifications and resolution of the receiving systems and recording equipment are determined.

Figure 7 shows the range decays of the sound levels in the underwater (Figs. 7a, 7b) and surface (Fig. 7c) channels for source and receiver depths of 35 and 20 m, respectively. The abscissa axis represents the distance (on a logarithmic scale), and the ordinate axis represents the sound level (in decibels). The upper straight lines (*1*) correspond to the spherical spread. Other lines (*2*) approximate the decay of the forerunners, which obeys a power-law dependence ($J \sim r^{-4}$). The values in the plot are obtained by averaging the maximal amplitudes of all signals in the sets. At long ranges, these values often correspond to the mean amplitudes of the near-axis components, which overlap in time and propagate at low characteristic angles. Variations in the levels of individual signal quartets were not higher than +3 dB relative to the mean value. The decays of the sound level agree well with the spherical law. At the end of the path, an additional exponential decay manifests itself because of the sound absorption in the sea water and the scattering by the rough sea surface. At 175–180 km, the total loss is 20–22 dB. The total attenuation coefficient that includes the dissipative loss and the effects of scattering by the inhomogeneities is not higher than 0.10–0.13 dB/km, with a depth-averaged water temperature of 8–9°C and a salinity of 18–23‰. The results obtained lead to the conclusion that, at a frequency of 3 kHz, the true value of the absorption coefficient (i.e., the value caused by nothing but energy dissipation) is close to 0.09–0.10 dB/km.

In the near zone of the surface channel, the field decay follows the spherical law. Starting from 2–6 km, a considerable deviation from the straight line is observed reaching 10 dB at 8–15 km and 25–30 dB at 20–38 km. At long ranges, the signals propagating in the surface channel (with an angular width of 0.2° of the ray bundle) attenuate rather rapidly and cannot be

noticed in the records. At these long distances, only refracted components of the field with large characteristic angles (12°–14°) are present; they propagate in deep water layers and undergo surface reflections. The levels of the signals propagating solely in the surface channel can be approximated by the exponential with an exponent of 0.5–0.7 dB/km. In spite of the additional loss due to multiple reflections by the rough surface, the levels of the deep-water field components decay rather slowly: the total loss is 20–22 dB at a distance of 180 km, this value corresponding to 0.11–0.12 dB/km and coinciding with that for the purely refracted components, which are attenuated by nothing but the scattering from the volume inhomogeneities. Thus, comparing these two values of losses, one can see that they are of the same order of magnitude, thereby allowing one to identify the factors causing them. In other words, one can estimate the extent of sound absorption (which is close to the purely dissipative loss) governed by the water temperature and salinity. Note that the estimated loss coefficients are lower than those obtained from the relation $a = 0.027f^{3/2}$ dB/km (0.14 dB/km in our case) and are nearly two times lower than the loss (0.187 dB/km) given by the formula $a = 0.036f^{3/2}$ dB/km, where f is the frequency in kilohertz.

In accordance with the aforementioned increased attenuation in the surface channel, it is advantageous to consider its origin in more detail and quantitatively estimate the allowable loss determined from the known theoretical models for the observed hydrological and meteorogical environments. For this purpose, we specify the loss to be 20–22 dB according to the measured value at a distance of 38 km (Fig. 4a). In view of the fact that, in accordance with the calculations, the focusing factor of the refracted rays was no higher than +5 to +6 dB, the estimated loss seems to be very high. The calculated loss due to the scattering by the rough surface is far from that high, even for the maximal observed wind speed, which was 8 m/s. With the surface spectrum of the Pierson–Moskovits type, the rms surface height is $h = 0.35$ m. At grazing angles of 1.26° and 1.47°, for the limiting rays of the ray bundle, the Rayleigh parameter is 0.018 and 0.022, and the loss is as little as 0.148 and 0.219 dB per bounce. In view of the numbers of reflections for the axis and limiting rays (10 and 8, respectively), the total loss due to the surface reflections should be no higher than 1.48 and 1.75 dB. According to the experimental estimates for the refracted components propagating in the underwater channel and for those having maximal characteristic angles and reflected by the surface at the grazing angles 0°–5° (see Fig. 6), the absorption- and scattering-caused losses are nearly the same for these components and are no higher than 0.10–0.13 dB/km. Thus, at a distance of 38 km, the total loss caused by the surface scattering (1.5 dB/km on average) and absorption (4.3 dB/km on average) is 5.8 dB. Since the generation of air bubbles by the surface waves at sea states lower than Beaufort 3 is nearly absent, they have no noticeable effect on the loss and can be neglected in estimating the diffraction-caused sound penetration below the discontinuity layer. Even if one takes into account the air bubbles, their effect can hardly be greater than that of the rough surface. As a result, in view of all these losses (7.3 dB), the regular component should lose about 14 dB (i.e., 0.37 dB/km) in the surface waveguide due to the diffraction-caused leakage of the energy below the discontinuity layer. In obtaining these data, we assumed that the decay of the field level obeys the spherical law in the surface waveguide with a zero propagation anomaly. According to the calculations, starting from some distance, the level decay follows the law $J \approx r^{-1}$. In our case, this distance is $r_0 = 5$ km. Then, the positive propagation anomaly at a distance of 38 km will be 8.8 dB. The total loss will reach 23.5 dB or 0.6 dB/km. Such a value of the loss in the surface waveguide cannot be obtained from ray considerations and can only be explained by wave theory.

ACKNOWLEDGMENTS

This work was supported by the Russian Foundation for Basic Research, project no. 99-02-18359.

REFERENCES

1. L. M. Brekhovskikh, *Waves in Layered Media*, 2nd ed. (Nauka, Moscow, 1973; Academic, New York, 1980).
2. N. V. Studenichnik, in *Abstracts of 9th All-Union Acoustical Conference, Section D IV* (Acoustics Inst., USSR Academy of Sciences, Moscow, 1977), p. 45.
3. L. M. Brekhovskikh, Yu. P. Lysanov, and N. V. Studenichnik, Dokl. Akad. Nauk SSSR **239** (1), 211 (1978).
4. N. V. Studenichnik, in *Proceedings of Third Seminar on Acoustic Statistical Models of the Ocean* (Acoustics Inst., USSR Academy of Sciences, Moscow, 1981), p. 48.
5. N. V. Studenichnik, in *Proceedings of Fourth Seminar on Acoustic Statistical Models of the Ocean* (Acoustics Inst., USSR Academy of Sciences, Moscow, 1982), p. 19.
6. N. V. Studenichnik, in *Proceedings of Thirteenth All-Union School–Seminar on Statistical Hydroacoustics* (Acoustics Inst., USSR Academy of Sciences, Moscow, 1984), p. 29.
7. N. V. Studenichnik, Akust. Zh. **43**, 283 (1997) [Acoust. Phys. **43**, 245 (1997)].
8. N. V. Studenichnik, in *Proceedings of School–Seminar of Academician L.M. Brekhovskikh* (GEOS, Moscow, 1998), p. 330.
9. J. R. Buck, J. C. Preisig, and K. E. Wage, J. Acoust. Soc. Am. **103**, 1813 (1998).
10. G. V. Norton and J. C. Novarini, J. Acoust. Soc. Am. **103**, 1836 (1998).

Translated by E. Kopyl

Acoustical Physics, Vol. 49, No. 2, 2003, pp. 217–229. Translated from Akusticheskiĭ Zhurnal, Vol. 49, No. 2, 2003, pp. 262–277.

Some Applications of the Reciprocity Principle in Experimental Vibroacoustics[1, 2]

F. J. Fahy

Institute of Sound and Vibration Research, University of Southampton, Southampton, S017 1BJ United Kingdom

Received October 21, 2002

This paper is dedicated to the memory of Professor Leonid Lyamshev, whose publications inspired my initial interest in vibroacoustic reciprocity

Abstract—The principles of acoustic and vibroacoustic reciprocity are explained. Examples are then given of applications of acoustic reciprocity to the experimental analysis of sound radiation by various systems of interest to noise control engineers. The final part of the paper is devoted to a presentation of examples of the practical application of Lyamshev reciprocity to problems of identifying and quantifying sources of noise that operate in a variety of engineering systems. © *2003 MAIK "Nauka/Interperiodica".*

1. INTRODUCTION

In its most general sense, the principle of vibrational reciprocity states that the response of a linear system to a time-harmonic disturbance that is applied at some point by an external agent is invariant with respect to exchange of the points of input and observed response.

The Hon. J.W. Strutt (Lord Rayleigh) presented the most comprehensive proposition of the general principle of reciprocity for vibrating systems in a paper read before the Mathematical Society of London in 1873. However, it was the great German scientist Hermann von Helmholtz who first asserted that acoustic fields exhibited reciprocity, in a paper of 1860 on the acoustic behavior of open-ended pipes. He subsequently formalized his expression of the principle as applying to simple sources (point volumetric monopoles) and field point pressures in the presence of an arbitrary number and form of rigid scatterers in the fluid.

In a development of crucial significance for the practical application of reciprocity, Rayleigh demonstrated that the principle can be extended to harmonic vibration of all *nonconservative* (dissipative) vibrating systems in which the dissipative forces are linearly dependent upon the velocities, or relative velocities, of the system elements. He concluded his 1873 paper by stating, in relation to acoustic reciprocity, that *"we are now in a position to assert that* (acoustic) *reciprocity will not be interfered with, whatever the number of strings, membranes, forks, etc. may be present, even though they are subject to damping."* Rayleigh was aware that his reciprocity theorem *"on account of its extreme generality, may appear vague."* In this he was indeed prescient. It was not until 1959 that the Russian scientist L.M. Lyamshev published a formal proof of the correctness of this supposition and paved the way for many of the modern applications of the principle of reciprocity to vibroacoustic problems, a selection of which are presented below. This paper is dedicated to his memory.

The paper begins with a reiteration of the basic principle as enunciated by Rayleigh. Special cases that are of interest to acoustical engineers and scientists are then presented. Following a review of the general problem of predicting the sound field generated by a vibrating body, the remainder of the paper is devoted to a presentation of a selection of examples which illustrate the practical and economic benefits of applying the Lyamshev form of reciprocity to the experimental determination of the vibroacoustical behavior of complex systems. Some of the examples are taken from my 1995 *Acustica* paper [7], and others are taken from more recent publications.

2. RAYLEIGH AND RECIPROCITY

2.1. Vibrational Reciprocity

In his paper of 1873, Lord Rayleigh presents the general theory of vibrational reciprocity as applied to passive linear, distributed elastic systems having time-invariant physical parameters. He employs the classical description of the dynamic configuration of a system in terms of a set of independent coordinates ψ which specify the time-dependent displacements of the discrete system elements: these are the degrees of freedom of the system. He expresses the work done in an arbitrary

[1] This paper was presented by the author in English.

[2] The beginning sections of this paper are extracted from a paper published in *Acustica* [7], for which the permission of the publishers is gratefully acknowledged.

1063-7710/03/4902-0217$24.00 © 2003 MAIK "Nauka/Interperiodica"

small displacement from equilibrium (potential energy) as a homogeneous quadratic function of the coordinates ψ, and the kinetic energy as a homogeneous quadratic function of coordinate velocities $\dot{\psi}$, as follows:

$$V = \frac{1}{2}c_{11}\psi_1^2 + \frac{1}{2}c_{22}\psi_2^2 + \ldots + c_{12}\psi_1\psi_2 + c_{23}\psi_1\psi_3\ldots$$

and

$$T = \frac{1}{2}a_{11}\dot{\psi}_1^2 + \frac{1}{2}a_{22}\dot{\psi}_2^2 + \ldots + a_{12}\dot{\psi}_1\dot{\psi}_2 + a_{23}\dot{\psi}_2\dot{\psi}_3\ldots.$$

Lagrange showed in 1788 that the equations of motion of a system may be derived from these energy functions through the equation

$$\frac{d}{dt}\left(\frac{\partial T}{\partial \dot{\psi}}\right) - \frac{\partial T}{\partial \psi} + \frac{\partial V}{\partial \psi} = \Psi,$$

where Ψ are the forces that are not associated with potential energy of system deformation (e.g., applied external forces).

In the absence of dissipative forces, it is possible to find a special set of coordinates that allow the energies to be expressed as functions purely of the squared displacements and velocities: in other words, the product terms disappear. We know these as the natural modes of the system; any form of free vibration may be expressed in terms of a sum of vibrations in each natural mode, the associated motions being independent.

Rayleigh identified another group of forces for which a function of form similar to T and V may be identified. These are forces which are proportional to the velocities, or relative velocities, of the original system coordinates. They act so as to dissipate vibrational energy into heat: gyrostatic forces, which are also proportional to velocities, are excluded from this category. The associated *dissipation function* takes the form

$$F = \frac{1}{2}b_{11}\dot{\psi}_1^2 + \frac{1}{2}b_{22}\dot{\psi}_2^2 + \ldots + b_{12}\dot{\psi}_1\dot{\psi}_2 + b_{23}\dot{\psi}_2\dot{\psi}_3\ldots.$$

Rayleigh says *"It is well known that friction, and other sources of dissipation, may be usefully represented as following this law approximately; and even when the true law is different, the principal features of the case will be brought out."* In this statement, he anticipates possible problems with nonviscous frictional mechanisms.

The presence of dissipative mechanisms generally precludes the possibility of finding an independent set of coordinates representing free vibration in independent modes in which displacements are everywhere in phase (or antiphase). Only special (generally artificial) distributions of damping yield such uncoupled modes. However, this condition is not necessary for vibrational reciprocity to hold good.

After separation of the dissipative forces from the term Ψ, substitution of the three functions T, V, and F into Lagrange's equation yields the following system of equations:

$$\begin{aligned}
\overline{11}\psi_1 + \overline{12}\psi_2 + \overline{13}\psi_3 + \ldots &= \Psi_1,\\
\overline{21}\psi_1 + \overline{22}\psi_2 + \overline{23}\psi_3 + \ldots &= \Psi_2,\\
\overline{31}\psi_1 + \overline{32}\psi_2 + \overline{33}\psi_3 + \ldots &= \Psi_3,
\end{aligned}$$

where each coefficient $\overline{rs}$ is an abbreviation for the quadratic operator; thus,

$$\overline{rs} \text{ is equivalent to } (a_{rs}) + (b_{rs}) + (c_{rs}).$$

These operations exhibit the important property that $\overline{rs} = \overline{sr}$. If a point harmonic force is applied to one coordinate and the oscillatory displacement is observed at another, solutions of the above equations of motion show that the complex ratio of displacement to force is invariant with respect to exchange of input and output coordinates.

In the "Acoustician's Bible," *The Theory of Sound*, Rayleigh presents explicit examples which clarify the implications of his theory. These are important because they demonstrate applications in which forces and couples, as well as translational and rotational displacements, are involved. The cases are illustrated in Fig. 1, in which the tilde indicates complex amplitude of a harmonically varying quantity.

2.2. Acoustic Reciprocity

A homogeneous fluid at rest behaves like a linear elastic medium in response to small applied disturbances and therefore obeys Rayleigh's vibrational reciprocity principle. In air, energy dissipation arises from viscothermal and molecular relaxation mechanisms; but, in cases of practical interest in the field of vibroacoustics, dissipative effects are weak, and reciprocity is found to apply provided that nonlinear sound propagation is avoided (sound pressure level less than about 130 dB in air). However, the acoustic input and field variables that are most appropriate (and measurable) differ from those appropriate to solid structural systems. In a fluid, unlike a structural plate or shell, it is difficult to generate a known force in a known direction and also difficult to measure particle displacement or velocity (although the development of sound intensity measurement instruments has eased the latter problem). The fundamental acoustic source (the point monopole) displaces fluid at a rate described by its volume velocity Q, and the most common form of acoustic transducer, the pressure microphone, transduces the force F applied by the fluid to its diaphragm. Provided that this force is not significantly altered by diaphragm motion and that the microphone diaphragm is small compared with an acoustic wavelength (omnidirectional), this system should exhibit reciprocal behavior (for exchange of positions) in the ratio F/Q, according to

Rayleigh's principle. Rayleigh also extended the reciprocity relationship to acoustic dipoles and particle velocities in the resulting sound fields. Since a point dipole can also be represented by a point force applied to a fluid, this should not cause any surprise. The basic cases of acoustic reciprocity in fluids bounded by rigid surfaces are illustrated by Fig. 2.

3. FLUID BOUNDARIES

The question of the influence of the dynamic behavior of the boundaries of a fluid on the validity of the acoustic reciprocity principle has exercised the minds of many scientists (see, for example, [2]). Rayleigh implied that the presence of *locally reacting boundaries*, or, in modern parlance, *impedance* boundaries, does not invalidate reciprocity. Subsequently, Skudrzyk (1954) confirmed the correctness of this conclusion. The physical meaning of these terms is that the ratio of complex amplitude of surface pressure at any point on a surface to the complex amplitude of particle velocity normal to that surface is independent of the nature of the incident acoustic field (e.g., plane wave, diffuse field, spherical field). The implication is that disturbances simultaneously created elsewhere on the surface are not effectively communicated to the point under consideration. This is a reasonable assumption in the case of highly dissipative boundary systems, such as fibrous absorbers, but is not satisfied by elastic structures such as plates or shells or all interfaces with other elastic media, such as that between the sea and a mud or rock bottom.

The implication of Rayleigh's general reciprocity principle is that all components taking part in the dynamic behavior can be incorporated into the total system, subject to the *proviso* that their kinetic, potential and dissipational energy functions are positive definite quadratic functions of velocity. The practical implications for the application of reciprocity to vibroacoustic problems are profound. It was nearly a hundred years later that Lyamshev formally demonstrated that linear elastic structures that are contiguous with a fluid may be incorporated into the total dynamic system to which reciprocity applies [20, 21]. An important practical consequence of this conclusion is that the transfer function between a mechanical vibrational force applied to an elastic plate or shell and the resulting sound pressure in a contiguous fluid (at rest) may be determined by insonifying a structure by means of an omnidirectional "point" source, as illustrated by Fig. 3. The ratio of sound pressure to applied force is equal in magnitude and opposite in sign to the ratio of the acoustically induced response acceleration component in the force direction to the volume acceleration dQ/dt (source strength) of the source. In observance of the dedication of this paper we shall refer to this specific form of reciprocal relation as *Lyamshev reciprocity.*

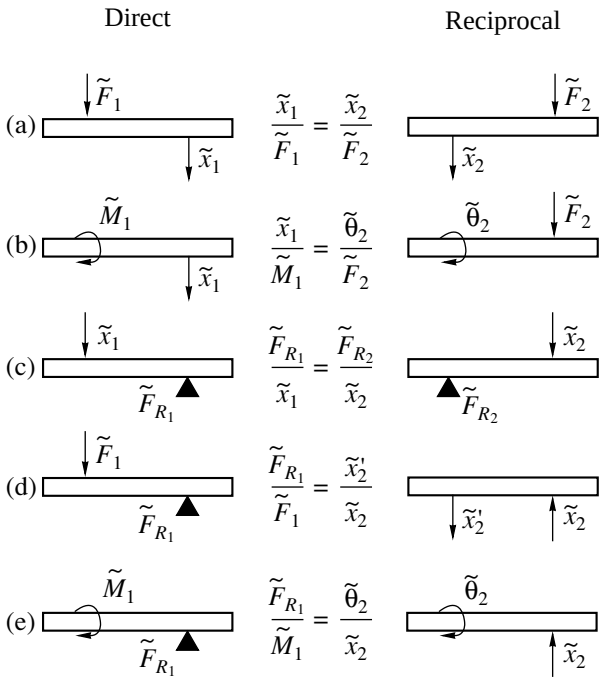

Fig. 1. Various realizations of Rayleigh's reciprocity principle (~indicates complex amplitude of a time-harmonic quantity).

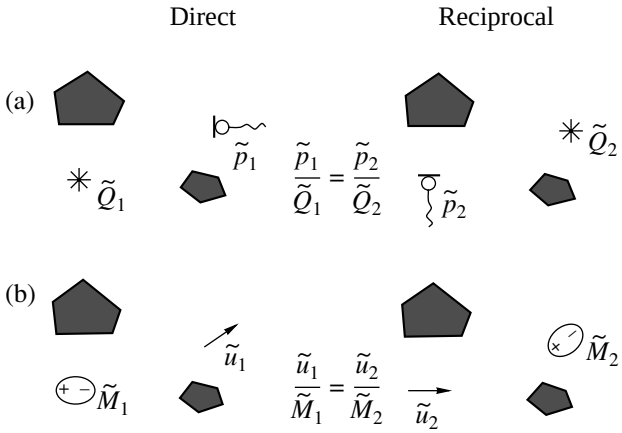

Fig. 2. Acoustic reciprocity in fluids: (a) monopole source; (b) dipole source.

As a corollary, the transfer function between an acceleration externally imposed at a point on a structure and the resulting sound pressure at an observation point in a contiguous fluid is reciprocal with that between the volume acceleration (source strength) of a point monopole located at the former observation point and the reaction force generated at the point on the structure by a constraint which forces the structure to have zero velocity in the direction of the originally applied velocity but otherwise leaves the structure free.

It is very difficult indeed to control and quantify the three components of force applied to a structure by an

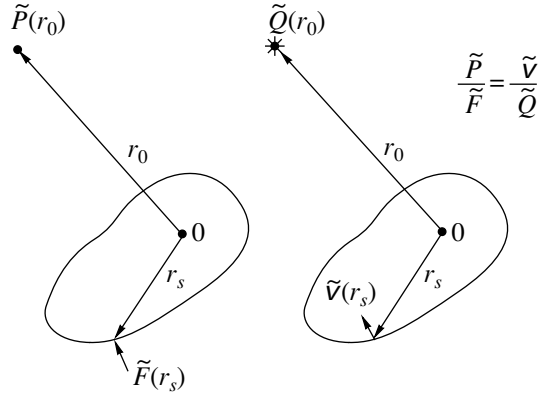

Fig. 3. Lyamshev reciprocity relation for elastic structures excited by point forces.

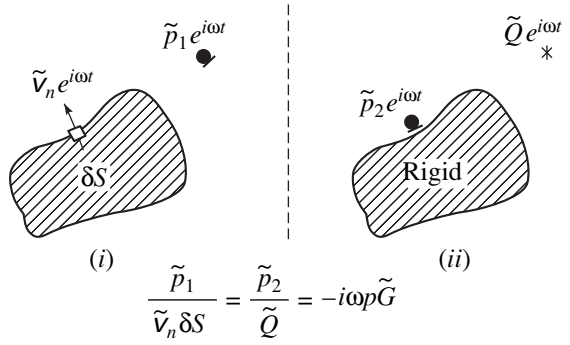

Fig. 4. Reciprocal measurement of the Green's function having zero normal derivative at the surface.

electromagnetic shaker or even by an impact hammer and even more difficult to apply a controlled couple. A particular practical advantage of the application of Lyamshev reciprocity to problems involving excitation of mechanical structures by localized forces and couples is that triaxial and rotational accelerometers may be used to quantify the relative contributions to the radiated sound of the three orthogonal components of applied forces and couples.

4. SOUND RADIATION BY VIBRATING STRUCTURES

4.1. The General Problem

Before specifically illustrating the applications of Lyamshev reciprocity, we review the general problem of relating the surface vibration field of an arbitrary body to the radiated sound field and present a few examples based upon acoustic reciprocity. The prediction of the sound field radiated by a vibrating body is a problem shared by many theoreticians and practitioners in the field of engineering acoustics, including the designers of active sonar transducers, submarine hulls, car engines, and loudspeaker cabinets. Analytical estimates are largely limited to bodies of regular geometry that can be modeled as rigidly baffled flat plates or cylindrical shells. In cases of bodies of irregular geometry, the theoretical requirement is to determine the *Green's function* that relates surface normal vibrational acceleration to the sound pressure in the radiated field. Computational techniques such as finite element and boundary element analysis are now available for treating radiation from bodies or arbitrary geometry. They employ the *free-space* Green's function, which means that the radiated field is expressed in the distributions of *both* normal acceleration and pressure over the surface of the vibrating body (or pressure difference in the cases of thin open shells).

If the structure radiates into a confined, or partially confined, volume of fluid, such as that enclosing the engine of an automobile, or into a volume of fluid containing a number of other bodies that act as acoustic scatterers, such as in an industrial workshop, the computation must account for the pressure field over the whole of the exposed surface(s). This presents an enormous task, even with today's computer technology. An alternative empirical method of determining the appropriate Green's function is offered by the reciprocity principle; it is illustrated by Fig. 4.

An elemental area of a vibrating surface may be represented by a monopole source acting at the surface of the otherwise *motionless* body. The transfer function between source and receiver point is identical with that generated on the surface of the *rigid* body by a monopole at the original receiver point, irrespective of the acoustical environment (provided it is linear and has time-invariant physical properties). The total field generated by a continuous distribution of time-harmonic normal acceleration over the surface of the body may be represented by a discrete array of surface monopoles of appropriate amplitude and phase. Hence, the total field at a receiver point may be estimated by summing the product of measured (or calculated) surface accelerations, sampled at a set of discrete points on the surface, with the corresponding Green's functions. (If the surface vibration field is not periodic, but random, the expression for the mean square pressure in the fluid involves the cross-spectral distribution (or space–time correlation) properties of the field.) The Green's functions are measured by insonifying the rigid body with a calibrated omnidirectional point source and measuring the transfer function between the source strength and (blocked) sound pressures on the surface of the body with a small, omnidirectional roving microphone placed close to the surface; to be valid, this measurement requires that the impedance of the structure be sufficiently large that its response affects the surface pressure to a negligible degree. A major practical advantage of the reciprocal measurement of Green's functions is that the "rigid" structure may be represented by a reduced scale model of the source geometry, constructed in wood, the

insonification frequency range being scaled inversely as the length scale. Naturally, the acoustic environment should be the same for the reciprocal measurement as for the required estimation.

This technique may be used to identify those regions of a radiator contributing most strongly to the sound pressure received at a field point. Phasor (complex amplitude) or cross-spectral representation is necessary in the case of spatially coherent sources. However, in many cases, it is necessary only to evaluate sound pressure in 1/3 octave bands (or wider). The integration over frequency is often found to weaken the spatial correlation of the structural vibration field, especially in cases where the analysis band contains a number of structural mode resonance frequencies, often to such an extent that relative phase data may be neglected. Only the squared magnitudes of the Green's functions are then required to compute the radiated sound level.

If the radiation conditions of interest are essentially free field (e.g., in the deep sea), a further simplifying refinement is possible. The reciprocal determination of the Green's functions will be performed under anechoic conditions. In this case, the source needs to generate a uniform, spherically spreading field only over the volume occupied by the body, which is no problem if the body subtends a small solid angle at the source.

4.2. Some Examples

4.2.1. Tire noise

It is difficult to separate the contribution of the airborne sound radiated by a tire to noise in an automobile passenger compartment (cabin) from that generated by structure-borne transmission without disconnecting all structural connection paths. In an attempt to avoid this complication, Kim [19] applied reciprocity to the problem. The appropriate transfer functions were determined by operating an omnidirectional point source within the cabin and measuring the distribution of blocked sound pressures on the tire. By combining these with many point samples of the vibrational field of the tire surface, he was able to determine the relative contributions of the various regions of the tire surface to the noise at the location of the point source in the cabin.

4.2.2. Engine noise

In another automotive application, a number of automobile manufacturers and suppliers of insulation materials now routinely apply acoustic reciprocity to the determination of the contributions of the surface vibration of various regions of engines and ancillary equipment to noise in the cabin by measuring the blocked sound pressures generated on those regions by an omnidirectional source in the cabin. The effect of varying the sound insulation materials that line the cabin is then easily quantified, as are the effects of penetrations of the firewall (bulkhead), air conditioning ducts, and other possible sound leakage paths. This technique complements the use of engine noise simulators which must be installed in the engine compartment in place of the engine. However, characterization and quantification of the complicated surface vibration fields for the purpose of determining the absolute level of sound transmitted to the cabin are not straightforward.

4.2.3. Rail vehicle noise

One approach to the reduction of railside noise generated by the vibration of the wheels of railway vehicles and of the associated rail is to place low railside barriers beside the track. In order to evaluate the insertion loss of such barriers, it is necessary to correctly model the wheels and rail as acoustic sources, together with the diffraction behavior of the barrier. Although theoretical models may be employed for this purpose, the scattering of the radiated sound by the complex geometry of the lower parts of a rail wagon, together with the scattering and absorption properties of the ballast and sleepers, render this a formidable computational task.

An experimental technique, based upon acoustic reciprocity, which offers a simpler means of estimating the effectiveness of barrier shielding of wheel noise has been developed [11]. A calibrated, omnidirectional, acoustic source is located at a number of railside target receiver positions in turn, and the (complex) transfer functions between the source volume velocity and the (blocked) sound pressure at points judicially distributed over the wheel surface are determined over the frequency range of importance. This procedure may be applied to a small-scale model if ballast effects are discounted. The distribution of the normal vibrational velocity of a wheel surface at the selected points may either be calculated theoretically or measured; these are converted to a set of equivalent (substitution) monopole and doublet point sources. The resulting source distribution may either retain relative phase, in which case the relative phases of the transfer functions must be retained, or be represented as a set of uncorrelated monopoles and doublets, in which case only the transfer function amplitudes are required. Appropriate combination of equivalent point source strengths with the transfer functions yields the sound pressure at each target point. The barrier insertion loss is determined using the transfer functions measured reciprocally in the presence and absence of the barrier. Comparison with the results obtained from a mechanical source substitution method (described below) indicated that the inclusion of doublets to represent wheel flange and web vibration, together with retention of the relative phases of the equivalent point sources, was essential for accurate estimates of barrier insertion loss.

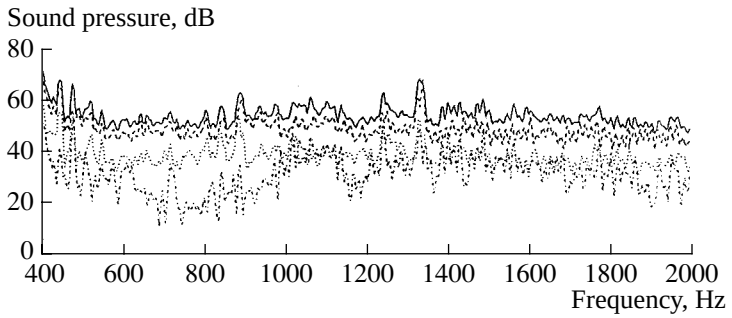

Fig. 5. Estimated sound pressure contributions from various components: (solid line) complete engine, (dashed line) engine block, (dotted line) valve cover, (dash–dotted line) gear box.

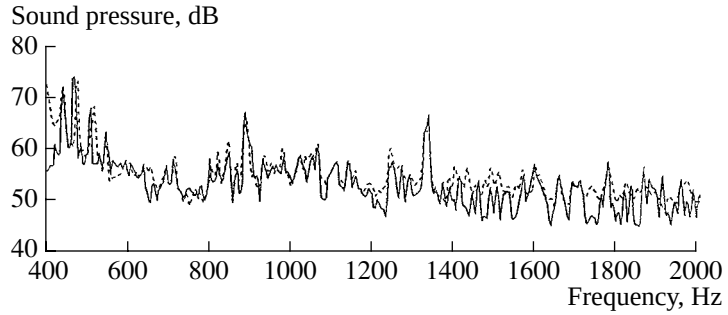

Fig. 6. Comparison of the measured sound pressure level spectrum with that estimated from reciprocity and near-field intensity measurements.

4.2.4. Radiation modes of a vibrating structure

Radiation modes are defined as distributions of normal surface velocity that radiate independently so that the total sound power radiated by a vibrating structure is given by the sum of the powers radiated by each mode. The radiation modes of a structure may be found by analysis of the Green's functions that relate radiated sound pressure to surface. These functions are readily determined experimentally by the application of acoustic reciprocity velocity [3].

4.2.5. The problem of vibration field sampling

A fundamental problem in attempting to apply the reciprocity principle as described above is the characterization of the surface vibration field, particularly in cases where the structure is highly nonuniform in stiffness or mass distribution. It is clear that it is only necessary to acquire data that will allow a reasonably accurate estimate of the supersonic wavenumber components ($k_s \le k$) of surface vibration, because the subsonic components ($k_s > k$) do not radiate. A study of the spatial aliasing effect has been made on a vibrating rectangular panel [15].

One approach to overcoming this sampling problem was successfully developed under the auspices of the European Research program PIANO. Measurements of the 1/3 octave spatial cross-correlation characteristics of the surface vibration field of truck engines indicated that regions separated by more than about 300 mm were almost uncorrelated in the frequency range that contributed most strongly to pass-by noise. Hence, the surface vibration could be represented by an array of *uncorrelated* "monopoles." The strengths of each monopole were determined from near-field intensity scans [28]. This technique has also been used to evaluate the contribution of airborne radiation by marine engines to sound in the water [30].

In a study of the sound radiation by a motored diesel engine, Zheng *et al.* [33] applied the monopole array model to the determination of the contribution of various components of the engine to the sound pressure level at a point in the radiation field. The principal results are shown in Figs. 5 and 6. The discrepancy between the predicted and directly measured sound pressure at frequencies below 450 Hz is attributed to the failure of the uncorrelated monopole model to correctly represent a discrete overall mode of the engine.

In order to overcome the problem of spatial aliasing, the Institute of Sound and Vibration Research of the University of Southampton has devised two forms of noncontact spatial filters for the measurement of surface vibration fields. One takes the form of an anechoically terminated tube in which a microphone senses the plane wave field generated by a vibrating surface in close proximity to the open end [13]. This

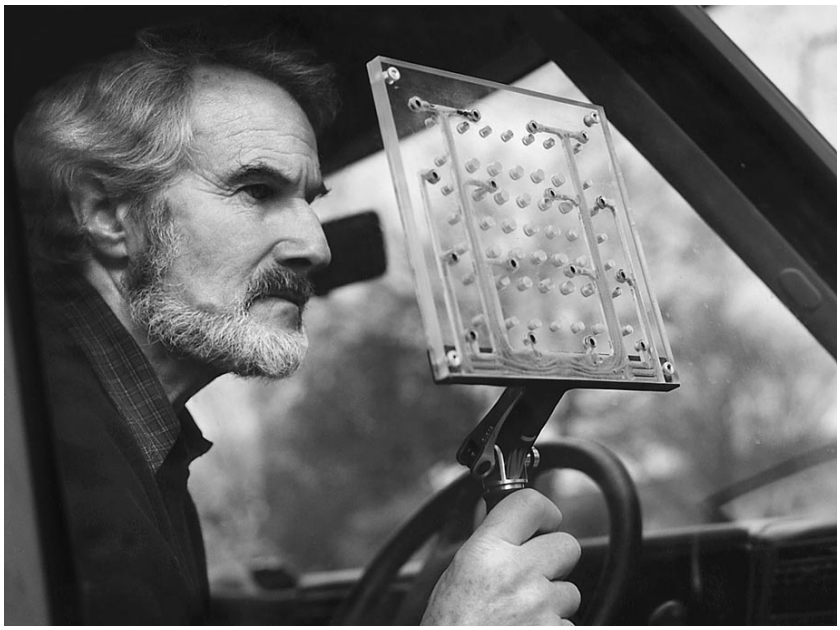

Fig. 7. The ISVR volume acceleration sensor (VAS) (photo).

has been applied with moderate success to the identification of the regions of the internal surface of the driver's cabin of a light commercial vehicle to the sound pressure level at the driver's ear [14]. This study clearly indicated that it is necessary to retain the relative phase data for the cabin surface vibration field below about 300 Hz but not at higher frequencies. This conclusion is in accord with the results of other studies of sound radiation into vehicle cabins by envelope vibration.

The second area-integrating, noncontact, surface vibration transducer (volume acceleration sensor (VAS)) utilizes an array of pressure difference microphones incorporated in a perforated Perspex sheet (Fig. 7). It is specifically designed for the sampling of vehicle surface vibration in the frequency range 30–500 Hz [8].

5. APPLICATIONS OF LYAMSHEV RECIPROCITY

Sound radiation for structures subject to localized input forces and couples is of considerable practical interest; for example, vibrational sources mounted on resilient isolators are often modeled as force sources acting on the support structure. The Lyamshev form of the reciprocity principle can be usefully applied to such problems. As mentioned in "Structure-Borne Sound" [5], points of minimum structural response to incident acoustic field would appear to be good locations at which to mount such resilient supports. Unfortunately, however, they do not unequivocally indicate good points to make *rigid* attachments to sources of vibration because such attachments kinematically constrain the attachment points and do not represent sources of known force. The concepts and models described in Sections 5.1–5.3 below are not essentially dependent upon reciprocal methods of measurement, but reciprocity may be advantageously employed in their implementation.

5.1. Noise Generation by Known Forces Acting at Known Locations

The evaluation of the relative contributions of mechanical vibrational inputs to the sound field radiated by the excited structure forms a central procedure in the application of noise control technology to the reduction of noise generated by road, rail, and marine vehicles. If the locations and magnitudes of the force/couple inputs are known, Lyamshev reciprocity may be used to determine the force-to-pressure transfer functions relevant to target receiver positions in a fluid in which the inputs generate sound. An omnidirectional acoustic source is used to insonify the structure and the components of acceleration responses at the (unconstrained) input positions in the direction of the input forces are determined. An excellent example of the application of this technique is presented by Pankoke [26]. The sound pressures generated at each of the driver's ears by the vibrational force acting at the rear support of a car engine/gearbox were estimated by determining the acceleration produced at the (unconstrained) support by a special acoustic source that radiated from the two "ear" orifices of a dummy driver's head. The principal results are shown in Fig. 8. This technique, which is now routinely applied by many

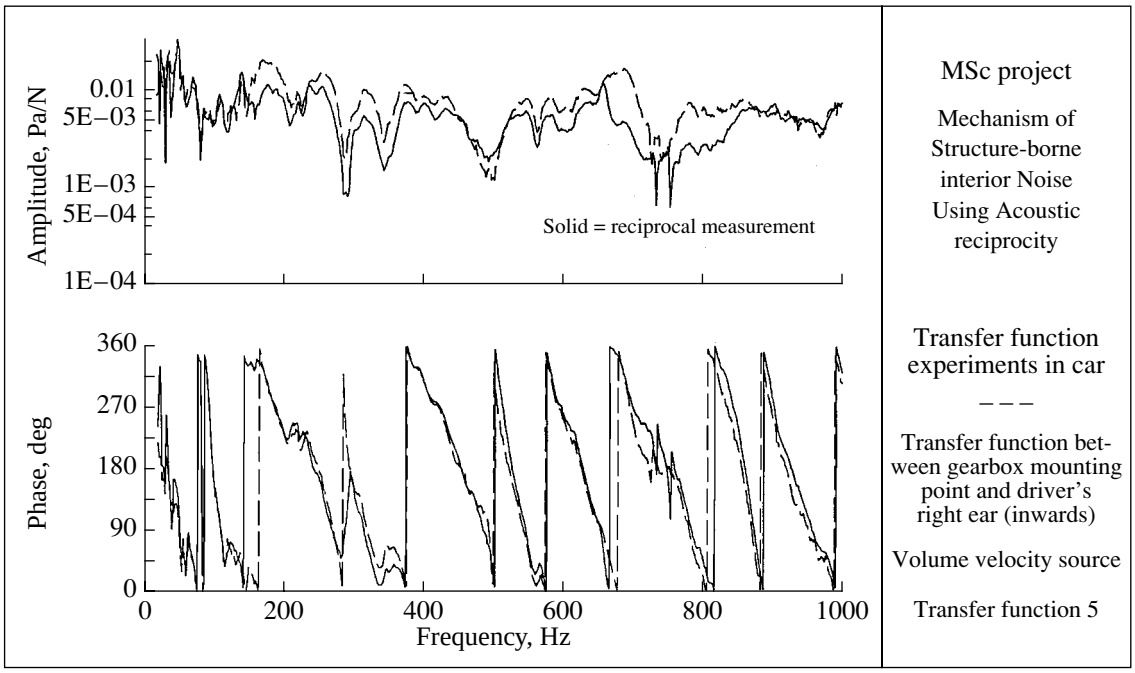

Fig. 8. Comparison of directly and reciprocally measured transfer functions between sound pressure at the right ear and the force applied at the gearbox mounting point.

automobile manufacturers, may also be used to investigate inputs from engine and exhaust system supports.

The same basic technique has been applied to the determination of the insertion loss of railside barriers by a method based upon mechanical substitution forces applied to the static wheel of a rail wagon and to the supporting rail [10]. The relevant force-to-sound pressure transfer functions were obtained reciprocally by exciting the system by a railside source and measuring the resultant accelerations at the locations of the substitute sources (a wheel has to be jacked up for this purpose). Good agreement was obtained between the results of this method and that based upon substitution acoustic sources described above.

5.2. Noise Generation by Unknown Forces Acting at Known Locations

If the *operational* forces that act at known locations and directions (ports) are not precisely known, inverse force identification techniques may be applied. In one method, vibrational (or impact) inputs are applied in appropriate directions to the passive structure (not operating) at each input port in turn by means of electromagnetic shakers or instrumented hammers. The force-to-sound pressure transfer functions may then be directly evaluated at a number of points in the fluid (which must include target points of specific interest). This number is usually chosen to exceed the number of assumed inputs in order to produce an overdetermined inverse problem which allows subsequent suppression of measurement errors, noise, and ill-conditioned data. These transfer functions may, in principle, also be determined reciprocally by insonifying the structure by means of a monopole source placed sequentially at the sound field response points and measuring the acceleration responses at the (unconstrained) input ports; that is, by the application of Lyamshev reciprocity.

The cross-spectral matrix of sound pressure responses at the selected points is then measured during vehicle operation. Pseudoinversion of the transfer function matrix, together with the application of a regularization procedure to improve the model, allows the operational input forces and their individual contributions sound pressure to be determined. This method is not very reliable because many sources other than the selected input forces contribute to the operational noise in the cabin, the measured vibroacoustic transfer functions are subject to considerable measurement error, and the transfer function matrix is generally not well-conditioned.

In an alternative, three-stage method, acceleration responses per unit force (vibrational transfer functions) are determined at a number of easily accessible points on the passive structure, preferably clustered in the region of the structure around each input port. These may be determined reciprocally by applying impacts to the structure at the selected points and measuring the acceleration responses in the appropriate directions at the (unconstrained) input ports. As before, the number of excitation points is chosen to produce an overdetermined inverse problem. The operational acceleration

responses may then be employed to determine the input forces by pseudoinversion of the matrix of vibrational transfer functions. The use of purely vibrational response transfer functions to determine the unknown forces is more reliable than the vibroacoustic method described above.

The force-to-pressure transfer functions at selected target points in the fluid may then be reciprocally determined by insonification of the passive structure by a monopole source located sequentially at the target points in the fluid. The contributions of each input force to the sound pressure at each target point is simply determined by matrix multiplication of the previously determined force vector by the appropriate force-to-pressure transfer function. Examples are presented by Hendrics [12] and Mas *et al.* [23]. An excellent review of the inverse technique, together with recommendations for its implementation, are presented by Blau [4].

5.3. The Equivalent Force and Pseudo Force Models

Many successful applications were made in the 1970s to sound radiation from ship and building structures by engineers at TPD/TNO in Delft, where many practical engineering applications of reciprocity were pioneered [27]. This institute has been principally responsible for a number of the more recent developments of reciprocal methods, particularly those based upon the concepts of *equivalent* and *pseudo* force distributions. In cases where noise is generated by complex assemblages of components subject to a number of simultaneous forms of excitation, such as the power trains and pipework of ships, the forms, locations, and directions of inputs are not precisely known and access to the suspected input regions is often difficult or impossible. It is therefore impracticable to simulate the excitations by externally applied artificial sources such as electromagnetic shakers and impact hammers. The application of the inverse technique described above is not practicable for the same reasons.

The concept and method of *equivalent* forces is employed in cases where it is required to determine the contribution of a particular structural or fluid (or coupled) transmission path from a primary source to noise received at some target location(s) of particular interest [30]. A set of equivalent input forces is assumed to act on an accessible (external) region of the structure that is considered to act as a principal transmission path. A number of response positions (greater than the number of equivalent forces) is selected between the locations of the assumed forces and the target receivers. Transfer functions between these assumed inputs and the acceleration responses are measured, either directly, by applying external excitation at the points of application, and in the directions, of the assumed equivalent forces, or indirectly, by exploiting vibrational reciprocity. Operational cross-spectral matrices of accelerations are measured and the best fit magnitudes and phases of the assumed equivalent forces are determined inversely on the basis of best least-square error fit: these are called "equivalent forces." Regularization is usually applied to the matrix inversion process to improve the quality of the results. Having reduced the system of inputs to a set of known forces at known positions, Lyamshev reciprocity may be exploited to determine the transfer functions between these forces and the sound pressure at target receiver points, and hence the contribution to the sound pressure of the selected transmission path. An example of the application of the equivalent source strategy to the determination of contributions to pass-by noise of the superstructure and bogies of a rail freight wagon is presented by De Beer and Verheij [6]. Janssens and Verheij [16] describe an application to the experimental quantification of structural sound transmission in ships.

A more general method, in which the noise generated at target points in a fluid by individual mechanical components such as motors, pumps, and gearboxes (defined as "sources"), is based upon the concept of *pseudo* forces. The success of the technique depends upon the judicious selection of the number and location of equivalent forces, each set of which is selected to be strongly related to one of the assumed principal physical source mechanisms. It is implicitly assumed, and has to be confirmed in each case, that the derived pseudo forces are rather independent of the source environment (the system(s) to which it is connected). The positions of the acceleration responses are principally confined to the external surface of each principal source, although ancillary positions may be selected on receiver structures to which the sources are connected, or to positions in a contiguous fluid. The process of best matching of the pseudo force to the operational acceleration is similar to that described for equivalent forces. However, it may be necessary to apply principal component analysis in cases where two (or more) uncorrelated excitation mechanisms contribute substantially to the response of an individual "source." The theoretical basis of the technique is presented by Janssens and Verheij [17]. An example of the application of the pseudo force strategy to the characterization of an air compressor as a structure-borne sound source is presented by Janssens *et al.* [18].

In many cases, it is found that the number of equivalent or pseudo forces necessary to represent the vibroacoustic behavior of quite complex structural or liquid-structural systems is surprisingly small. It should be emphasized that considerations of the errors, uncertainties, and confidence estimates associated with these techniques are of vital importance in ensuring that the results of the techniques described above are reliable and physically valid.

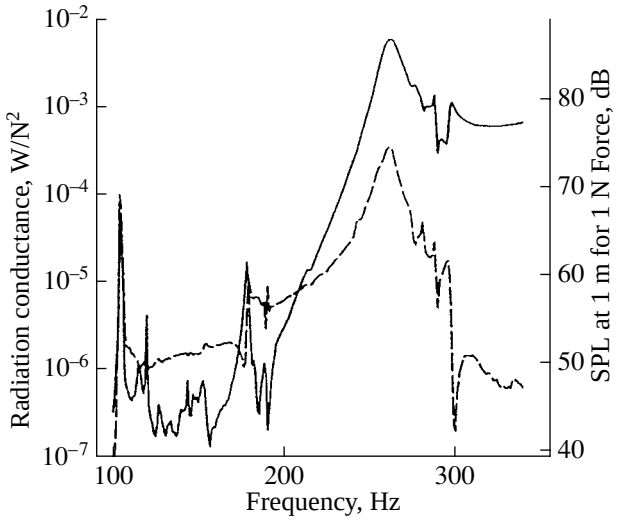

Fig. 9. Power radiation properties of violin SUS180 (Hutchins). The scale on the left is that fraction of the real part of the bridge admittance, as seen by the string, which is attributable to sound radiation. When multiplied by the square of the rms force (in newtons) applied by the string to the bridge, it yields the radiated power (in watts). The scale on the right specifies the sound power in terms of the SPL 1 m from the violin (again with a force of 1 N rms applied). The solid line is the monopole contribution; the dashed line, the dipole contribution. In the latter case, interpretation of the SPL scale requires that the sound intensity be averaged over the 1-m sphere.

5.4. Vibroacoustic Modal Analysis

In an interesting paper concerning the representation of the vibroacoustic behavior of coupled structural-fluid systems in terms of the vibroacoustic modes of the total system, Wyckaert *et al.* [32] demonstrate that although the set of second order governing equations in terms of the variables acoustic pressure, structural displacement, excitation force, and acoustic source strength are not symmetric, the system nevertheless obeys Lyamshev reciprocity. However, they sound a warning about the use of modes determined using point acoustic excitation to estimate the response to structural excitation, and vice versa. The modal participation factors must be scaled by a mode-dependent factor to obtain dynamic equivalence. Lyamshev reciprocity is not satisfied by individual modes, as it is for purely structural or purely acoustic modes, but is satisfied when all active modes are incorporated into the response function. It is thus important that modal series truncation does not exclude any significant modal contributions. Experimental results are presented which illustrate the need for correct scaling of model contributions.

5.5. Acoustically Induced Response

Lyamshev reciprocity was exploited by Garrelick and Martini [9] in an investigation of the vibrational response of a wall structure to sonic boom pressure in the frequency range 0–100 Hz. The sonic boom was simulated by the sound of a cannon. Below 75 Hz, the directly measured magnitude of the wall response in the frequency domain corresponded closely with that estimated from the acoustic response at the source position to point impact applied to the wall. The response of the wall to supersonic flyovers by an F-15 aircraft was also measured. The peak *transient* acceleration responses measured directly and computed via reciprocity exhibited significant discrepancies that were attributed to inadequacies in the representation of the sonic boom pressure field.

5.6. Violin Acoustics

In a fascinating investigation of the radiative properties of violins, G. Weinreich [31] of the University of Michigan evaluated the monopole and dipole source strengths due to a force applied to the bridge by means of reciprocal measurements. He insonified a violin in an anechoic chamber with four loudspeakers of which the outputs were adjusted in amplitude and phase to generate sound fields corresponding to the first two spherical harmonics at the violin position. Measurements of the motion of the bridge allowed him to evaluate the monopole and dipole sound powers per unit squared bridge force, as shown in Fig. 9.

5.7. Airborne Sound Transmission

The process of transmission of sound from one fluid volume to another via an intervening solid partition involves both acoustically induced response and radiation from the vibrating structure. The term “airborne” sound transmission will be used, although the principles described apply to any combinations of fluid media. Acoustic reciprocity in the frequency domain applies essentially to relationships between harmonic amplitudes and phases of inputs and outputs at pairs of discrete points. The airborne sound transmission characteristics of partitions are defined and measured in term of power quantities. Consequently, reciprocity relationships cannot be applied directly to this problem without introducing assumptions about the relationships between complex pressure amplitudes and sound powers. This is relatively easily done in the case of the standard transmission suite measurement of transmission loss (TL). Under the assumption of diffuse fields in both source and receiver rooms, the space-average mean-square pressure in the source room, and hence the intensity incident upon a partition, can be related to the source strength and the source room absorption; while that in the receiver room can be related to the transmitted power and the absorption of the receiving room. Hence the ratio p/Q, which strictly applies to pairs of points, can be translated into TL to show that it is invariant with respect to exchange of source and receiver rooms (under the rather sweeping theoretical

assumptions on which the method is based). Similar arguments based upon reciprocity can be advanced to demonstrate that the sum of the airborne and impact insulations of floors at supercritical frequencies is constant [5].

The specific application described below is to aircraft fuselage structures subject to propeller noise, but the measurement principle and the practical implementation could be applied to any airborne sound transmission problem. A basic problem that faces acousticians and structural designers concerned with developing efficient, minimum weight side-wall sound insulation systems for aircraft fuselages is that of devising experimental performance evaluation procedures. The principal source of cabin noise in current turbofan driven airliners during cruise is the turbulent boundary layer which exists on the fuselage surface: surface pressure fluctuation spectra have their major energy in the frequency range of about 500 to 3000 Hz. It is impossible to simulate a fluctuating boundary layer pressure field in a full-scale ground test facility. Consequently, sidewall treatments are normally tested between conventional transmission suite rooms and subjected to "diffuse" incident fields. Experience gathered over many years allows engineers to translate the results into a rank order that generally corresponds within acceptable tolerances to in-flight performance.

The problem of developing optimum structures and insulation systems for reducing *propeller* noise to acceptable values in a cabin is more difficult because of the low blade passage frequencies (typically 80–140 Hz) and the very complex fuselage surface pressure field, which is significantly affected by convection in forward flight. It is extremely difficult to develop passive sidewall treatments that have adequate low frequency performance and can be accommodated within the small space available between the fuselage skin and the inner trim panels. Various "simulation" facilities have been constructed by aircraft manufacturers: some favor arrays of phased loudspeakers; others run propellers close to full-scale fuselage sections in a static rig. None, however, can simulate the effects of forward flight on the propeller field, except on small models in wind tunnels, in which case insulation performance cannot be properly simulated.

Given the practical problems outlined above, and the fact that computational methods for predicting propeller sound fields were advancing very rapidly, ISVR decided to concentrate on the development of a means of characterizing a fuselage structure/insulation combination as a *transducer* of external surface pressure fields into internal sound. A technique based upon exploitation of the Lyamshev reciprocity principle has been developed and validated on 1/4-scale, bare fuselage structures. The details of the procedure were published by Mason and Fahy [24] and in Mason's PhD thesis [25]; only an outline account will be presented here.

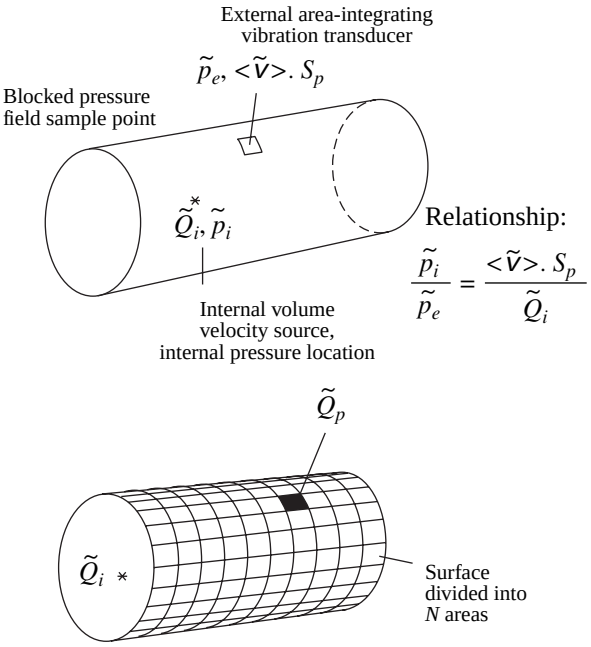

Fig. 10. Modification of Lyamshev's reciprocal relation to include distributed pressure field excitation.

The transfer function of concern is that between a point force acting on the external surface of a fuselage and the sound pressure generated at a point in the cabin space. Because a fuselage structure takes the form of a shell stiffened by frames and stringers, and it also contains windows and doors, the response of the structure, and hence the acoustic transfer function, will vary markedly with location of the force. This poses a dilemma in attempting experimentally to characterize dynamic behavior in terms of transfer functions. However, because a forcing pressure field has a continuous and coherent distribution, it may be represented by an array of discrete, contiguous "patches" of *uniform* pressure, provided that the dimensions of each patch are suitably small. On the basis that such a distribution may be represented by a dense distribution of uniform point forces acting on each patch, it is possible to extend Lyamshev's reciprocity principle, as illustrated in Fig. 10.

The vital innovation is that the surface vibration velocity produced by the operation of the monopole source in the receiver space is spatially integrated over each patch by a capacitive transducer to generate a signal proportional to the surface volume velocity. (Today, a VAS would probably be used.) A major advantage of such a transducer is that it acts as a spatial frequency (wavenumber) filter, thereby avoiding the aliasing problem encountered when making point measurements with the accelerometers.

A set of transfer functions between a source at a receiver point in the cabin and the surface volume velocities represents a unique, once-for-all calibration of the fuselage as a pressure transducer. The sound gen-

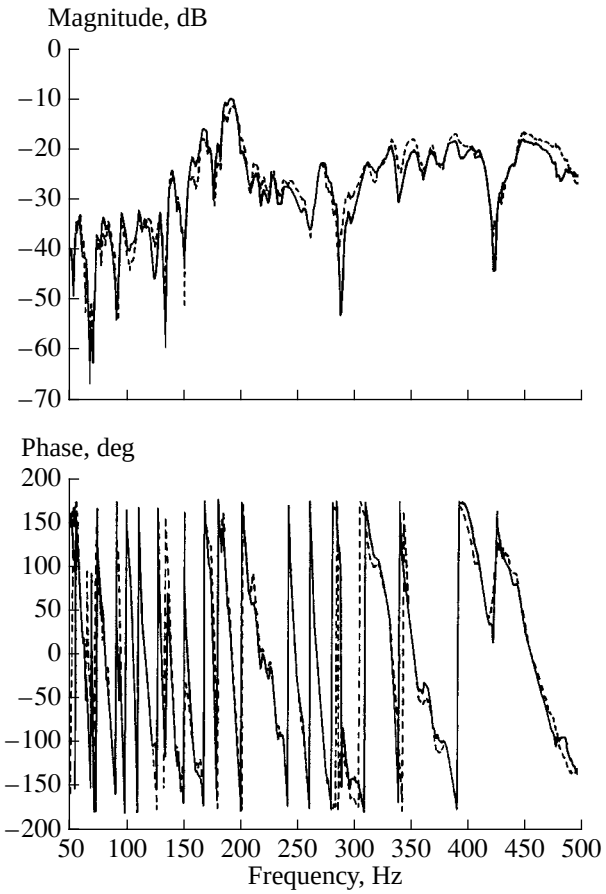

Fig. 11. Comparison of directly measured and reciprocally estimated transfer functions between external sound pressure on the fuselage of a full-scale aircraft and the sound pressure generated in the cabin.

erated at that receiver point by any externally applied pressure field that satisfies the spatial discretization criterion (1/8 wavelength) may be computed. Hence, the response to theoretically modeled propeller fields, plane waves, diffuse fields, concentrated pressure fields, etc., may be compared. Propeller and flight parameters may also be varied to study their influence on cabin noise. The method may be applied to full-scale static structures, with and without side-wall insulation, furnishings, etc., to provide rank-ordered performance data. Of course, the procedure may be repeated at a number of receiver points to obtain a "spatial-average" estimate of mean square pressure. This technique has been successfully applied to a full-scale aircraft, as illustrated by Fig. 11 [22].

5.8. Sonar Self Noise and Turbulent Flow Noise in Vehicles

The vibration of a sonar window generated by turbulent flow over a surface ship or submarine generates unwanted sound pressures on the sensors and associated noise in the sonar signal. The transfer functions between the external turbulent pressures and the pressure on a sensor element may be approximately evaluated by driving the sensor and measuring the vibrational acceleration at an array of points on the window [1].

In principle, the same technique could be exploited to evaluate the noise generated at a point in a vehicle by the unsteady pressure field generated by the airflow over the vehicle. The acceleration response of the relevant region(s) of the structure to insonification by a monopole source located at the receiver target point(s) would be measured at a sufficiently large number of points on the structure: the required density of points would be defined by the correlation scale of the external pressure field. The resulting transfer functions would be combined with theoretical or measured external pressure field data. No example of the application of this technique to this problem has been found in the open literature, but it is possible that it could be useful in dealing with wind noise in automotive vehicles.

6. CONCLUSION

The vibroacoustic reciprocity principle may be exploited in many cases of practical interest to provide information in a simpler, faster, and cheaper manner than by direct test methods.

POSTSCRIPT

A very useful summary of a range of mechano–electroacoustic reciprocity relations is presented by Verheij [30].

REFERENCES

1. Ph. Audet, P. Marin Curtoud, T. Rohan, and M. Lagier, in *Proceedings of Réunion du Groupement Acoustique Industrielle et Environnement de la Société Française d'Acoustique* (1990).
2. Yu. I. Belousov and A. V. Rimskii-Korsakov, Sov. Phys. Acoust. **21**, 103 (1975).
3. A. P. Berkhoff, E. Sarajlic, B. S. Cazzolato, and C. H. Hansen, in *Proceedings of the 8th International Congress on Sound Vibration* (2001), Vol. 3, p. 1629.
4. M. Blau, in *Proceedings of InterNoise* (2000), Paper 243.
5. L. Cremer, M. Heckl, and E. Ungar, *Structure-borne Sound*, 2nd ed. (Springer, Berlin, 1987).
6. F. G. De Beer and J. W. Verheij, J. Sound Vibr. **231** (3), 639 (2000).
7. F. J. Fahy, Acustica **81**, 544 (1995).
8. F. J. Fahy, Proc. Inst. Acoust. (UK) **21** (3), 161 (1999).
9. J. Garrelick and Kyle Martini, J. Acoust. Soc. Am. **101**, 1456 (1997).
10. A. C. Geerlings and J. W. Verheij, in *Proceedings of InterNoise* (1999), p. 265.

11. A. C. Geerlings, D. J. Thompson, and J. W. Verheij, Appl. Acoust. **62**, 979 (2001).
12. W. Hendrics, in *Proceedings of the 19th International Seminar on Modal Analysis* (Leuven, Belgium, 1994), p. 1037.
13. K. R. Holland and F. J. Fahy, Proc. Inst. Acoust. (UK) **15** (3), 246 (1993).
14. K. R. Holland and F. J. Fahy, in *Proceedings of Inter-Noise 96: Noise Control Foundation* (Poughkeepsie, New York, 1996), p. 2581.
15. K. R. Holland and F. J. Fahy, Noise Control Eng. J. **45** (5), 217 (1997).
16. M. H. A. Janssens and J. W. Verheij, J. Sound Vibr. **226** (2), 305 (1999).
17. M. H. A. Janssens and J. W. Verheij, Appl. Acoust. **61**, 285 (2000).
18. M. H. A. Janssens, J. W. Verheij, and T. Loyau, Appl. Acoust. **63**, 9 (2001).
19. G. J. Kim, PhD Thesis (Univ. of Southampton, 1998).
20. L. M. Lyamshev, Sov. Phys. Dokl. **4**, 406 (1959).
21. L. M. Lyamshev, Sov. Phys. Acoust. **5**, 122 (1959).
22. D. G. MacMartin, G. L. Basso, F. W. Slingerland, and L. Hurtubise, *NRC-CNRC Report LTR-ST-1942* (National Research Council of Canada, 1993).
23. P. Mas, P. Sas, and K. Wyckaert, in *Proceedings of the 19th International Seminar on Modal Analysis* (Leuven, Belgium, 1994), p. 1049.
24. J. M. Mason and F. J. Fahy, Noise Control Eng. J. **34** (2), 43 (1990).
25. J. M. Mason, PhD Thesis (Univ. of Southampton, 1990).
26. J. Pankoke, MSc Dissertation (Univ. of Southampton, 1993).
27. T. Ten Wolde, Acustica **28**, 23 (1973).
28. J. W. Verheij, in *Proceedings of the Third International Congress on Recent Developments in Air- and Structure-borne Sound Vibration* (1994), Vol. 1, p. 647.
29. J. W. Verheij, Int. J. Acoust. Vibr. **2** (1), 11 (1997).
30. J. W. Verheij, Int. J. Acoust. Vibr. **2** (3), 103 (1997).
31. G. Weinreich, J. Acoust. Soc. Am. **77**, 710 (1985).
32. K. Wyckaert, F. Augusztinovicz, and P. Sas, J. Acoust. Soc. Am. **100**, 3172 (1996).
33. J. H. Zheng, F. J. Fahy, and D. Anderton, Appl. Acoust. **42**, 333 (1994).

Acoustical Physics, Vol. 49, No. 2, 2003, pp. 230–232. Translated from Akusticheskiĭ Zhurnal, Vol. 49, No. 2, 2003, pp. 278–280.

SHORT COMMUNICATIONS

In memory of L.M. Lyamshev, who paid much attention to experimental studies and to physical interpretation of nontrivial data

Diurnal Studies of the Sound Field Intensity in the Vicinity of the First Convergence Zone

R. A. Vadov

Andreev Acoustics Institute, Russian Academy of Sciences, ul. Shvernika 4, Moscow, 117036 Russia

e-mail: vadov@akin.ru

Received January 21, 2002

In comparing the measured intensity structure of the sound field produced by a point source in the vicinity of the first convergence zone with the calculated one, researchers often faced noticeable disagreements between these data, both in the levels of the sound field within certain parts of the first zone and in the distances at which the convergence zone begins. One of the most probable reasons for the disagreements is the indefiniteness in specifying the vertical sound speed profile $c(z)$ in calculating the sound field. In fact, as a rule, the sound speed is measured either before the acoustic experiment or after it; in addition, the depths of measurements do not reach the sea floor but rather have some finite value (often smaller than 1.5–2 km). The time variability of the sound speed field, which can take place during experimentation, is ignored.

To reveal the time (diurnal) variability of the intensity structure of the sound field in the vicinity of the first convergence zone, researchers from the Acoustics Institute have performed a number of experiments in different regions of the ocean all over the world. One of these experiments was carried out in the Norwegian Sea. Let us consider the data of this experiment.

The experiment was performed in autumn (the end of September) in the southern part of the region (near the Norwegian Basin) with a towed piezoceramic sound source. The technique used in the experiment was described in [1] in detail. The receiving vessel drifted carrying omnidirectional sound receivers that were deployed at depths of 15, 60, 150, and 500 m. The transmitting vessel moved off the receiving one or towards it, thereby repeatedly crossing the first convergence zone. The sound source was towed at a depth of 120–125 m. A continuous noiselike signal was transmitted in a 1/3-octave frequency band around the central frequency of 3 kHz. The towing speed was 2–3 knots. Every 3–5 minutes, the distance between the source and the receivers was measured. The time of a single tack of the vessel was determined by the length of the zone at the 500-m horizon. Five tacks were performed in one day.

At the beginning of each tack, the vertical profile of the sound speed was measured from the receiving vessel in the most dynamical subsurface water layer, down to 400–600 m. Figure 1 shows a set of five profiles $c(z)$ measured during the experimentation to demonstrate the diurnal variability of the upper water layers. The measured profiles $c(z)$ exhibit small variations (up to 10 m) in the depth of the temperature discontinuity layer, changes (from –0.1 to –0.14 1/s) in the sound speed gradient at a depth of 50–100 m, and changes (from 130 to 190 m) in the depth of the weakly pronounced minimum of the sound speed.

As the starting data for analyzing the diurnal variability of the sound field, sound field levels were used that were measured at the same distances in each of the five crossings of the first convergence zone. Continuous

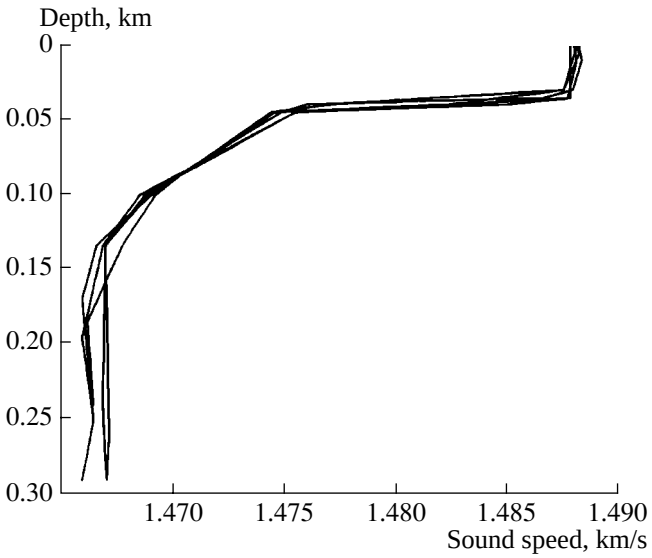

Fig. 1. Vertical sound speed profiles measured in the Norwegian Sea during the experiment on studying the diurnal variability of the sound field in the first convergence zone.

1063-7710/03/4902-0230$24.00 © 2003 MAIK “Nauka/Interperiodica”

records of the sound field levels were made by a 2307 Bruel & Kjer device in the mode of recording absolute mean values (with slide-averaging over 1–2 s). The levels of the sound pressure varying along the convergence zone were digitized at 25-m distance increments.

The diurnal variability of the sound field is illustrated by Fig. 2, which presents the measured levels of the sound pressure for 60- and 500-m reception depths. The tacks, at which the sound pressure levels were measured, are ordered in time (from the bottom to the top of the figure). To avoid overlapping, the adjacent curves are shifted vertically by 15 dB relative to each other. The first tack (at approaching) was started at 11 : 20 a.m. (local time). The last tack (also at approaching) was terminated at 11 : 00 a.m. of the next day.

Further data processing was performed by a computer. At each distance, the mean value of the sound field level was determined, along with its rms spread. From the threshold sound field level specified for the beginning of the zone, the mean value was calculated for the distance from the source to the nearest boundary of the convergence zone, along with its rms spread.

At depths of 15, 60, and 150 m, the maximal value of the rms spread in the sound field level, as averaged over 5 tacks, corresponded to the beginning of the zone and was equal to 3–4 dB. The distance from the source to the nearest boundary of the convergence zone (as determined at a level of about 72–75 dB relative to 2×10^{-5} Pa) was 44.0, 41.4, and 40.5 km, respectively, with an rms spread of 150–170 m (at a 15-m depth, the rms spread was as high as 300 m!). At a 500-m depth, the convergence zone split into two half-zones. The distance from the source to the nearest boundary of the first half-zone was 36.3 km, and the distance to the second half-zone was 45.7 km, with rms spreads of 100 and 150 m, respectively. The deeper the reception horizon, the lower was the rms spread in the distance to the nearest boundary of the zone.

To reveal the role of the upper 400-m water layer in the diurnal variability of the sound field in the first convergence zone, a series of calculations were performed. The sound field was calculated separately for five profiles $c(z)$ whose upper parts are shown in Fig. 1. In the calculations, the ray-approximation computer code [2] developed by Tebyakin was used. The missing part of the profiles $c(z)$ (for horizons deeper than 500–1000 m) was reconstructed from the data of the deep-water measurements that were closest to the experiment in time. The results of calculations were used to analyze the resulting groups of five curves, where each curve represented the change in the sound field level for one of the five reception depths. As a result, we obtained the rms spreads of the sound field levels at each distance from the source, the distances to the nearest boundary of the convergence zone, and the rms spreads of these distances. The calculations yielded the values of the distance to the nearest boundary of the convergence zone that were 1–1.3 km lower than the experimental value.

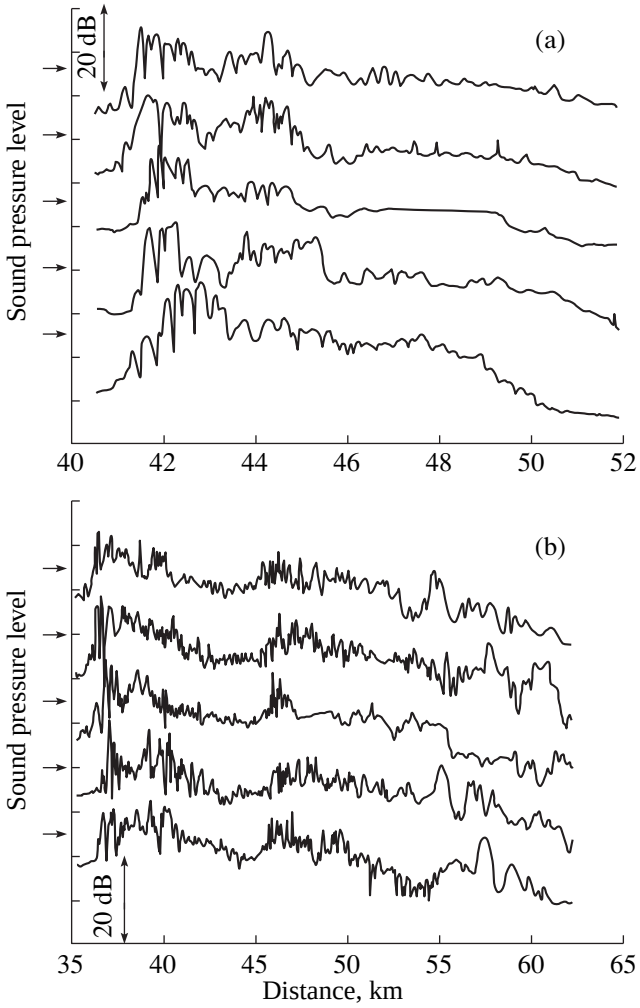

Fig. 2. Sound pressure levels measured in the first convergence zone. The source depth is 120–150 m, the receiver depths are (a) 60 and (b) 500 m. The sound pressure levels measured at different times of the day are shifted by 15 dB relative to each other. The arrows (on the left of each curve) indicate the level of 75 dB relative to 2×10^{-5} Pa.

The values obtained for the rms spread were either greater or smaller than the experimental ones. Thus, for a 60-m reception horizon, the calculated mean distance to the zone was found to be 40.2 km instead of 41.3 km for the measured distance, with rms spreads of 129 and 150–170 m, respectively. For a 500-m reception depth, the calculated distances to the first and second half-zones are 35 km instead of 36.3 and 44.5 km instead of 45.7 km, respectively, with rms spreads of 300 and 110 m in the calculations against 100 and 150 m in the experiment. As in the experiment, the maximal calculated variance of the sound field level corresponds to the initial part of the zone; it reaches 3.5–4.5 dB (this value is slightly higher than the experimental one).

A comparison of the data obtained with those published earlier [1] for the eastern region of the Atlantic Ocean suggests the conclusion that, in the Norwegian

Sea, the diurnal variability of the sound field is weaker. One can also notice that, with the same difference between the calculated and experimental distances to the zone (about 1 km), the calculation yields higher values (as compared to the experiment) for the Atlantic Ocean and lower values for the Norwegian Sea. Presumably, these features are governed by a certain indefiniteness in specifying the profile $c(z)$ for horizons deeper than 1000–1500 m (the direct measurements of the profiles $c(z)$ were performed down to 400–600 m). The calculations carried out for the experiment in the Norwegian Sea showed that, if at these depths the sound speed gradient varies by as little as –0.0006 1/s, the distance to the first convergence zone increases by 1 km.

Thus, the main factor responsible for the diurnal variability of the sound field in the first convergence zone seems to be the disturbance of the 400-m upper water layer. The diurnal variability of the sound field in the Norwegian sea is quite comparable (and even somewhat lower) with that in the eastern region of the Central Atlantic, which is rather stable in its characteristics governing sound propagation.

ACKNOWLEDGMENTS

This work was supported by the Russian Foundation for Basic Research, project no. 01-02-16636.

REFERENCES

1. R. A. Vadov, Akust. Zh. **41**, 202 (1995) [Acoust. Phys. **41**, 172 (1995)].
2. V. P. Tebyakin *et al.*, A Report (Akust. Inst. Akad. Nauk SSSR, Moscow, 1990).

Translated by E. Kopyl

Acoustical Physics, Vol. 49, No. 2, 2003, pp. 233–235. Translated from Akusticheskiĭ Zhurnal, Vol. 49, No. 2, 2003, pp. 281–283.

SHORT COMMUNICATIONS

Secondary Streaming Accompanying the Wave Propagation in Narrow Pipes

R. G. Galiullin*, L. A. Timokhina*, and S. E. Filipov**

** Kazan State University, ul. Kremlevskaya 18, Kazan, 420008 Russia*

*** Institute of Mechanics and Mechanical Engineering, Kazan Science Center, Russian Academy of Sciences, ul. Lobachevskogo 2/31, Kazan, 420111 Russia*

e-mail: Sergey.Philipov@ksu.ru

Received October 23, 2001

Abstract—A theory describing the secondary streaming that accompanies the acoustic wave propagation in a narrow cylindrical pipe of infinite length is presented. © *2003 MAIK "Nauka/Interperiodica".*

Studies of acoustic wave propagation in narrow pipes [1–5], including the accompanying secondary acoustic streaming, are topical in view of the thermoacoustic effects [6], which can serve as a basis for designing heat (cooling) engines [6, 7].

The description of secondary streaming in a traveling wave is given in [8], but this description cannot be considered as adequate, because it uses the following limitations: first, the problem is solved for a one-dimensional model, whereas real acoustic streaming is not one-dimensional [9], and, second, the problem is considered for a non-heat-conducting liquid. Below, we present a theory that describes secondary streaming in a travelling wave without using the aforementioned limitations.

Consider a pipe whose one end ($x = 0$) contains a piston performing harmonic oscillations with a displacement amplitude l_0. To characterize the oscillations, we introduce the parameters

$$M_p = \frac{\omega l_0}{c_0}, \quad H = R\sqrt{\frac{\omega}{\nu}}, \quad N = \frac{\omega R}{c_0}. \tag{1}$$

The first two of them (M_p and H) were considered in [10], and the third, in view of the relation $k_0 \sim \lambda^{-1}$ (where λ is the wavelength), has the meaning of the ratio of the pipe radius to the wavelength. Hence, the condition $N \ll 1$ corresponds to the case of a narrow pipe.

Assume that $M_p \ll 1$, $H \gg 1$, and $N \ll 1$. The solution of the equations in the first approximation by the perturbation method for $M_p \ll 1$ and $N \ll 1$ can be found in [10]. One can easily show that a wave traveling to the right has the form

$$p_1 = C\exp i(\omega t - kx),$$

$$u_1 = \frac{p_1}{\rho_0 c_0}(1 - e^{-(1+i)\eta}),$$

$$\rho_1 = \frac{1}{c_0^2}[1 + (\kappa - 1)e^{-(1+i)\eta\sqrt{\sigma}}]p_1,$$

$$v_1 = \frac{(1+i)\omega\delta}{2\rho_0 c_0^2} \tag{2}$$

$$\times\left\{\left(1 + \frac{\kappa-1}{\sqrt{\sigma}}\right)\frac{r}{R} - e^{-(1+i)\eta} - \frac{\kappa-1}{\sqrt{\sigma}}e^{-(1+i)\eta\sqrt{\sigma}}\right\}p_1,$$

$$k = k_0\{(1 + \beta') + i\beta''\}, \quad \beta'' = -\beta',$$

$$\beta' = \frac{1}{2}\left(1 + \frac{\kappa-1}{\sqrt{\sigma}}\right)\frac{\delta}{R}, \quad \eta = \frac{R-r}{\delta}, \quad C = \rho_0 c_0^2 M_p$$

with allowance for the fact that, at the piston, $u_p = \omega l_0 \exp(i\omega t)$. Here, p, u, v, ρ, and k are the pressure, the axial and radial velocities, the density, and the wave number, respectively; δ is the boundary layer thickness; $\kappa = C_P/C_V$ is the specific heat ratio; $\sigma = \nu/\chi$ is the Prandtl number determined as the ratio of the kinematic viscosity ν to the thermal diffusivity of the medium α; and the subscript 1 indicates that the quantities correspond to the first approximation.

The equations describing the stationary acoustic streaming in the second-order approximation have the form

$$\frac{\partial\langle p_2\rangle}{\partial x} - \frac{\mu}{r}\frac{\partial}{\partial r}\left(r\frac{\partial\langle u_2\rangle}{\partial r}\right)$$

$$= -\rho_0\left(\left\langle u_1\frac{\partial u_1}{\partial x}\right\rangle + \left\langle v_1\frac{\partial u_1}{\partial r}\right\rangle\right) - \left\langle \rho_1\frac{\partial u_1}{\partial t}\right\rangle,$$

$$\rho_0\left[\frac{1}{2}\frac{\partial}{\partial r}(r\langle v_2\rangle) + \frac{\partial\langle u_2\rangle}{\partial x}\right] \tag{3}$$

$$= -\left\langle v_1\frac{\partial\rho_1}{\partial r}\right\rangle - \left\langle u_1\frac{\partial\rho_1}{\partial x}\right\rangle - \left\langle\frac{\rho_1}{\rho_0}\frac{\partial\rho_1}{\partial t}\right\rangle,$$

1063-7710/03/4902-0233$24.00

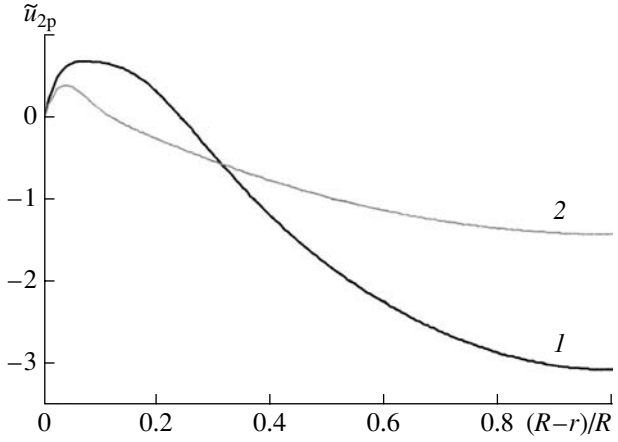

Fig. 1. Dependence of $\tilde{u}_{2p}$ on the dimensionless radial coordinate $(R - r)/R$ for two values of the Prandtl number σ = (*1*) 0.1 and (*2*) 0.7.

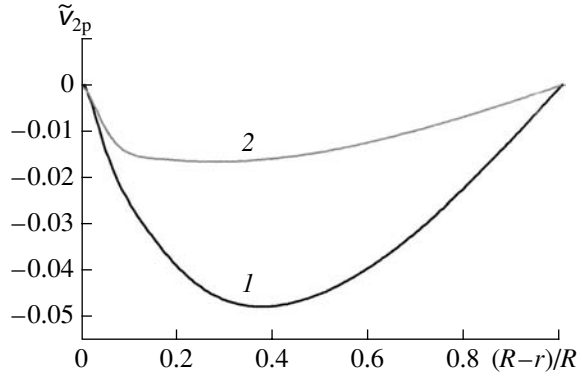

Fig. 2. Dependence of $\tilde{v}_{2p}$ on the dimensionless radial coordinate $(R - r)/R$ for two values of the Prandtl number σ = (*1*) 0.1 and (*2*) 0.7.

$$\frac{\partial \langle p_2 \rangle}{\partial r} = 0,$$

where the angular brackets mean the time averaging.

Equations (3) are solved by the method described in [11], and the resulting expressions for $\langle u_2 \rangle$ and $\langle v_2 \rangle$ are as follows:

$$\langle u_2 \rangle = -\frac{M_p^2 c_0}{2} e^{-2k_0 x\beta'} \times \left[g_1(\eta, \sigma) + g_1(0, \sigma)\left(1 - \frac{2r^2}{R^2}\right) + 2\left(1 - \frac{r^2}{R^2}\right)\right],$$

$$\langle v_2 \rangle = -\frac{1}{2}\beta' \omega R M_p^2 e^{-2k_0 x\beta'} \times \left[g_1(0, \sigma)\left(\frac{r}{R} - \frac{r^3}{R^3}\right) + \left(\frac{2r}{R} - \frac{r^3}{R^3}\right) - \frac{g_2(\eta, \sigma)}{g_2(0, \sigma)}\right], \quad (4)$$

where

$$g_1(\eta, \sigma) = -\left(1 + \frac{\kappa - 1}{\sqrt{\sigma}}\right)e^{-\eta}\sin\eta + e^{-\eta}\cos\eta - \frac{1}{2}e^{-2\eta} + \frac{\kappa - 1}{\sigma}e^{-\eta\sqrt{\sigma}}\cos\eta\sqrt{\sigma} - \frac{\kappa - 1}{1 + \sigma}e^{-(1 + \sqrt{\sigma})\eta}\cos(1 - \sqrt{\sigma})\eta + \frac{\kappa - 1}{\sqrt{\sigma}(1 + \sigma)}e^{-(1 + \sqrt{\sigma})\eta}\sin(1 - \sqrt{\sigma})\eta,$$

$$g_2(\eta, \sigma) = -e^{-\eta}\cos\eta - e^{-\eta}\sin\eta + (\kappa - 1)\left(1 + \frac{\kappa - 2}{\sqrt{\sigma}}\right)e^{-\eta\sqrt{\sigma}}\cos\eta\sqrt{\sigma} - (\kappa - 1)\left(1 + \frac{\kappa}{\sqrt{\sigma}}\right)e^{-\eta\sqrt{\sigma}}\sin\eta\sqrt{\sigma} - \frac{(\kappa - 1)^2}{\sqrt{\sigma}}e^{-2\eta\sqrt{\sigma}} - (\kappa - 1)e^{-(1 + \sqrt{\sigma})\eta}\cos(1 - \sqrt{\sigma})\eta - (\kappa - 1)e^{-(1 + \sqrt{\sigma})\eta}\sin(1 - \sqrt{\sigma})\eta,$$

$$g_1(0, \sigma) = \frac{1}{2} + \frac{\kappa - 1}{\sigma(1 + \sigma)}, \quad g_2(0, \sigma) = -\left(1 + \frac{\kappa - 1}{\sqrt{\sigma}}\right),$$

$$\frac{1}{2\beta'}\frac{\delta}{R}g_2(0, \sigma) = -1.$$

Consider the properties of these solutions. One can see that the direction of the axial velocity component $\langle u_2 \rangle$ is opposite to the direction of the wave propagation. This situation is different from that of an Eckart flow, where the beam direction coincides with the direction of $\langle u_2 \rangle$ [9]. Another difference consists in the fact that an Eckart flow disappears when the beam touches the pipe wall.

The structure of the flows is determined by the expressions $\tilde{u}_2 = \langle u_2 \rangle / M_p^2 c_0$ and $\tilde{v}_2 = \langle v_2 \rangle / M_p^2 \omega R$. The dependence of $\tilde{u}_{2p}$, where the subscript p indicates the value at the piston, on the quantity $(R - r)/R$ is shown in Fig. 1 for two values of σ: curves *1* and *2* refer to σ = 0.1 and 0.7, respectively. One can see that a decrease in the Prandtl number leads to a considerable increase in the absolute value of $\tilde{u}_{2p}$. One also can notice that, near the wall, the latter quantity is positive, $\tilde{u}_{2p} > 0$, and proves to be much smaller than in the flow core. An increase in the Prandtl number leads to a decrease in the region where $\tilde{u}_{2p} > 0$.

Figure 2 presents the dependence of $\tilde{v}_{2p}$ on $(R - r)/R$ for two different Prandtl numbers (curves *1* and *2* correspond to σ = 0.1 and 0.7, respectively). One can see that a decrease in σ leads to an increase in the absolute values of $\tilde{v}_{2p}$ with a simultaneous shift of the maximum of $\tilde{v}_{2p}$ toward the pipe axis.

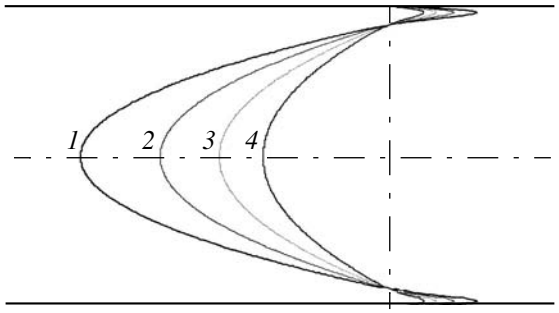

Fig. 3. Profiles of $\tilde{u}_2$ corresponding to different distances $\bar{x} = x/\lambda$ for $\sigma = 0.7$: $\bar{x}$ = (*1*) 0, (*2*) 1, (*3*) 2, and (*4*) 3.

The profiles of $\tilde{u}_2$ corresponding to different distances $\bar{x} = x/\lambda$ (λ is the wavelength) to the piston are presented in Fig. 3 for $\sigma = 0.7$. Curves *1*, *2*, *3*, and *4* correspond to the distances $\bar{x}$ = 0, 1, 2, and 3, respectively.

Thus, the presence of heat conduction and the non-one-dimensionality of the flow considerably affect the characteristics of acoustic streaming in narrow pipes.

REFERENCES

1. J. Kordomenos, A. A. Atchley, R. Raspet, and H. E. Bass, J. Acoust. Soc. Am. **98**, 1623 (1995).
2. H. S. Roh, W. P. Arnott, R. Raspet, and J. M. Sabatier, J. Acoust. Soc. Am. **89**, 2617 (1991).
3. W. P. Arnott, H. E. Bass, and R. Raspet, J. Acoust. Soc. Am. **90**, 3228 (1991).
4. K. S. Peat, J. Sound Vibr. **203** (5), 855 (1997).
5. Luc Bauwens, J. Fluid Mech. **324**, 135 (1996).
6. N. Rott, Adv. Appl. Mech. **20**, 135 (1980).
7. P. H. Ceperly, J. Acoust. Soc. Am. **77**, 1239 (1985).
8. V. Niborg, in *Physical Acoustics*, Ed. by W. Mason (Academic, New York, 1964; Mir, Moscow, 1966), Vol. 1.
9. O. V. Rudenko and S. I. Soluyan, *Theoretical Foundations of Nonlinear Acoustics* (Nauka, Moscow, 1975; Consultants Bureau, New York, 1977).
10. H. Tijdeman, J. Sound Vibr. **39** (1), 1 (1975).
11. R. G. Galiullin, L. A. Timokhina, and S. E. Filipov, Akust. Zh. **47**, 611 (2001) [Acoust. Phys. **47**, 529 (2001)].

Translated by E. Golyamina

Acoustical Physics, Vol. 49, No. 2, 2003, pp. 236–238. Translated from Akusticheskiĭ Zhurnal, Vol. 49, No. 2, 2003, pp. 284–286.

LETTER TO THE EDITOR

Self-Focusing and Other Anomalous Effects in Media with Backward Waves

V. M. Byrdin

Ul. Éngel's 134-6, Taganrog, Rostov oblast, 347900 Russia

e-mail: V_M_Byrdin@mail.ru

Received April 4, 2002

1. The possibility of an anomalous negative refraction of a backward wave because of the opposition of its phase and group velocities was predicted for the first time by L.I. Mandel'shtam in the 1940s [1, 2]. Since that time, investigations of backward waves and their practical applications have been carried out in many fields of science and technology, in Russia and in other countries [3–10].[1] In particular, in 1965, Mandel'shtam's idea was used in a book by Agranovich and Ginzburg [13] (p. 276 and Fig. 17) as applied to new problems of crystal optics. In 1982, I continued analyzing the reflection and refraction in multimode systems with backward waves [14]. The general pattern of the phenomenon is represented in Fig. 1. It is important to note that anomalous effects occur precisely in the case of opposite transformations [15–19], i.e., from the incidence of a backward wave to the reflection of an outgoing (direct) wave and so on.[2]

This paper reports on a fundamentally new phenomenon that consists in the self-focusing of divergent wave fronts in the case of the reflection, refraction, and diffraction of waves in homogeneous multimode systems with backward waves, i.e., in negatively dispersive homogeneous media or waveguide structures. The paper also considers the laws of reflection and refraction for such systems and indicates the possibility of anomalous "negative" diffraction.

2. Let us formulate the following statements on the basis of the radiation principles [11, 12, 22].

Statement 1. The first and second modified Snell–Descartes laws expressed in terms of the projections of wave vectors and group velocities onto the boundary [onto the z axis of the $x0z$ incidence plane (Fig. 1)] and onto the normal (the x coordinate) have the forms $k_{\mathrm{refl},\,z} = k_{\mathrm{inc},\,z}$, $U_{\mathrm{refl},\,x}/U_{\mathrm{inc},\,x} < 0$ (the first law) and $k_{\mathrm{refr},\,z} = k_{\mathrm{inc},\,z}$, $U_{\mathrm{refr,\,X}}/U_{\mathrm{inc},\,x} > 0$ (the second law), where the subscripts inc, refl, and refr indicate the incident, reflected, and refracted modes, respectively. In multimode systems, the angle equal and opposite to the incidence angle is the reflection angle of the mode of the same branch of the dispersion spectrum as the incident wave, and only this angle. The positive angles of other like modes lie within 0°–90°. Contrary to classical concepts, unlike rays have anomalous directions with negative angles: a reflected ray lies within the quadrant of the incident ray, and a refracted ray, within the quadrant adjacent through the z axis. An unlike reflected mode is directed and carries energy and momentum against the incident wave.

Statement 2. Whole spectra of surface waves of the *SJB*, *SCB*, and *SRB* types, which correspond to the complete set of imaginary (j), complex (c), and overcritical real (r) wave numbers (the critical incidence

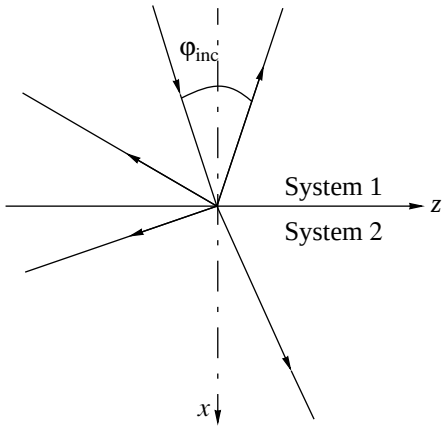

Fig. 1. Negative refraction and reflection of unlike waves in multimode systems with backward waves.

[1] One of the fundamental principles of theoretical and mathematical physics, namely, the energy radiation principle for wave, dynamic, and statistical problems of mechanics and electrodynamics of continuous media and extended bodies [11, 12, etc.], originates from the same works by Mandel'shtam [1, 2].

[2] According to the terms originating in acoustics and mathematical physics from G.D. Malyuzhinets (1951) [18–20] and in electronics and radio engineering from the efficient practical applications of backward-wave tubes (M.F. Stel'makh (1948), W. Brown (1949), and others [5, 9, 17]), we distinguish the concepts and synonyms of a backward or incoming wave [18, 19] and an outgoing or direct wave. In a general anisotropic case, for noncollinear vectors of phase and group velocities, we consider a traveling wave as an incoming one when the angle between these vectors is obtuse and as an outgoing one when the angle is acute (R.A. Silin and the author (2000); see also [13, 21]).

1063-7710/03/4902-0236$24.00

angles are $\varphi^{(i)}_{\text{inc, cr}} = \arcsin(\kappa_i)$, $\kappa_i = k_i/k_{\text{inc}} < 1$, $i = 1, 2$, or with "refl" or "refr"), arise in the case of wave reflection and refraction in multimode systems. All *SB* waves have a common phase velocity $V_{\text{inc}}/\sin\varphi_{\text{inc}}$ along the z axis (Fig. 1). Like *SRB* waves are directed along the incident wave, and unlike ones, against it. Since, as a rule, the backward wave numbers are small, the *SR* modes are formed more often in the case of the incidence of an outgoing wave. Analogously, refracted *SRB* waves are more probable in the case of wave incidence on an acoustically (or optically) sparser medium or waveguide section: $\sin\varphi^{(2)}_{\text{inc, cr}} = k_{\text{refr}}/k_{\text{inc}} < 1$, $\omega \gg 1$. The region of condensation of *SJ* and *SC* modes are the low frequencies $\omega < \inf\omega_{\text{cr}, i}$, $k_i(\omega_{\text{cr}, i}) = 0$.

3. The phenomenon of wave self-focusing necessarily occurs in the case of the reflection or refraction of spherical, cylindrical, or other divergent beams incident on a plane interface between two systems or on a plane inhomogeneity of one system when the intrinsic spectra of these systems contain backward waves.[3] The focal regions are extended along the symmetry axis, e.g., the x axis in the case of normal incidence (Fig. 2), according to the formula obtained by the author for diffuse focuses at the points of beam convergence $f_i = |x_F/x_S| = (\kappa_i^2 - \sin^2\varphi_{\text{inc}})^{0.5}/\cos\varphi_{\text{inc}}$ and lie within the limits $f_i > \kappa_i > 1$ or $1 > \kappa_i > f_i > 0$. Evidently, in the second case (when $k_{\text{inc}} > k_i$), the focusing will be more pronounced. The principal focus, i.e., the strongest of the diffuse ones, will probably coincide, as one may expect, with the point of ray concentration, because $\Delta x_F \approx \Delta\varphi\partial x_F/\partial\varphi = \Delta\varphi|x_S|(\kappa_i^2 - 1)\tan\varphi_{\text{inc}}/(f\cos^2\varphi_{\text{inc}})$; $\min\partial x_F/\partial\varphi = 0$ at $\varphi_{\text{inc}} = 0$ or at $\kappa_i = 1$. The corresponding focal distances are $f_P = \kappa_i$ and $f_P = 1$. The latter (i.e., at $k_i = k_{\text{inc}}$) corresponds to the absolute point self-focusing, or rather to the quasi-absolute one: the real focus is broadened to a certain extent by various aberrations, diffraction, dissipation, and nonlinearity.

Remark 1. In the anisotropic case, the self-focusing is also determined by the noncollinearity of the phase and group velocity vectors [R.A. Silin (2001)]. However, as has been determined by the author, the results presented above are valid on the whole for transversally isotropic systems[4] and for the majority of anisotropic systems, and anomalous effects are also partially realized by outgoing modes.

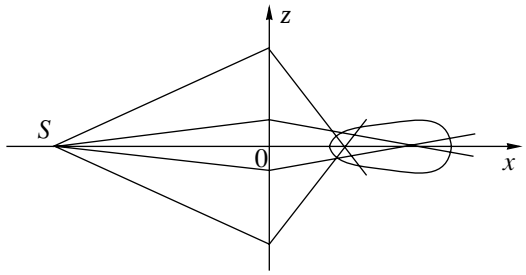

Fig. 2. Self-focusing of a refracted wave.

4. For diffraction processes with backward waves, one can expect interesting accompanying phenomena that are opposite to classical ones, as well as some new significant effects. For example, a divergent lens can work as a concentrator (but in the case of an unlike incident wave). A sharp reflection of Lamb backward waves in a plate from the boundary with a liquid was observed experimentally in [26]. In [27], it was found that an inhomogeneous magnetic field focuses backward surface magnetostatic waves and defocuses outgoing waves.

One should expect that, in a multimode medium (system) in the classical experiments on skirting a screen, the diffraction rings or fringes of backward modes will be opposite in their positions to the antinodes of outgoing modes (in the case of an outgoing incident wave and vice versa).

Thus, on the whole, one may presume a multitude of elementary phenomena of anomalous "negative" diffraction.

5. In practice, fundamentally new solutions can be obtained on the basis of wave systems with backward waves for some problems in acoustics, optics, and radio electronics, and new original devices and instruments can be designed (for example, see [9, 21, 23, 26, 28–32]).

Backward waves have many remarkable fundamental properties, and their analysis will be continued in future publications.

FROM THE EDITORIAL BOARD

The letter by V.M. Byrdin, where many important statements are made without proof, is published to attract the attention of our readers to the problem of so-called backward waves, i.e., waves whose phase and group velocities have noncoincident directions. The Editorial Board expects the author of the letter and

[3] I reported on the phenomenon of self-focusing and "absolute" self-focusing in acoustics as early as 1981 [15, 30]. In foreign publications in electrodynamics, the self-focusing in the case of the transmission through a plate in the backward wave regime was studied in [31]. Much earlier, in 1966 and 1977, the geometric-optical analysis of the same problem in connection with the focusing of spherical beams or image transfer was performed by Russian researchers [6, 23]. One way or another, the aforementioned studies deal with the fundamentally new phenomenon of self-focusing, as opposed to its other types and allied effects in optical and acoustic systems and other waveguide structures [18, 24, 25, 32]. It is important to note that parallel beams cause no self-focusing in the case of plane boundaries [3, 6]. In this case, only an insignificant "negative" diffraction of extreme beams manifests itself (see Paragraph 4).

[4] Such anisotropic media (and the corresponding systems) have a symmetry axis of the ∞ order (the y axis for Figs. 1 and 2): a rotation around this axis through any angle causes no changes in the physical properties of the medium.

other readers to present more detailed results on this interesting and little investigated problem.

REFERENCES

1. L. I. Mandel'shtam, Zh. Éksp. Teor. Fiz. **15** (9), 475 (1945); in *Complete Works* (Akad. Nauk SSSR, Moscow, 1947), Vol. 2, pp. 334–338.
2. L. I. Mandel'shtam, in *Complete Works* (Akad. Nauk SSSR, Moscow, 1950), Vol. 5, pp. 461–467.
3. R. A. Silin, Radiotekh. Élektron. (Moscow) (2002) (in press).
4. R. A. Silin, *Periodic Waveguides* (Fazis, Moscow, 2001).
5. R. A. Silin and V. P. Sazonov, *Slow-Wave Structures* (Sovetskoe Radio, Moscow, 1966).
6. V. G. Veselago, Usp. Fiz. Nauk **92**, 517 (1967) [Sov. Phys. Usp. **10**, 509 (1968)] (see also [7, 8]).
7. V. E. Pafomov, Zh. Éksp. Teor. Fiz. **32**, 366 (1957) [Sov. Phys. JETP **5**, 307 (1957)]; Tr. Fiz. Inst. im. P.N. Lebedeva Akad. Nauk SSSR **44**, 28 (1969).
8. N. F. Kovalev, in *Encyclopedia of Physics* (Bol'shaya Sovetskaya Éntsiklopediya, Moscow, 1992), Vol. 3, p. 383.
9. *Electronics: Physical Encyclopedic Dictionary*, Ed. by A. M. Prokhorov (Sovetskaya Entsiklopediya, Moscow, 1991).
10. D. R. Smith, Willie J. Padilla, D. C. Vier, *et al.*, Phys. Rev. Lett. **84** (18), 4184 (2000); Preprint (Dep. of Physics, Univ. of California, 2000).
11. B. M. Bolotovskiĭ and S. N. Stolyarov, in *Problems of Theoretical Physics: in Memory I.E. Tamm*, Ed. by V. I. Ritus (Nauka, Moscow, 1972), pp. 267–280.
12. V. M. Byrdin, Dokl. Akad. Nauk SSSR **238** (2), 293 (1978) [Sov. Phys. Dokl. **23**, 86 (1978)].
13. V. M. Agranovich and V. L. Ginzburg, *Crystal Optics with Spatial Dispersion and Excitons* (Nauka, Moscow, 1965; Springer, New York, 1984).
14. V. M. Byrdin, Opt. Spektrosk. **54** (3), 456 (1983) [Opt. Spectrosc. **54**, 268 (1983)].
15. V. M. Byrdin, in *Proceedings of 28th Scientific Conference* (Taganrog. Radio–Tekh. Inst., Taganrog, 1982), p. 48.
16. V. M. Byrdin, Izv. Taganrog. Radio–Tekh. Univ., No. 2, 56 (1997).
17. V. M. Byrdin, Candidate's Dissertation in Physics and Mathematics (Taganrog Radio Engineering Univ., Taganrog, 1996).
18. G. D. Malyuzhinets, Dokl. Akad. Nauk SSSR **78** (2), 229 (1951).
19. G. D. Malyuzhinets, Zh. Tekh. Fiz. **21** (8), 940 (1951).
20. *In Memory of Georgiĭ Danilovich Malyuzhinets*, Tr. Akust. Inst. Akad. Nauk SSSR, No. 15 (1971).
21. R. A. Silin, *Unusual Laws of Refraction and Reflection* (Fazis, Moscow, 1999).
22. R. A. Silin and I. P. Chepurnykh, Radiotekh. Élektron. (Moscow) **46** (10), 1212 (2001).
23. R. A. Silin, Opt. Spektrosk. **44**, 189 (1978) [Opt. Spectrosc. **44**, 109 (1978)].
24. A. L. Mikaélyan, *Self-Focusing Waveguides and Lenses with Variable Index of Refraction* (VINITI, Moscow, 1980).
25. L. A. Ostrovskiĭ, Vestn. Akad. Nauk SSSR, No. 11, 140 (1982).
26. B. V. Dyudin, Candidate's Dissertation in Engineering (Inst. of Radio Engineering, Taganrog, 1973).
27. V. I. Zubkov and V. I. Shcheglov, Radiotekh. Élektron. (Moscow) **45** (1), 116 (2000).
28. G. D. Malyuzhinets, Usp. Fiz. Nauk **69** (2), 321 (1959) [Sov. Phys. Usp. **2**, 749 (1959)].
29. I. G. Kondrat'ev and G. D. Malyuzhinets, in *Encyclopedia of Physics* (Sovetskaya Éntsiklopediya, Moscow, 1988), Vol. 1, pp. 664–667; *Physical Encyclopedic Dictionary* (Sovetskaya Éntsiklopediya, Moscow, 1960), Vol. 1, pp. 606–609.
30. V. M. Byrdin, in *Proceedings of 7th International Conference on Modern Problems of Mechanics of Continuous Media* (Rostov-on-Don, 2001).
31. J. Mullins, IEEE Spectr. **37** (1), 25 (2001).
32. V. E. Zakharov, in *Fundamentals of Plasma Physics*, Ed. by A. A. Galeev and R. Sudan (Énergoatomizdat, Moscow, 1984), Vol. 2; in *Encyclopedia of Physics* (Sovetskaya Éntsiklopediya, Moscow, 1988), Vol. 1, pp. 313–314.

Translated by M. Lyamshev

Acoustical Physics, Vol. 49, No. 2, 2003, pp. 239–240. Translated from Akusticheskiĭ Zhurnal, Vol. 49, No. 2, 2003, pp. 287–288.

CHRONICLE

In Memory of Alekseĭ Sergeevich Nikiforov (March 28, 1927–October 1, 2002)

On October 1, 2002, Alekseĭ Sergeevich Nikiforov—Professor, Doctor of engineering, principal researcher of the Krylov Central Research Institute, Honored Scientist of the Russian Federation, a prominent scientist, and a wonderful person—passed away due to a serious illness.

Nikiforov's first job was at the printing department of one of the design offices of the shipbuilding industry in Kazan. There, he began working in 1942. In 1947, he graduated from the Leningrad Shipbuilding College, after which he worked for some time at the Rubin Central Design Office of Marine Technology and at the Aĭsberg Central Design Office. Then he became a student of the Ul'yanov (Lenin) Electrotechnical Institute, Leningrad. After graduation, he started working at the Krylov Central Research Institute, which became his main place of work. Over a period of 30 years, Nikiforov headed one of the leading laboratories of this institute. The research projects carried out at his laboratory were related to the vibration control in ship structures—one of the burning problems of shipbuilding.

At the Krylov Central Research Institute, Nikiforov's talent for science has made itself evident. He developed an energy theory for describing the vibration fields in complex engineering structures and proposed methods for calculating these fields. The latter methods have found application in ship design. Nikiforov fundamentally contributed to the development of the theory underlying the design of vibration absorption and vibration insulation means for complex engineering structures. His studies formed a foundation for the development of the rules regulating the design of vibration control means for ship structures. Nikiforov founded a new area of research: the acoustic design of engineering structures. He managed to implement his research and development works in practice by realizing them as standard industrial techniques for vibration field calculations, rules for designing means of protection, and approved requirements imposed on the vibration characteristics of ship equipment. For achievements in ship design and in practical implementation of new technologies, Nikiforov was awarded the Badge of Honor, the Order of People's Friendship, and several medals.

The results of Nikiforov's scientific studies were published in five monographs and more than 120 scientific papers. Many of these publications have become well known among the international scientific community and were translated into different languages. Nikiforov was a member of the Acoustical societies of Russia, US, and Japan and of the International Society of Audio Engineers. He was editor-in-chief of *Technical Acoustics* (Russia) and a member of the editorial councils of *Acoustical Physics* (Russia) and *Building Acoustics* (United Kingdom).

Nikiforov was highly esteemed among scientist–acousticians. He was a member of the Scientific Council on Acoustics of the Russian Academy of Sciences and a member of the St. Petersburg Engineering Academy. For a number of years, he was a member of a section of the Scientific Council on Hydrophysics of the Academy of Sciences of the USSR and a member of the Expert Council of the USSR Supreme Certifying Commission on the Problems of Fleet and Shipbuilding.

1063-7710/03/4902-0239$24.00 © 2003 MAIK "Nauka/Interperiodica"

Nikiforov was deeply involved in tutorial activities. Eight postgraduate students prepared their candidate's dissertations and received candidate degrees under his supervision. Three of them later became doctors of science. Nikiforov was a member of the Councils authorized to confer scientific degrees at the Krylov Research Institute and the Baltic Technical University.

For many years, Professor Nikiforov, whose pedagogical talent was generally acknowledged, delivered lectures on the physical fields of ships to the students of the Marine Technical University. He chaired the theoretical seminar "Vibration of Mechanical Structures and Sound Emission from Them," which was run by the Scientific Council on Acoustics of the Academy of Sciences of the USSR. He also chaired the scientific-engineering seminars "Application of Vibration Absorption and Vibration Damping Means in Industry and Transport" and "Methods and Means of Sound and Vibration Control in Industry and Transport" at the Leningrad Science and Engineering Popularization Club.

Over a period of ten years, from 1992 to 2002, Nikiforov was the president of the East European Acoustical Association. This association had been recognized in Russia and in other countries and was a collective member of the International Commission on Acoustics (ICA) and the International Institute of Noise Control Engineering (I-INCE). From 1996 to 2001, Nikiforov was one of the seven members of the ICA.

Over the last 12 years, Nikiforov organized six international symposia under the title "Noise and Vibration in Transportation." He paid much attention to the environmental problems of noise pollution. A noise map of St. Petersburg was completed under his supervision. He participated in the development of the project of the express railroad between St. Petersburg and Moscow and took part in the parliamentary discussion concerning this project.

Colleagues of Alekseĭ Sergeevich Nikiforov deeply mourn the death of this wonderful person and sympathetic friend whose shining memory will last for many years to come.

Translated by E. Golyamina